

Quark Gluon Plasma and Cold Nuclear Matter modification of  $\Upsilon$  states at  
 $\sqrt{s_{\text{NN}}} = 5.02$  TeV with the CMS Detector

By

SANTONA TULI  
DISSERTATION

Submitted in partial satisfaction of the requirements for the degree of

DOCTOR OF PHILOSOPHY

in

Physics

in the

OFFICE OF GRADUATE STUDIES

of the

UNIVERSITY OF CALIFORNIA

DAVIS

Approved:

---

Manuel Calderón de la Barca Sánchez, Chair

---

Daniel A. Cebra

---

Ramona L. Vogt

Committee in Charge

2019

*To Papa and Ma*



## ACKNOWLEDGMENTS

It is with great pleasure that I extend my sincere gratitude to all those who have played a part, small or large, in getting me to this significant and most valuable milestone. First and foremost, I would like to thank my advisor, mentor and friend Manuel Calderón de la Barca Sánchez, who has supported me in countless ways throughout my doctorate. Manuel showed me through demonstration that it is possible to maintain good work-life balance even when the pressure is high and the deadlines are imminent. Manuel has also given me constant encouragement in my work and has shared and celebrated the milestones along the way with me. I hope I can continue to learn from you in the next phase of my life.

I have had the privilege of having not one but two advisors during my PhD. Daniel Cebra has enriched my education through lively discussions and astute career guidance. Daniel, you have the biggest heart of anyone I know and I thank you deeply for every kindness you have shown me. I am grateful to have had you as my friend, mentor, house mate and fellow softball team member.

I would like to extend my heartfelt thanks to Ramona Vogt, who engaged me in formative discussions, proofread my dissertation tirelessly, and always pushes me to hold myself to higher standards. Ramona, you are a great role model as a physicist, a woman in science, and a running fanatic. Attending conferences with you, especially when I'm sneaking into them, is nerve-racking but lot of fun.

I would like to thank my parents, AFM Nurul Alam and Hosneara Maya, for supporting and encouraging me throughout my life. I truly draw happiness and meaning in this world through you. Thank you for your unwaivering love and support. Thank you for the role you play in all my endeavors and accomplishments. I dedicate this degree to you.

Finally, I extend my thanks to my husband Brent Follin and my brothers Dipto Provas and Mukto Akash for their generosity, thoughtfulness and patience with me. You teach and inspire me constantly through discussions and by example. I love you all profoundly.

# Contents

<b>List of Figures</b>	<b>vii</b>
<b>List of Tables</b>	<b>xx</b>
<b>Abstract</b>	<b>xxi</b>
<b>1 Theoretical Background</b>	<b>1</b>
1.1 Physics of the Strong Interaction . . . . .	1
1.2 Quark-Gluon Plasma . . . . .	6
1.3 Probing Nuclear Matter using Quarkonia . . . . .	9
1.4 Effects of the QGP on Quarkonia . . . . .	10
1.5 Effects of Cold Nuclear Matter on Quarkonia . . . . .	15
1.5.1 Initial-State CNM Effects . . . . .	16
1.5.2 Final-State CNM Effects . . . . .	25
1.6 A Clean Probe . . . . .	29
1.7 A Challenge: Quarkonium Production . . . . .	32
1.8 Observables . . . . .	36
1.9 Outline of the Report . . . . .	39
<b>2 Experimental Facilities</b>	<b>41</b>
2.1 CERN and the LHC . . . . .	41
2.2 Compact Muon Solenoid Detector . . . . .	42

2.2.1	Coordinate System . . . . .	44
2.2.2	Detector Components . . . . .	44
<b>3</b>	<b>Some Analysis Techniques</b>	<b>60</b>
3.1	Data Collection . . . . .	60
3.2	Data Augmentation . . . . .	62
3.3	Checking Robustness of Results . . . . .	64
<b>4</b>	<b>Bottomonia in the QGP</b>	
	<i>Strong suppression of <math>\Upsilon</math> mesons in PbPb collisions at <math>\sqrt{s_{NN}} = 5.02</math> TeV</i>	<b>67</b>
4.1	Data selection and simulation samples . . . . .	68
4.2	Analysis procedure . . . . .	70
4.2.1	Signal extraction . . . . .	70
4.2.2	Corrections . . . . .	73
4.2.3	Systematic uncertainties . . . . .	75
4.3	Results . . . . .	77
4.3.1	Differential cross sections in pp and PbPb collisions . . . . .	78
4.3.2	Nuclear modification factor $R_{AA}$ . . . . .	78
4.4	Summary and Outlook . . . . .	84
<b>5</b>	<b>Analysis Setup</b>	<b>86</b>
5.1	Data Analysis at CMS . . . . .	86
5.1.1	Labeling Streaming Data . . . . .	87
5.1.2	Software Framework for Processing Data . . . . .	88
5.2	Analysis Workflow and Software . . . . .	89
5.3	Data Processing . . . . .	90
5.3.1	Proton-lead Collision Data . . . . .	91
5.3.2	Proton-proton Collision Data . . . . .	93
5.3.3	Monte Carlo Simulations . . . . .	94

5.4	Data Reduction . . . . .	98
5.4.1	Collision Event Selection . . . . .	98
5.4.2	Muon Quality Selection . . . . .	99
<b>6</b>	<b>Regression Model</b>	<b>102</b>
6.1	Defining the Analysis Domain . . . . .	104
6.2	Data Binning . . . . .	105
6.3	Building the Model . . . . .	107
6.3.1	Signal Model . . . . .	107
6.3.2	Background Model . . . . .	113
6.4	Yield Extraction . . . . .	116
6.4.1	Integrated Bin . . . . .	116
6.4.2	Transverse Momentum Binning . . . . .	118
6.4.3	Rapidity Binning . . . . .	121
6.4.4	Additional Kinematic Binning . . . . .	125
6.4.5	Activity Binning . . . . .	127
<b>7</b>	<b>Transformation of Extracted Yields</b>	<b>131</b>
7.1	Reweighting the Kinematic Distributions in Simulated Data . . . . .	133
7.2	Acceptance . . . . .	135
7.3	Efficiency . . . . .	140
<b>8</b>	<b>Estimation of Systematic Uncertainties</b>	<b>147</b>
8.1	Choice of Signal Model . . . . .	149
8.2	Choice of Background Model . . . . .	152
8.3	Choice of Acceptance Correction . . . . .	156
8.4	Choice of Efficiency Correction . . . . .	157
8.5	Study of total systematic uncertainty in results . . . . .	158
<b>9</b>	<b>Results and Discussion</b>	<b>163</b>

9.1	Inclusive Cross Section . . . . .	164
9.2	Cold Nuclear Matter Modification . . . . .	166
9.3	Forward-Backward Production Ratio . . . . .	171
9.4	Suppression in Hot and Cold Nuclear Matter . . . . .	172
9.5	Comparisons to Other Experiments . . . . .	175
9.6	Conclusions . . . . .	177
<b>Appendix A Consistency Checks</b>		<b>180</b>
A.1	Comparison of $\Upsilon$ cross sections in pPb data in two directions . . . . .	181
A.2	Comparison of $\Upsilon$ cross sections in pp data measured in two analyses . . . . .	183
A.3	Study of efficiency with and without T&P weighting . . . . .	184
A.4	Variations in efficiency due to sources of T&P uncertainty . . . . .	185
A.5	Relative contributions of T&P uncertainties . . . . .	186

# List of Figures

1.1	The building blocks of ordinary matter [1]. . . . .	2
1.2	The running coupling constant of QCD. The different bands correspond to different renormalization schemes used in perturbative QCD at short distances. The bands are extended to the nonperturbative regime characterized by confinement using AdS/QCD continuation of the perturbative regime. The transition scale $\mathfrak{Q}_0$ for each renormalization scheme is shown [2]. See reference [2] for a description of the schemes indicated. . . . .	5
1.3	The phase diagram of QCD matter [3]. . . . .	7
1.4	$\Upsilon$ mesons are produced early in heavy-ion collisions and survive long enough to outlive the thermodynamic phase of the QGP [4]. . . . .	10
1.5	The evolution of bottomonium spectral functions with increasing temperature of the QGP [5]. . . . .	14
1.6	EPPS16 calculation of $R_i^A(x, \mathfrak{Q}_0^2)$ as a function of $x$ [6]. . . . .	19
1.7	The same probe resolves fewer gluons due to fluctuations in a low energy proton (left) than in a high energy proton (right) [7]. . . . .	20
1.8	The gluon cascades of two high energy partons merge together in the saturation regime [7]. . . . .	22
1.9	Quarkonium production in a proton-nucleus collision showing the various time scales involved. The color octet state is long lived, and the gluon emission amplitudes of the incident gluon and the produced color octet state can interfere [8]. . . . .	25

1.10	Observed nuclear modification of charmonium states along with predictions of modification from nPDF (dashed black line) and comover interaction (solid blue and red lines) effects [9]. . . . .	29
1.11	The mass ordering of bottomonia. The possible hadronic and radiative decay paths of dissociating S-wave states $\Upsilon(1S)$ , $\Upsilon(2S)$ and $\Upsilon(3S)$ are illustrated [10].	32
1.12	Factorization of $\Upsilon$ production in a proton-proton collision [4]. . . . .	34
1.13	Increasing $J/\psi$ multiplicity with associated track multiplicity in proton-proton collisions [11]. . . . .	35
2.1	Cartoon showing the location of the LHC tunnel and the four major experiments at CERN [12]. . . . .	43
2.2	A longitudinal view (top) and cross section (bottom) of the CMS detector [13].	45
2.3	A sectional view of the CMS detector showing the detector components [13].	47
2.4	Longitudinal cross section of one quadrant of the CMS detector showing the layout of the tracking system [14]. . . . .	48
2.5	Photo of pixel detectors in the tracker next to the beam pipe [15]. . . . .	49
2.6	Photo of strip detectors in the tracker in the barrel region [16]. . . . .	49
2.7	Photos of a single crystal of the endcap ECAL with a VPT attached (left) and a collection of crystals arranged to form one half of an endcap disk of the ECAL (right) [14]. . . . .	51
2.8	Photo of an barrel HCAL ring being inserted into the solenoid of CMS [17]. .	52
2.9	Photo of an HF tower before installation into CMS showing the quartz fibers [18].	53
2.10	Longitudinal cross section of one quadrant of the CMS detector showing the layout of muon detectors [19]. . . . .	54
2.11	Transverse cross section of the barrel region of the CMS detector showing paths and stopping of different types of particles [13]. . . . .	56
2.12	Schematic cross section of a drift tube (DT) [14]. . . . .	56
2.13	Schematic cross sections of a cathode strip chamber (CSC) and its response to an incident muon [20]. . . . .	58

2.14	Schematic cross section of a resistive plate chamber (RPC) [21]. . . . .	59
3.1	The workflow of performing full simulations of CMS data [22]. . . . .	63
3.2	Technical overview of the stages of MC simulation of CMS data [22]. . . . .	64
4.1	Invariant mass distribution of opposite-sign muon pairs in pp (left) and PbPb (right) collisions, for the kinematic range $p_T^{\mu\mu} < 30$ GeV and $ y^{\mu\mu}  < 2.4$ . In both figures, the GLM fitted to the data are shown as solid blue lines. The separate yields for each $\Upsilon$ state in pp are shown as dashed red lines in the left panel. In order to depict the level of suppression of the $\Upsilon$ states in PbPb collisions, the amplitudes of the peaks in the fit are scaled by the inverse of the measured $R_{AA}$ for each state. This is shown as dashed red lines in the right panel. . . . .	73
4.2	Differential cross sections of the $\Upsilon(1S)$ , $\Upsilon(2S)$ , and $\Upsilon(3S)$ mesons as a function of $p_T$ for pp (left) and PbPb (right) collisions. The error bars represent the statistical uncertainties and the boxes the systematic uncertainties. For the $\Upsilon(3S)$ meson in PbPb collisions, the upper limits at 68 % (green box) and 95 % (green arrow) CL are shown. The global integrated luminosity uncertainties of 2.3 % in pp collisions and $^{+3.4}_{-3.9}$ % in PbPb collisions are not shown. . . . .	79
4.3	Differential cross sections of the $\Upsilon(1S)$ , $\Upsilon(2S)$ , and $\Upsilon(3S)$ mesons as a function of $ y $ for pp (left) and PbPb (right) collisions. The global integrated luminosity uncertainties are not shown. . . . .	79
4.4	Nuclear modification factors for $\Upsilon(1S)$ , $\Upsilon(2S)$ , and $\Upsilon(3S)$ mesons as functions of $p_T$ (left) and $ y $ (right). The gray box near the line at unity displays the global uncertainty, which combines the uncertainties from $T_{AA}$ , pp luminosity, and PbPb $N_{MB}$ . . . . .	80

4.5	Nuclear modification factors for the $\Upsilon(1S)$ , $\Upsilon(2S)$ , and $\Upsilon(3S)$ mesons as a function of $\langle N_{\text{part}} \rangle$ . The boxes at the dashed line at unity represent global uncertainties: the open box for the integrated luminosity in pp collisions and $N_{\text{MB}}$ in PbPb collisions, while the full boxes show the uncertainties in $\Upsilon(1S)$ (red) and $\Upsilon(2S)$ (blue) yields in pp collisions. . . . .	81
4.6	Nuclear modification factors for the $\Upsilon(1S)$ (left) and $\Upsilon(2S)$ (right) mesons as a function of $\langle N_{\text{part}} \rangle$ compared to calculations from Krouppa and Strickland [23], and Du, He, and Rapp [24]. The box at the dashed line at unity represents the global uncertainty from the integrated luminosity in pp collisions, $N_{\text{MB}}$ in PbPb collisions, and the total uncertainty in the pp yields. The data-to-prediction ratios are shown in the bottom panels. The orange points and their errors correspond to predictions using $4\pi\eta/s = 2 \pm 1$ in reference [23]. The green points and their errors correspond to the central value and width of the predicted range in reference [24]. . . . .	82
4.7	Comparison of $R_{AA}$ values for the $\Upsilon(1S)$ , $\Upsilon(2S)$ , and $\Upsilon(3S)$ mesons at $\sqrt{s_{\text{NN}}} = 5.02$ TeV and $\sqrt{s_{\text{NN}}} = 2.76$ TeV [25] for integrated centrality in the full kinematic range. . . . .	83
5.1	Dimuons in the generator level MC with acceptance cuts as function of $p_T$ vs. $y_{\text{CM}}$ for pp. The left, middle and right plots show dimuons in the $\Upsilon(1S)$ , $\Upsilon(2S)$ and $\Upsilon(3S)$ MC, respectively. . . . .	95
5.2	Dimuons in the generator level MC with acceptance cuts as function of $p_T$ vs. $y_{\text{CM}}$ for pPb. The left, middle and right plots show dimuons in the $\Upsilon(1S)$ , $\Upsilon(2S)$ and $\Upsilon(3S)$ MC, respectively. . . . .	96
5.3	Dimuons in acceptance in the fully-reconstructed MC as a function of $p_T$ and $y_{\text{CM}}$ for pp collisions. The left, middle and right plots show dimuons in the $\Upsilon(1S)$ , $\Upsilon(2S)$ and $\Upsilon(3S)$ MC simulations, respectively. . . . .	97

5.4	Dimuons in acceptance in the fully-reconstructed MC as a function of $p_T$ and $y_{CM}$ for pPb collisions. The left, middle and right plots show dimuons in the $\Upsilon(1S)$ , $\Upsilon(2S)$ and $\Upsilon(3S)$ MC simulations, respectively. . . . .	98
6.1	Plots of the dimuon $p_T$ (left) and invariant mass vs $p_T$ (right) distributions in pPb data. . . . .	105
6.2	Nominal fits to the pp (left) and pPb (right) invariant mass distributions in the integrated bin. . . . .	117
6.3	A visual representation of the measured $R_{pA}$ of the three $\Upsilon$ states. The nominal fit to the pPb data in the integrated $p_T$ , $y_{CM}$ bin is once again shown by the solid blue line. The dashed red line is obtained by scaling the $\Upsilon(1S)$ , $\Upsilon(2S)$ , and $\Upsilon(3S)$ signal shapes by the inverse of the measured $R_{pPb}$ for each state. . . . .	117
6.4	Nominal fits to the pp (left) and pPb (right) data for $p_T \in [0 - 2]$ GeV/ $c$ . . . . .	118
6.5	Nominal fits to the pp (left) and pPb (right) data for $p_T \in [2 - 4]$ GeV/ $c$ . . . . .	119
6.6	Nominal fits to the pp (left) and pPb (right) data for $p_T \in [4 - 6]$ GeV/ $c$ . . . . .	119
6.7	Nominal fits to the pp (left) and pPb (right) data for $p_T \in [6 - 9]$ GeV/ $c$ . . . . .	119
6.8	Nominal fits to the pp (left) and pPb (right) data for $p_T \in [9 - 12]$ GeV/ $c$ . . . . .	119
6.9	Nominal fits to the pp (left) and pPb (right) data for $p_T \in [12 - 30]$ GeV/ $c$ . . . . .	120
6.10	Nominal fits to the pp (left) and pPb (right) data for $p_T \in [0 - 4]$ GeV/ $c$ . . . . .	120
6.11	Nominal fits to the pp (left) and pPb (right) data for $p_T \in [4 - 9]$ GeV/ $c$ . . . . .	120
6.12	Nominal fits to the pp (left) and pPb (right) data for $p_T \in [9 - 30]$ GeV/ $c$ . . . . .	120
6.13	Nominal fits to the pp (left) and pPb (right) data for $p_T \in [0 - 6]$ GeV/ $c$ . . . . .	121
6.14	Nominal fits to the pp (left) and pPb (right) data for $p_T \in [6 - 30]$ GeV/ $c$ . . . . .	121
6.15	Nominal fit to pPb data for $-2.87 < y_{CM} < -1.93$ . . . . .	121
6.16	Nominal fits to the pp (top) and pPb (bottom) data for $ y_{CM}  \in [1.2 - 1.93]$ . . . . .	122
6.17	Nominal fits to the pp (top) and pPb (bottom) data for $ y_{CM}  \in [0.8 - 1.2]$ . . . . .	122
6.18	Nominal fits to the pp (top) and pPb (bottom) data for $ y_{CM}  \in [0.4 - 0.8]$ . . . . .	123
6.19	Nominal fits to the pp (top) and pPb (bottom) data for $ y_{CM}  \in [0 - 0.4]$ . . . . .	123

6.20	Nominal fits to the pp (top) and pPb (bottom) data for $ y_{\text{CM}}  \in [0.8 - 1.93]$ .	124
6.21	Nominal fits to the pp (top) and pPb (bottom) data for $ y_{\text{CM}}  \in [0 - 0.8]$ .	124
6.22	Nominal fits to the pp (top) and pPb (bottom) data for $ y_{\text{CM}}  \in [0 - 1.93]$ .	125
6.23	Nominal fits to the pp (top) and pPb (bottom) data for $p_{\text{T}} \in [0, 6]$ GeV/ $c$ (low $p_{\text{T}}$ ) and $ y_{\text{CM}}  \in [0 - 1.93]$ .	126
6.24	Nominal fits to the pp (top) and pPb (bottom) data for $p_{\text{T}} \in [6, 30]$ GeV/ $c$ (high $p_{\text{T}}$ ) and $ y_{\text{CM}}  \in [0 - 1.93]$ .	126
6.25	Nominal fits to the pPb data in backward (left) and forward (right) $y_{\text{CM}}$ for $E_{\text{T}} \in [0 - 12]$ GeV.	127
6.26	Nominal fits to the pPb data in backward (left) and forward (right) $y_{\text{CM}}$ for $E_{\text{T}} \in [12 - 19]$ GeV.	127
6.27	Nominal fits to the pPb data in backward (left) and forward (right) $y_{\text{CM}}$ for $E_{\text{T}} \in [19 - 27]$ GeV.	128
6.28	Nominal fits to the pPb data in backward (left) and forward (right) $y_{\text{CM}}$ for $E_{\text{T}} \in [27 - 120]$ GeV.	128
6.29	Nominal fits to the pPb data in backward (left) and forward (right) $y_{\text{CM}}$ for $E_{\text{T}} \in [12 - 120]$ GeV.	128
6.30	Nominal fits to the pPb data in backward (left) and forward (right) $y_{\text{CM}}$ for $N_{\text{tracks}} \in [0 - 40]$ .	129
6.31	Nominal fits to the pPb data in backward (left) and forward (right) $y_{\text{CM}}$ for $N_{\text{tracks}} \in [40 - 62]$ .	129
6.32	Nominal fits to the pPb data in backward (left) and forward (right) $y_{\text{CM}}$ for $N_{\text{tracks}} \in [62 - 88]$ .	129
6.33	Nominal fits to the pPb data in backward (left) and forward (right) $y_{\text{CM}}$ for $N_{\text{tracks}} \in [88 - 400]$ .	130
6.34	Nominal fits to the pPb data in backward (left) and forward (right) $y_{\text{CM}}$ for $N_{\text{tracks}} \in [40 - 400]$ .	130

7.1	The measured $p_T$ distributions of muon pairs in the $\Upsilon(1S)$ mass range in data and MC (top) and their ratio (bottom) in pp collisions. . . . .	134
7.2	The measured $p_T$ distributions of muon pairs in the $\Upsilon(1S)$ mass range in data and MC (top) and their ratio (bottom) in pPb collisions. . . . .	135
7.3	Nominal and systematically varied acceptance correction factors as functions of $p_T$ for $\Upsilon(1S)$ , $\Upsilon(2S)$ and $\Upsilon(3S)$ in pPb collisions. . . . .	136
7.4	Nominal and systematically varied acceptance correction factors as functions of $p_T$ for $\Upsilon(1S)$ , $\Upsilon(2S)$ and $\Upsilon(3S)$ in pp collisions. . . . .	136
7.5	Nominal and systematically varied acceptance correction factors as functions of $y_{CM}$ for $\Upsilon(1S)$ , $\Upsilon(2S)$ and $\Upsilon(3S)$ in pPb collisions. . . . .	137
7.6	Nominal and systematically varied acceptance correction factors as functions of $ y_{CM} $ for $\Upsilon(1S)$ , $\Upsilon(2S)$ and $\Upsilon(3S)$ in pp collisions. . . . .	137
7.7	Nominal and systematically varied acceptance correction factors in backward and forward regions for low- $p_T$ (left) and high- $p_T$ (right) $\Upsilon(1S)$ in pp collisions.	137
7.8	Nominal and systematically varied acceptance correction factors in backward and forward regions for low- $p_T$ (left) and high- $p_T$ (right) $\Upsilon(2S)$ in pp collisions.	138
7.9	Nominal and systematically varied acceptance correction factors in backward and forward regions for low- $p_T$ (left) and high- $p_T$ (right) $\Upsilon(3S)$ in pp collisions.	138
7.10	Nominal and systematically varied acceptance correction factors in backward and forward regions for low- $p_T$ (left) and high- $p_T$ (right) $\Upsilon(1S)$ in pPb collisions.	138
7.11	Nominal and systematically varied acceptance correction factors in backward and forward regions for low- $p_T$ (left) and high- $p_T$ (right) $\Upsilon(2S)$ in pPb collisions.	139
7.12	Nominal and systematically varied acceptance correction factors in backward and forward regions for low- $p_T$ (left) and high- $p_T$ (right) $\Upsilon(3S)$ in pPb collisions.	139
7.13	T&P corrected reconstruction efficiency for $\Upsilon(1S)$ as functions of $p_T$ (left) and $y_{CM}$ (right) in pp (top) and pPb (bottom) collisions. . . . .	143
7.14	T&P corrected reconstruction efficiency for $\Upsilon(2S)$ as functions of $p_T$ (left) and $y_{CM}$ (right) in pp (top) and pPb (bottom) collisions. . . . .	144

7.15	T&P corrected reconstruction efficiency for $\Upsilon(3S)$ as functions of $p_T$ (left) and $y_{CM}$ (right) in pp (top) and pPb (bottom) collisions. . . . .	144
7.16	T&P corrected reconstruction efficiency for low- (left) and high- (right) $p_T$ $\Upsilon(1S)$ in pp collisions. . . . .	145
7.17	T&P corrected reconstruction efficiency of $\Upsilon(1S)$ mesons for $(p_T, y_{CM}) \in [0, 6, 30] \text{ GeV}/c \otimes [-1.93, 0, 1.93]$ . The blue line depicts the integrated efficiency in the backward (left) and forward (right) regions, needed for the $R_{FB}$ . . . . .	145
7.18	T&P corrected reconstruction efficiency for low- (left) and high- (right) $p_T$ $\Upsilon(2S)$ in pp collisions. . . . .	146
7.19	T&P corrected reconstruction efficiency of $\Upsilon(2S)$ mesons for $(p_T, y_{CM}) \in [0, 6, 30] \text{ GeV}/c \otimes [-1.93, 0, 1.93]$ . The blue line depicts the integrated efficiency in the backward (left) and forward (right) regions, needed for the $R_{FB}$ . . . . .	146
7.20	T&P corrected reconstruction efficiency of $\Upsilon(3S)$ mesons for $(p_T, y_{CM}) \in [0, 6, 30] \text{ GeV}/c \otimes [-1.93, 0, 1.93]$ . The blue line depicts the integrated efficiency in the backward (left) and forward (right) regions, needed for the $R_{FB}$ . . . . .	146
8.1	Results of a hundred pseudoexperiments in the integrated bin for $\Upsilon(1S)$ showing the percentage deviations between nominal and alternate signal models in the yields in pp and pPb as well as the $R_{pA}$ . . . . .	150
8.2	Results of a hundred pseudoexperiments in the integrated bin for $\Upsilon(2S)$ showing the percentage deviations between nominal and alternate signal models in the yields in pp and pPb as well as the $R_{pA}$ . . . . .	151
8.3	Results of a hundred pseudoexperiments in the integrated bin for $\Upsilon(3S)$ showing the percentage deviations between nominal and alternate signal models in the yields in pp and pPb as well as the $R_{pA}$ . . . . .	151

8.4	Weighting the kinematic distribution of single muons in the MC simulation used to construct the alternate background PDF for pPb collisions in bins containing low- $p_T$ $\Upsilon$ . . . . .	154
8.5	Plots of fitted MC invariant mass distributions in the four $p_T$ intervals: $p_T \in [0, 1.5, 3, 4.5, 30]$ GeV/ $c$ . The fitted shapes are used as basis functions for building a linear combination which can be used to model the background distribution in most analysis bins. . . . .	155
8.6	Results of a hundred pseudoexperiments in the integrated bin for $\Upsilon(1S)$ showing the percentage deviations between nominal and alternate background models in the yields in pp and pPb as well as the $R_{pA}$ . . . . .	156
8.7	Comparison of systematics uncertainties in pp cross section as a function of $p_T$ .	159
8.8	Comparison of systematics uncertainties in pPb cross section as a function of $p_T$ . . . . .	159
8.9	Comparison of systematics uncertainties in pp cross section as a function of $ y_{CM} $ . . . . .	160
8.10	Comparison of systematics uncertainties in pPb cross section as a function of $y_{CM}$ . . . . .	160
8.11	Comparison of systematics uncertainties in $R_{pA}$ as a function of $p_T$ . . . . .	160
8.12	Comparison of systematics uncertainties in $R_{pA}$ as a function of $y_{CM}$ . . . . .	161
8.13	Comparison of systematics uncertainties in $R_{pA}$ in forward and backward $y_{CM}$ for low $p_T$ . . . . .	161
8.14	Comparison of systematics uncertainties in $R_{pA}$ in forward and backward $y_{CM}$ for high $p_T$ . . . . .	161
8.15	Comparison of systematics uncertainties in $R_{FB}$ as a function of $E_T$ . . . . .	162
8.16	Comparison of systematics uncertainties in $R_{FB}$ as a function of $N_{tracks}$ . . . . .	162

- 9.1 Cross section times dimuon branching fraction of  $\Upsilon(1S)$  (red circles),  $\Upsilon(2S)$  (blue squares), and  $\Upsilon(3S)$  (green diamonds) as a function of  $p_T$  (left) and rapidity (right) in pPb collisions. Error bars on the points represent statistical and fit uncertainties and filled boxes represent systematic uncertainties. A 3.5 % global uncertainty in determining the integrated luminosity of pPb collisions, applicable to all points, is not included in the point-by-point uncertainties. . . . . 165
- 9.2 Cross section times dimuon branching fraction of  $\Upsilon(1S)$  (red circles),  $\Upsilon(2S)$  (blue squares), and  $\Upsilon(3S)$  (green diamonds) as a function of  $p_T$  (left) and rapidity (right) in pp collisions. Error bars on the points represent statistical and fit uncertainties and filled boxes represent systematic uncertainties. A 2.3 % global uncertainty in determining the integrated luminosity of pp collisions, applicable to all points, is not included in the point-by-point uncertainties. . . . . 165
- 9.3  $R_{pPb}$  of  $\Upsilon(1S)$  (red circles),  $\Upsilon(2S)$  (blue squares), and  $\Upsilon(3S)$  (green diamonds) as a function of  $p_T$  for  $|y_{CM}| < 1.93$  (left) and versus  $y_{CM}$  for  $p_T < 30$  GeV/ $c$  (right). Error bars on the points represent statistical and fit uncertainties and filled boxes represent systematic uncertainties. The gray box around the line at unity represents the global uncertainty due to luminosity normalization. All three  $\Upsilon$  states are suppressed in pPb collisions compared to pp collisions throughout the kinematic region explored. For each  $\Upsilon$  state, the measured  $R_{pPb}$  is consistent with a constant value across the kinematic range. The  $\Upsilon$  states show a sequential pattern of suppression, with  $\Upsilon(1S)$  the least suppressed. 167
- 9.4  $R_{pPb}$  of  $\Upsilon(1S)$  (red circles) versus  $y_{CM}$  with initial-state model calculations: nPDF modification from R. Vogt [26] (left) and energy loss with and without shadowing corrections from F. Arleo and S. Peigné [27] (right). Error bars on the points represent statistical and fit uncertainties and filled boxes represent systematic uncertainties. The gray box around the line at unity represents the global uncertainty due to luminosity normalization. . . . . 168

9.5	<p><math>R_{\text{pPb}}</math> versus <math>y_{\text{CM}}</math> with comover effect predictions from E. Ferreiro and J.-P. Lansberg [28] with shadowing corrections using nCTEQ15 and EPS09 for <math>\Upsilon(1\text{S})</math> (upper left; red circles), <math>\Upsilon(2\text{S})</math> (upper right; blue squares) and <math>\Upsilon(3\text{S})</math> (lower; green diamonds). Error bars on the points represent statistical and fit uncertainties and filled boxes represent systematic uncertainties. The gray box around the line at unity represents the global uncertainty due to luminosity normalization. . . . .</p>	170
9.6	<p><math>R_{\text{pPb}}</math> of <math>\Upsilon(1\text{S})</math> (red circles), <math>\Upsilon(2\text{S})</math> (blue squares), and <math>\Upsilon(3\text{S})</math> (green diamonds) at forward and backward rapidity for <math>0 &lt; p_{\text{T}} &lt; 6</math> GeV/<math>c</math>(left) and <math>6 &lt; p_{\text{T}} &lt; 30</math> GeV/<math>c</math> (right). The points are shifted horizontally for better visibility. Error bars on the points represent statistical and fit uncertainties and filled boxes represent systematic uncertainties. The gray box around the line at unity represents the global uncertainty due to luminosity normalization. . . .</p>	171
9.7	<p><math>R_{\text{FB}}</math> vs. <math>N_{\text{tracks}}</math> at mid pseudorapidity (left) and vs. <math>E_{\text{T}}</math> at forward/backward pseudorapidity (right) of <math>\Upsilon(1\text{S})</math> (red circles), <math>\Upsilon(2\text{S})</math> (blue squares), and <math>\Upsilon(3\text{S})</math> (green diamonds) for <math>p_{\text{T}} &lt; 30</math> GeV/<math>c</math> and <math> y_{\text{CM}}  &lt; 1.93</math>. Error bars on the points represent statistical and fit uncertainties and filled boxes represent systematic uncertainties. . . . .</p>	172
9.8	<p><math>R_{\text{pPb}}</math> of <math>\Upsilon(1\text{S})</math>, <math>\Upsilon(2\text{S})</math> and <math>\Upsilon(3\text{S})</math> (red circles) for the integrated kinematic range <math>0 &lt; p_{\text{T}} &lt; 30</math> GeV and <math> y_{\text{CM}}  &lt; 1.93</math>. The <math>R_{\text{pPb}}</math> results are compared to the CMS results on <math>\Upsilon R_{\text{AA}}</math> (blue squares for <math>\Upsilon(1\text{S})</math> and <math>\Upsilon(2\text{S})</math> and blue arrow for <math>\Upsilon(3\text{S})</math> at 95 % confidence level) for <math>0 &lt; p_{\text{T}} &lt; 30</math> GeV and <math> y_{\text{CM}}  &lt; 2.4</math> at the same energy [29]. Error bars represent statistical and fit uncertainties and filled boxes around points represent systematic uncertainties. The gray and red boxes around the line at unity depict the uncertainty in the pp and pPb luminosity normalizations, respectively. The blue box around unity depicts the global uncertainty pertaining to PbPb data. . . . .</p>	174

9.9	$R_{pPb}$ of $\Upsilon(1S)$ versus $y_{CM}$ according to CMS (red circles), ATLAS [30] (green diamonds), ALICE [31] (blue squares) and LHCb [32] (purple vertical crosses) compared to predictions (shaded gray region) using nPDF [26] (left) and E. loss [27] (right) effects. Error bars on the points represent statistical and fit uncertainties and filled boxes represent systematic uncertainties. The green, blue and red boxes around the line at unity depict the global uncertainties for the ATLAS, ALICE and CMS data, respectively. All the uncertainty in the LHCb data are already incorporated into the uncertainties on the values shown.	176
9.10	Integrated $R_{FB}$ of $\Upsilon(1S)$ mesons according to CMS (red circle), ALICE [31] (teal open diamond) and LHCb [32] (brown open square) as a function of $y_{CM}$ . Error bars represent statistical and fit uncertainties and filled boxes around points represent systematic uncertainties.	177
A.1	Comparison of cross sections of $\Upsilon(1S)$ using yields extracted from Pb-p and p-Pb data.	181
A.2	Comparison of cross sections of $\Upsilon(2S)$ using yields extracted from Pb-p and p-Pb data.	182
A.3	Comparison of cross sections of $\Upsilon(3S)$ using yields extracted from Pb-p and p-Pb data.	182
A.4	Cross Section of $\Upsilon(1S)$ , $\Upsilon(2S)$ and $\Upsilon(3S)$ as a function of $p_T$ and $ y $ in pp collisions obtained in the analysis presented here compared with those obtained in reference [33] on a log scale (top) and a linear scale (bottom).	183
A.5	Efficiencies of $\Upsilon(1S)$ versus $p_T$ and rapidity in pp (top) and pPb (bottom) MC with and without T&P weighting.	184
A.6	Variations in the $\Upsilon(1S)$ efficiency in pp collisions due to T&P corrections shown as a function of $p_T$ and $ y $ .	185
A.7	Variations in the $\Upsilon(1S)$ efficiency in pPb collisions due to T&P corrections shown as a function of $p_T$ and $y_{CM}$ .	185

A.8	Relative contributions to the uncertainty in $\Upsilon(1S)$ efficiency of various sources of T&P systematic variations in pp collisions. . . . .	186
A.9	Relative contributions to the uncertainty in $\Upsilon(1S)$ efficiency of various sources of T&P systematic variations in pPb collisions. . . . .	186

# List of Tables

5.1	The generator-level MC samples used to evaluate the acceptance corrections for pp and pPb collisions at $\sqrt{s_{\text{NN}}} = 5.02$ TeV. . . . .	95
5.2	The fully-reconstructed MC samples used to evaluate efficiency corrections for pp and pPb collisions at $\sqrt{s_{\text{NN}}} = 5.02$ TeV. . . . .	97
6.1	Multiplicity-related bins in $N_{\text{tracks}}^{ \eta <2.4}$ (left) and $E_{\text{T}}^{ \eta >4}$ (right) and the fraction of recorded events belonging to each bin. . . . .	107
6.2	Comparison of $\chi^2$ per degree of freedom for fits to pp data using a double Crystal Ball (DCB) versus a Crystal Ball plus Gaussian (CBG) as the signal PDF. The DCB is chosen as the nominal signal PDF. . . . .	109
6.3	Comparison of $\chi^2$ per degree of freedom for fits to pPb data using a double Crystal Ball (DCB) versus a Crystal Ball plus Gaussian (CBG) as the signal PDF. The DCB is chosen as the nominal signal PDF. . . . .	110

## ABSTRACT

### Quark Gluon Plasma and Cold Nuclear Matter modification of $\Upsilon$ states at $\sqrt{s_{\text{NN}}} = 5.02$ TeV with the CMS Detector

Quantum chromodynamics describes the phases of strongly-interacting matter and their boundaries, including the deconfined quark-gluon plasma (QGP) phase reached in the high energy density regime. Properties of the QGP are studied using ultrarelativistic collisions of fully-ionized heavy nuclei, which also exhibit (cold) nuclear matter properties unrelated to the plasma. An indicator of the QGP temperature is the modification of quarkonium production in collisions between two heavy ions relative to collisions between two protons. The modification in collisions between a heavy ion and a proton, where the QGP is typically not produced but nuclear matter is abundant, provides an essential baseline.

Production cross sections of  $\Upsilon(1S)$ ,  $\Upsilon(2S)$ , and  $\Upsilon(3S)$  mesons decaying into  $\mu^+\mu^-$  in proton-lead (pPb) collisions are measured using data collected by the CMS experiment at  $\sqrt{s_{\text{NN}}} = 5.02$  TeV. Nuclear modification factors  $R_{\text{pPb}}$  for all three  $\Upsilon$  states, obtained using measured proton-proton (pp) cross sections at the same collision energy, show that  $\Upsilon$  states are suppressed in pPb collisions compared to pp collisions. Sequential ordering of the  $R_{\text{pPb}}$ , with  $\Upsilon(1S)$  least suppressed and  $\Upsilon(3S)$  most suppressed, indicates presence of final-state modification of  $\Upsilon$  mesons in pPb collisions. The  $R_{\text{pPb}}$  of individual  $\Upsilon$  states are found to be consistent with constant values when studied as functions of transverse momentum and center-of-mass rapidity. Predictions using the final-state comover interaction model, which incorporates sequential suppression of bottomonia in pPb, are found to be in better agreement with the measured  $R_{\text{pPb}}$  versus rapidity than predictions using initial-state modification models. Nuclear modification is less pronounced in pPb collisions than in lead-lead collisions, where the additional lead nucleus and QGP effects result in greater  $\Upsilon$  suppression. Forward-backward production ratios  $R_{\text{FB}}$  of  $\Upsilon$  states, which help investigate regions of different nuclear matter densities, are found to be consistent with unity and constant with increasing event activity measured both far away from and near to the measured  $\Upsilon$ .

# Chapter 1

## Theoretical Background

### 1.1 Physics of the Strong Interaction

The strong force is one of four fundamental forces in nature, alongside electromagnetic, weak and gravitational forces. The strong force has the second shortest interaction distance, after the weak force, and under ordinary conditions is the strongest of the fundamental forces, although this changes as the available energy increases. As a result, the strong force is invisible to us in our daily experience of the world around us. Particles that interact via the strong interaction are fundamental fermions known as quarks and the gauge bosons, gluons, which mediate the force. The property of fundamental particles that allows them to interact via the strong force is known as color charge. Quarks bind together to form color-neutral particles known as hadrons. Hadrons comprised of three quarks are known as baryons, and those of two quarks (a quark-antiquark pair) are called mesons. Protons and neutrons are hadrons (baryons) which can bind together to form nuclei. Since the matter around us is composed of hadronic units that can be isolated and observed, it is referred to as hadronic matter. Figure 1.1 shows a cartoon of the building blocks of matter.

The strong force manifests itself in two ways: it dictates interactions of quarks and gluons (partons) inside the nucleons (protons and neutrons), as well as interactions of nucleons

within the nucleus. The latter of these is known as the residual strong force, which holds together protons and neutrons in the nucleus, despite the Coulomb repulsion between protons. A unique aspect of the strong interaction is gluon self-interactions: gluons themselves carry color and therefore interact with other gluons as well as with quarks. This behavior is in sharp contrast to that of photons, the mediator of electromagnetic force, which are electrically neutral.

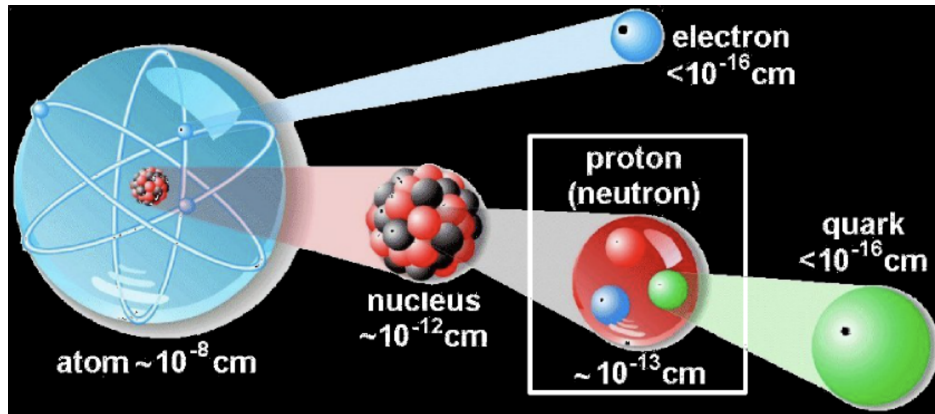


Figure 1.1: The building blocks of ordinary matter [1].

Quantum Chromodynamics (QCD) is a non-Abelian gauge theory that describes the physics of particles that interact via the strong interaction. The non-Abelian description captures the ability of gluons to couple to each other. In general, QCD is largely non-perturbative and cannot be fully represented using exact symmetries. The color charges in QCD comprise three distinct types and their respective anti-colors. The color degrees of freedom can be described by a local  $SU(3)$  gauge symmetry, with the eight generators of the symmetry group corresponding to the gluonic gauge fields [10]. In addition to color charge, quarks also have flavor: the light quarks up, down and strange, and the heavy quarks charm, bottom and top. Due to the large mass separation ( $> 1$  GeV) between the light and heavy quarks, an approximate  $SU(3)$  symmetry can be used to describe the flavor degrees of freedom in QCD [34]. Chiral symmetry is broken in QCD for ordinary nuclear matter because quarks have mass. However, because it is a spontaneously-broken symmetry, chiral symmetry can be restored in the high energy density limit of nuclear matter, giving rise to

the chiral condensate as an order parameter for QCD phase transitions [1, 10, 34].

The lack of a natural separation of energy scales in QCD, and the resulting lack of a suitable scale for renormalization, renders the development of a complete theory for the strong interaction an arguably more formidable challenge than the well-behaved electromagnetic force [10, 35, 36, 37]. When two color charges are pulled apart, the attractive force between them increases with increasing distance. When the distance between two quarks becomes sufficiently large, the potential energy contained in the field can be transformed into mass for new quarks and a quark-antiquark pair will pop out of vacuum. The length scale for this to occur is on the order of hadronic sizes ( $\sim 1$  fm), causing this scale of nuclear physics to be nonperturbative [35, 36, 37, 38, 39]. The confinement of quarks and gluons within composite hadrons means that free quarks and gluons cannot be found in nature. On the other hand, the strong force acting between inter-hadron confined quarks and gluons results in the residual strong force [35, 36, 37, 39].

At the short distances at which quarks and gluons interact within a hadron, the coupling is weaker and they behave almost like free particles, rendering this realm of QCD perturbative. Since large momentum scales correspond to small distance scales, a similar effect is achieved even when quarks and gluons moving with asymptotically large momenta interact with each other. The weaker interaction strength of strongly interacting particles at high energies, a phenomenon unique to QCD known as asymptotic freedom, allows perturbative calculations of the theory to be carried out in this regime [1, 10, 35, 36, 37, 38, 39].

In order to study low-energy properties of QCD, such as confinement, chiral symmetry breaking and the emergence of a mass gap, nonperturbative methods are needed. Lattice gauge theory can be used to numerically calculate thermodynamic quantities in the nonperturbative regime of QCD. This method, known as lattice QCD, involves the discretization of the QCD Lagrangian. In the lattice QCD framework, the thermodynamic partition function of the strongly-interacting medium is related to the path integral formulation of quantum mechanics. Amongst other relationships, imaginary time on the lattice is related to the

inverse temperature of the medium [5, 10, 40].

Lattice QCD is an extremely powerful tool, with high predictive power for phenomena involving large momentum transfer as well as support for hadronic spectrum reconstruction. The framework is used to study the phase transition of QCD at the limit of zero medium density, which we will discuss further in the next section. With increased computational power enabling the shortening of lattice spacing, lattice simulations are even being extended to finite medium density and temperature. It is worth noting, however, that lattice QCD can only provide a numerical estimate, not a concrete understanding of phenomena such as confinement based on some definite approximation. I.e. although confinement is verified in numerical calculations using lattice QCD, it has not yet been derived from QCD theory [1, 5, 10, 35, 36, 37, 40, 41].

Furthermore, in order to describe hadronic interactions at both long and short distances, the unified strong coupling  $\alpha_s$  over the complete momentum transfer  $\mathbf{Q}$  range is needed. Such an unification is obtained in lattice QCD through the analytic matching of the non-perturbative and perturbative regimes of strongly-interacting matter, by relating the scale parameter  $\Lambda$  of perturbative QCD at short distances to the mass scale of hadrons. One technique for the analytic continuation involves an anti-de Sitter space representation of QCD AdS/QCD [41, 42, 43]. Figure 1.2 shows  $\alpha_s$  as a function of  $\mathbf{Q}^2$  obtained using different renormalization schemes, where the analytic continuation is performed using AdS/QCD. The transition scale  $\mathbf{Q}_0$  between the long- and short-distance regimes of QCD, also determined in this process, is identified using arrows [2]. Notice that as  $\mathbf{Q}^2$  increases,  $\alpha_s$  plateaus and approaches a similar value across all renormalization schemes. This is equivalent to the observation that probing QCD is less challenging in the high energy regime and by using heavier probes, both of which we seek to achieve in the study presented here.

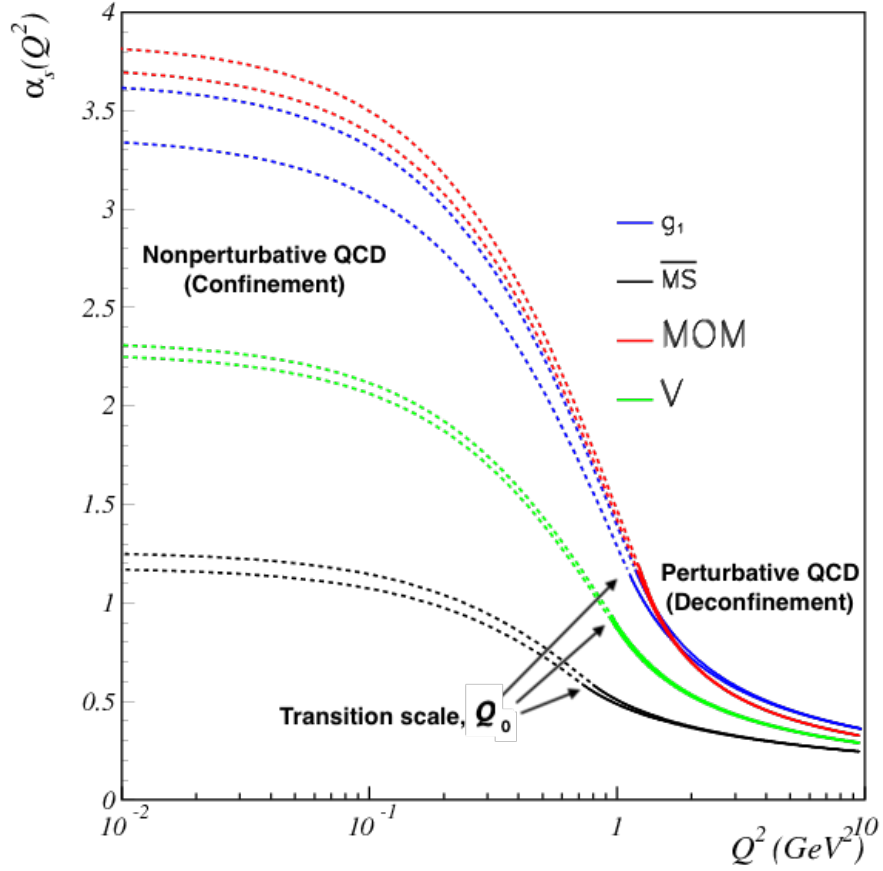


Figure 1.2: The running coupling constant of QCD. The different bands correspond to different renormalization schemes used in perturbative QCD at short distances. The bands are extended to the nonperturbative regime characterized by confinement using AdS/QCD continuation of the perturbative regime. The transition scale  $\mathcal{Q}_0$  for each renormalization scheme is shown [2]. See reference [2] for a description of the schemes indicated.

## 1.2 Quark-Gluon Plasma

As suggested earlier, the high energy density behavior of strongly-interacting matter is distinct from that of the low-energy state of ordinary hadronic matter. Energy density in QCD can be increased principally in two ways: by increasing the temperature of a system and by increasing its baryo-chemical potential  $\mu_B$ , a quantity signifying the energy available in the system to produce additional baryons without needing to create corresponding anti-baryons. Alternatively, it can be thought of as the net baryon *density* in the system, representing the excess of baryons over anti-baryons. In both the high temperature and high  $\mu_B$  limits, strongly-interacting matter undergoes a rapid increase of energy and entropy densities, entering a new phase. The degrees of freedom in QCD increase and the asymptotically-free region of color fields and forces extends beyond typical hadronic sizes. This phenomenon is known as color deconfinement and the resulting medium consisting of mobile color charges is known as the quark-gluon plasma (QGP) [44, 45]. As alluded to previously, chiral symmetry is restored in this phase of strongly-interacting matter [1, 34].

Figure 1.3 shows a schematic diagram of the  $T - \mu_B$  phase space of QCD. The net baryon density in the system, i.e. the excess of baryons over anti-baryons, is used as the measure of  $\mu_B$ . The ordinary state of hadronic matter sits within the hadron gas phase of QCD, at a normalized net baryon density of one ( $\mu_B = m_p c^2 \approx 1000$  MeV) and at ordinary temperatures ( $T \approx 0$  MeV). If the temperature of the system is increased while the baryo-chemical potential is held near  $\mu_B = 0$  MeV, the phase transition to QGP occurs around temperatures slightly greater than the crossover temperature  $T_c \simeq 157$  MeV [46, 47]. The QGP is thought to have been produced about a microsecond after the big bang, at low net baryon density and temperatures several orders of magnitude higher than the core of the sun today. It eventually cooled down, giving rise to the hadronic matter around us. At the core of neutron stars, where the matter-antimatter asymmetry is thought to be significant, one might find a QGP with low temperatures but high net baryon density.

A phase transition band separates the hadronic gas phase from the partonic phase of the

QGP. Two kinds of phase transition are predicted by lattice QCD. At low  $\mu_B$ , a continuous crossover occurs, producing no experimentally detectable signatures of the phase change. At high  $\mu_B$ , a first-order transition, characterized by discontinuities in measurable quantities, is expected. The order parameters which can be calculated on the lattice include the chiral condensate and the gluon condensate, which is a more direct indicator of deconfinement related to the quark free energy [48, 49]. The point at which the nature of the phase transition changes from crossover transition to a first-order transition is known as the critical end point (CEP). The nature of the phase change has implications for the equation of state (EoS) of strongly-interacting matter. Unlike a crossover transition, during a first-order phase transition, the system experiences a softening of the EoS due to the mixed phase.

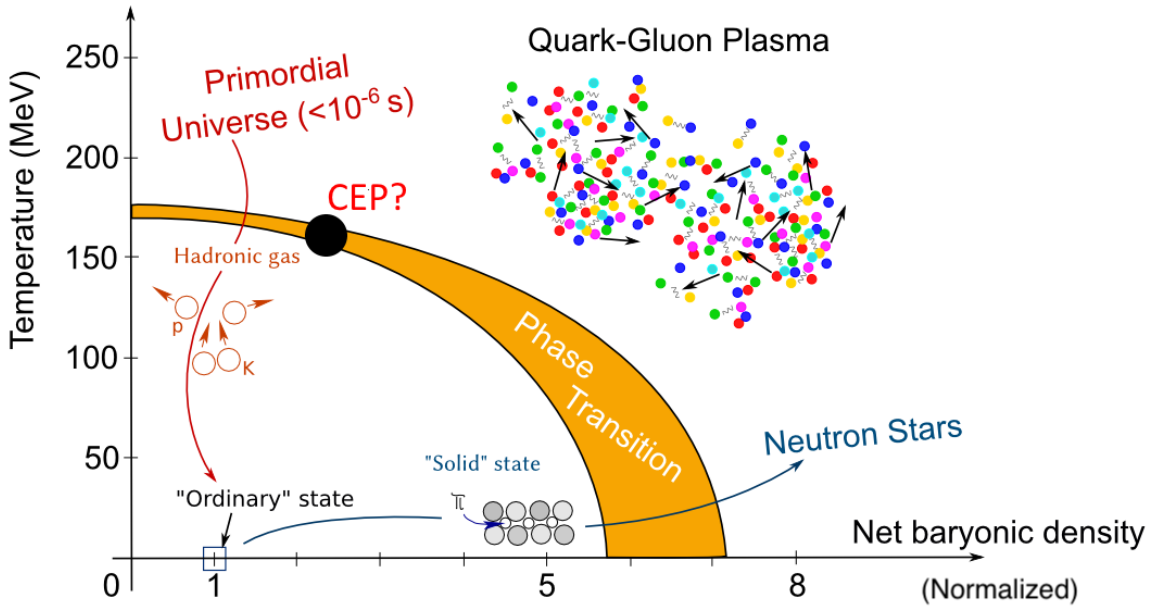


Figure 1.3: The phase diagram of QCD matter [3].

In order to study the QGP, we must be able to access this region of the QCD phase space. The QGP can be produced by colliding heavy ions at extremely high energies at particle colliders such as the Large Hadron Collider (LHC). At such energies, distances smaller than partonic radii can be resolved. Thus, scatterings occur at the partonic scale, well beyond the hadronic scale where baryon stopping could manifest. At the LHC, the high-temperature, low- $\mu_B$  QGP produced and its subsequent crossover phase transition are

studied using various probes in the heavy-ion sector. A beam energy scan at the Relativistic Heavy Ion Collider (RHIC) provides a complementary study of the QGP by colliding heavy ions at lower energies, where baryon stopping allows the formation of the QGP on the basis of a higher  $\mu_B$ , even at lower temperatures. As the QGP evolves in these collisions, markers of a first order phase transition can be observed [50, 51, 52, 53].

The deconfined plasma produced at the LHC thermalizes on time scales on the order of 1 fm/ $c$  with initial temperatures of about 500 – 700 MeV [23, 24, 29]. The system, which can be modeled hydrodynamically, then expands and cools. The hydrodynamic phase of the QGP occurs over a time scale of about 20 fm/ $c$ . When its temperature reaches the crossover temperature, the system hadronizes but continues interacting. At temperatures slightly below the cross-over temperature, the energy density no longer supports interactions that can change particle types, leading to chemical freezeout of hadron species. Momentum changing elastic collisions continue until kinetic freezeout occurs at temperatures on the order of 120 MeV. Particles created in the initial scatterings and throughout these stages of evolution of the medium are detected experimentally and offer valuable insight into the properties of the QGP [45, 54, 55].

Understanding the QGP is instrumental to the theory of QCD, for understanding the phenomena of confinement and chiral-symmetry restoration. Changes in the equation of state allow us to infer the nature of the phase transition from hadronic matter to the plasma state and to search for the critical end point. Heavy-ion experiments at particle colliders such as the LHC and RHIC can be used to study the properties of the QGP they create. Thermal properties of the QGP, such as its early stage temperature, are of particular interest. In addition to being a fundamental thermodynamic property of the color-deconfined phase of strongly-interacting particles, the initial temperature of the plasma also presents a view into the evolutionary path of the QGP follows in the  $T - \mu_B$  phase space, as the energy density lowers and the system eventually evolves to ordinary hadronic matter.

### 1.3 Probing Nuclear Matter using Quarkonia

Quarkonia are mesons comprised of a heavy quark  $Q$  and its antiquark  $\bar{Q}$ , referring particularly to charmonia (bound states of  $c\bar{c}$ ) and bottomonia (bound states of  $b\bar{b}$ ), since the extraordinarily high mass of the top quark precludes the existence of a bound  $t\bar{t}$  state. A significant amount of energy is needed to produce heavy quarks ( $m_c \approx 1.3 \text{ GeV}/c^2$ ,  $m_b \approx 5 \text{ GeV}/c^2$ ) and their high-mass bound states. Quarkonia, which consist of not one but two heavy quarks, are therefore primarily produced in the initial hard scattering of partons in high-energy collisions, where a large amount of momentum is transferred. In collisions at the LHC, gluon-gluon fusion is the primary process for the production of heavy quark pairs. In particular, since bottomonium masses are at least an order of magnitude higher than the temperatures produced in even the highest-energy collisions, bottomonium production is dominated by the initial hard scatterings of gluons [56].

Moreover, on account of the strong process involved, the heavy quark pairs are formed extremely quickly. Although the exact mechanism is yet unknown, the hadronization of the  $Q\bar{Q}$  into color neutral quarkonia also happens on a short time scale relative to the hydrodynamization of the QGP. Furthermore, the strongly bound, heavy quarkonia have a long lifetime. Unlike free quarks and gluons, the hadronized quarkonia are virtually unaffected by elastic or radiative energy loss in the final state in the medium [57, 58]. Thus, not only are quarkonia produced and fully hadronized even before the QGP in heavy-ion collisions has had a chance to thermalize, thanks to their long lifetime, the non-thermalized quarkonia typically also traverse and escape the QGP before they decay—unless they are dissociated by the medium itself [24, 59, 60].

Figure 1.4 shows the cartoon of a S-wave bottomonium state, known as an Upsilon  $\Upsilon$  meson, in the medium produced during a collision of heavy ions. A  $b\bar{b}$  quark pair created during initial hard scatterings hadronizes into an  $\Upsilon$  at the beginning of the collision. The  $\Upsilon$  subsequently traverses the QGP that develops around it. Unless explicitly broken up by the QGP, the  $\Upsilon$  remains intact in the QGP as the system evolves and eventually hadronizes

into particle species. The formation of an  $\Upsilon$  from free  $b$  and  $\bar{b}$  quarks in the medium is so unlikely that it is not depicted in the figure.

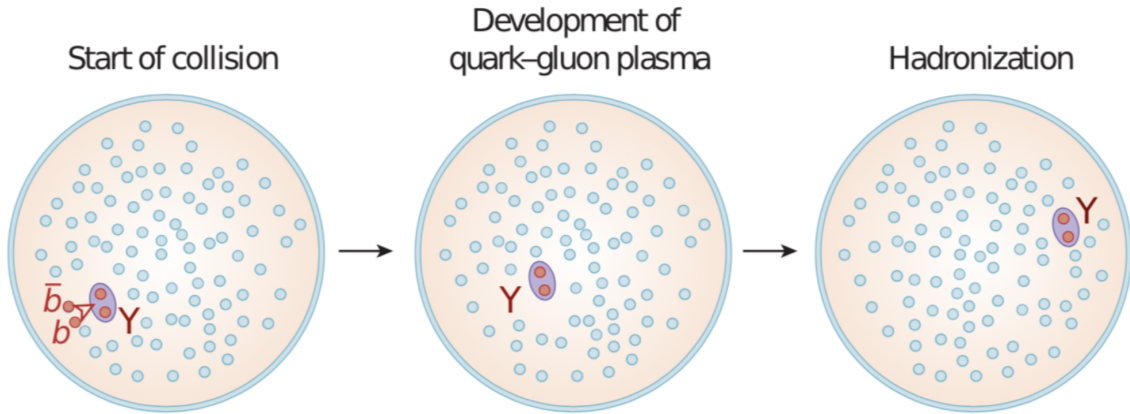


Figure 1.4:  $\Upsilon$  mesons are produced early in heavy-ion collisions and survive long enough to outlive the thermodynamic phase of the QGP [4].

These features make quarkonia well suited as unthermalized, tomographic probes to study the medium produced in heavy-ion collisions where a QGP is produced. The yields of various quarkonium states encode information on the evolution of the plasma starting from its early stages. By measuring quarkonium states produced in nuclear collisions we can assess how they have been affected by the medium, and, in turn, learn about the medium itself [5, 54, 59, 61, 62, 63, 64]. From a theoretical point of view, calculations of quarkonium properties present an advantage over light hadron properties, since the heavy mass scale can justify approximations, allowing the use of analytic methods where numerical computations may be expensive.

## 1.4 Effects of the QGP on Quarkonia

In 1986, Matsui and Satz proposed that quarkonium production would be suppressed in the deconfined QGP due to color screening [61]. Debye screening of the quark color charge is similar to electric charge screening in quantum electrodynamics [54, 59]. The proximity of other charges obstructs the formation of a bound state between two given charges that are a

certain distance apart. In the QGP, when the screening radius becomes less than the binding radius of a quark system, the confining force can no longer hold the quarks together. The hadron therefore dissociates or melts.

Since the screening mechanism relies on the kinetic energy of the mobile color charges in a QGP, the Debye screening radius is inversely proportional to the temperature of the plasma. Therefore, the possible heavy-quark interaction range decreases with increasing temperature, causing bound states with smaller binding energies and corresponding larger radii to dissociate first [44, 59].

Lattice QCD and effective field theory (EFT) calculations have demonstrated that color screening in a deconfined QCD medium does, in fact, destroy increasingly heavy quark-antiquark bound states with increasing temperature [44, 61]. A quarkonium state survives in the QGP through some range of temperatures above  $T_c$ , but dissociates once  $T$  becomes sufficiently large to melt it. If the temperature of a QGP could be gradually increased, quarkonia would be observed to melt one by one, in a hierarchical pattern according to their binding energies. This concept is known as sequential melting.

The temperature distribution in a QGP is not uniform, however, either as a function of its spatial extent or its temporal evolution. Moreover, in actual experiments, we can only measure the total number of each quarkonium species that were created in a collision event. We do not have a way to separate quarkonia created earlier or later in the collision, or close to or far away from the center of the QGP, if it exists. Measurements of the yield of quarkonia in collisions therefore represent holistic information on the medium produced and its evolution.

Moreover, even if the temperature reached in a heavy-ion collision is not sufficiently high for a particular quarkonium state to melt, the state's yield may still be suppressed in the QGP. The observed quarkonium yield may be depleted relative to the expected yield in the absence of a QGP either because the  $Q\bar{Q}$  fails to form a bound quarkonium state in the first place or because the state is formed and subsequently destroyed through interactions in the

deconfined medium [10, 54].

As a result, we do not observe sequential melting of quarkonia as the disappearance of loosely-bound resonances from the collision data altogether while tightly-bound resonances remain completely intact. Instead, this signature of the QGP manifests itself as the sequential suppression of the yields of all quarkonia in heavy-ion collisions, with the most loosely bound states being the most suppressed, compared to collisions of protons where the QGP is not created [59]. Furthermore, we can observe this depletion of yields as functions of various measurable quantities that can be related to the temperature of the QGP.

Following the findings of Matsui and Satz [61] and through the early 2000's, the idea that medium effects on quarkonia could be understood in terms of a temperature-dependent potential led to the use of numerous screening potential models defined directly from Euclidean time observables to predict quarkonium properties at high temperature. However, the use of a potential model for quarkonia in the temperature regime of QCD characterized by the phase transition has traditionally proven to be problematic [5, 65, 66, 67]. In the mid to late 2000's the analytical continuation of the Euclidean correlators in lattice QCD to Minkowski spacetime was utilized to obtain, for the first time, a static in-medium (high temperature) quarkonium potential [44, 67, 68]. The analytical continuation allows us to recast the imaginary-time formalism in Euclidean space to real-time quantities. Quarkonium properties at high temperature can be calculated by determining Euclidean correlation functions in lattice QCD and reconstructing the corresponding spectral functions.

This first principles approach revealed the in-medium heavy quark potential to be complex in nature: consisting of an imaginary as well as a real part. In reality, color screening is not the only quarkonium suppression mechanism at play. Bound quarkonium states can also be dynamically dissociated in the QGP by inelastic collisions with its constituents. The leading order dissociation effect, known as gluo-dissociation, is due to inelastic collisions of the quarkonium state with soft gluons. The external gluons in the medium can couple to the gluon exchanged between the  $Q$  and  $\bar{Q}$  of the quarkonium. In the framework of EFT, the

mechanism can be described using a multipole expansion of QCD and an effective Lagrangian action of constituent quark fields [69].

Thus, gluo-dissociation, or Landau damping, in the QGP produced in collisions of heavy ions is found to modify quarkonium yields compared to collisions in vacuum in a sequential pattern as well [5, 44, 68, 69, 70]. The real portion of the in-medium heavy quark potential can be identified with the effects of Debye screening, while the imaginary part represents gluo-dissociation. In fact, in addition to the quarkonium potential, the threshold binding energy of quarkonia (open heavy quark threshold) is also modified as a function of temperature in the deconfined medium. Only when all these effects are taken together, can we draw a consistent picture of heavy quark bound states in a high-temperature QCD medium [5, 68].

As a result of the relationship between quarkonium binding energies and temperature-dependent suppression mechanisms, quarkonium dissociation may be used to gauge the temperature of the QGP formed in collisions of heavy ions. As explained in section 1.2, the temperature of the color-deconfined phase of QCD is a particularly attractive property to study. Figure 1.5 shows the in-medium bottomonium spectral function for a range of temperatures from  $T = 0$  to  $T = 1.66T_c$ , as calculated by an EFT based approach using a complex potential in reference [5]. In this framework, a spectral decomposition of the Euclidean time Wilson loop in lattice QCD reveals that the real-time Wilson loop is described by the same spectral function. With this access to the real-time Wilson loop, the spectrum can be used to extract values of the in-medium potential.

The well-defined peak features in the spectral function have correspondence with bottomonium states with the respective binding energies. As depicted by the red arrows, as the temperature of the medium increases, the peaks are seen to shift to lower masses as well as broaden. Effectively, the real part of the complex potential causes the spectral function peaks to shift to lower masses, while the imaginary part leads to their broadening. Both of these effects appear first in the highest excited state, followed sequentially by lower energy states. The authors are able to determine the dissociation point for different bottomonium

states by identifying it with the point when the binding energy of a state coincides with its spectral width. Thus, experimentally-measured modification of various quarkonium states can be used as a thermometer for the QGP through comparison to dissociation temperatures determined in such theoretical frameworks.

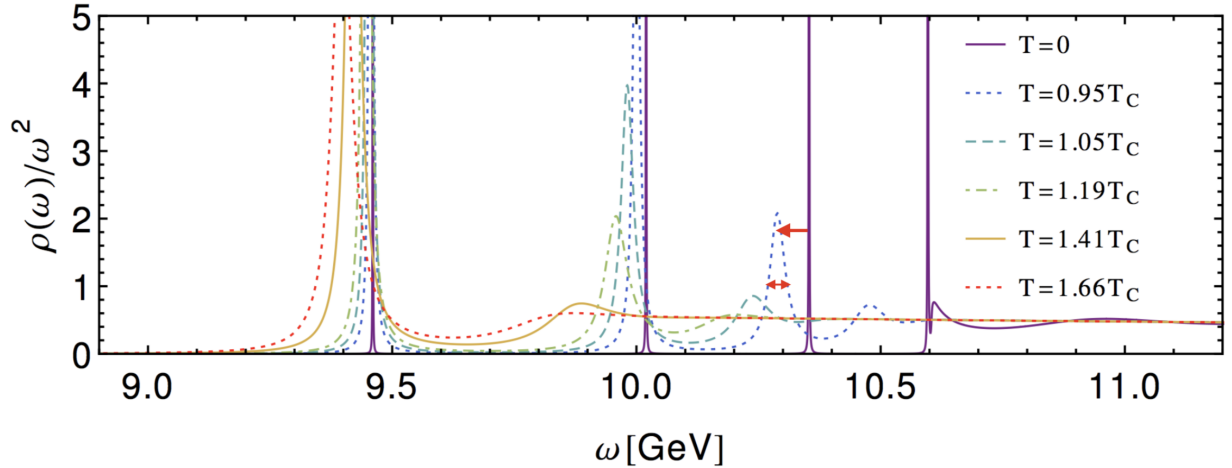


Figure 1.5: The evolution of bottomonium spectral functions with increasing temperature of the QGP [5].

Indeed, several aspects of the QGP can be investigated by measuring quarkonium production in collisions of heavy ions. The QGP produced in ultrarelativistic collisions has finite spatial and temporal dimensions, expands faster in the longitudinal direction, and has a nonuniform temperature distribution [45, 55, 56]. These features introduce dependencies of the quarkonium yield and its suppression on experimentally-accessible variables such as collision activity or centrality (a measure of how head-on a collision is), and quarkonium kinematic variables such as transverse momentum  $p_T$  and center-of-mass rapidity  $y_{CM}$ . Studying these dependencies allows us to investigate the temperature distribution of the produced QGP, which eventually helps constrain the high-temperature QCD model parameters [55, 56, 59].

Reference [55] explores the survival probability of bottomonium states for different initial conditions of the QGP as a function of bottomonium  $p_T$ , proposing that since the survival probability depends on a given state's dissociation temperature and formation time, one can

expect each state's yield to exhibit a unique  $p_T$  dependence. Similarly, forward rapidity measurements of quarkonium yield suppression helps map the temperature profile of the QGP in the forward pseudorapidity region, where the QGP expansion is most rapid [56]. By measuring the centrality dependence of quarkonium production we can verify our expectation that quarkonia are more suppressed in central events than in peripheral events due to the larger and hotter QGP volume created in the former [45]. In fact, states that can survive in the cooler peripheral collisions may dissociate in central collisions, exhibiting a clear signature of sequential suppression [71]. Thus, studying quarkonium suppression in the QGP as a function of collision centrality and quarkonium  $p_T$  and  $y_{CM}$  allows us infer model-dependent temperature profiles of the plasma [23, 24].

## 1.5 Effects of Cold Nuclear Matter on Quarkonia

We have seen that quarkonia are a unique tool for untangling the complexity inherent in the physics of strong interactions through the study of their production in collisions of heavy ions where the color-deconfined phase of QCD is produced. However, any collision involving a heavy nucleus in the initial state intrinsically experiences what is known as cold nuclear matter (CNM) effects [39, 44, 59, 71, 72, 73, 74]. In collisions where a QGP is produced, the modification of measured yields of quarkonia result from CNM effects as well as effects of the hot plasma. Thus, the initial conditions in nuclear collisions must be understood before final-state QGP effects can be isolated using quarkonia as a probe. Collisions of isolated protons in vacuum provide an insufficient baseline for QGP effects, since they cannot account for effects intrinsic to interactions of nuclei which are composed of neutrons and protons bound together by the residual strong force. Therefore, an additional baseline of nuclear collisions where a QGP is not produced is needed for distinguishing the level of quarkonium modification by the deconfined plasma [38, 75].

In order to isolate CNM effects, studies of heavy ions colliding with protons are performed.

In contrast to the case of collisions between heavy ions, modifications to quarkonium yields in collisions of heavy ions with protons are expected to be dominated by CNM effects, although there is recent evidence pointing to the formation of a QGP-like medium even in high-activity collisions of protons with heavy ions [76, 77, 78, 79]. Collisions between protons in vacuum can be used as the baseline to determine relative nuclear matter modification of quarkonia.

We turn our attention now to mechanisms that can cause quarkonium yields to be modified in nuclear collisions where a QGP is not produced. These effects can be broadly categorized into initial-state and final-state CNM effects, based on whether they affect the quarkonium production process before or after hadronization. Final-state CNM effects are particularly important to isolate from QGP effects which also occur post quarkonium hadronization as discussed in section 1.4. Moreover, final-state CNM effects have the potential to affect different quarkonium states differently, similar to the case of sequential melting in a deconfined plasma.

There are a number of possible CNM effects on quarkonium production, including modification of the parton densities in nuclei compared to free protons; the saturation of small- $x$  gluons and their coherence in nuclear systems; energy loss due to gluon bremsstrahlung radiation in nuclear matter; and the breakup of produced quarkonium states by inelastic interactions with surrounding nucleons or with other particles traveling with the quarkonium. Most CNM effects can be traced to multiple interactions of gluons induced by the colliding nucleus, either before, during or after quarkonium production. We now discuss the most important CNM effects on quarkonia, classify them as initial- or final-state effects, and indicate when they are not relevant in the high-energy collisions at the LHC we would like to investigate.

### 1.5.1 Initial-State CNM Effects

Since initial-state CNM effects are defined by their ability to modify quarkonium production yields at any stage prior to the hadronization of the  $Q\bar{Q}$ , they can incorporate a wide range

of mechanisms. The only characteristic initial-state CNM effects must have in common is their inability to result in different degrees of modification for quarkonium states of the same family. That is, all bottomonium states will be modified identically by an initial-state CNM effect. Similarly, all charmonia will be modified identically to each other, but differently to the bottomonia due to the mass difference between the two flavors of quarks.

## **Nuclear Modification of Parton Densities**

In the absence of any CNM effect on particle production, the per-nucleon cross section at a given energy would be equal across all collision systems where the QGP is not produced. Thus, the production cross section in proton-nucleus collisions can be expected to scale with the production cross section in proton-proton collisions as  $A$ , the mass number of the colliding nucleus. This approximation follows the simple argument that there are now  $A$  times as many nucleons that can support a particle-producing hard interaction with partons from the incident proton. However, as early as the 1980's, deep inelastic scattering (DIS) of leptons off nuclei revealed that the inelastic cross section was, in fact, significantly modified in a nuclear environment compared to isolated nucleons, indicating a kind of structure inside the nucleus. Prior to this, the nucleus was viewed as being composed of free nucleons and the partons within nucleons assumed to be virtually insensitive to the structure outside them [72, 80, 81, 82, 83, 84].

Parton distribution functions (PDFs) characterize the density of partons carrying a given momentum fraction  $x$  of the total momentum carried by the nucleon to which it belongs. The observed modification of particle production in various data from nuclear DIS (nDIS), as well as Drell-Yan cross section measurements from early fixed-target proton-nucleus collisions, were consistently described by an empirically developed modification of free-nucleon PDFs in a nuclear environment. These first measurements of the modified PDFs came to be known as nuclear PDFs (nPDFs) and the associated CNM effect as the EMC effect after the European Muon Collaboration where it was first observed in 1982 [72, 80, 81, 82, 83, 84].

Regions in  $x$  where the interaction cross section in a nuclear environment is lowered compared to a free-nucleon environment consisting of the same number of nucleons are known as shadowing; and regions observing the opposite effect as anti-shadowing. The origin of the term shadowing comes from the idea that nuclear matter casts a “shadow” over the interactions of would-be free-nucleon partons, thereby reducing interaction cross sections.

In addition to  $x$ , nPDFs also depend on the  $\mathcal{Q}^2$  scale. In the perturbative regime of QCD characterized by asymptotic freedom, where  $\mathcal{Q}^2$  is large, the evolution of the nPDFs with  $\mathcal{Q}^2$  can be projected using the Dokshitzer-Gribov-Lipatov-Altarelli-Parisi (DGLAP) [85] formalism [81, 86]. Figure 1.6 shows a calculation of the ratio between an nPDF and a free-proton PDF,  $R_i^A(x, \mathcal{Q}_0^2)$ , as a function of  $x$ , under the nPDF parametrization known as Eskola-Paakkinen-Paukkunen-Salgado-2016 (EPPS16). The variable  $i$  represents the index over all possible partons, such as gluons and different flavors of valence and sea quarks. The  $\mathcal{Q}_0^2$  scale is set by the renormalization scheme used; in this example  $\mathcal{Q}_0 \equiv m_c \simeq 1.3 \text{ GeV}/c^2$  [6]. The ratio is shown for fixed mass number  $A$  of the nucleus for which the bound-nucleon PDF is considered. A region of shadowing presides at small  $x$  while, at higher  $x$ , an anti-shadowing maximum followed by an EMC minimum is depicted.

Nuclear PDFs are useful for calculating hard processes in perturbative QCD. Since hard processes scale with the number of binary nucleon-nucleon collisions, the effect of a suppression of partons in nuclear collisions compared to the same number of isolated-nucleon collisions should be evident in the production cross section of hard probes. As illustrated in the figure, shadowing is most significant at low  $x$ , corresponding to hard processes at intermediate  $p_T$  being the most affected. The parton whose low- $x$  shadowing most affects quarkonium production in nuclear collisions at the LHC are gluons.

On the other hand, collisions where the sea quarks and gluons inside nucleons can be resolved show that gluon PDFs are different from quark (and antiquark) PDFs: the gluon densities are enhanced at low  $x$ . This is true regardless of whether the nucleon belongs to a

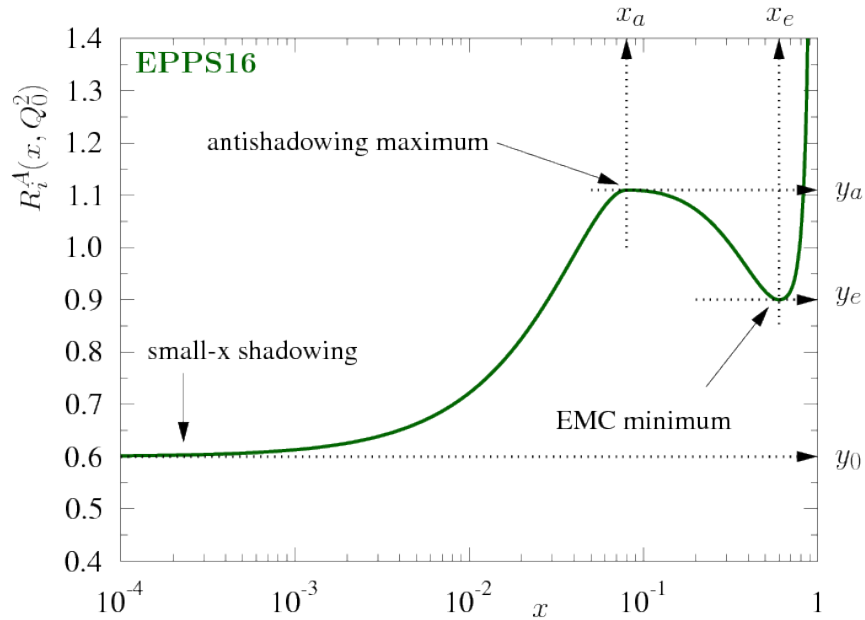


Figure 1.6: EPPS16 calculation of  $R_i^A(x, \mathbf{Q}_0^2)$  as a function of  $x$  [6].

nucleus or is a free proton.

To explain the gluon enhancement at low  $x$ , we can use figure 1.7 which shows a proton at low energy on the left and one at high energy on the right. In both instances, the proton is being observed by the same probe, depicted by the blue shaded region. The valence quarks, shown as colored circles, interact by exchanging gluons, and can also fluctuate into states that contain additional gluons. If such a fluctuation is longer lived than the resolution of the probe, the probe will be able to see it.

For the proton on the right, the time scales are Lorentz dilated: interactions between the quarks take place over much longer times. Since the probe itself is unchanged, however, it now sees free gluons in the fluctuations. Moreover, the probe can resolve more fluctuations for the higher energy proton on the right. Thus, the same probe sees that the higher-energy proton contains more gluons than the proton at lower energy [7, 38].

Thus, as  $\mathbf{Q}^2$  increases, so does the low- $x$  gluon density in nucleons. In order for the  $R_i^A(x, \mathbf{Q}_0^2)$  to show strong shadowing effects at small  $x$  as in figure 1.6, a balance must be

struck between the  $\mathcal{Q}_0^2$  scale and the nPDF effects, which themselves generally diminish with an increasing energy scale. At sufficiently high energy scales, in fact, gluon shadowing rapidly disappears [80]. Since hard processes are used for probing the QGP, quantifying the magnitude of low- $x$  shadowing effects at the LHC on parton densities, and gluon densities in particular, has been an important challenge [7, 38, 39, 75].

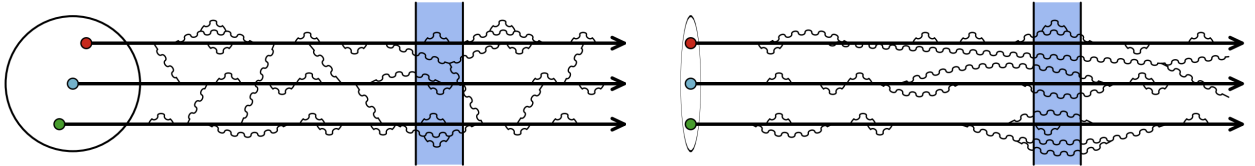


Figure 1.7: The same probe resolves fewer gluons due to fluctuations in a low energy proton (left) than in a high energy proton (right) [7].

Through the years, the nPDF models have improved considerably, thanks to the plethora of hard scattering observables being measured at RHIC and the LHC. It was not until the mid to late 2000's that pion production measurements in deuterium-gold collisions at RHIC [87] were used to develop nPDF models for gluons for the first time [6]. Prior to this, there was no direct probe of the nuclear gluon density [72]. Furthermore, it was within the last few years that dijet measurements in proton-lead collisions at the LHC were used to establish conclusively that the pion production data can be used to directly constrain gluon nPDFs [6]. The data show that the fragmentation of partons to pions is independent of nuclear modification, verifying this assumption in the two leading nPDF models EPS09 [88] and nCTEQ15 [89], which we will encounter later in this report. As we know, the hard scattering and fusion of gluons in the initial state dominate quarkonium production in collisions at the LHC [72]. Therefore, the firmer establishment of gluon nPDFs in the past decade marks a significant milestone for quarkonia as a probe of hot and cold nuclear matter effects in heavy-ion collisions.

## Gluon Saturation

An effect closely related to nPDF modifications of gluon densities is gluon saturation. Also in the early 1980's, it was established that at high energies small- $x$  partons are enhanced in colliding hadrons, as explained using figure 1.7 above. The smaller the  $x$ , the higher the number of sea quarks and gluons that can be resolved by a probe. The effective area occupied by a parton inside a nucleon scales inversely with the  $\mathcal{Q}^2$ . Therefore, although at high  $\mathcal{Q}^2$ , the excess of low- $x$  gluons contributes only incrementally to the total effective area occupied by gluons, at low  $x$  and low  $\mathcal{Q}^2$ , the nucleon can fill up with the low- $x$  gluons [7, 38, 39, 75]. Although the same principle holds for sea quarks, gluons in particular could quickly become unbounded through further splitting ( $g \rightarrow gg$  and even  $g \rightarrow ggg$ ) [39]. The DGLAP formalism for nPDF evolution cannot be used in this regime. Instead one can use the Balitsky-Kovchegov (BK) [90, 91] formalism, which preserves unitarity [75].

Clearly, this enhancement must be bounded as well; the multiplicity of small- $x$  gluons in a hadron cannot grow indefinitely. To resolve this paradox, the emergence of new non-linear, density-dependent dynamics of the soft color fields in QCD at sufficiently small  $x$  was proposed. Effectively, at low values of  $x$ , the gluon density may become so large that gluon recombinations become significant. This is depicted in figure 1.8, using two high-energy valence partons traveling to the right and their respective gluon cascades. When the occupancy becomes too large, the two gluon cascades merge, and in the end the probe (blue shaded region) sees fewer gluons than were initially generated by the partons. This phenomenon, known as gluon saturation, is responsible for curtailing the growth of small- $x$  gluons for  $\mathcal{Q}^2 < \mathcal{Q}_{sat}^2$ , where  $\mathcal{Q}_{sat}^2$  marks the momentum scale of the onset of saturation [7, 38, 39, 75, 92].

In ultrarelativistic collisions involving heavy nuclei, the  $\mathcal{Q}_{sat}^2$  is even higher than would be for similarly-boosted free nucleons. Due to Lorentz contraction along the beam axis, the gluon fields of nucleons in the nucleus superimpose. This triggers the soft color field dynamics at a relatively high transverse momentum. In this case, small- $x$  gluons can keep

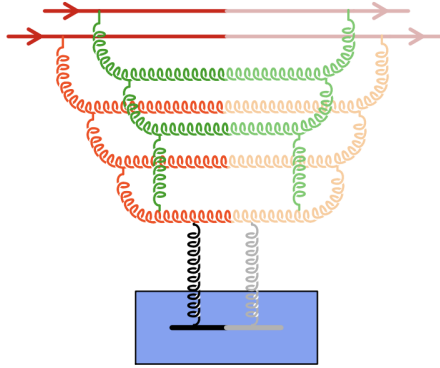


Figure 1.8: The gluon cascades of two high energy partons merge together in the saturation regime [7].

multiplying for longer before saturation eventually sets in. High gluon densities before and during collisions can lead to coherence effects in bulk medium properties in both nucleus-nucleus and proton-nucleus collisions. Thus, in addition to affecting gluonic hard processes in the appropriate regime, the phenomenon of gluon saturation in nuclear collisions contributes to coherence effects as well [38, 39, 75].

Gluon saturation plays an important role in semi-hard processes (which can still be approached perturbatively), and is particularly relevant for rapidity distributions of charge particle multiplicity and transverse energy in lower-energy collisions at RHIC. However, since in this report we are primarily concerned with  $\Upsilon$  production at the LHC, where  $\mathbf{Q}^2 \gg \mathbf{Q}_{\text{sat}}^2$ , gluon saturation is not relevant.

## Energy Loss

Another CNM effect is the loss of energy of a parton or hadron due to gluon radiation induced by the nuclear environment. Typically, the term energy loss is used to refer to the initial-state energy loss of partons. Prior to the hard collision, an energetic parton undergoes multiple scattering in the nucleus and loses energy due to medium-induced gluon bremsstrahlung. In this case, the time scale of the gluon formation (radiation) is on the order of the time it

takes the parton to traverse the medium. The radiative energy loss of a fast parton must be considered as an initial-state nuclear effect for most QCD processes [93].

However, in some hard processes, energy loss can extend beyond the initial state of the scattering partons and into the post-interaction phase of the process. The gluon associated with a hard process can interfere coherently with itself before and after the production, if the hard interaction produces a colored object traveling roughly collinearly with one of the scattering partons. The gluon emission amplitude of the fast incoming parton, which is established long before the parton enters the collision medium, interferes with the gluon emission amplitude of the fast outgoing colored object [8, 57, 93]. Therefore, the radiative energy loss in this case is connected holistically to the hard process, and not just to an incident parton.

The time scale for the gluon formation in such coherent energy loss is much longer than for the previously discussed initial-state parton energy loss. In fact, final-state energy loss of a hadron or parton (in the case of a jet) in a nuclear medium, including possibly a QGP, also occurs on a short time scale, similar to initial-state energy loss. In both the initial and final state, partonic energy loss is dominantly due to gluon bremsstrahlung induced by multiple scattering, in contrast to the coherent energy loss in hard processes with collinear emission of a colored object. Thus, although qualitatively similar for phenomenological purposes, coherent energy loss is fundamentally distinct from both initial- and final-state energy loss effects [8, 57].

The average coherent energy loss during production of a massive particle such as a quarkonium increases linearly with the particle energy in the rest frame of the nuclear medium, while the average initial-state partonic energy loss is independent of the energy of the parton. In proton-nucleus collisions, particles are almost always produced close to the beam axis [57]. Therefore, particularly in high-energy proton-nucleus collisions, the majority of radiative energy loss in hard processes is actually due to coherent energy loss (where possible), rather than the initial-state energy loss of partons. There are two notable exceptions to

this rule: when particles are produced at midrapidity in the medium rest frame, and when the produced particle from a hard process is color neutral and therefore does not radiate gluons. In both these cases, short-lived gluon bremsstrahlung is the dominant energy loss mechanism. The former is much more common as a final-state effect in the presence of a dense QGP and is likely to be a major contributor to jet quenching. The latter can be used to investigate initial-state partonic energy loss in proton-nucleus collisions using the production of Drell-Yan lepton pairs, where the partonic final state is color neutral [57].

The production of color-octet  $Q\bar{Q}$  pairs, created dominantly by gluon fusion in initial hard scattering of high- $x$  ( $x \gtrsim 0.1$ ) gluons, is highly sensitive to coherent energy loss. Whenever its longitudinal momentum in the nucleus rest frame is large compared to its transverse mass, the produced  $Q\bar{Q}$  pair travels ultrarelativistically almost along the axis of the projectile parton. Moreover, due to time dilation in the nucleus rest frame, the  $Q\bar{Q}$  pair remains in a color octet state for a long time [8, 93]. Thus, high- $x$  quarkonium production processes are expected to experience strong interference of the gluon emission amplitudes of the nearly collinear incoming and outgoing color charges. Coherent energy loss could therefore play a significant role in quarkonium suppression in proton-nucleus collisions.

Figure 1.9 shows quarkonium production in a proton-nucleus collision where, in the nucleus rest frame, the energy available for the hard scattering is significantly greater than the mass  $M$  of the  $Q\bar{Q}$ . The produced  $Q\bar{Q}$  is assumed to be color octet and to undergo soft color neutralization into a quarkonium; i.e. it is assumed to be long lived,  $\tau_{\text{octet}} \gg \tau_{Q\bar{Q}} \sim 1/M$ . Then, in the limit  $E \gg M \gtrsim p_T$ , the time scale of the perturbative hard process (illustrated in blue),  $t_{\text{hard}} = \tau_{Q\bar{Q}} \cdot E/M \sim E/M^2$ . Therefore, the overall time scale of the gluonic small-angle scattering that produces the color octet  $Q\bar{Q}$ ,  $t_{Q\bar{Q}} \gg t_{\text{hard}}$ . The  $Q\bar{Q}$  is created through the splitting of a gluon from the proton followed by the scattering of a gluon inside the nucleus. The long life of the  $Q\bar{Q}$  allows the two gluons to interfere, resulting in coherent energy loss. Here, the energy loss is an initial-state effect because it affects the pre-hadronized  $Q\bar{Q}$  which eventually hadronizes to a quarkonium state such as an  $\Upsilon$  meson [8].

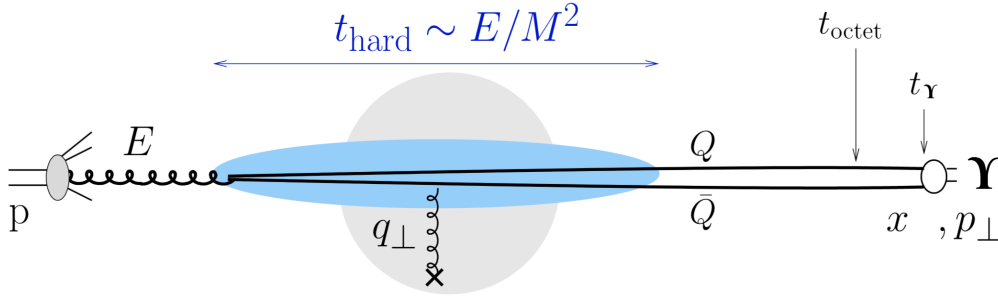


Figure 1.9: Quarkonium production in a proton-nucleus collision showing the various time scales involved. The color octet state is long lived, and the gluon emission amplitudes of the incident gluon and the produced color octet state can interfere [8].

### 1.5.2 Final-State CNM Effects

CNM mechanisms that affect hadronized quarkonium states, and may therefore modify each state to a different extent, are known as final-state effects. These effects typically constitute various interactions of the quarkonium state with surrounding particles that result in its break up or dissociation. These particles can be constituents of the projectiles in the initial state or of the medium produced in the collision. Phenomenologically, these effects are implemented by determining the cross section of such an interaction and assigning a corresponding survival probability to the quarkonium state. The survival probability is then used to weight the quarkonium production rate to obtain a modified production rate accounting for dissociation due to the given interaction mechanism. One principal feature of the interaction cross section across all final-state effects is its dependence on the density of particles near the quarkonium state with which it can interact. Apart from this, depending on the origin of the final-state mechanism, the interaction cross section may depend on various factors including the collision geometry and the size, location and path of the quarkonium.

#### Nuclear Absorption

The final-state CNM effect known as nuclear absorption involves absorption of produced quarkonia by nuclear matter in the collision, specifically within the colliding nucleus itself [72,

94, 95, 96]. As with nPDFs, nuclear absorption is primarily determined empirically using data. CNM effects that reduce the survival probability of quarkonia in a nuclear environment change the proton-proton to proton-nucleus scaling from  $A$  to  $A^\alpha$ . The exponent can be related to the nuclear absorption cross section in a non-linear way based on the collision geometry and location of quarkonium production as well as on what other CNM effects are active [72, 95, 97].

Confirming the evidence already surfacing in lower-energy fixed-target data [98, 99, 100, 101, 102], charmonium production in deuteron-gold collisions at  $\sqrt{s_{\text{NN}}} = 200$  GeV [103] verified nuclear absorption to be a final-state effect in the first decade of the millennium. The excited charmonium state was found to be more suppressed than the ground state. Moreover, this difference in the suppression level was found to decrease with increasing collision energy. These experiments are used to constrain the relationship between the cross section of nuclear absorption and  $\alpha$  [72, 95].

Given the trend of decreasing quarkonium absorption cross section with increasing center-of-mass collision energy, at LHC energies nuclear absorption and, in particular, its postulated  $A^\alpha$  dependence should be negligible. Moreover, this trend is supported by evidence that the quarkonium formation time tends to be longer than the time required by the produced  $Q\bar{Q}$  to traverse the nucleus in high energy proton-nucleus collisions. Indeed, at the energies and rapidities encountered in LHC collisions, most hadronic bound states are formed well outside the colliding nucleus because of their Lorentz-boosted formation time [9]. Thus, the constituent nucleons could at best influence the nascent  $Q\bar{Q}$  which would not produce any difference in measured yields of hadronized quarkonium states of the same species. As we have seen in 1.5.1, even such modification due to energy loss occurs on a relatively long time scale. In particular, since the high-mass  $b\bar{b}$  created in high-energy collisions at the LHC typically hadronize once outside the target nucleus, the  $\Upsilon$  states do not experience nuclear absorption [8, 9, 26, 95, 104].

## Comover Interactions

Next, we consider a final-state CNM effect on quarkonia that is active in proton-nucleus collisions even at high energies. Hadronized quarkonium mesons may be modified by comover interactions, where they are broken up by particles traveling with similar rapidities. Even high-mass states, which have a longer formation time, can be affected by comover interactions, as long as there are other particles traveling in the same kinematic phase space as the quarkonia.

The amount of modification of quarkonium production due to comover interactions depends primarily on the interaction cross section of a quarkonium state with its comoving particles and the density of such comovers. In the comoving medium, quarkonia may be broken up by interactions with hadrons such as light mesons. The formation of times of the soft particles produced in the collision are also boosted by Lorentz dilation, and scattering by comoving soft particles can continue long after the initial collision and well outside the nuclear volume. While the interaction rate may be energy dependent, the exact dependence is not well constrained, but is nonetheless expected to be small. As a result, the interaction cross sections determined from the low-energy experiments are often used for predictions at all energies in the comover interaction model (CIM) [9].

The comover density cannot be a free parameter when implementing the CIM, since assumptions regarding the density must be able to reproduce the measured total rapidity distribution  $dN/dy$  of particles in a given collision medium. The rapidity distribution can be estimated using the number of binary collisions in proton-nucleus collisions to scale up the charged particle multiplicity observed in proton-proton collisions. A multiplicative factor is applied to the rapidity distribution of the charged particle multiplicity to account for neutral comoving particles with which the quarkonia may also interact. Additionally, one takes into account shadowing by nPDFs by including a corrective factor determined by the number of binary collisions, the collision energy and the rapidity slice [9].

Comover interactions in proton-nucleus collisions are assumed to stop when the comover density, which dilutes as particles move further away from the collision vertex, reaches the density in proton-proton collisions at the same energy. The comover density is assumed to be boost-invariant in the longitudinal direction, justifying the use of an isentropic longitudinal expansion and neglecting transverse expansion, which is assumed to take place later after the nearly collinear quarkonia have traveled quite far [9].

The comover framework has two important features that result in differences in modification of different hadronized quarkonium states. First, higher excited states experience stronger comover dissociation rates due to their larger size, which increases their cross section of interaction with comovers. Therefore, in the absence of QGP-like effects in proton-nucleus collisions, observed differences in the production yields of bottomonium states at the LHC would be highly indicative of final-state dissociation by comovers. Second, comover-interaction modification of quarkonium states is stronger in regions where the comover density is higher, such as in the nucleus-going direction in asymmetric proton-nucleus collisions and in regions of higher event activity in nuclear collisions in general, where particle multiplicities are higher. Thus, proton-nucleus collisions present the opportunity to study differences in quarkonium modification by interaction with comovers in regions of different nuclear matter densities within the same collision system [9, 28, 96].

Studies of charmonium states  $J/\psi$  [105] and  $\psi(2S)$  [106] in proton-lead data have demonstrated a difference in the suppression pattern of the two states. Figure 1.10 shows the observed nuclear modification in these studies along with predictions using the CIM for  $J/\psi$  (blue) and  $\psi(2S)$  (red) as a function of center-of-mass rapidity. A dashed black line shows the predicted modification due to nPDF effects, identical for the two states: a slight anti-shadowing in the backward region and suppression in the forward region. Through increased comover interactions, however, the higher particle density in the backward region can produce a stronger suppression there, an effect which will be more pronounced for the excited state. The competing effects of anti-shadowing and dissociation by comovers result in an

enhancement of  $J/\psi$  mesons in the backward region. The stronger effect of comovers on the excited state in the backward region, however, ultimately produces a similar suppression in  $\psi(2S)$  yield everywhere, even though, unlike in the backward region, the two effects are not in competition at forward rapidity [9].

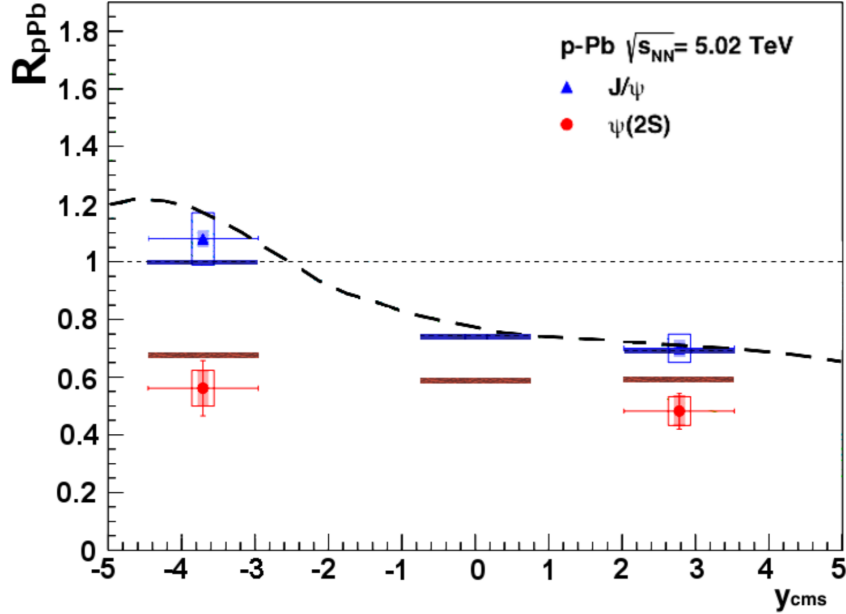


Figure 1.10: Observed nuclear modification of charmonium states along with predictions of modification from nPDF (dashed black line) and comover interaction (solid blue and red lines) effects [9].

## 1.6 A Clean Probe

We have already discussed some of the strengths of quarkonia as probes of nuclear matter in high-energy collisions based on their high mass, short formation time and long lifetime. Here we discuss some additional features of quarkonium states, and in particular the bottomonium family, which make them exceptionally powerful probes in ultra-relativistic heavy ion collisions.

Quarkonium states decay electromagnetically to lepton pairs of mass equal to that of the decaying bound state. The  $Q$  and  $\bar{Q}$  annihilate into a massive photon which then

converts to a pair of leptons,  $l^+l^-$ . Since leptons do not interact strongly with matter, they are well suited for studying the dense-matter dominated heavy-ion collisions [10, 54, 107]. Irrespective of the nature or volume of nuclear matter it encounters, the daughter lepton pair from a quarkonium state encodes information on the impact of the collision environment on the state, without introducing features due to its own interactions with the environment. This makes the dilepton decay channel of quarkonia an equally good probe of the collision medium in all collision systems: proton-proton, proton-nucleus and nucleus-nucleus. The peaks in the opposite-sign dilepton invariant mass spectrum corresponding to quarkonium bound states appear as clean features in all experimental data [10].

Furthermore, the dilepton decay channel has unique significance in the study of hot nuclear matter from a theoretical perspective. The dilepton emission rate from quarkonium decay in the QGP at a certain temperature is given by the product of the Bose-Einstein factor with the in-medium spectral function obtained from lattice QCD using an effective complex potential as discussed in section 1.4 [5, 108]. Changes in the in-medium spectral functions are directly related to changes in the dilepton emission rate from quarkonium decay. Thus, the area under a peak in the in-medium spectral function shown in figure 1.5, which can be identified with a given state, encodes information on the experimentally-accessible dilepton emission spectrum of that state in a thermalized QGP [5].

Next, we turn to some advantages of studying bottomonia over charmonia in heavy-ion collisions. While both charmonia and bottomonia are created in the initial hard scatterings in high-energy collisions and have similar decay rates, bottomonium states are particularly effective for exploring suppression effects over a wide range of temperatures of the early stage QGP. The effective field theory approach is better suited to bottomonia than their charmonium counterparts due to the greater separation of binding energies of bottomonium excited states as well as their higher dissociation temperatures [44, 56, 59]. Since they do not thermalize with the QGP, bottomonia are a dynamic probe of the evolving QGP [4]. Moreover, due to the larger  $b$  quark mass, CNM effects, such as shadowing are expected to

be less significant for bottomonia than for charmonia [56, 59].

Moreover, due to the comparatively small  $b\bar{b}$  cross section, in-medium recombination of uncorrelated  $b$  quarks are expected to be less prevalent for the bottomonium family than of uncorrelated  $c$  quarks for the charmonium family [24, 44, 45, 56, 59, 104, 109]. While quarkonia produced in initial hard scatterings in collisions of heavy ions encode information on the evolution of the QGP, those created by recombination of uncorrelated quarks cannot be confidently used as a probe in the same way. The observed smaller suppression of charmonia in higher-energy collisions at the LHC compared to collisions at RHIC, although initially startling, results from the larger contribution from recombination of uncorrelated  $c$  quarks to the yield at the higher energy. By contrast, measured bottomonium yields at the LHC are expected to have only a small contribution from statistical recombination of uncorrelated  $b$  quarks, similar or smaller in magnitude to the effect of recombination of  $c$  quarks on charmonium yield at RHIC.

Finally, one of the challenges of using the sequential melting of quarkonia to study QGP temperature is that the decay modes of higher excited states of quarkonia include decay to lower states. This is known as feed down. Feed down can contribute to the measured yield of lower quarkonium states, introducing some ambiguity to experimental inferences. Figure 1.11 shows the mass ordering the bottomonium family, including the  $\Upsilon$  ( $J^{PC} = 1^{--}$ ) as well as other S and P state bottomonium mesons. The possible decay paths of dissociating  $\Upsilon(1S)$ ,  $\Upsilon(2S)$  and  $\Upsilon(3S)$  states are illustrated. Hadronic decays are indicated using thick arrows, and radiative decays using thinner arrows. Note that the  $\Upsilon(4S)$  and higher excited  $\Upsilon$  states are not studied experimentally in the same way since they are above the  $B\bar{B}$  threshold and therefore decay strongly to  $B$  mesons rather than electromagnetically to lepton pairs [10]. In general, feed-down contributions of higher states to lower states need to be considered for all quarkonium states used to probe the QGP. Only total yields (irrespective of the source) can be measured experimentally. Therefore, theoretical models typically include both direct production and feed-down contributions to the predicted inclusive yield. However, since recent

measurements and theoretical calculations [110] suggest that the  $\Upsilon(3S)$  is almost entirely directly produced, it provides an especially clean probe for studying nuclear modifications at high temperatures [44, 111]. In this report, we focus on the  $\Upsilon(1S)$ ,  $\Upsilon(2S)$  and  $\Upsilon(3S)$  states and their decays to  $\mu^+\mu^-$ .

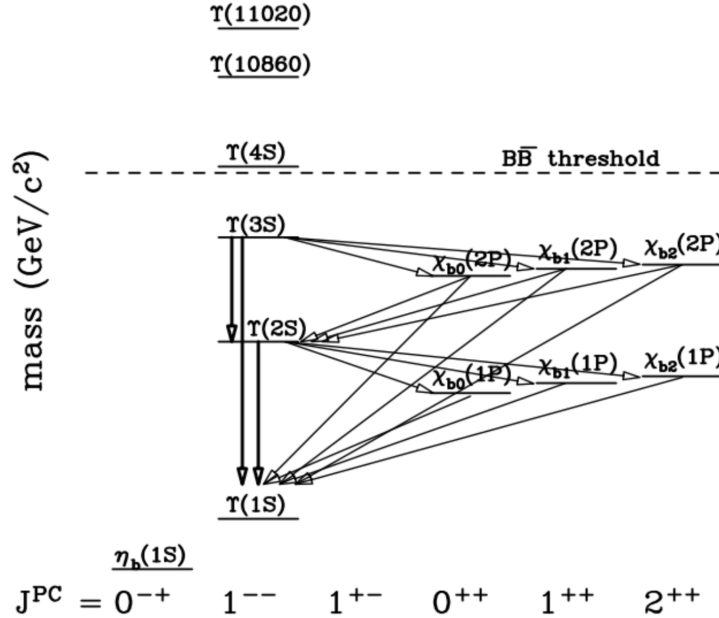


Figure 1.11: The mass ordering of bottomonia. The possible hadronic and radiative decay paths of dissociating S-wave states  $\Upsilon(1S)$ ,  $\Upsilon(2S)$  and  $\Upsilon(3S)$  are illustrated [10].

## 1.7 A Challenge: Quarkonium Production

Before moving on to discussing the analysis of  $\Upsilon(nS)$  yields in pPb collisions, we briefly mention some challenges associated with quarkonium production. Although we have evoked quarkonium production yields in proton-proton collisions as a baseline for understanding QGP and CNM effects, the process by which quarkonia are created is in fact one of the least understood ingredients in the use of quarkonia to study QCD physics.

Figure 1.12 illustrates the stages involved in the production of an  $\Upsilon$  meson in the collision of two protons. Experts generally agree that the overall cross section for  $\Upsilon$  production in the collision nicely factorizes into two parts: the production of the heavy quark pair (blue),

and the transition of the quark pair into a bound state (green), although this assumption has been found to break down in certain regimes [44, 59]. In this example, two gluons, one from each incoming proton, fuse together in the initial stage through a hard process. The  $b\bar{b}$  production cross section can be calculated perturbatively, using the gluon PDFs and the cross section of gluon fragmentation to  $b\bar{b}$ . The transition of the quark pair to the bound state, however, cannot be calculated perturbatively because of the lack of a separation of mass scales. Further convolving factors include the need to produce a color singlet quarkonium state, with particular angular and spin quantum numbers, whereas the  $Q\bar{Q}$  pairs are typically produced as color octet objects. A different nonperturbative matrix element must be calculated to determine the probability of producing the quarkonium state for each set of possible quantum numbers of the  $Q\bar{Q}$  in the initial state. Therefore, not only is the hadronization of the heavy quark pair into a quarkonium state difficult to calculate because it is nonperturbative, but it also presents some formidable conceptual hurdles [4, 10, 44, 59, 112, 113].

Several models have been devised to describe quarkonium production, including the color singlet model, non-relativistic QCD, and the color evaporation model. While each has had some degree of success, particularly at reproducing specific features in observed data, none are without flaw. In order to improve the models and develop a more complete understanding of quarkonium production mechanisms, we must study quarkonia across all available phase space in proton-proton collisions as well as nuclear collisions, investigating not only the production cross section but also characteristics such as flow and polarization.

Furthermore, quarkonium yields in LHC proton-proton collisions have been found to increase with associated track multiplicity [114], a result not expected if quarkonia are produced in hard partonic scattering only. This suggests the possibility of quarkonium production mechanisms that have previously been underestimated. For instance, soft mechanisms for quarkonia production, or a relationship between quarkonium production and underlying event characteristics, may be significant.

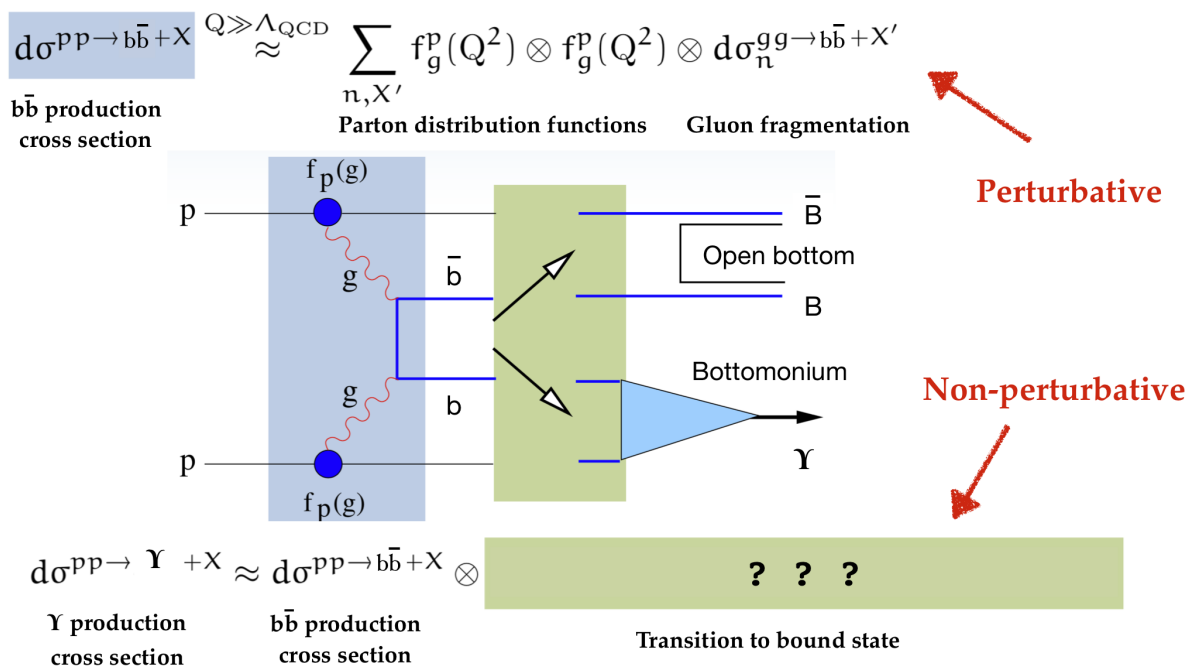


Figure 1.12: Factorization of  $\Upsilon$  production in a proton-proton collision [4].

As shown in figure 1.13, coherence effects in a high-density medium produced even in high-multiplicity proton-proton collisions have been employed to explain the quadratic relationship between  $J/\psi$  multiplicity and charged particle multiplicity observed in data at midrapidity (red) and forward-rapidity (blue) [11, 114]. The possible existence of collectivity in high-multiplicity proton-proton collisions can be investigated using the relation between quarkonium production and underlying event characteristics. In particular, the underlying event may be connected to the evolution of the heavy quark pair into a bound quarkonium state. The average contribution from each  $\Upsilon$  state to the global event characteristics and, conversely, the contribution of the underlying event to the production of individual  $\Upsilon$  states could be different. Therefore, investigating the relationship between the underlying event and  $\Upsilon$  production in proton-proton collisions promises insight into the stages of quarkonium production not related to partonic hard scattering.

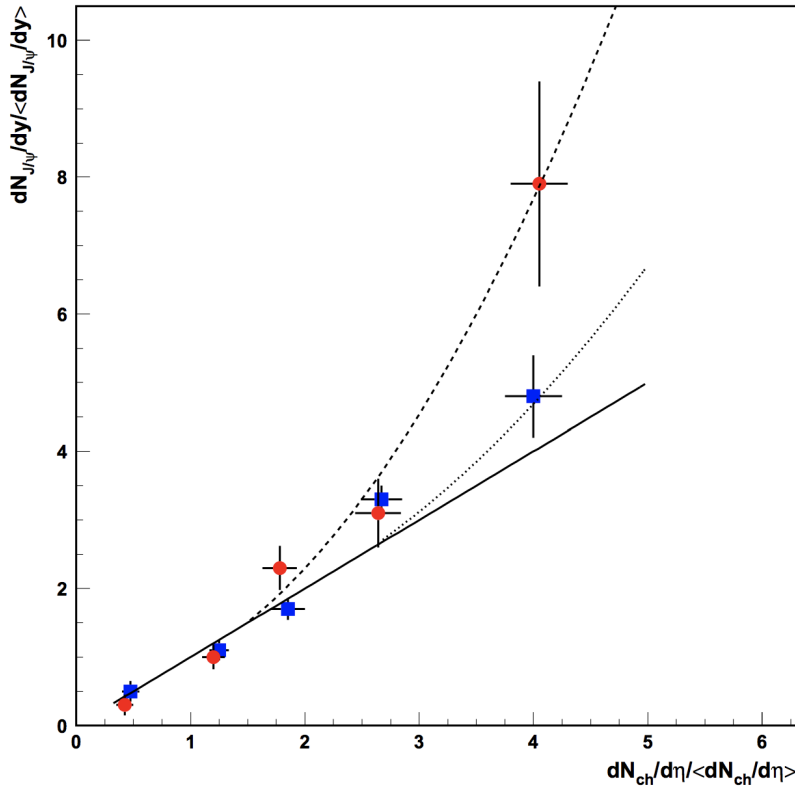


Figure 1.13: Increasing  $J/\psi$  multiplicity with associated track multiplicity in proton-proton collisions [11].

## 1.8 Observables

Quarkonium states have been studied in various available heavy-ion collision data collected at laboratories worldwide. Quarkonia are also studied in proton-proton (pp) collisions by heavy-ion physicists, as these provide a baseline for QGP and CNM effects in nuclear collisions. The dedicated heavy ion collider RHIC in Brookhaven, New York, has provided a breadth of gold-gold collision data at relatively low per nucleon center-of-mass energy  $\sqrt{s_{NN}}$ , at the highest of which ( $\sqrt{s_{NN}} = 200$  GeV) a relatively high temperature QGP is thought to be produced. Other nuclear collision systems explored at RHIC include deuteron-gold and, more recently, aluminum-gold collisions. The higher-energy LHC, straddling France and Switzerland, has provided collision data for lead-lead (PbPb) at  $\sqrt{s_{NN}} = 2.76$  TeV and  $\sqrt{s_{NN}} = 5.02$  TeV, and, most recently, for xenon-xenon at  $\sqrt{s_{NN}} = 5.44$  TeV. Proton-lead (pPb) collision data have also been collected at the LHC in recent years at  $\sqrt{s_{NN}} = 5.02$  TeV and  $\sqrt{s_{NN}} = 8.16$  TeV. A wealth of quarkonium results have been published and are currently being explored with these data.

As explained in sections 1.4 and 1.5, the modification of bottomonium production yields in proton-nucleus and nucleus-nucleus collision systems is representative of differences in the collision medium. For an effective comparison of these collision systems, both sets of data at the same  $\sqrt{s_{NN}}$  are required. Additionally, we also require proton-proton collisions at the same energy to use as reference. Indeed, the LHC has provided data for all three collision systems: pp, pPb and PbPb at  $\sqrt{s_{NN}} = 5.02$  TeV. Moreover, the data collected from these collisions by the Compact Muon Solenoid (CMS) detector, which has excellent muon momentum resolution, show all three  $\Upsilon$  resonances in the dimuon invariant mass spectra. This makes it possible for the first-time to study the production of all S-wave bottomonium states under the  $B\bar{B}$  threshold in vacuum as well as CNM and QGP media at the same energy.

Nuclear modification factors  $R_{pPb}$  and  $R_{AA}$  are ratios of quarkonium production cross sections in nuclear collisions such as pPb or PbPb to the appropriately scaled cross sections

in pp collisions. They help compare bottomonia yields in pp, pPb, and PbPb collisions. The yields in pp collisions are scaled by the mean number of binary nucleon-nucleon collisions in PbPb to determine the  $R_{AA}$ . The  $R_{pPb}$  is typically determined under the assumption that the quarkonium cross sections in pPb scale as  $\sigma_{pPb} = A\sigma_{pp}$ , where  $A$  is the mass number of Pb.

In this dissertation, we use  $R_{pPb}$  and  $R_{AA}$  to quantify the nuclear modification of the three bottomonium states  $\Upsilon(1S)$ ,  $\Upsilon(2S)$ , and  $\Upsilon(3S)$ , in pPb and PbPb collisions at  $\sqrt{s_{NN}} = 5.02$  TeV using data collected by the CMS detector at the LHC. We measure  $\Upsilon$  mesons via their decays to dimuons:  $\Upsilon(nS) \rightarrow \mu^+\mu^-$ . The branching fraction for this decay is  $\sim 2.5\%$  on average for all three states. We investigate the relation of the  $R_{pPb}$  and  $R_{AA}$  to measured quantities in data such as  $\Upsilon$  kinematic distributions and, when possible, event activity distributions. These relationships help us test theoretical models and their predictions, and ultimately allow us to constrain the theory of the strong interaction.

Ratios of production cross sections of excited bottomonium states to that of the  $\Upsilon(1S)$  state, known as excited-to-ground state ratios  $\Upsilon(nS)/\Upsilon(1S)$ , may also be used to quantify the relative modification of excited  $\Upsilon(nS)$  production in heavy ion collisions, when compared to the same ratios in pp collisions. However,  $R_{pPb}$  and  $R_{AA}$  allow us to quantify the absolute nuclear modification relative to pp collisions, including the modification of  $\Upsilon(1S)$ . Theoretical calculations of the  $R_{pPb}$  incorporating CNM effects and of the  $R_{AA}$  incorporating additional deconfinement effects are available for direct comparison to data. When scaled appropriately to account for the presence of two lead ions in the PbPb system, the  $R_{pPb}$  determined using pPb collisions can be used to anticipate the amount of CNM modification already encapsulated in  $R_{AA}$  measurements from PbPb collisions.

Additionally, asymmetric pPb collisions create an imbalance of nuclear matter in the proton-going (defined as forward rapidity) and lead-going (backward rapidity) directions. Therefore, they can be used to investigate differences in CNM effects in regions of varying nuclear matter within the same collision system. CNM modification mechanisms that rely

on the abundance of nuclear matter include comover interactions, where the cross section of interaction increases with particle multiplicity in the rapidity region of the produced  $\Upsilon$  [9, 28]. We measure the forward-backward production ratios  $R_{\text{FB}}$  of  $\Upsilon$  states in pPb collisions at  $\sqrt{s_{\text{NN}}} = 5.02$  TeV. The  $R_{\text{FB}}$  help compare  $\Upsilon$  yields in the proton- and lead-going directions, without the need for a pp baseline.

The LHCb [32] and ALICE [31] collaborations reported measurements of  $\Upsilon(n\text{S})/\Upsilon(1\text{S})$  (LHCb for  $n = 2, 3$ ; ALICE for  $n = 2$ ), along with  $\Upsilon(1\text{S})$   $R_{\text{pPb}}$  and  $R_{\text{FB}}$  in pPb collisions at  $\sqrt{s_{\text{NN}}} = 5.02$  TeV using  $\Upsilon$  detected away from midrapidity. In those studies, when required, the proton reference was obtained via interpolation. In the midrapidity region, the ATLAS collaboration studied bottomonia in pPb collisions using same-energy pp reference data [30], reporting  $\Upsilon(n\text{S})/\Upsilon(1\text{S})$  (for  $n = 2, 3$ ), as well as the  $\Upsilon(1\text{S})$  self-normalized yield and  $R_{\text{pPb}}$ . The CMS collaboration has also previously reported  $\Upsilon(n\text{S})/\Upsilon(1\text{S})$  (for  $n = 2, 3$ ) and  $\Upsilon$  self-normalized yields versus event activity in the pPb system in the midrapidity region, without use of pp reference data [115]. In the charmonium sector, the CMS collaboration reported the  $R_{\text{pPb}}$  of  $\psi(2\text{S})$  [116] and the  $R_{\text{pPb}}$  as well as  $R_{\text{FB}}$  of  $J/\psi$  [117] in pPb collisions at  $\sqrt{s_{\text{NN}}} = 5.02$  TeV. Each of these measurements contribute to the understanding of CNM effects on quarkonium production.

To study the QGP, measurements of  $\Upsilon(1\text{S})$ ,  $\Upsilon(2\text{S})$ , and  $\Upsilon(3\text{S})$  states have been carried out at  $\sqrt{s_{\text{NN}}} = 2.76$  TeV [25, 118] and, most recently, at  $\sqrt{s_{\text{NN}}} = 200$  GeV at RHIC [119, 120, 121]. Since the excited states are highly suppressed at  $\sqrt{s_{\text{NN}}} = 5.02$  TeV, however, only the CMS detector with its powerful magnetic field is able to resolve and measure all three  $\Upsilon$  states. Measurements by the CMS Collaboration have shown strong suppression of both  $\Upsilon(2\text{S})$  and  $\Upsilon(3\text{S})$  relative to the  $\Upsilon(1\text{S})$  ground state at this energy [122]. The suppression of the excited  $\Upsilon(2\text{S})$  relative to the  $\Upsilon(1\text{S})$  ground state persists at very forward rapidity,  $2.5 < y < 4$  [123]. In the case of charmonia, both  $J/\psi$  and  $\psi(2\text{S})$  mesons were measured by the CMS collaboration to be strongly suppressed at  $\sqrt{s_{\text{NN}}} = 5.02$  TeV [124, 125]. All of these measurements help constrain theoretical models of the deconfined medium.

In this dissertation, we present the first ever measurements of  $\Upsilon$  cross sections in cold nuclear matter incorporating the excited states. We then compute the ratios  $R_{\text{pPb}}$  and  $R_{\text{FB}}$ , which can be used to investigate the separation of initial-state versus final-state mechanisms for CNM modification. Additionally, we present the cross sections and  $R_{\text{AA}}$  of  $\Upsilon(\text{nS})$  mesons in PbPb collisions at  $\sqrt{s_{\text{NN}}} = 5.02$  TeV, which we recently published [29]. These results are also the first measurement of the absolute QGP modification of all three states at this energy. We make comparisons between the  $R_{\text{pPb}}$  and the  $R_{\text{AA}}$  measurements at the same energy: the first direct comparison of bottomonia in hot and cold nuclear matter. The  $R_{\text{pA}}$  and  $R_{\text{AA}}$  are presented as functions of the  $\Upsilon$  transverse momentum ( $p_{\text{T}}$ ) and center-of-mass rapidity ( $y$  or  $y_{\text{CM}}$ ), and in the case of the  $R_{\text{AA}}$ , also as a function of collision centrality (i.e, the degree of overlap of the two lead nuclei). We present the event activity dependence of the  $R_{\text{FB}}$  in pPb collisions.

## 1.9 Outline of the Report

In the remainder of this dissertation, we discuss the analysis techniques employed to determine  $\Upsilon$  modification in CNM and the QGP at  $\sqrt{s_{\text{NN}}} = 5.02$  TeV. We begin in chapter 2 with a description of the experimental facilities used to collect the data. A discussion of a few important data analysis strategies is presented in chapter 3. In chapter 4, we present a concise description of the study of  $\Upsilon R_{\text{AA}}$  in PbPb, which were recently published [29]. Next, in chapters 5 to 9 we provide an in depth discussion of the analysis of  $\Upsilon R_{\text{pPb}}$  and  $R_{\text{FB}}$  in pPb.

We lay out various quality selections applied to the data to maximize signal to background ratio for feature extraction in chapter 5. We also outline the ways in which we augment our analysis by generating Monte Carlo simulations sampling the underlying distributions. In chapter 6, we develop complex multivariate generalized linear models (GLMs) to extract  $\Upsilon(\text{nS})$  yields from features in data. The GLMs include two signal models and

two background models, which we test against each other to choose the models with highest goodness-of-fit. We reduce overfitting by mapping fitted parameters to known physical processes and investigating parameter correlations throughout available phase space. Once we are confident in our analysis choices, we perform constrained and unconstrained optimization of the objective functions in our GLMs, using penalty methods when necessary. We propagate the statistical and regression uncertainties from data to the measured quantities and, using p-value and studentized residual testing, we determine the significance of the results.

In chapter 7, we calculate correction factors to our results to account for losses in  $\Upsilon$  yield due to the detector geometry and type I and type II errors in various particle detection and analysis stages. In chapter 8, we use the worst performing signal and background models of those tested to determine the robustness of our results to our choices of the GLMs. In the same spirit, we also investigate any systematic variation of the results due to other choices in the analysis, such as the use of imperfect MC simulations. In chapter 9, we present the results and compare them to theoretical predictions as well as similar measurements published by other collaborations. We conclude this report by discussing the significance of our results in the field of heavy-ion physics and suggesting topics for further investigation.

# Chapter 2

## Experimental Facilities

### 2.1 CERN and the LHC

The European Organization for Nuclear Research (CERN) is an international research laboratory for ultrarelativistic particle and nuclear physics. Founded in 1954, CERN straddles the French-Swiss border near Geneva, Switzerland, and is currently supported by 23 member states (countries). Scientists and engineers at CERN are responsible for maintaining, operating and advancing the Large Hadron Collider (LHC) accelerator complex and the particle detectors housed at CERN.

The LHC, which first began operation in 2008 and is currently in long shutdown two (LS2), is the largest particle accelerator in the world. The 27 km circumference LHC ring replaced the earlier Large Electron-Positron Collider in the underground tunnel at CERN. The tunnel is located at an average depth of 100 m underground, in part under the Jura mountain range. Hadron beams were preferred to lepton beams for the LHC because the higher mass-to-charge ratio of hadrons exposes them to less synchrotron energy loss [126].

Using superconducting dipole magnets and RF cavities, the LHC simultaneously accelerates two beams of particles in circular orbit in opposite directions. The beams are focused

and made to collide using quadrupole magnets at four interaction points (IPs) interspersed around the tunnel. Beams are composed of bunches to ensure discretized beam interactions at the IPs, although several collisions can take place during the crossing of two bunches.

The LHC was designed with upgrades to higher energies and luminosities in mind. The highest center-of-mass energies attained by the LHC so far are 13 TeV for proton-proton collisions, 5.02 TeV for lead-lead collisions and 5.44 TeV for xenon-xenon collisions. The ongoing upgrades during LS2 will help the LHC achieve its design energy (14 TeV) and luminosity through a series of improvements, including the installation of a new injector. Once LS2 is over in 2021, the LHC will deliver its third and final round of particle collisions as designed, concluding the first phase (phase I) of the scientific project at CERN. During a planned long shutdown three, the collider will be upgraded to high luminosity LHC (HL-LHC), whose design luminosity will be 10 times higher than the LHC.

Four major collaborations are present at CERN: A Toroidal Large LHC Apparatus (ATLAS), A Large Ion Collider Experiment (ALICE), the Large Hadron Collider beauty (LHCb), and the Compact Muon Solenoid (CMS) experiments. Each collaboration has a namesake particle detector built around a different IP in the LHC tunnel. Figure 2.1 shows a cartoon of the LHC and the relative locations of the four major experiments. The detectors collect data from the collisions and the members of each collaboration have a chance to analyze the data first, before releasing them to scientists worldwide. Among areas of study of data collected from the LHC are precision Higgs measurements, beyond standard model physics and quark-gluon plasma physics.

## 2.2 Compact Muon Solenoid Detector

The CMS detector is located 90 m underground, in an experimental cavern built around IP5 of the LHC. Directly aboveground is the CERN site known as point 5 in Cessy, France, where the CMS control room is situated. Point 5 also houses the powerful high-level trigger

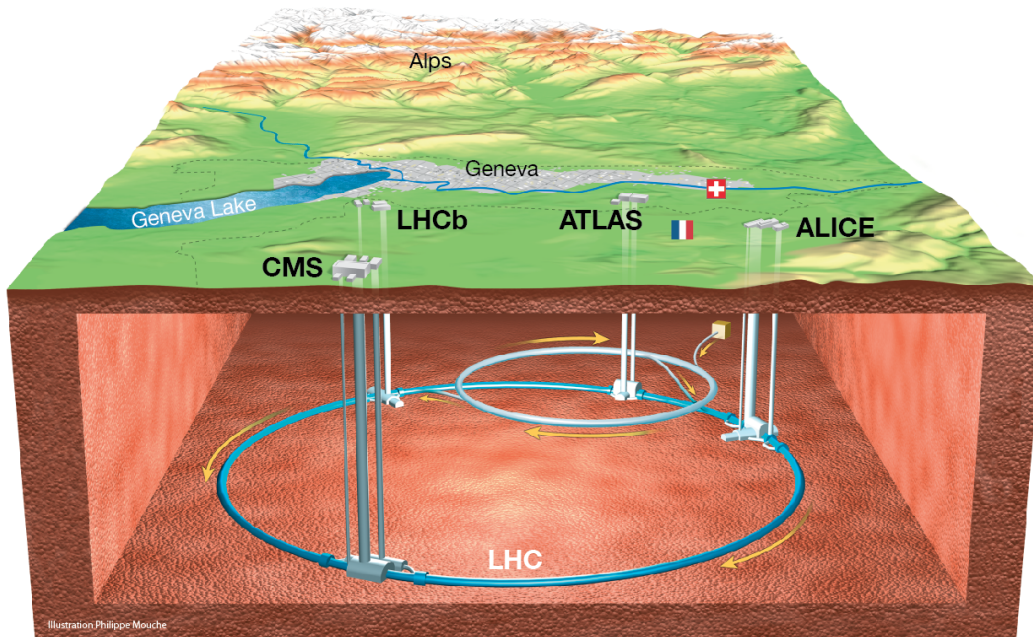


Figure 2.1: Cartoon showing the location of the LHC tunnel and the four major experiments at CERN [12].

(HLT) processor farm used for reduction of online (streaming) data collected by CMS.

The CMS detector is currently being upgraded in preparation for the higher luminosity and energy data the LHC will deliver during the upcoming “run” III of its phase I operation set to begin in 2021. Details of the ongoing and planned upgrades for the CMS detector during LS2 can be found in references [127, 128, 129, 130]. These upgrades, known as CMS phase I upgrades, include a new pixel detector and upgrades to the hadron calorimeter, muon and trigger systems.

Reference [14] provides a detailed description of the CMS detector and its components as they were during runs I and II of phase I of operation of the LHC. The data used to produce all the results presented here, as well as any LHC data used to make comparisons, were collected with these detector settings. In this section, we highlight the mechanisms of the detector components which were most pertinent to the results presented here. First, we provide a short discussion of the coordinate system used in measurements with CMS.

## 2.2.1 Coordinate System

The CMS detector uses a right-handed cylindrical coordinate system, with the beam line defining the  $z$ -axis. Figure 2.2 shows a longitudinal view (top) and cross section (bottom) of the CMS detector, including cartoons of individuals for scale. In symmetric collisions such as pp or PbPb, the direction of the  $z$ -axis is not consequential and is therefore defined by an  $x$ -axis that points to the center of the LHC ring and a  $y$ -axis that points vertically upward. In asymmetric collisions such as pPb, however, the positive  $z$ -axis points along the direction of the proton beam. The azimuthal angle  $\phi$  in the  $x$ - $y$  plane goes from 0 to  $2\pi$ . The polar angle  $\theta$ , measured from the positive  $z$ -axis, ranges from 0 to  $\pi$ . An additional coordinate, pseudorapidity  $\eta$ , is defined in relation to  $\theta$  as:

$$\eta = -\ln \left[ \tan \left( \frac{\theta}{2} \right) \right] \quad (2.1)$$

The rapidity  $y$  of a relativistic particle is defined as:

$$y = \frac{1}{2} \ln \left( \frac{E + p_z c}{E - p_z c} \right) \quad (2.2)$$

where  $E$  is the total energy of the particle, and  $p_z$  is its momentum in the direction along the beam axis. Differences in  $y$  are invariant under Lorentz boosts along the beam axis, providing a useful way to describe multi-particle decays and collisions. For highly relativistic particles, the rapidity  $y$  can be approximated by  $\eta$ .

## 2.2.2 Detector Components

Figure 2.3 shows a sectional view of the CMS detector, with its components labeled. Detector components parallel to the cylindrical surface in the “barrel” region are used for detecting particles with low  $y$ . Similarly, the flat surfaces perpendicular to the beam axis, known as

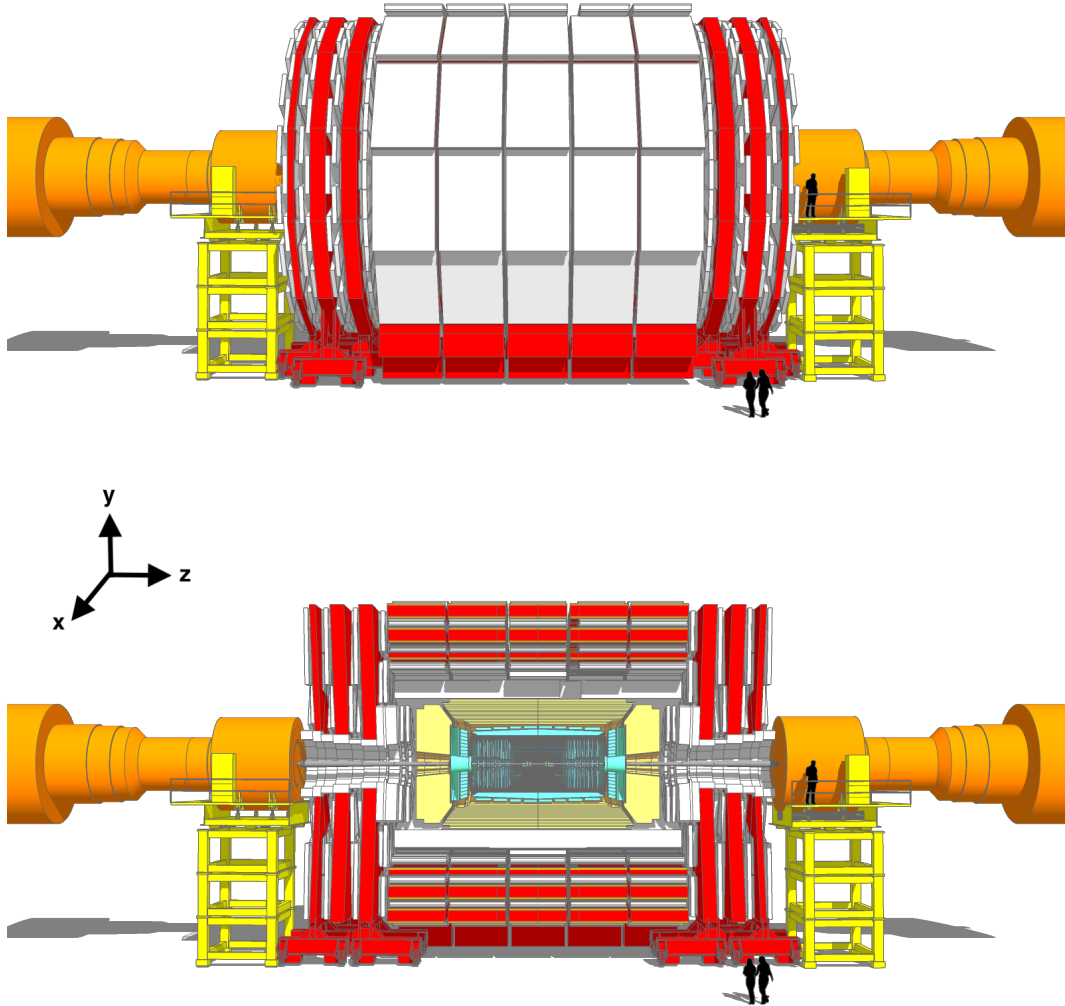


Figure 2.2: A longitudinal view (top) and cross section (bottom) of the CMS detector [13].

endcaps, are equipped with detector components so that particles traveling with high  $y$  may be measured.

The main feature of the CMS detector is a superconducting solenoid of 6 m internal diameter and 12.5 m length, which produces a 3.8 T magnetic field. The solenoid houses the silicon pixel and strip tracker which extends to  $|\eta_{\text{lab}}| < 2.5$ . The electronic calorimeters as well as most of the hadronic calorimeters are also located within the solenoid. A vacuum is maintained inside the solenoid. Muons are detected in the pseudorapidity range  $|\eta_{\text{lab}}| < 2.4$  in gas-ionization detectors embedded in the steel flux-return yoke outside the solenoid, with detection planes based on drift tube, cathode strip chamber, and resistive plate chamber technologies. Matching muons to tracks measured in the silicon tracker leads to a relative transverse momentum resolution on the order of 1 % for a typical muon in the analyses presented here [19].

Event activity in the mid pseudorapidity region is estimated using the number of tracks  $N_{\text{tracks}}$  in the silicon tracker. Forward calorimetry is facilitated by two steel and quartz-fiber Cherenkov hadron forward (HF) calorimeters, which cover the range  $2.9 < |\eta_{\text{lab}}| < 5.2$ . Event activity measurements in this region, and in particular, the centrality measurement for nucleus-nucleus collisions is based on the sum of transverse energy deposited in the HFs,  $E_{\text{T}}^{\text{HF}}$ . Centrality is evaluated as percentiles of the distribution of the energy deposited in the HF, with 0 % centrality corresponding to the most central events. A Glauber Monte Carlo simulation [131] is used to estimate the average number of nucleons,  $N_{\text{part}}$ , that participate in interactions for a given event activity or centrality class [33, 132].

## Tracking

The innermost component of the CMS detector, closest to the IP of beams, is a state-of-the-art silicon tracking system featuring high granularity and fast response. Objectives of the tracking system include precise and efficient measurement of charged particle trajectories, as well as precise reconstruction of secondary vertices. Additionally, the high-level trigger

### CMS DETECTOR

Total weight : 14,000 tonnes  
Overall diameter : 15.0 m  
Overall length : 28.7 m  
Magnetic field : 3.8 T

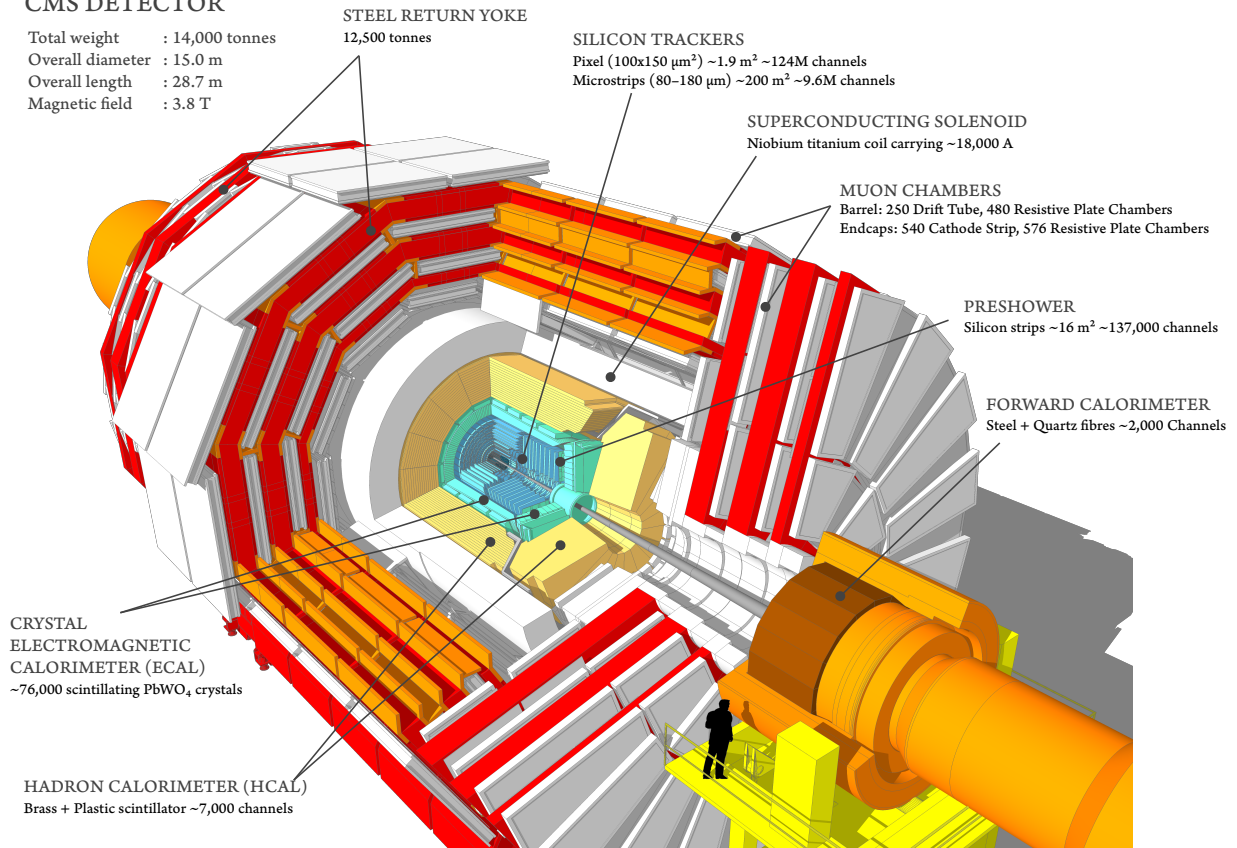


Figure 2.3: A sectional view of the CMS detector showing the detector components [13].

(HLT) of CMS relies heavily on the tracking system to reduce data produced during a bunch crossing by over six orders of magnitude prior to writing to disk.

Tracking is performed at smallest radii using space-economic pixel detectors, and at slightly larger radii using strip detectors, both made from silicon. Silicon is chosen in part for its hardness to radiation, since this first layer of the detector receives a remarkably high volume of particle incidence during collisions [14]. As shown in figure 2.3, both pixel and strip detectors comprise layers in the barrel and disks in the endcaps and provide tracking information in the full intended pseudorapidity coverage of  $|\eta_{\text{lab}}| < 2.5$ .

Figure 2.4 shows the schematic of a longitudinal cross section of a quadrant of the tracking system. The pixel detector provides similar track resolution in both transverse and longitudinal directions, allowing for 3D vertex reconstruction. It achieves a spatial resolution for charged particles of about  $15 \mu\text{m}$ . Figure 2.5 shows a photo of the pixel layers and electronics and their proximity to the beam pipe.

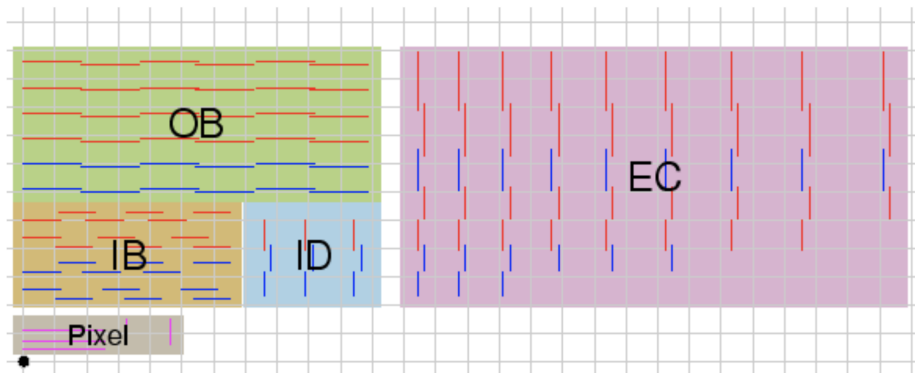


Figure 2.4: Longitudinal cross section of one quadrant of the CMS detector showing the layout of the tracking system [14].

The strip detector is composed of strips parallel to the beam axis in the barrel and radial on the disks, and comprises three different subsystems. The inner barrel (IB) and disks (ID), which form the first layer, closest to the pixel detector, consist of  $320 \mu\text{m}$  thick micro-strips. Figure 2.6 shows a photo of a layer of strip detectors in the tracker IB. They provide up to four measurements for a track in the transverse plane and a spatial resolution of  $23 - 35 \mu\text{m}$ . The IB/ID is surrounded by the outer barrel (OB), which consists of thicker micro-strips



Figure 2.5: Photo of pixel detectors in the tracker next to the beam pipe [15].

( $500\ \mu\text{m}$ ) to minimize the number of readout channels needed. The OB provides another six transverse measurements of a track, with single point resolution between  $35 - 53\ \mu\text{m}$ . Finally, the endcaps (EC+ and EC-, where the sign indicates the location along the  $z$  axis) are composed of disks, carrying up to seven rings of silicon micro-strip detectors of both thicknesses depending on distance from the IP. The EC provide up to nine measurements per trajectory in the longitudinal direction. Additionally, a second micro-strip detector module is mounted on several of the strip detector subsystems, in both the barrel and endcap regions, in order to provide a measurement of the second coordinate (longitudinal in the barrel and transverse on the disks).



Figure 2.6: Photo of strip detectors in the tracker in the barrel region [16].

The sensory and readout technologies in the tracker are designed to provide fast response while minimizing their interaction with tracks. The pixels are mounted with  $n$ -on- $n$  sensors created by introducing high dose  $n$  implants into a high resistance  $n$  substrate. The sensor elements in the strip tracker are single sided  $p$ -on- $n$  type silicon micro-strip sensors.

## Calorimetry

Calorimetry is carried out by electromagnetic calorimeters (ECAL) and hadronic calorimeters (HCAL) placed inside the solenoid, as well as HF calorimeters placed close to the beamline, at either end of the detector. ECAL and HCAL detectors are present in both the barrel and endcaps, as shown in figure 2.3. Working radially outward, the ECAL is the next detector component particles produced in collisions interact with, after the tracking system. Following the ECAL is the HCAL, which extends to fill up the remaining space inside the solenoid. This orientation is chosen to allow charged hadrons to leave a signal in both the ECAL and HCAL. An orientation with the HCAL closer to the IP would cause charged hadrons to deposit all their energy in the HCAL and fail to be detected by the ECAL.

The ECAL relies on photodetection technology to convert deposited energy from incident electromagnetic particles to a signal output. The scintillator used is polished lead tungstate ( $\text{PbWO}_4$ ) crystals, which feature a high density, short radiation length and small Molière radius, providing the desired granularity and compactness. The optically clear, fast and radiation-hard crystals have scintillation decay time on the same order as the bunch crossing time at the LHC, minimizing the dead time of the ECAL.

Avalanche photodiodes (APD) are used in the barrel, covering  $|\eta| < 1.5$ , and vacuum phototriodes (VPT) in the endcaps, extending the coverage up to  $|\eta| < 3.0$ . Figure 2.7 shows photos a polished endcap crystal with its attached VPT (left) and half of an endcap ECAL disk constructed out of a collection of such crystals. Since the performance of the ECAL is temperature dependent, it is kept at an operating temperature of  $18^\circ\text{C}$ . When combined with information from the tracker, the ECAL can discriminate between photons

and electrons, since photons will not be detected in the tracker.

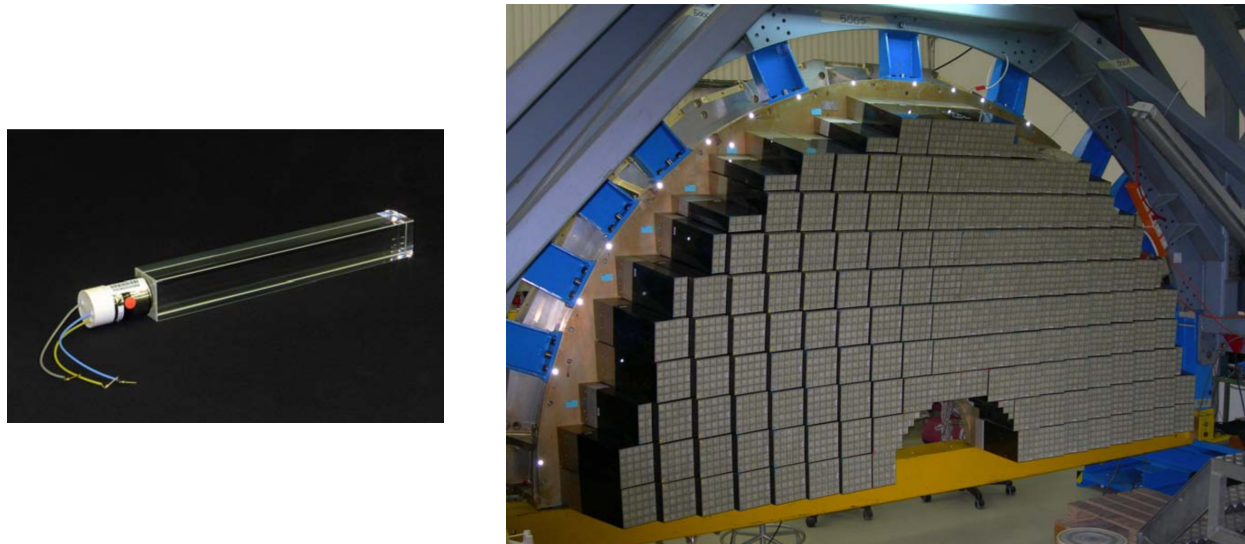


Figure 2.7: Photos of a single crystal of the endcap ECAL with a VPT attached (left) and a collection of crystals arranged to form one half of an endcap disk of the ECAL (right) [14].

A preshower detector is placed in front of the endcap ECAL crystals. The preshower is a sampling calorimeter with a layer of lead radiators followed by silicon strip sensors. The radiators initiate electromagnetic showers from incoming photons and electrons, while the strip sensors measure the deposited energy and the transverse shower profiles from these electromagnetic showers. The goal of the preshower detector is to identify neutral pions in the endcaps in the region  $1.7 < |\eta| < 2.6$ . Additionally, it facilitates the identification of electrons against minimum ionizing particles, and improves the position determination of electrons and photons due to its high granularity.

The HCAL not only provides calorimetry data for hadronic particles produced in collisions, but can also be used to determine missing energy signatures of neutrinos by requiring energy and momentum conservation. The HCAL is made of alternating layers of brass (70 % Cu and 30 % Zn) absorber plates and plastic scintillator trays. When a hadron traverses the HCAL it first collides with nuclei in the absorber and produces secondary particles. These particles travel through the scintillator and produce light that is collected by wavelength-shifting fibers and sent for processing. This process continues as particles that do not interact

in the first region will undergo particle production in the next absorber layer, producing secondary particles that produce light signals in the next scintillator layer, creating a shower.

The barrel portion of the HCAL provides coverage for  $|\eta| < 1.3$ , while the endcap portion provides coverage over  $1.3 < |\eta| < 3.0$ . The absorber plates and scintillator trays are placed parallel to the beam axis in the barrel, and perpendicular in the endcaps. Optical cables transfer signals from scintillator trays to multipixel hybrid photodiodes (HPDs), which are chosen for their low sensitivity to magnetic fields and large dynamical range. Figure 2.8 shows a barrel ring of the HCAL (golden ring) as it is being inserted using an industrial crane into the solenoid (gray). The barrel return yoke (red) with embedded muon detectors (gray) can be seen surrounding the solenoid.

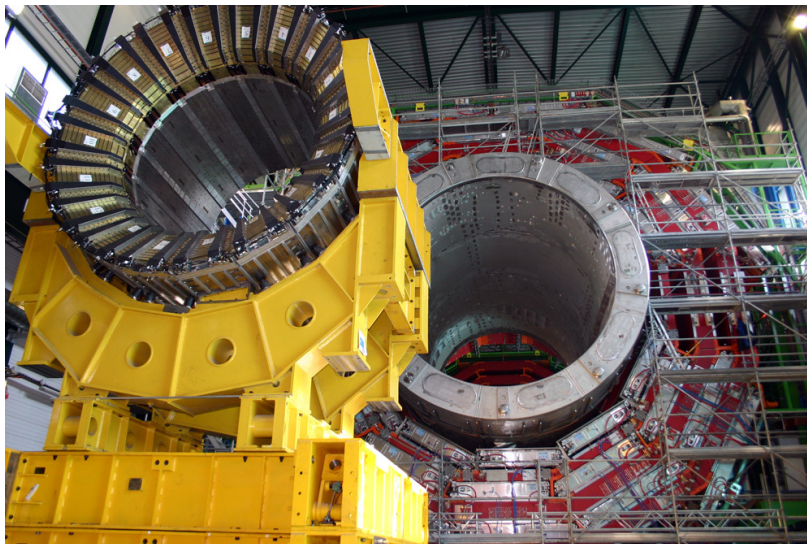


Figure 2.8: Photo of an barrel HCAL ring being inserted into the solenoid of CMS [17].

In the central pseudorapidity region, the barrel and endcap HCAL portions described do not provide sufficient stopping power for hadron showers. As a result, the HCAL is extended outside the solenoid with a tail catcher called the outer calorimeter (HO), placed in the first layer of the return yoke. The HO is used to identify and measure late starting showers.

The HF, which further extends the coverage of hadronic calorimetry to  $|\eta| < 5.2$ , receives several times more particle flux than do the rest of the detector components. Quartz fibers featuring a fused-silica core and polymer hard-cladding are chosen as the active material,

for their radiation hardness. The HF is a cylindrical structure with its front face located 11.2 m from the IP. A cylindrical hole of radius 12.5 cm allows passage of the beam. The HF consists of grooved steel absorber plates, perpendicular to the beam axis, into which the quartz fibers are inserted. The fibers run parallel to the beam line, and are bundled to form towers which run directly to conventional photomultiplier tubes used for signal readout. Figure 2.9 shows an HF tower before installation.



Figure 2.9: Photo of an HF tower before installation into CMS showing the quartz fibers [18].

An HF signal is generated when charged shower particles above the Cherenkov threshold generate Cherenkov light. The HF is therefore primarily sensitive to the electromagnetic component of showers. Signal from the HF is immediately deserialized and used to construct trigger primitives which are sent to the calorimeter trigger. The HF signal is one of the techniques capable of providing suitable luminosity information for the beams circulating in the LHC in real time.

## Muon System

The CMS detector is especially suited for the dimuon final state we use to reconstruct quarkonia for the results presented here. The muon system comprises detectors based on three different gas-ionization technologies: resistive plate chambers (RPC), drift tubes (DT), and cathode strip chambers (CSC). Figure 2.10 shows a longitudinal cross section of one

quadrant of the CMS detector, with the muon detectors emphasized. The barrel region relies on DTs and RPCs, while the endcap region consists of CSCs and RPCs, with the CSCs providing coverage up to the highest  $\eta$ .

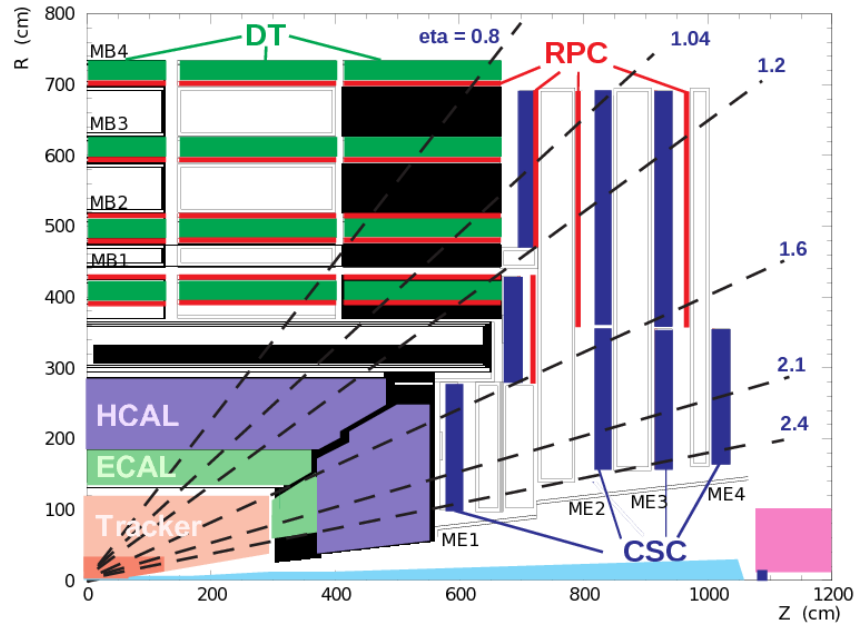


Figure 2.10: Longitudinal cross section of one quadrant of the CMS detector showing the layout of muon detectors [19].

As suggested by the name, the CMS detector specializes in the triggering, identification and precise momentum resolution of muons. The strong magnetic field solenoid enables the CMS detector to achieve excellent muon momentum resolution without requiring extremely accurate spatial resolution or prescriptive placing of the muon chambers. The magnetic flux generated by the inner magnetic field is sufficiently large that four muon stations can be installed along any path radially outward from the center of the detector, without saturating the outer flux return yoke [19]. This not only allows muons to be measured using multiple hits in the muon chambers, but also enables triggering using muon stations. Furthermore, the high curvature of the muon path due to the strong magnetic field allows efficient muon measurement up to  $|\eta| < 2.4$ . Finally, a sophisticated alignment system measures the positions of the muon detectors with respect to each other and to the inner tracker, in order to maximize muon momentum resolution.

Additionally, the muons studied have average  $p_T$  of a few GeV, which lies within the Bethe-Bloch region of energy loss for muons, not far from minimum ionization [133]. Muons are able to penetrate through to the outer muon detectors with relatively little Bremsstrahlung radiation or multiple Coulomb scattering with the inner detector material. Muons therefore leave a particularly clean signal throughout the tracking system and well into the muon detectors which extend up to 7 m from the center of the detector.

Figure 2.11 shows a transverse cross section of the barrel region of the CMS detector, with a section enlarged to illustrate the signatures left by various types particles that may be produced in collisions. While photons and electrons are stopped by the electronic calorimeters, and hadrons by the hadronic calorimeters, the high-mass, minimally-ionizing muons leave a relatively clean S-shaped signature ranging from the inner to the outer parts of the detector. Negligible punch-through reaches the muon system due to the amount of material in front of it, which exceeds 16 interaction lengths.

The offline muon momentum resolution using nothing but hits in the muon system, referred to as the standalone muon reconstruction, is about 9 % for muons traveling up to  $p_T \sim 200$  GeV but with small  $|\eta|$ . A global momentum fit using the inner tracker as well improves the momentum resolution by an order of magnitude at low momenta. The muon system and the inner tracker provide independent muon momentum measurements, enabling cross checking between the systems to identify incorrect measurements.

Gas-ionization detectors require a volume of relatively inert gas occupying the space between a narrowly separated anode and cathode. When a charged particle, in this case a muon, passes through a muon detector based on the DT, RPC or CSC technologies, it ionizes the gas, causing electrons to collect on the anode wire. Additionally, negatively-charged ions are attracted to and induce a charge on the cathode strips.

The drift tube technology used for muon detection in the barrel region,  $|\eta| < 1.2$ , comprises an anode wire running through a rectangular tube. The cell design includes two field-shaping electrode strips at the top and bottom of the tube, and two cathode strips

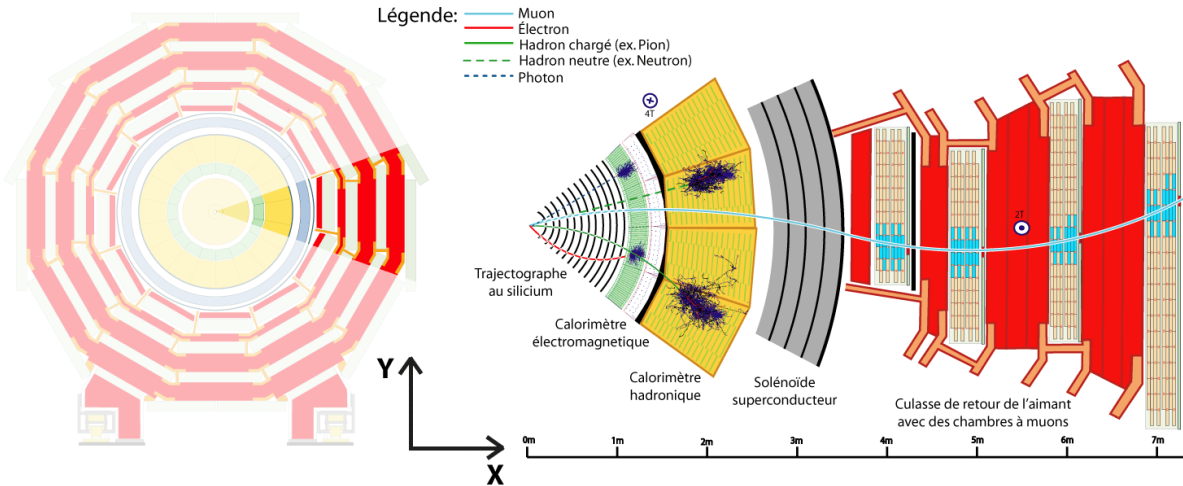


Figure 2.11: Transverse cross section of the barrel region of the CMS detector showing paths and stopping of different types of particles [13].

on the sides. Figure 2.12 shows the schematic cross section of a DT. The multi-electrode design improves spatial resolution ( $\approx 100 \mu\text{m}$  in  $r-\phi$ ) and ensures excellent performance in the presence of stray magnetic fields present in some regions of the outer barrel. The tube is filled with a gas mixture of Ar and a smaller amount of  $\text{CO}_2$ , since the latter helps to amplify the signal gain. Four concentric cylinders composed of DTs are embedded in the return yoke of the barrel. Using tubes running parallel to the beam axis, as well as a few that run perpendicular to it, DTs are able to provide location information on muons in all three coordinates.

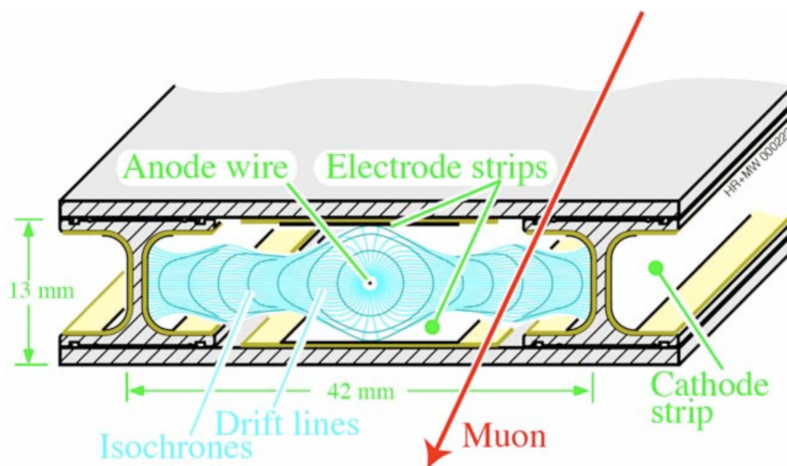


Figure 2.12: Schematic cross section of a drift tube (DT) [14].

In the endcap regions, where both muon and background rates are high, the muon stations comprise cathode strip chambers (CSC). With their fast response time, fine segmentation, and radiation resistance, the CSCs detect muons in the region  $0.9 < |\eta| < 2.4$ . The CSC technology relies on trapezoidal chambers containing six anode wires that run azimuthally and seven cathode strips that run along the beam axis, to provide position resolution of  $75 - 150 \mu\text{m}$ . In the gas mixture, a small amount of  $\text{CF}_4$  is added to Ar and  $\text{CO}_2$ , to prevent the wires from polymerizing. Four stations of CSCs are positioned perpendicular to the beam line and interspersed between the flux return plates in each endcap. The cathode strips of each chamber run radially outward, providing precise location measurement in the  $r$ - $\phi$  plane. The anode wires run approximately perpendicular to the strips and provide measurements of  $\eta$  as well as the beam-crossing time of a muon.

CSCs rely on the avalanching of electrons between the anode-cathode planes to magnify the signal. When an incident muon ionizes a gas atom, electrons that are knocked off subsequently ionize other atoms. This causes an avalanche of electrons and ionization, which eventually transmits the signal to the cathode strips. Figure 2.13 shows a cartoon of the response of a CSC to an incident muon. The top is a longitudinal cross section, while the bottom shows a transverse one. The muon coordinate in the  $\phi$  direction, along the wire, is obtained by interpolating charges induced on strips. Using pattern recognition, CSCs excel at rejecting non-muon backgrounds and efficiently matching hits to those in other muon stations and in the inner tracker.

The DT and CSC subsystems can each trigger on the  $p_T$  of muons with good efficiency and high background rejection rate, independent of the rest of the detector. The resistive plate chambers offer a complementary, dedicated trigger system in both barrel and endcap regions. They provide a fast and highly-segmented trigger for  $|\eta| < 1.6$  with a sharp  $p_T$  threshold, independent of the DTs and CSCs, albeit with poorer position resolution. RPCs also help resolve ambiguities during standalone muon track reconstruction.

RPC chambers rely on Bakelite gaps with gas space between the plates, organized in a

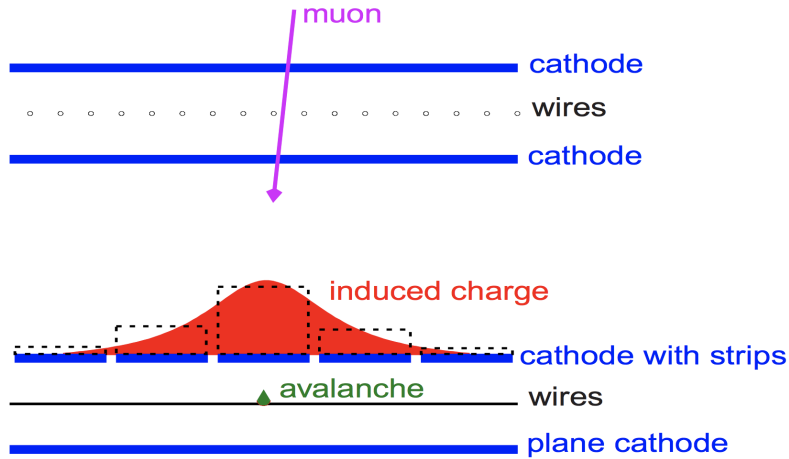


Figure 2.13: Schematic cross sections of a cathode strip chamber (CSC) and its response to an incident muon [20].

double gap design with a copper strip readout panel placed in between. Graphite anodes sandwich the Bakelite gaps. The RPC gas mixture is composed of primarily of  $C_2H_2F_4$ , with a small amount of  $iC_4H_{10}$  and trace amounts of  $SF_6$ . Similar to CSCs, RPCs operate in avalanche mode in order to cope with high background rates. They ensure precise bunch-crossing assignments using an excellent time resolution of  $\approx 2$  ns, much smaller than the LHC bunch-crossing rate. A schematic cross section of an RPC is shown in figure 2.14. A total of six layers of RPCs are embedded in the barrel muon system and four are embedded in the endcaps.

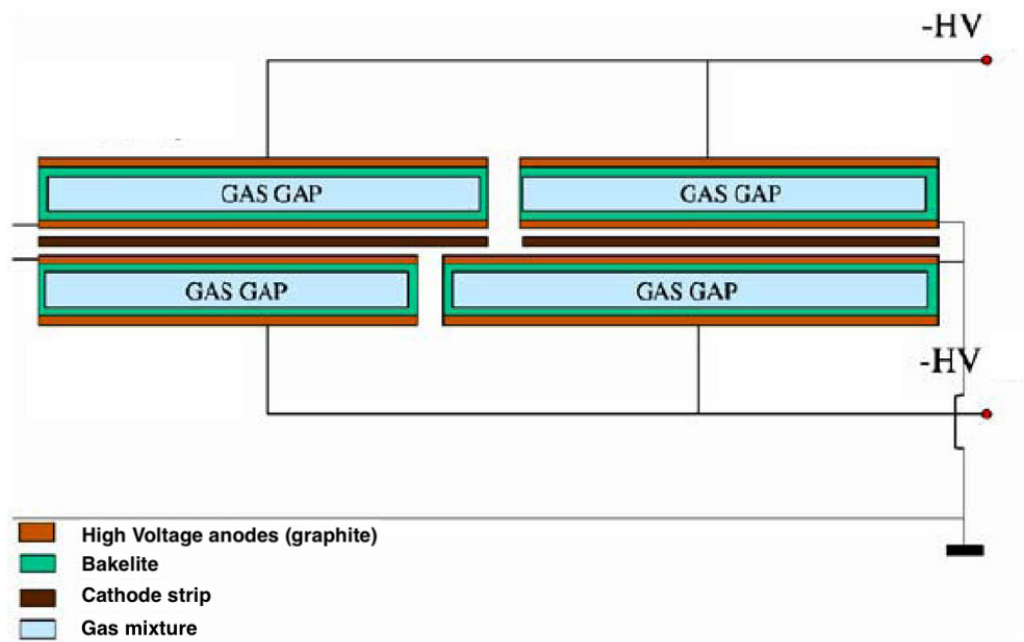


Figure 2.14: Schematic cross section of a resistive plate chamber (RPC) [21].

# Chapter 3

## Some Analysis Techniques

### 3.1 Data Collection

Tremendous amounts of data could be collected from collisions of the ultra-relativistic particle beams at the LHC. So much so, that the datasets could not be stored using all the world's hard drives. Therefore, a bulk of the data generated in these collisions actually have to be discarded as soon as it comes in. The decision to record or discard data has to be made in real time as collisions take place, producing signatures in the detector which the electronics nearly instantaneously read out as digital signal.

In order to explore directed physics using meaningful datasets, we must choose how to record relevant data, and what to discard. Often, we are interested in collision events containing fairly rare or exotic objects such as high-momentum jets or high-mass quarkonia, while the vast majority of the signatures left in the detector by collisions are from softer particles which are produced bountifully in all events. As a result, we need to come up with clever selection requirements on the data as it is streaming in. We would like to record events with specific signatures corresponding to the physics objects we are interested in, while discarding the multitudes of events that do not exhibit such signature. The art of doing so is known as triggering. At CMS, triggering is performed in two stages, first using

detector hardware at “level one” (L1) and then using a fast software verification at “high level”. Trigger reduces the size of streaming data at CMS by over six orders of magnitude prior to recording.

The data from collisions are simultaneously recorded into a number of different datasets, each with a specific set of requirements events must satisfy in order to be recorded. When an event’s signatures pass the requirements for a given dataset, we say the event triggered its recording into that dataset. Colloquially, the different datasets are referred to by the trigger requirements associated with them. Thus, a high-momentum jet dataset triggers on signatures likely coming from a high-momentum jet event. We call the recorded events in a dataset candidates for events containing the actual object. Even after all our analysis, we can never be fully certain that an event we classify as an  $\Upsilon$  event, for example, did in reality contain an  $\Upsilon$  particle. It is for this reason that collecting higher and higher statistics data is one of the primary drivers in our field. The more data we can analyze to test our hypothesis, the more confidence we can have in the inferences.

Although, the analyses we perform would not be possible without directed triggering of high-energy physics data, triggering can also bias the data collected in collisions. We want to be careful not to only collect data that helps us make a certain observation or claim. Much of physics is about being aware of the consequences of our choices and avoiding accidentally making choices that bias our results. To combat the issue of possibly biasing sampled data with our physics triggers, a minimum-bias trigger is used to record events with very minimal requirements. The minimum-bias dataset is used in various physics analyses whenever information regarding an underlying quantity in the collisions is needed. If we can be fairly certain a collision took place, we would like to record it in this dataset. However, as we argued above, all events satisfying some minimal set of conditions cannot be stored permanently. Even if they could, this large volume of data would simply be useless for studying rare phenomena, as any offline analysis software attempting to reject the massive amount of ordinary events would be extremely inefficient. For this reason, datasets with

fewer requirements, such as the minimum-bias trigger, are prescaled, i.e. only a fraction of the events satisfying the requirement are recorded. In this way, we get an unbiased (random) sample of the data satisfying a loose set of requirements.

## 3.2 Data Augmentation

Since we have prior intuition for signatures in collision data, we can facilitate our analysis using simulations. Physics processes, such as different channels of particle decays, can be generated using Monte Carlo (MC) simulation. We can then use these simulations to set expectations for particle yields in a given channel, for example. Additionally, it is important that we have a thorough understanding of how our detector affects the data we are able to collect. Fortunately, the detector’s response to specific signatures can be simulated as well. Such MC simulations can be used to determine corrections to particle yields extracted from data, based on the geometrical acceptance of the detector or inefficiencies in data collection. Simulations can also be used to test analysis software even before the data has become available, making a blind analysis possible. Blind analyses can be particularly useful in searches for exotic particles, which are extremely sensitive to statistical fluctuations in data.

Figure 3.1 shows the workflow of CMS data simulation. Kinematic information on the daughter particles from physics process generators such as PYTHIA8.209 [134] are fed into a CMS detector response simulator known as GEANT4 [135]. For a QGP environment, a generator such as HYDJET1.9 [136] can be used to simulate jet production, jet quenching and flow effects. The particle decay processes from PYTHIA8.209 can be embedded into HYDJET1.9 environments. GEANT4 incorporates the geometry of CMS, as well as the material both in active detector components and the filler material needed for electronics and cooling of the detector. The output from GEANT4 are a collection of simulated detector “hits”, or signatures, such as charged particle tracks in the tracker and energy deposits in calorimeter towers, that correspond to a generated event.

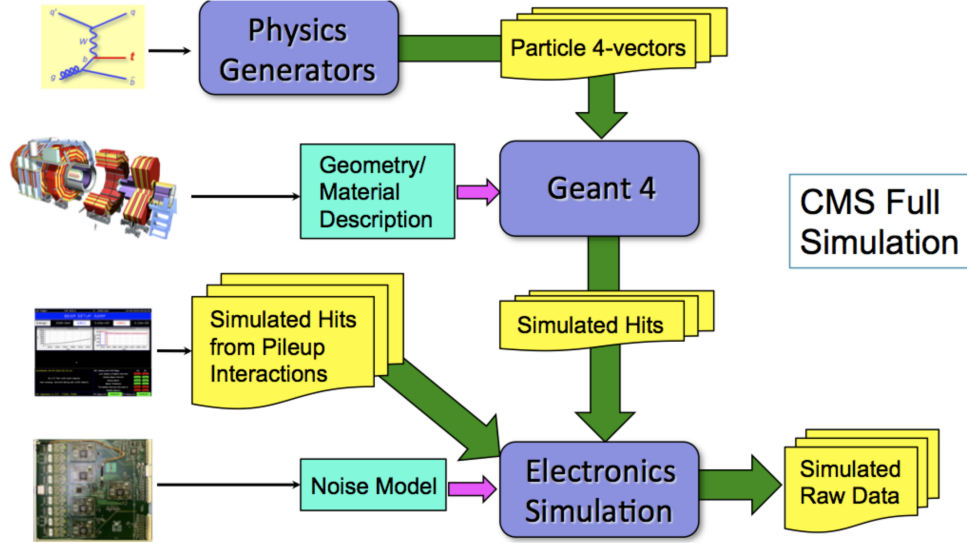


Figure 3.1: The workflow of performing full simulations of CMS data [22].

Concurrently, detector hits that would arise from the pile-up of other collision events that are spatially and temporally close to the event of interest, are also simulated. This is particularly important for mimicking pp data, where many collisions can occur during one bunch crossing. Finally, noise models are used to generate MC simulated detector hits from random processes, such as cosmic rays. All simulated hits are then run together through a rendering of the electronics of the detector. At this stage, the conversion of detector hits to digital readout signals are simulated, and various reconstruction algorithms, like the ones used for triggering of real data, are run over the simulated signals. The final output is a dataset of MC simulated events similar to the raw (unprocessed) collision data stream that is output by the CMS high-level trigger (HLT).

A more technical overview of the MC generation process is shown in figure 3.2. The MC generation and detector simulation is broadly grouped into a GEN-SIM category, while the digitization (conversion to digital signals) and reconstruction of signatures are known as DIGI-RECO. With some further processing, the MC output is put into analysis object data (AOD) format, just like event objects from promptly-reconstructed (prompt-reco) real data. Both MC and real data in AOD format need to be certified and processed into entity dataframes for ease of analysis. Details of the software architecture used for the handling

and processing of data will be provided later in section 5.1.

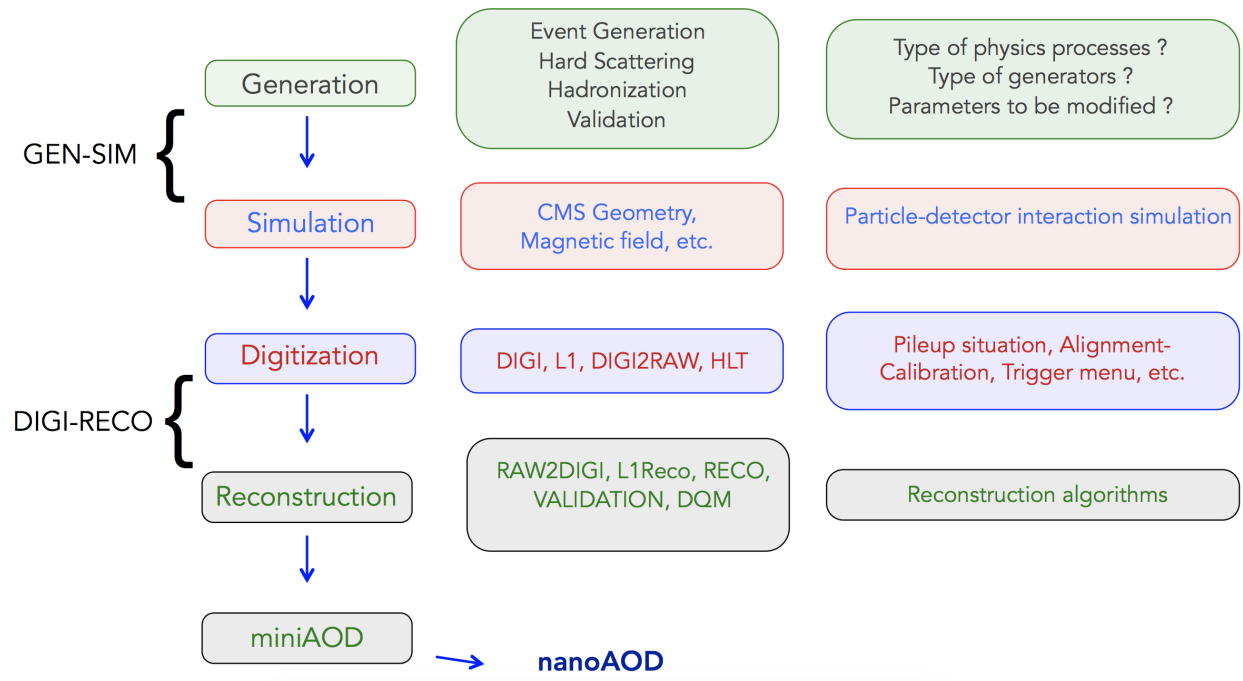


Figure 3.2: Technical overview of the stages of MC simulation of CMS data [22].

The dataframes used at CERN for analysis are known as “trees” and are stored in a format easily maneuverable by the high-energy physics data analysis framework developed at CERN called ROOT. Trees contain entries of event data stored as n-tuples of particle kinematic variables and collision meta data. The n-tuples, which are lists of lists, are referred to as branches. ROOT provides a simple user interface for querying the trees and visualizing histograms.

### 3.3 Checking Robustness of Results

The overall target in data analysis is to identify signal and background features in data, maximize the signal-to-background ratio, and extract the signal. In going from the raw recorded data to the final inferences (results), several steps such as data reduction and feature extraction are performed. A certain amount of data may be discarded at each step.

The steps may also involve the estimation of an intermediate quantity which cannot be measured directly from data, or the calculation of a correction factor based on detector error rates. Thus, when determining the methodology for analyzing a dataset, the analysis team discusses and makes choices at every step. Some degree of freedom is involved in making each of these decisions and careful statistics and physics insights must be employed when making them. Nonetheless, the choices of analysis methodology leave us prone to introducing biases in our results. As a simple example, even how we choose to histogram a measured observable (independent variable) has an effect on the features that appear in its spectrum. If we use the features to determine an inferred quantity (dependent variable), it may be biased by the width of the histogram bins.

As already mentioned, one of our goals when analyzing data is to be cognizant of the impact of our choices on the inferences we draw. Thus, we check the robustness of our derived results to those choices and check for any systematic bias they introduce. We quantify the degree of uncertainty in the results corresponding to each analysis choice by performing the same procedure or calculation with another, equally reasonable choice. Typically, the choice we have most confidence in is used as the “nominal” method, and a second option, which one can argue with similarly strong reasoning, is used as the alternate method. The difference in results obtained using the nominal and alternate options can be a measure of the uncertainty in the results due to the choice.

If we can verify that the effects of choices made during different steps are independent of each other, then the uncertainty estimates obtained in this way can be combined in quadrature to estimate the overall uncertainty in the results due to the aggregated choices. This is known as the systematic uncertainty in the inferred quantities from data due to our analysis method. The statistical uncertainty innate to the data should not be confused with the systematic uncertainty. When a generalized linear model is used to extract features in data, the statistical uncertainty contributes to the regression uncertainty and therefore to the extracted features (such as  $\Upsilon$  yield). One method to isolate pure systematic uncertainty

from the influence of statistical uncertainty is by averaging over a large number of trials involving fitting the data with the nominal and alternate linear models. Systematic trends, if they exist, will appear as a statistically-significant feature across a sufficiently large number of trials, while stochastic noise is averaged out. Once we are able to isolate the systematic uncertainty, it can be quoted as an additional uncertainty in our results, along with the statistical uncertainty.

# Chapter 4

## Bottomonia in the QGP

*Strong suppression of  $\Upsilon$  mesons in PbPb collisions at*

$$\sqrt{s_{NN}} = 5.02 \text{ TeV}$$

In this chapter, we report measurements of the differential cross sections and nuclear modification factors for  $\Upsilon(1S)$ ,  $\Upsilon(2S)$ , and  $\Upsilon(3S)$  mesons using their decay into two oppositely charged muons in PbPb and pp collisions at  $\sqrt{s_{NN}} = 5.02$  TeV. The data were collected with the CMS detector at the CERN LHC during the heavy-ion data collection period in November-December, 2015. Results are presented as functions of the  $\Upsilon$  transverse momentum ( $p_T$ ) and rapidity ( $y$ ), as well as PbPb collision centrality (i.e., the degree of overlap of the two lead nuclei). These results form an important backdrop for interpreting the implications of the primary analysis presented in this dissertation. The author's introductory years in her PhD program were devoted to the analysis presented in this chapter, which served as inspiration for conducting her primary analysis on the nuclear modification of  $\Upsilon$  mesons in pPb collisions, using data collected by the CMS detector at the same energy. A summarized description of the analysis procedure is provided here, with primary emphasis on the results. The discussions are geared towards the physics concepts relevant at different analysis stages. A more technical description may be found in reference [29].

Modifications of particle production in nucleus-nucleus (AA) collisions are quantified using the nuclear modification factor,  $R_{AA}$ , which is the ratio of the yield measured in AA to that in pp collisions, scaled by the mean number of binary NN collisions. As explained in sections 1.3 and 1.4, comparisons of the bottomonium data with dynamical models incorporating the heavy-quark potential effects found in high-temperature lattice QCD are expected to extend our understanding of the nature of color deconfinement in heavy-ion collisions.

## 4.1 Data selection and simulation samples

In both pp and PbPb collisions, dimuon events are selected by a fast hardware-based online requirement (trigger) that two muon candidates are detected in the muon system in a given bunch crossing. No explicit requirement on muon momentum beyond the intrinsic selection due to the acceptance coverage of the CMS muon detectors is applied. In pp collisions, this trigger registered a total luminosity (also referred to as integrated luminosity) of  $28.0 \text{ pb}^{-1}$ . The same pp dataset is used to compare to pPb, so more details on it can be found later in section 5.3.1.

The PbPb data were recorded simultaneously using two triggers. Both triggers had the same muon requirement as for the pp data. The first mode was designed to enhance the event count for muon pairs from peripheral events. Peripheral events are events with the least overlap of colliding Pb nuclei, which corresponds to small event activity. Centrality is calibrated using percentiles of energy deposited in the forward hadronic (HF) calorimeters. So the peripheral trigger records data belonging to the (30 – 100) % event activity class. This trigger sampled the full integrated luminosity delivered by colliding lead beams in the CMS detector,  $464 \mu\text{b}^{-1}$ . The second mode did not have additional requirements, but was prescaled during part of the data collection. It therefore sampled a smaller effective integrated luminosity of  $368 \mu\text{b}^{-1}$ . Data recorded with the second trigger mode are used to analyze  $\Upsilon$  yields in the (0 – 30) % (i.e. most central) as well as (0 – 100) % (full centrality)

centrality classes.

In order to keep hadronic collisions and reject beam-related background processes such as beam-gas collisions and beam scraping events, an offline event selection is applied to the recorded data. Events are required to have at least one reconstructed primary vertex. In pp collision events at least 25 % of all recorded tracks are required to pass a tight track-quality selection [137]. A filter on the compatibility of the silicon pixel detector cluster width and vertex position is also applied [138]. Once again, more details for the pp dataset can be found in section 5.3.1. The PbPb collision events are additionally required to contain at least three towers in the HF on both sides of the interaction point with an energy above 3 GeV.

The combined efficiency for these event selections and the remaining contamination due to non-hadronic ultra-peripheral events (which can raise the efficiency above 100 %) is found to be  $(99 \pm 2)$  % [139, 140]. The minimum-bias trigger requirement removes a negligible fraction of the events with a hard collision producing  $\Upsilon$  candidates. We also study possible contamination of  $\Upsilon$  yield from photoproduction processes in the peripheral region. Such contamination is found to be negligible. Multiple-collision events (pileup) have a negligible effect on the measurement as well, since the average number of additional collisions per bunch crossing is approximately 0.9 for pp at this energy and much smaller for PbPb data.

Muons are selected in the kinematic range  $p_T^\mu > 4$  GeV and  $\eta^\mu < 2.4$ , as the CMS detector's geometry prevents it from collecting muon data outside this range. This is known as the acceptance of the detector for muons. With such muons,  $\Upsilon$  candidates down to  $p_T^{\mu\mu} = 0$  GeV can be reconstructed. Muons are required to be reconstructed using combined information from the tracker and muon detectors, a criterion producing “global muons” as defined in reference [19]. To remove muons from cosmic rays, the distance of the muon track from the closest primary vertex must be less than 20 cm in the beam direction and 3 mm in the transverse direction. Oppositely charged muons are required to arrive at a closest point of approach which coincides with a primary vertex, i.e. they must originate from a

common reconstructed collision vertex. The studied dimuon kinematic range is limited to  $p_T^{\mu\mu} < 30$  GeV and  $|y^{\mu\mu}| < 2.4$ . Dimuons in this  $p_T$  range comprise 99 % of those passing all of the analysis selection criteria.

Simulated Monte Carlo (MC)  $\Upsilon$  events are used to calculate corrections to the results based on the geometrical acceptance and triggering efficiency of the detector, as well as the efficiency of the dimuon reconstruction algorithm and various offline selections. The events are generated using PYTHIA8.209 [134] for the pp collisions and PYTHIA8.209 embedded in HYDJET1.9 [136] for PbPb. The PbPb simulation is tuned to reproduce the observed charged-particle multiplicity and  $p_T$  spectrum in PbPb data. The CMS detector response is simulated using GEANT4 [135]. Since the simulated  $p_T$  spectrum of  $\Upsilon$  mesons is not identical to the spectrum observed in  $\Upsilon$  extracted from data, an event-by-event weight is applied to the simulations in order to match the distributions. The weight is given by a simple generalized linear model (GLM) fit to the ratio of data over MC  $p_T$  spectra.

## 4.2 Analysis procedure

### 4.2.1 Signal extraction

The yields of  $\Upsilon$  mesons in both the pp and PbPb collisions are extracted using unbinned maximum-likelihood fits to the invariant mass spectra of opposite-sign muon pairs. The GLM used in the regression has two components: a model for the signal features, i.e.  $\Upsilon$  peaks, and a model for the background (noise) distribution. The largest source of background arises from uncorrelated opposite-sign muon pairs that do not result from the decay of an  $\Upsilon$  but do reconstruct to an invariant mass similar to that of an  $\Upsilon$ . We will discuss this in more detail in chapter 6, in reference to the pPb analysis.

The  $\Upsilon$  resonance in a dilepton decay channel follows a Breit-Wigner (BW) distribution. In the absence of any modifications, the BW decay width of a  $\Upsilon(1S)$  resonance is roughly

54 keV, corresponding to the long lifetime ( $\sim 10^{-20}$  s) of the particle in the electromagnetic decay channel. On the other hand, bottomonium spectral function peaks undergo significant broadening in the QGP, as discussed in section 1.4. Lattice QCD calculations predict in-medium BW decay widths for  $\Upsilon$  states to be  $\sim 200$  MeV, a few orders of magnitude larger than in vacuum, corresponding to short enough lifetimes for bottomonia to decay while still inside the QGP [141]. The measured distribution of  $\Upsilon$  states in the reconstructed dimuon invariant mass spectrum, however, are much wider in both pp and PbPb data, due to detector resolution effects and the radiative decay of daughter muons in the material they encounter. Therefore, when extracting the yields, the data are fit with models that are empirically supported by the observed peak features, rather than physical intuition. In particular, since lower-momentum muons lose more energy by bremsstrahlung radiation, an asymmetric function, with a longer low-mass tail, is needed to model the  $\Upsilon$  peaks.

The peak feature of each  $\Upsilon$  state is modeled by a double Crystal-Ball (CB) function which is the sum of two CB functions [142]. This choice is made in order to account for the different mass resolution in the barrel compared to the endcap region of the detector. The area under the double CB, minus the estimated background in the region, represents the yields of the states. A parameter relates the widths of the two CB functions, the first of which is left free while the second is constrained to be narrower than the first. The mean and the two radiative-tail parameters of both CB functions for a given state are constrained to be identical, as these are not affected by the detector resolution. The mean corresponds to the reconstructed mass of a state. The mass parameter of the ground state is left free to allow for possible shifts in the absolute momentum calibration of the reconstructed tracks. For the excited states ( $\Upsilon(2S)$  and  $\Upsilon(3S)$ ), all fit parameters are fixed to be identical to those for the ground state except for the mass and width parameters, which are fixed to their values for the ground state scaled by the excited-to-ground state ratio of the published masses [143]. In this way, we ensure that the shapes of the double CB functions used to model the peak features are identical for the three states.

In order to avoid overfitting, we perform constrained optimization. During regression, the two radiative-tail parameters and the parameter for the ratio of the two CB widths are constrained to their average value in free-parameter fits to the data binned in rapidity. A Gaussian penalty is applied, whose width is given by the standard deviation of the parameters in the same fits. A similar method is applied to pp data and pPb data for the  $R_{\text{pPb}}$  analysis, which will be discussed in detail in chapter 6. In PbPb fits, the parameter representing the relative contribution of the two CB functions to the peak shapes is constrained as well. In this case, the mean and the width of the Gaussian penalty correspond, respectively, to the value of the parameter and its regression uncertainty in the fit to pp data in the same kinematic region. The  $\Upsilon$  peak features are more prominent in the pp data, where higher statistics were collected.

The background is modeled using the product of an error function and an exponential function. This choice, unique to  $\Upsilon$  analyses with the CMS detector, will be explained in chapter 6. The error function's two parameters and the decay parameter of the exponential function are all allowed to vary freely. For bins with  $p_{\text{T}} > 6$  GeV, an exponential without the error function provides the best fit, and was therefore used for the nominal result. The total number of events identified as background is given by the area under the fitted background GLM.

Figure 4.1 shows the dimuon invariant mass distributions in pp and PbPb data for the full kinematic range  $p_{\text{T}}^{\mu\mu} < 30$  GeV and  $|y^{\mu\mu}| < 2.4$ . The blue lines represent fits to the data using the GLM described. It is already evident from these plots, that the  $\Upsilon$  states are strongly suppressed in PbPb collisions compared to the collisions in vacuum. The extracted  $\Upsilon$  yields from fits like these to data split into various regions of  $\Upsilon$   $p_{\text{T}}$  and  $|y|$  and collision centrality, are used to study the dependence of the production cross section of bottomonia in pp and PbPb collisions on these variables.

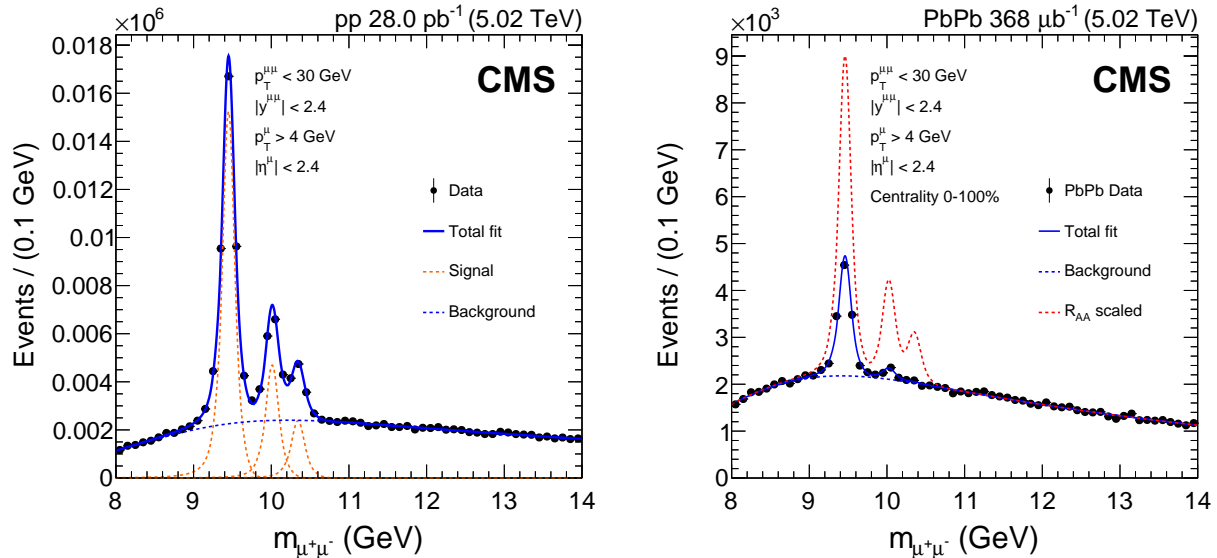


Figure 4.1: Invariant mass distribution of opposite-sign muon pairs in pp (left) and PbPb (right) collisions, for the kinematic range  $p_T^{\mu\mu} < 30$  GeV and  $|y^{\mu\mu}| < 2.4$ . In both figures, the GLM fitted to the data are shown as solid blue lines. The separate yields for each  $\Upsilon$  state in pp are shown as dashed red lines in the left panel. In order to depict the level of suppression of the  $\Upsilon$  states in PbPb collisions, the amplitudes of the peaks in the fit are scaled by the inverse of the measured  $R_{AA}$  for each state. This is shown as dashed red lines in the right panel.

## 4.2.2 Corrections

In order to obtain the normalized cross sections, the yields extracted from the fits to the dimuon invariant mass spectra are corrected by detector acceptance and efficiency factors, and scaled by the inverse of the integrated luminosity. Acceptance, which is determined using MC simulations, estimates the fraction of  $\Upsilon$  mesons produced in data that could be detected in the CMS detector given its geometric limitations. It is defined as the fraction of all generated dimuon events for which both daughter muons individually satisfy the kinematic selections placed on muons during data collection. The acceptance values for the considered kinematic region are 22.5 % ( $\Upsilon(1S)$ ), 27.8 % ( $\Upsilon(2S)$ ), and 31.0 % ( $\Upsilon(3S)$ ) for PbPb collisions and differ by  $< 1$  % from the corresponding values for pp data.

The efficiency correction factor, also determined primarily using MC simulations, provides an estimate of the type II error rate of the CMS detector at identifying and reconstructing

dimuon events. We start with only the generated events within acceptance and check the efficiency of reconstructing the dimuons offline. Additionally, we check if these dimuon events would satisfy the trigger conditions employed during data collection, as well as the analysis quality selections described in section 4.1. Together, these checks provide a simulation-based answer to: what fraction of the time would an  $\Upsilon$  meson created in a real collision be successfully detected in the CMS detector, provided it was within the kinematic acceptance?

Additionally, we also determine the type II error rates of the individual components of detecting a single muon in the CMS detector: track reconstruction, muon identification and selection, and triggering. We use single muons from  $J/\psi$  meson decays in both simulated and real collision data in a method known as *tag-and-probe* (T&P) [19], to determine the necessary correction to the efficiency determined from MC. A detailed discussion of this method as it pertains to the pp and pPb data will be provided in section 7.3. For the muons used in this analysis, the single-muon efficiencies in data and MC differ only in the case of triggering, and there only by  $\lesssim 1\%$ . For this case, scaling factors (SFs), calculated as the ratio of data over simulated single-muon efficiencies as a function of  $p_T^\mu$  and  $\eta^\mu$ , are applied to the dimuon efficiency on an event-by-event basis. The other components of the T&P efficiency are used only for the estimation of systematic uncertainties. The average efficiencies integrated over the full kinematic range are 73.5 % ( $\Upsilon(1S)$ ), 74.4 % ( $\Upsilon(2S)$ ), and 75.0 % ( $\Upsilon(3S)$ ) in PbPb collisions. As we will see later, the efficiencies are (8 – 9) % higher for pp collisions.

The remaining correction factor for  $\Upsilon$  yields in pp is the integrated luminosity of  $28.0 \text{ pb}^{-1}$ . The product of the acceptance, efficiency and luminosity factors are used to normalize the yields in pp data, in order to obtain the luminosity-independent would-be yields using a perfectly efficient detector with no acceptance gaps. For PbPb collisions, instead of the luminosity, the product of the number of minimum-bias collision events ( $N_{\text{MB}}$ ) and the average nuclear overlap function ( $T_{\text{AA}}$ ) is used for normalization. The overlap function  $T_{\text{AA}}$  is given by the number of binary NN collisions divided by the inelastic NN cross section. It

can be interpreted as the NN equivalent of the integrated luminosity per heavy-ion collision.

A Glauber model MC simulation [131, 144] is used to determine the  $T_{AA}$ , as well as calculate the average number of participating nucleons,  $\langle N_{\text{part}} \rangle$ , in a given collision. The latter quantity is highly correlated with the impact parameter of the collision, and is therefore used as the abscissa when plotting results as a function of collision centrality. In collisions of heavy ions, the  $\langle N_{\text{part}} \rangle$  provides a measure of the volume of the QGP formed, independent of the species of colliding ions.

### 4.2.3 Systematic uncertainties

As discussed previously, the choices of signal and background models can introduce systematic uncertainties in the results. Additional sources of systematic uncertainty include the choice of the central value in the Gaussian penalty applied to parameters in the signal model, as well as choices made during the determination of acceptance and efficiency corrections. Larger relative uncertainties are seen when the background level is higher (at lower  $p_T$  or more forward  $|y|$  regions), and, in particular for the  $\Upsilon(3S)$ , when the absolute yield is small compared to the background spectrum.

The uncertainty from the choice of signal model is estimated by fitting the data using an alternate model: a single CB function in combination with a Gaussian function. The uncertainty is taken as the difference between the yield obtained with the alternate model compared to the nominal one. For the PbPb (pp) yields, the differences are in the ranges (1–7) % ((0.1–4.6) %) for the  $\Upsilon(1S)$ , (2–19) % ((0.1–1.3) %) for the  $\Upsilon(2S)$ , and (5–78) % ((0.7–7) %) for the  $\Upsilon(3S)$  mesons. The lower statistics of the PbPb data contribute to the larger uncertainty in this collision system. In particular, the strong suppression of  $\Upsilon(3S)$  in PbPb collisions makes the yield extracted using this peak particularly sensitive to the choice of the signal model.

The systematic uncertainty from the choice of the central value of the Gaussian penalty

is estimated by using the parameter values from free-parameter fits in individual analysis bins, rather than their average value across  $|y|$  bins. The differences in the PbPb (pp) signal yields due to this choice is found to be below 4 % (4.5 %) for the  $\Upsilon(1S)$ , below 8 % (3 %) for the  $\Upsilon(2S)$ , and roughly 45 % (2 %) for the  $\Upsilon(3S)$ .

The systematic uncertainty due to the choice of background model is estimated using two alternative background functions, depending on the shape of the background in the kinematic region probed. One is a fourth-order polynomial function (better at describing the background at low  $p_T$ ) and the other is an exponential plus an additional linear function. The maximal deviations of the PbPb (pp) yield between these two models compared to the nominal are quoted as the uncertainty. They are typically in the range (1 – 6) % ((1 – 5) %) for the  $\Upsilon(1S)$ , (2 – 23) % ((2 – 4) %) for the  $\Upsilon(2S)$ , and (5 – 200) % ((3 – 5) %) for the  $\Upsilon(3S)$  mesons.

For the estimation of systematic uncertainties due to acceptance and efficiency corrections, the source of uncertainty is the imperfect knowledge of the simulated  $p_T$  distribution shape. To take this source into account, the function used to weight the MC  $p_T$  spectra event-by-event is modified within its fit uncertainty. The acceptance and efficiency obtained from the simulated  $p_T$  distribution are compared with and without the variation of the function, with the difference between the two used as an estimate of the systematic uncertainty. In addition, the correction of the MC-based dimuon efficiency using T&P single-muon efficiency SFs also introduces systematic uncertainty. The systematic uncertainties in the SFs for trigger, tracking, and muon identification single-muon efficiencies are propagated to the dimuon efficiency values. Variation of the dimuon efficiency within this uncertainty produces differences in the results, which is used to estimate the uncertainty in the results due to this source. The contribution of the statistical uncertainty inherent to the data used for T&P studies to the corrected extracted yields is also estimated. The PbPb (pp) systematic uncertainties for all three  $\Upsilon$  states are in the range (3.5 – 6.4) % ((2.6 – 3.9) %) due to the total efficiency correction, and in the range (0.1 – 3.0) % ((0.1 – 0.8) %) due to acceptance

correction.

Finally, sources of correlated uncertainties, i.e. global uncertainties common to all points, are considered: the integrated luminosity for pp, and the  $T_{AA}$  and  $N_{MB}$  estimates for PbPb. The uncertainty on the integrated luminosity measurement for the pp dataset is 2.3 % [145]. The uncertainty on  $N_{MB}$  in PbPb collisions is 2 %, which accounts for the inefficiency of triggering and event selection. In the  $R_{AA}$  calculation,  $T_{AA}$  uncertainties are estimated by varying the Glauber model parameters within their uncertainties [140]. The total combined global uncertainty is calculated by adding the results from these sources in quadrature.

The global uncertainty in the differential  $\Upsilon$  cross section measurements in pp and PbPb collisions arises due only to the integrated luminosity and the  $N_{MB}$ , respectively. The global uncertainty on  $R_{AA}$  combines the total uncertainties from  $T_{AA}$ , the pp luminosity, and  $N_{MB}$  in PbPb for bins integrated over centrality. For centrality-dependent  $R_{AA}$  results, the uncertainty from  $T_{AA}$  is included bin-by-bin, while the total uncertainty from the pp measurement is included in the global uncertainty.

### 4.3 Results

The  $\Upsilon(nS)$  cross sections and  $R_{AA}$  are measured in several  $\Upsilon$   $p_T$  and  $y$  bins. The behavior of the  $R_{AA}$  is also investigated as a function of collision centrality. When plotted as a function of one variable ( $p_T$ ,  $|y|$  or centrality), values are integrated over the full range of the other variables. The  $\Upsilon(3S)$  mesons show a very strong suppression in PbPb collisions, with yields statistically consistent with zero for all bins. The upper limits at 68 % and 95 % confidence level (CL) for the  $\Upsilon(3S)$  cross section and  $R_{AA}$  measurements are determined using the Feldman–Cousins method [146], including the appropriate systematic uncertainties in the computation.

### 4.3.1 Differential cross sections in pp and PbPb collisions

The differential production cross section of  $\Upsilon$  mesons decaying in the dimuon channel in pp collisions is given by

$$\mathbb{B} \frac{d\sigma^2}{d|y|dp_T} = \frac{N/(a \cdot \varepsilon)}{\mathcal{L}_{\text{int}} \Delta|y| \Delta p_T}. \quad (4.1)$$

The branching fraction for the decay  $\Upsilon \rightarrow \mu\mu$  is denoted by  $\mathbb{B}$ . The variable  $N$  corresponds to the extracted yield of  $\Upsilon$  mesons in a given  $(p_T, |y|)$  bin,  $(a \cdot \varepsilon)$  represents the product of the average acceptance and efficiency in the bin,  $\mathcal{L}_{\text{int}}$  is the integrated luminosity of the data, and  $\Delta p_T$  and  $\Delta|y|$  are the bin widths. In PbPb data,  $\mathcal{L}_{\text{int}}$  is replaced by  $(N_{\text{MB}} T_{\text{AA}})$ , as explained in Section 4.2.2, to compare the pp and PbPb data under the hypothesis of binary-collision scaling.

Figure 4.2 shows the differential production cross sections of  $\Upsilon$  mesons as a function of  $p_T$  in pp and PbPb collisions. The corresponding results as a function of  $|y|$  are shown in Fig. 4.3. The cross sections for all three  $\Upsilon$  states are higher in pp than in PbPb collisions, showing clear signs of suppression in the QGP produced in the nuclear system.

### 4.3.2 Nuclear modification factor $R_{\text{AA}}$

The nuclear modification factor is derived from the pp cross sections and PbPb normalized yields as

$$R_{\text{AA}}(p_T, |y|) = \frac{N^{\text{AA}}(p_T, |y|)}{\langle T_{\text{AA}} \rangle \sigma^{\text{pp}}(p_T, |y|)}, \quad (4.2)$$

where  $\langle T_{\text{AA}} \rangle$  is the average value of the  $T_{\text{AA}}$  computed in each centrality bin. The quantities  $N^{\text{AA}}$  and  $\sigma^{\text{pp}}$  refer, respectively, to the normalized yield of  $\Upsilon$  mesons in PbPb collisions corrected by acceptance and efficiency, and the fully-corrected pp cross section for a given kinematic range.

Figure 4.4 shows the nuclear modification factor for the  $\Upsilon(1S)$ ,  $\Upsilon(2S)$ , and  $\Upsilon(3S)$  mesons as functions of  $p_T$  (left) and  $|y|$  (right). Within the systematic uncertainties, the  $R_{\text{AA}}$  values

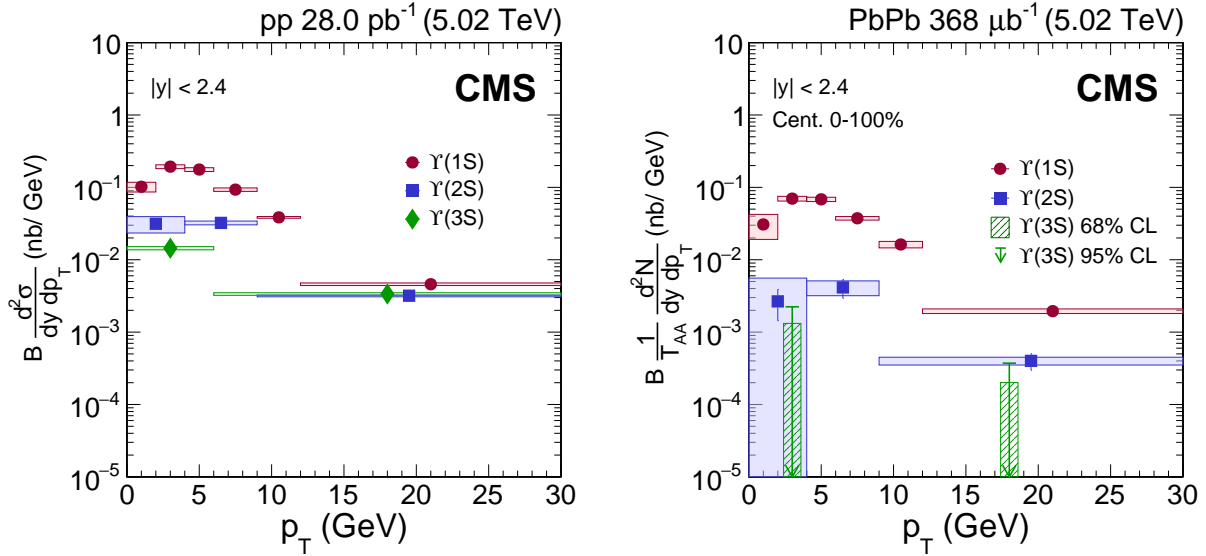


Figure 4.2: Differential cross sections of the  $\Upsilon(1S)$ ,  $\Upsilon(2S)$ , and  $\Upsilon(3S)$  mesons as a function of  $p_T$  for pp (left) and PbPb (right) collisions. The error bars represent the statistical uncertainties and the boxes the systematic uncertainties. For the  $\Upsilon(3S)$  meson in PbPb collisions, the upper limits at 68 % (green box) and 95 % (green arrow) CL are shown. The global integrated luminosity uncertainties of 2.3 % in pp collisions and  $^{+3.4}_{-3.9}$  % in PbPb collisions are not shown.

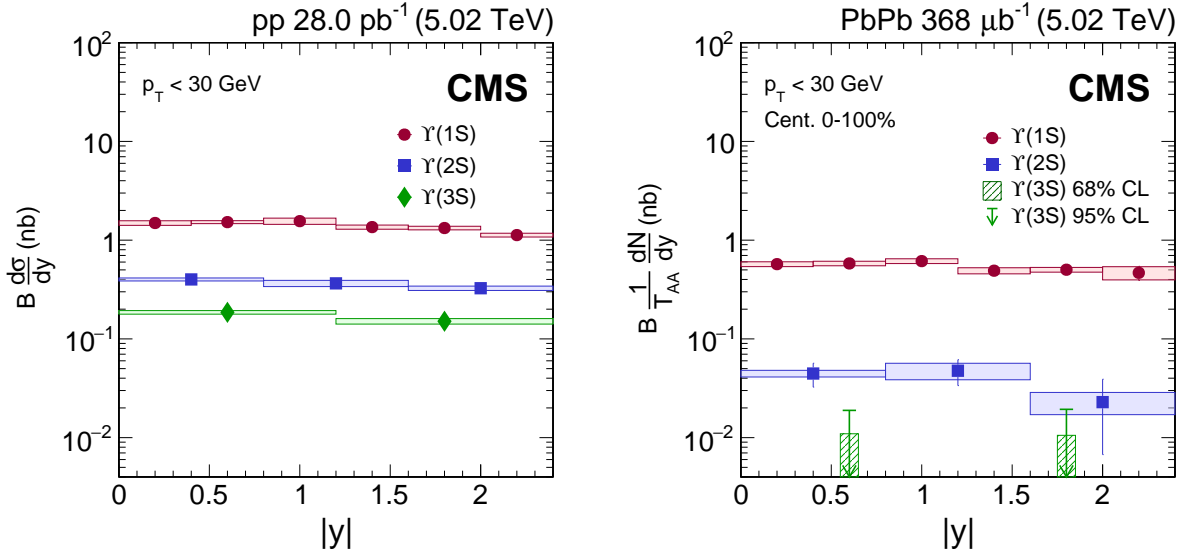


Figure 4.3: Differential cross sections of the  $\Upsilon(1S)$ ,  $\Upsilon(2S)$ , and  $\Upsilon(3S)$  mesons as a function of  $|y|$  for pp (left) and PbPb (right) collisions. The global integrated luminosity uncertainties are not shown.

show no clear dependence on  $p_T$  or  $|y|$ . The excited  $\Upsilon$  states are found to have larger suppression than the ground state, with  $R_{AA} < 0.2$  over the full kinematic range explored here. The kinematic dependence of the  $R_{AA}$  is useful to constrain models of  $\Upsilon$  meson suppression in a deconfined medium as explained in section 1.4.

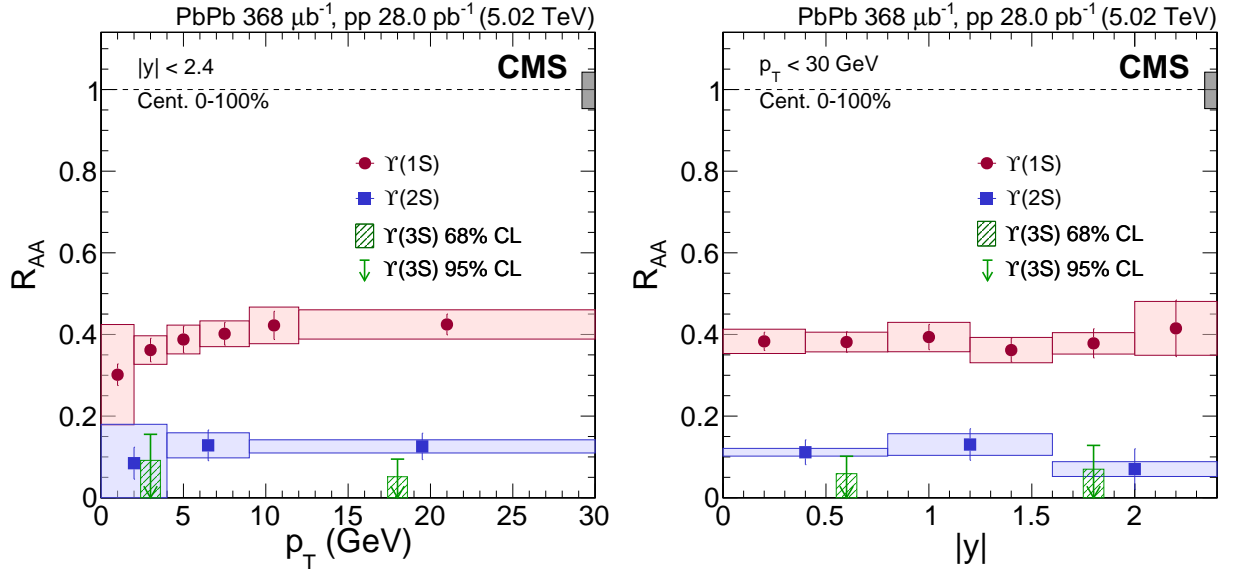


Figure 4.4: Nuclear modification factors for  $\Upsilon(1S)$ ,  $\Upsilon(2S)$ , and  $\Upsilon(3S)$  mesons as functions of  $p_T$  (left) and  $|y|$  (right). The gray box near the line at unity displays the global uncertainty, which combines the uncertainties from  $T_{AA}$ , pp luminosity, and PbPb  $N_{MB}$ .

The dependence of the  $R_{AA}$  on PbPb collision centrality is depicted in Fig. 4.5. Centrality is quantified using the estimated average  $\langle N_{\text{part}} \rangle$ . Strong suppression of the  $\Upsilon(3S)$  meson is observed in both central and peripheral events. The  $R_{AA}$  decreases with increasing centrality in the case of the  $\Upsilon(1S)$  and  $\Upsilon(2S)$  mesons. A hint of this centrality dependence of the  $\Upsilon(2S)$   $R_{AA}$  was first seen in data at  $\sqrt{s_{NN}} = 2.76$  TeV [25] and is now confirmed using the larger and higher-energy data at 5.02 TeV. A similar decrease of the  $\Upsilon(3S)$   $R_{AA}$  with increasing centrality is indicated by the data but cannot be inferred using the upper limits. Additional statistics for PbPb data at 5.02 TeV, which has been collected very recently in November-December 2018, may help verify this expectation. The trends observed in these results are a clear signature of the hypothesized sequential melting of quarkonia, since the temperature of the QGP created in heavy-ion collisions increases with collision centrality.

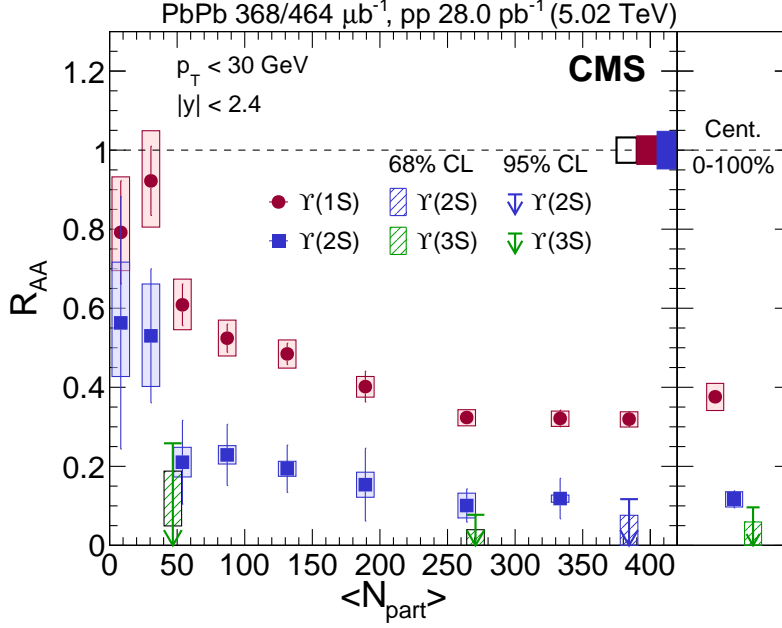


Figure 4.5: Nuclear modification factors for the  $\Upsilon(1S)$ ,  $\Upsilon(2S)$ , and  $\Upsilon(3S)$  mesons as a function of  $\langle N_{\text{part}} \rangle$ . The boxes at the dashed line at unity represent global uncertainties: the open box for the integrated luminosity in pp collisions and  $N_{\text{MB}}$  in PbPb collisions, while the full boxes show the uncertainties in  $\Upsilon(1S)$  (red) and  $\Upsilon(2S)$  (blue) yields in pp collisions.

Figure 4.6 shows the measured  $R_{AA}$  for  $\Upsilon(1S)$  (left) and  $\Upsilon(2S)$  (right) mesons compared to predictions from two different models for bottomonium suppression. The green band represents the prediction and its uncertainty from Du, He, and Rapp [24], while the orange curves correspond to three predictions from Krouppa and Strickland [23] where the viscosity to entropy ratio,  $\eta/s$ , is varied. Both models incorporate Debye color screening effects on the bottomonium family as well as feed-down contributions from decays of heavier quarkonia. Possible regeneration of bottomonia in the QGP as well as CNM effects are incorporated into the first model, while neither is included in the second. Krouppa and Strickland treat the dynamical evolution of the QGP using anisotropic hydrodynamics, where the relevant initial conditions are changed by varying  $\eta/s$  and the initial momentum-space anisotropy. The initial temperature is determined by requiring agreement with charged particle multiplicity and elliptic flow measurements from PbPb data. The model from Du, He, and Rapp uses a kinetic rate equation to simulate the time evolution of bottomonium abundance in the collision medium. Deconfinement effects are incorporated using temperature-dependent

binding energies for quarkonia and a lattice QCD based equation-of-state for QGP evolution.

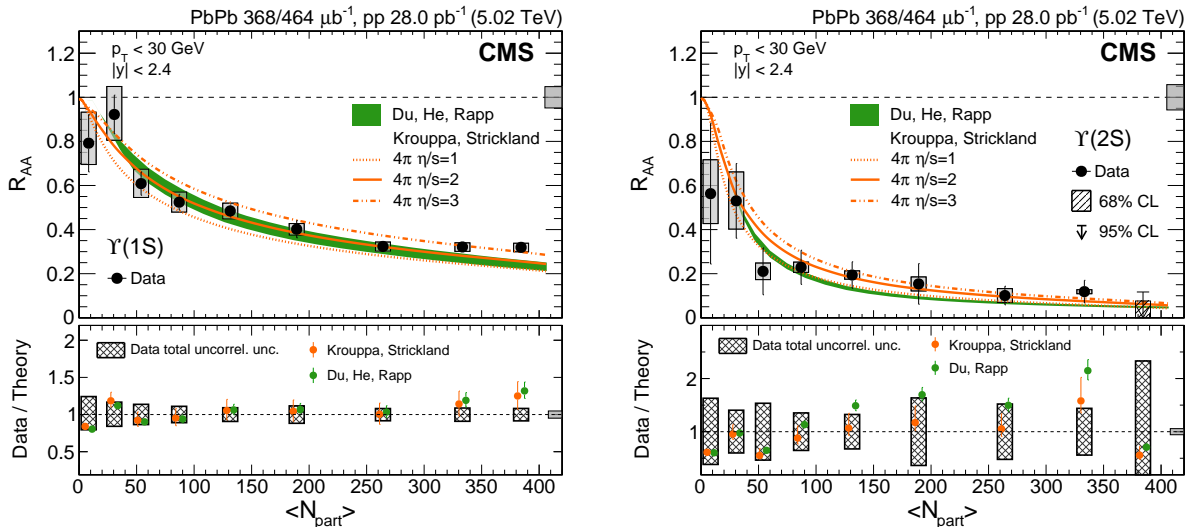


Figure 4.6: Nuclear modification factors for the  $\Upsilon(1S)$  (left) and  $\Upsilon(2S)$  (right) mesons as a function of  $\langle N_{part} \rangle$  compared to calculations from Krouppa and Strickland [23], and Du, He, and Rapp [24]. The box at the dashed line at unity represents the global uncertainty from the integrated luminosity in pp collisions,  $N_{MB}$  in PbPb collisions, and the total uncertainty in the pp yields. The data-to-prediction ratios are shown in the bottom panels. The orange points and their errors correspond to predictions using  $4\pi\eta/s = 2 \pm 1$  in reference [23]. The green points and their errors correspond to the central value and width of the predicted range in reference [24].

Within the current theoretical and experimental uncertainties, both models are in agreement with the measured  $R_{AA}$  for both  $\Upsilon(1S)$  and  $\Upsilon(2S)$  states. Future  $\Upsilon$   $R_{AA}$  measurements, as well as measurements of the nuclear modification of charmonia, using higher-statistics or higher-energy nucleus-nucleus collision data can help identify the ingredients of each model that embody more accurate characteristics of the deconfined phase of QCD. Several other bottomonium suppression models also exist to which the data can be compared.

Figure 4.7 shows the centrality-integrated  $\Upsilon$   $R_{AA}$  values at  $\sqrt{s_{NN}} = 5.02$  TeV, and compares these to the lower energy results at 2.76 TeV. The centrality-integrated  $R_{AA}$  for  $\Upsilon(1S)$  is measured to be  $0.376 \pm 0.013$  (stat)  $\pm 0.035$  (syst), while the result at 2.76 TeV is  $0.453 \pm 0.014$  (stat)  $\pm 0.046$  (syst) [25]. The suppression at 5.02 TeV is larger by a factor of  $\sim 1.20 \pm 0.15$  (in which only the  $T_{AA}$  uncertainty was considered correlated and therefore removed), although the two  $R_{AA}$  values are compatible within their uncertainties.

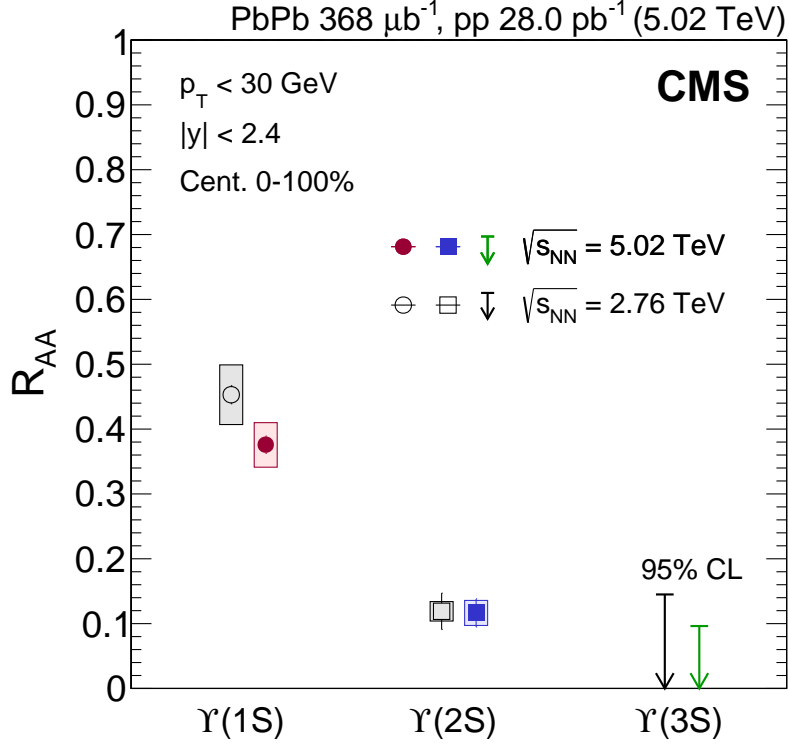


Figure 4.7: Comparison of  $R_{AA}$  values for the  $\Upsilon(1S)$ ,  $\Upsilon(2S)$ , and  $\Upsilon(3S)$  mesons at  $\sqrt{s_{NN}} = 5.02$  TeV and  $\sqrt{s_{NN}} = 2.76$  TeV [25] for integrated centrality in the full kinematic range.

Since quarkonium suppression is expected to be larger for higher temperatures in the medium, the  $R_{AA}$  results at the two different collision energies can provide information on the medium temperature. In the predictions shown in Fig. 4.6, Krouppa and Strickland report medium temperatures  $T = 641$ ,  $631$ , and  $629$  MeV, corresponding to  $4\pi\eta/s = 1$ ,  $2$ , and  $3$ , respectively. Du, He, and Rapp, expect QGP temperatures in the range  $T = 550 - 800$  MeV using their model framework. Both models also predict  $\Upsilon$   $R_{AA}$  values in PbPb collisions at  $2.76$  TeV in agreement with the data at that energy [24, 147]. These bottomonium suppression models estimate the medium temperature in PbPb collisions to increase by  $\sim 16\%$  (Krouppa and Strickland) and  $\sim 7\%$  (Du, He, and Rapp) between  $\sqrt{s_{NN}} = 2.76$  TeV and  $\sqrt{s_{NN}} = 5.02$  TeV.

The centrality-integrated results for the  $\Upsilon(2S)$  and  $\Upsilon(3S)$  states at  $5.02$  TeV (also shown in figure 4.7) are  $R_{AA}(\Upsilon(2S)) = 0.117 \pm 0.022$  (stat)  $\pm 0.019$  (syst) and  $R_{AA}(\Upsilon(3S)) = 0.022 \pm 0.038$  (stat)  $\pm 0.016$  (syst) ( $< 0.096$  at 95 % CL). Although the  $\psi(2S)$  meson has

been previously observed [125, 148, 149], the more loosely bound  $\Upsilon(3S)$  meson remains elusive in the PbPb data at 5.02 TeV in all studied kinematic regions.

## 4.4 Summary and Outlook

In this chapter, we described the analysis to determine bottomonium suppression in the QGP using pp and PbPb collisions at  $\sqrt{s_{\text{NN}}} = 5.02$  TeV. We measure the cross sections of  $\Upsilon(1S)$ ,  $\Upsilon(2S)$ , and  $\Upsilon(3S)$  mesons and their nuclear modification factors as functions of  $\Upsilon$  transverse momentum ( $p_T$ ) and rapidity ( $y$ ), as well as PbPb collision centrality. A gradual decrease in  $R_{\text{AA}}$  with  $\langle N_{\text{part}} \rangle$  for the  $\Upsilon(1S)$  and  $\Upsilon(2S)$  states is observed, while no significant dependence on  $p_T$  or  $|y|$  is found in the measured region. The suppression of  $\Upsilon(1S)$  is larger than that seen at  $\sqrt{s_{\text{NN}}} = 2.76$  TeV, although the two are compatible within uncertainties. The  $R_{\text{AA}}$  of the  $\Upsilon(3S)$  state is measured to be below 0.096 at 95 % confidence level, making this the strongest suppression observed for a quarkonium state in heavy-ion collisions to date.

Having quantified the nuclear modification of bottomonia in the QGP produced in PbPb collisions, one is naturally left with curiosity about the extent to which the observed suppression arises due to cold nuclear matter effects. In the next chapter, we begin to describe an equivalent analysis to the one just presented, where we study the nuclear modification of bottomonia in pPb collisions at  $\sqrt{s_{\text{NN}}} = 5.02$  TeV. Along with the collision energy, the collision systems also share the same experimental apparatus, details of which were presented in chapter 2. Many of the techniques are also similar in the two analyses, although some clever new tricks are introduced in the latter study.

The following analysis constitutes the author's main contribution to the field of ultra-relativistic heavy ion physics, as she has had the privilege of leading the analysis team and serving as the primary contact person for the study within the CMS collaboration. The goal of the analysis is to determine the CNM modification of  $\Upsilon(nS)$  yields at the same energy as for hot medium effects, in order to help constrain phenomenology that aims to connect what

is known, what is predicted, and what is observed about the physics of the strong interaction and its deconfined phase of matter.

# Chapter 5

## Analysis Setup

In this chapter, we provide details of the data and analysis methodology used to determine the nuclear modification of  $\Upsilon(nS)$  in pPb, including how the data are processed and reduced. The locations of the data and analysis software framework are indicated, so that the reader may be able to reproduce the results presented in this report.

### 5.1 Data Analysis at CMS

As mentioned earlier, the reduction of the large volume of collision data generated at the interaction points (IPs) of the LHC is crucial to any physics-motivated analysis. Although the streaming data is reduced by several orders of magnitude at the CMS detector even before recording, the recorded data need to be further reduced during analysis by making clever selections on the measured quantities. The fundamental guiding principle for data reduction is to discard a maximal number of noise (or background) events, while retaining a maximal number of events anticipated to contain the signature sought (signal). This optimization problem is approached using Bayesian inference, and several different selections are typically tested before settling on the ideal ones.

In addition to reducing the number of events, the size of events in a dataset can also be reduced. This is achieved by stripping the event data of information irrelevant to a particular analysis. For instance, it is unlikely that jet information will be required for a quarkonia analysis, and so for a quarkonia dataset the jet information may be filtered out. Before we delve into specifics of the selections made on the data used in this analysis, let us introduce some nomenclature and workflows particular to the CMS collaboration.

### 5.1.1 Labeling Streaming Data

Although there can be months dedicated to the acquisition of data for a given collision system and energy, maintaining beams circulating in the LHC tunnel at a specific energy is a technical challenge which is only surmountable for short periods at a time. The protons and ions to be collided need to be accelerated from rest in stages. Beams are injected in bunches into the LHC tunnel only when they reach a minimum threshold energy and can be accelerated using the LHC magnets around the large accelerator ring.

When beams are finally up to the desired energy for collisions, we say the beams are stable. We collide the beams traveling in opposite directions by focusing them to intersect at the IPs. This continues for as long as there are a sufficient number of ions in the bunches to sustain collisions. When the collision intensity drops sufficiently, the beams are dumped. The acceleration process is then restarted with a new set of non-relativistic ions. Several other reasons, such as the malfunctioning of a sufficiently large portion of the detector, can lead to beams being dumped as well. The period of colliding stable beams is known as a run. Runs are numbered sequentially.

During a run, the CMS detector records event data from collisions and labels them by the run number. The lifetime of a run is highly variable. The detector conditions during a single run are usually kept constant. However, the triggering rate of datasets can vary during a run, especially at the beginning of data acquisition for a specific system or energy, when the triggering algorithms are still being calibrated. Therefore, during a given run, the collected

data may be further split into luminosity sections corresponding to stable trigger rates.

### 5.1.2 Software Framework for Processing Data

The backend software architecture for the handling of all CMS data and simulation as well as processing tools is known as CMS software (CMSSW). The executables of CMSSW can be configured at run time by the user using job-specific configuration files. The executables then call modules, which are modular units having clearly defined event-processing functionality. The framework is developed and versioned regularly, partly to account for changing detector conditions, and is publicly accessible at [github.com/cms-sw/cmssw](https://github.com/cms-sw/cmssw). Within the framework, global tags are used to specify the detector conditions which are relevant for various datasets being handled by a given CMSSW version. The versioning of CMSSW and tagging by detector conditions are also useful for processing simulated data under the same specifications as real data.

CMSSW uses a data structure called an event data model (EDM). An Event in the EDM is an object container for all raw and reconstructed data corresponding to a particular collision. It is the trigger system that first produces an Event. The output of the HLT is an Event containing: the readout signals from detector components, the results of the L1 trigger and HLT requirements, and meta data created during data processing at the HLT. The trigger results are stored as a bit-wise correspondence with the trigger paths implemented prior to data acquisition. During processing, data can only be accessed through the Event object container and are passed between modules as such.

In the months leading up to nuclear collision data collection at CMS, a heavy-ion compatible CMSSW framework is developed to account for the difference in particle incidence and relative payload of the data generated in pp vs. pPb or PbPb collisions. Members of the working groups work closely with detector operation personnel to develop, test and optimize the multi-level trigger algorithms. Predictions for the triggering rates of datasets are particularly useful for calibrating the subdetectors and estimating required trigger prescales.

## 5.2 Analysis Workflow and Software

The lifecycle of an analysis published by the CMS collaboration begins with the formation of a small team of principal analyzers interested in investigating a physical phenomenon suggested by theory using certain data. A team lead is identified, who serves as the primary contact person responsible for guiding the analysis through all stages of planning, execution and review leading to its publication in a journal and presentation at conferences. In addition to conducting meetings with other principal analyzers, the team lead organizes meetings and reaches consensus with reviewers of the analysis. Prior to submission to a journal, the analysis undergoes an internal review process within the collaboration involving four steps:

**Pre-approval** an endorsement from the working group, in our case the dilepton physics interest group (PInG), following an incubation period during which weekly progress reports are given. These reports begin with data quality assurance (QA) plots and ultimately involve the presentation of preliminary results highlighting the physics being investigated. The analysis techniques are developed by the analyzers and are typically improved during these weekly meetings with the working group which consists of physicists with similar interests. After pre-approval, an analysis review committee (ARC) consisting of four members of the collaboration with different physics interests is assigned to the analysis.

**Green-light** an endorsement from the ARC after working closely with the analysis team to help refine analysis techniques, statistical inferences and result visualization. The paper and physics analysis summary (PAS) are prepared and put under version control during this processes.

**Approval** final endorsement from the physics analysis group (PAG) overseeing all results pertaining to a given subfield of the physics that can be studied using the CMS detector. In our case, the heavy ion (HIN) PAG endorses the analysis following a presentation open to all heavy-ion physicists within the collaboration, and with feedback from the

PInG and the ARC. The presentation justifies all analysis choices and provides all proposed plots and inferences to be included in the paper seeking publication. The target journal must also be specified at this stage.

**Collaboration wide review (CWR)** a review of the final draft of the paper open to the entire collaboration. Comments received during the CWR must be addressed by the analysis team and validated by the PAG, before the paper is submitted to the journal.

At the time of preparing this thesis, the analysis of the nuclear modification and forward-backward ratio of  $\Upsilon$  production in pPb collisions at  $\sqrt{s_{NN}} = 5.02$  TeV is at the Approval stage. We expect to be approved shortly, and enter the CWR seeking publication in Physics Letters B. A webpage dedicated to the documentation of presentations, feedback and outcome during the internal review process for this analysis, known as a “twiki” amongst collaborations at CERN, can be found here: [twiki.cern.ch/twiki/bin/view/CMS/HiUpsilonRpPb5TeV2017](http://twiki.cern.ch/twiki/bin/view/CMS/HiUpsilonRpPb5TeV2017). The working drafts of the analysis note are archived at [cms.cern.ch/iCMS/user/notefinfo?cmsnoteid=CMS%20AN-2017/221](http://cms.cern.ch/iCMS/user/notefinfo?cmsnoteid=CMS%20AN-2017/221), and drafts of the PAS and paper are versioned at [cms.cern.ch/iCMS/analysisadmin/cadilines?line=HIN-18-005](http://cms.cern.ch/iCMS/analysisadmin/cadilines?line=HIN-18-005). The analysis software are available in the git repository [github.com/stuli/RpA502TeV](https://github.com/stuli/RpA502TeV). The software can be broadly divided into: signal extraction from data using regression, determination of corrections to the extracted signal using simulations, determination of systematic biases in the analysis methodology, and visualization of the computed results.

### 5.3 Data Processing

The collision data used in this analysis were collected in January-February, 2013 (pPb) and November-December, 2015 (pp) at the LHC. Both the pp and pPb data consist of collisions at center-of-mass energy per nucleon pair,  $\sqrt{s_{NN}} = 5.02$  TeV. The pPb data were collected in two sets, with the beam directions reversed between the two.

The AOD datasets in ROOT-based tree format are available to CMS members at the

following locations:

- pPb first set: `/eos/cms/store/group/phys_heavyions/dileptons/Data2013/pPb502TeV/Upsilon/RD2013_pa_1st_run_merged.root`
- pPb second set: `/eos/cms/store/group/phys_heavyions/dileptons/Data2013/pPb502TeV/Upsilon/RD2013_pa_2nd_run_merged.root`
- pp: `/eos/cms/store/group/phys_heavyions/dileptons/Data2015/pp502TeV/TTrees/PromptAOD/OniaTree_DoubleMu_Run2015E-PromptReco-v1_Run_262157_262328.root`

With this information, the reader should be able to reproduce the results presented in this report. In case of questions, the author can be contacted at [santonatuli@gmail.com](mailto:santonatuli@gmail.com).

### 5.3.1 Proton-lead Collision Data

The prompt-reco datasets of pPb collisions used in the analysis are triggered on muons. Consequently, they are reconstructed following specifications from the muon physics object group (POG) at CMS. The prompt-reco AOD datasets based on muon object reconstruction for the 2013 proton-lead collision data can be searched in the CMS data aggregation system (DAS) as `/PAMuon/HIRun2013-PromptReco-v1/RECO`. The DAS is a distributed, noSQL database service powered by MongoDB, which can be queried to obtain meta information for any CMS dataset, including its storage location, number of events, CMSSW version and global tag etc.

The pPb data are reconstructed in CMSSW version `CMSSW_5_3_8_HI_patch2`, primarily with the global tag `GR_P_V43D::A11`. Since the first seven runs (run numbers 210498–210658) were misaligned with respect to the detector, a different global tag, `GR_P_V43F::A11`, is used to reprocess the prompt-reco data from these runs. A JSON file is used to specify the optimal detector conditions that could be realized during any period of dedicated data collection at CMS. The following JSON file is used to skip luminosity sections of the pPb data that were

not collected under optimal detector conditions: `/afs/cern.ch/cms/CAF/CMSCOMM/COMM_DQM/certification/Collisions13/pPb/Prompt/Cert_210498-211631_HI_PromptReco_Collisions13_JSON_MuonPhys_v2.txt`.

All events in the pPb data are selected using the trigger `HLT_PAL1DoubleMu0Open_v1`, which requires two muon candidates in the muon detectors, both within detector acceptance  $-2.4 < \eta_{\text{lab}} < 2.4$ , with no explicit limitations on their combined reconstructed  $p_T$  or  $y_{\text{lab}}$ . The trigger is kept unrescaled during the whole run.

As previously mentioned, the two sets of pPb data correspond to two data acquisition periods, with the beam directions reversed between the two. During the first period, the proton beam travels towards negative pseudorapidity in the CMS detector frame,  $-\eta_{\text{lab}}$ , (refer to section 2.2.1 for details) with an energy of 4 TeV and the lead beam travels towards  $+\eta_{\text{lab}}$  with an energy of 1.58 TeV. Due to the asymmetry in the energies of the proton and lead beams, the center-of-mass of collisions are boosted towards  $-\eta_{\text{lab}}$  by  $\Delta\eta = 0.465$ . Similarly, during the second data acquisition period, the proton beam travels toward  $+\eta_{\text{lab}}$  and is once again boosted compared to the lead beam traveling in the opposite direction, creating a boost for the collision center-of-mass in the opposite direction. As is convention, in this analysis we define the “forward” region (the positive pseudorapidity in the center-of-mass frame,  $+\eta_{\text{CM}}$ ) by the proton-going direction. We can convert the  $\eta_{\text{lab}}$  to  $\eta_{\text{CM}}$  using,

$$\eta_{\text{CM}} = -(\eta_{\text{lab}}^{\text{1st}} + 0.465), \quad (5.1)$$

$$\eta_{\text{CM}} = \eta_{\text{lab}}^{\text{2nd}} - 0.465. \quad (5.2)$$

The set of pPb data recorded during the first acquisition period correspond to run numbers 210498 through 211256, with an integrated luminosity of  $20.7 \text{ nb}^{-1}$ . The run numbers corresponding to the second set are 211313 through 211631, providing further integrated luminosity of  $14.0 \text{ nb}^{-1}$ . The two sets of pPb data, one corresponding to each beam direction, are merged together once it is determined that the combined data and the individual sets of

data produce mutually consistent results when the same analysis is performed on them. This study can be found in appendix A.1. The merged data is then used for the entire analysis. The integrated luminosity values are obtained using the command `lumiCalc2.py overview -i JSONfile`. Further details on processing of the pPb data can be found at [twiki.cern.ch/twiki/bin/view/CMS/HIOnia2MuMuSkimProcessingDetails2013](http://twiki.cern.ch/twiki/bin/view/CMS/HIOnia2MuMuSkimProcessingDetails2013).

### 5.3.2 Proton-proton Collision Data

The prompt-reco AOD dataset `/DoubleMu/Run2015E-Onia-PromptReco-v1/RECO` comprises pp collision data collected during the 2015 heavy-ion data acquisition period, using the trigger `HLT_HIL1DoubleMu0_v1` without prescale. The PbPb data discussed in chapter 4 were collected during the same period. The pp data are used as the vacuum production reference in both  $\Upsilon$  nuclear modification analyses presented in this report.

Once again, the trigger requires two muon candidates in the muon detectors each having  $-2.4 < \eta_{\text{lab}} < 2.4$ , with no explicit limitations on their combined  $p_T$  or  $y_{\text{lab}}$ . However, during pp data acquisition, an additional high-quality `HighQ` condition was applied to L1 muon candidates, requiring that they are either:

- Resistive plate chamber (RPC) unconfirmed candidates, or
- (Drift tube (DT) or cathode strip chamber (CSC)) unconfirmed candidates, or
- (DT/RPC or CSC/RPC) matched candidates.

That is, in order to trigger this dataset, the two muons are each required to leave sufficient hits either in the RPC detector alone, which provides coverage everywhere, or in either the DT (barrel) or CSC (endcap) detectors. Muons will clearly be accepted as candidates if their signature can be matched between the RPC and DT or the RPC and CSC detectors at L1 reconstruction. Furthermore, the double-muon triggering is required to be coincident with the triggering of the beam pick-up timing experiment (BPTX), in order to ensure that the events arise from real pp collisions.

The pp data thus triggered are reconstructed in CMSSW version CMSSW\_7\_5\_8 with the global tag 75X\_dataRun2\_Prompt\_ppAt5TeV\_v1. The JSON file used to select luminosity sections corresponding to optimal detector conditions is: `/afs/cern.ch/cms/CAF/CMSCOMM/COMM_DQM/certification/Collisions15/5TeV/Cert_262081-262328_5TeV_PromptReco_Collisions15_25ns_JSON_MuonPhys.txt`. The integrated luminosity in pp collisions is estimated using `brilcalc lumi -u /pb --hltpath HLT_HIL1DoubleMu0_v1 -i JSONfile`, and found to be  $\mathcal{L}_{\text{int}} = 28.0 \text{ pb}^{-1}$ . Details on how the pp data were processed can be found at <https://twiki.cern.ch/twiki/bin/view/CMS/PPAA2015OniaSkims>.

### 5.3.3 Monte Carlo Simulations

As described in section 3.2, Monte Carlo (MC) simulations are used to facilitate the analysis of real collision data whenever possible. In this analysis, we use MC samples to determine necessary corrections to the yield extracted from data to compensate for the limited geometric acceptance of the CMS detector and the finite efficiency of various data acquisition steps. MC simulations of pp and pPb collisions are generated separately for the production of  $\Upsilon(1S)$ ,  $\Upsilon(2S)$  and  $\Upsilon(3S)$  mesons at  $\sqrt{s_{\text{NN}}} = 5.02 \text{ TeV}$  and their subsequent decay to muon pairs using PYTHIA8.209 [134]. These samples are not embedded into a QGP-like environment, as we do not anticipate the formation of a QGP in most pp and pPb collisions.

In order to determine the correction factor needed to compensate for detector acceptance (referred to simply as the “acceptance”), the generator-level MC samples, without full reconstruction in the detector, produced with the pp configuration—i.e. with both proton beams having equal momenta—are used for both pp and pPb collisions. Moreover, these samples are also used to determine the acceptance for pp collisions in the analysis described in chapter 4. Within the CMS DAS, the MC samples can be found in the directories listed in table 5.1.

The exact method for determining the acceptance correction to extracted yields is described later in chapter 7. Here we simply note that the correction, determined using selec-

Table 5.1: The generator-level MC samples used to evaluate the acceptance corrections for pp and pPb collisions at  $\sqrt{s_{NN}} = 5.02$  TeV.

Simulated Particle	DAS Directory
$\Upsilon(1S)$	/Ups1SMM_5p02TeV_TuneCUETP8M1/ pp502Fa1115-MCRUN2_71_V1-v1/GEN-SIM
$\Upsilon(2S)$	/Ups2SMM_5p02TeV_TuneCUETP8M1/ pp502Fa1115-MCRUN2_71_V1-v1/GEN-SIM
$\Upsilon(3S)$	/Ups3SMM_5p02TeV_TuneCUETP8M1/ pp502Fa1115-MCRUN2_71_V1-v1/GEN-SIM

tions on only the kinematics (i.e.  $p_T$  and  $\eta$ ) of the daughter muons, is fiducial in nature. As a result, we can use the same generator level MC for both pp and pPb collisions if we simply shift the dimuon  $\eta$  distribution by the amount expected due to the boosted center-of-mass in pPb collisions. The shift of  $\Delta\eta = -0.465$  results in a shift for MC simulated dimuons in pPb of:  $\eta_{\text{new}} = \eta_{\text{old}} - 0.465$ . Distributions of dimuons within the CMS detector acceptance as a function of  $p_T$  and  $y_{CM}$  in the generator-level MC are shown in figures 5.1 for pp and 5.2 for pPb collisions for all  $\Upsilon$  states.

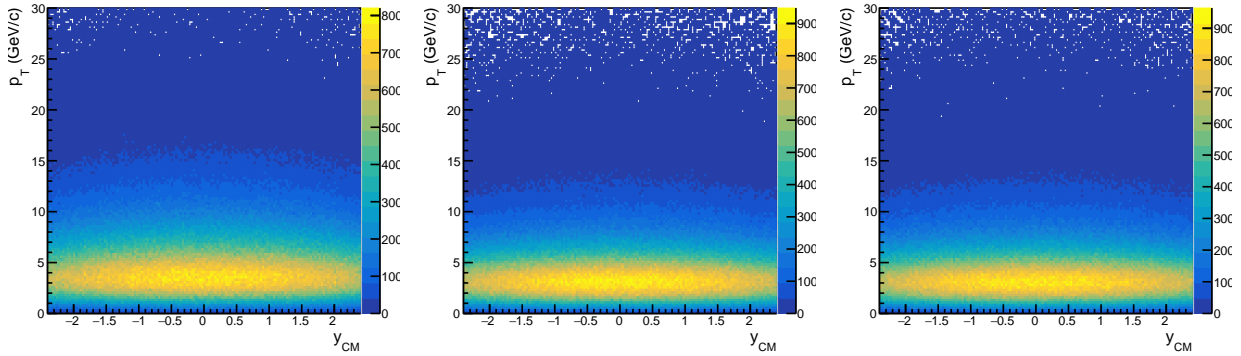


Figure 5.1: Dimuons in the generator level MC with acceptance cuts as function of  $p_T$  vs.  $y_{CM}$  for pp. The left, middle and right plots show dimuons in the  $\Upsilon(1S)$ ,  $\Upsilon(2S)$  and  $\Upsilon(3S)$  MC, respectively.

For full reconstruction, the CMS detector response is simulated using GEANT4 [135]. The Bremsstrahlung radiation that daughter muons experience in the detector is simulated using a final-state detector effect simulation software called PHOTOS215.5 [150]. These fully-reconstructed MC samples are used to determine the correction factors needed to compensate for the finite efficiency of data acquisition using the CMS detector. The correction factors

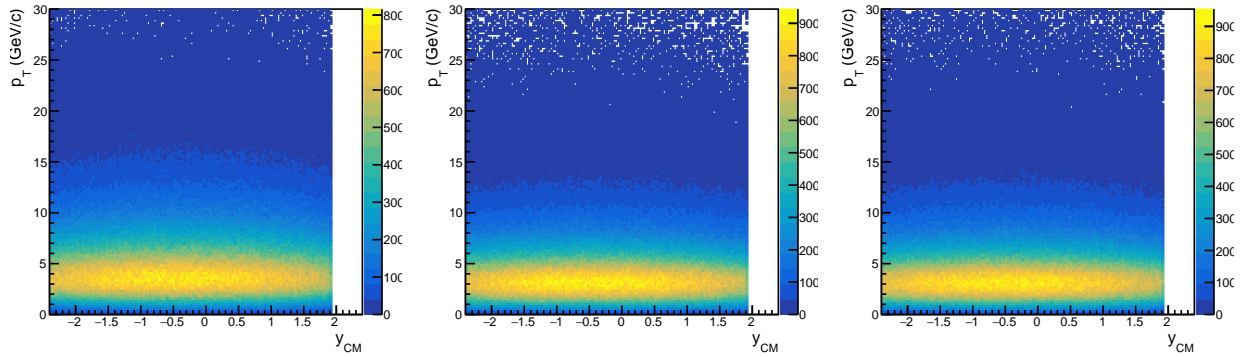


Figure 5.2: Dimuons in the generator level MC with acceptance cuts as function of  $p_T$  vs.  $y_{CM}$  for pPb. The left, middle and right plots show dimuons in the  $\Upsilon(1S)$ ,  $\Upsilon(2S)$  and  $\Upsilon(3S)$  MC, respectively.

are referred to in shorthand as “efficiency”.

Reconstruction is performed for simulated pPb collisions using the CMSSW release `CMSSW_5_3_27` and with the global tag `STARTHI53_V27::A11`. Generated particles are boosted by  $\Delta y_{lab} = -0.465$  in order to reproduce the observed asymmetry in data using the beamspot command `Realistic5TeVPPbBoost` within the CMSSW framework. In the case of pp collisions, the CMSSW version used is `CMSSW_7_5_8_patch3`, with global tag `75X_mcRun2_asymptotic_ppAt5TeV_v3`. Once again, the fully-reconstructed pp MC sample is the same as the one used to determine efficiency corrections in the analysis [29] described in chapter 4. The DAS directories for fully-reconstructed MC samples used for efficiency determination are listed in table 5.2.

Distributions of dimuons in acceptance as a function of  $p_T$  and  $y_{CM}$  in the fully-reconstructed MC are shown in figures 5.3 for pp and 5.4 for pPb collisions for all  $\Upsilon$  states. More information on how these official CMS MC samples were generated and processed are accessible to members of the CMS collaboration at <https://twiki.cern.ch/twiki/bin/viewauth/CMS/PPb5TeVOfficialMC> for pPb and <https://twiki.cern.ch/twiki/bin/view/CMS/PP5TeVOfficialMC> for pp collisions.

Table 5.2: The fully-reconstructed MC samples used to evaluate efficiency corrections for pp and pPb collisions at  $\sqrt{s_{NN}} = 5.02$  TeV.

Collision System	Simulated Particle	DAS Directory
pp	$\Upsilon(1S)$	/Ups1SMM_5p02TeV_TuneCUETP8M1/ HINppWinter16DR-75X_mcRun2_asymptotic_ ppAt5TeV_v3-v1/AODSIM
	$\Upsilon(2S)$	/Ups2SMM_5p02TeV_TuneCUETP8M1/ HINppWinter16DR-75X_mcRun2_asymptotic_ ppAt5TeV_v3-v1/AODSIM
	$\Upsilon(3S)$	/Ups3SMM_5p02TeV_TuneCUETP8M1/ HINppWinter16DR-75X_mcRun2_asymptotic_ ppAt5TeV_v3-v1/AODSIM
pPb	$\Upsilon(1S)$	/Upsilon1S_PbP_5p02-Pythia8/ pAWinter13DR53X-pa_PbP_STARHI53_ V27-v1/GEN-SIM-RECO
	$\Upsilon(2S)$	/Upsilon2S_PbP_5p02-Pythia8/ pAWinter13DR53X-pa_PbP_STARHI53_ V27-v1/GEN-SIM-RECO
	$\Upsilon(3S)$	/Upsilon3S_PbP_5p02-Pythia8/ pAWinter13DR53X-pa_PbP_STARHI53_ V27-v1/GEN-SIM-RECO

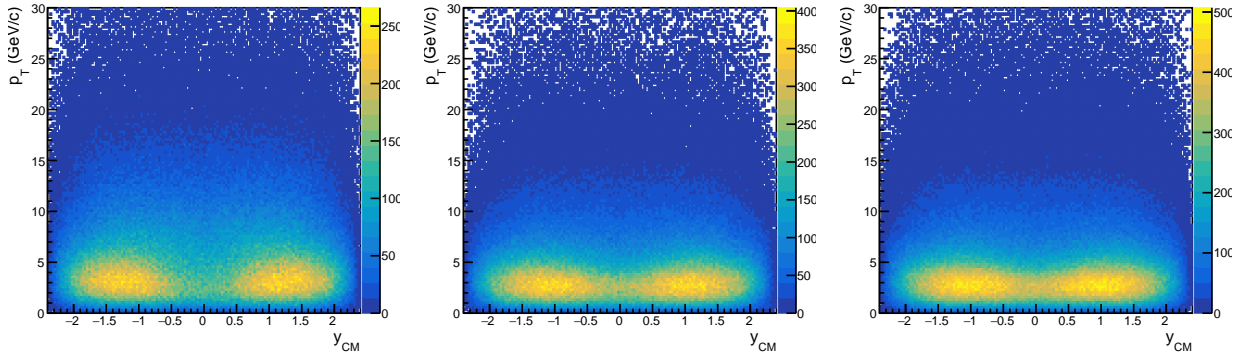


Figure 5.3: Dimuons in acceptance in the fully-reconstructed MC as a function of  $p_T$  and  $y_{CM}$  for pp collisions. The left, middle and right plots show dimuons in the  $\Upsilon(1S)$ ,  $\Upsilon(2S)$  and  $\Upsilon(3S)$  MC simulations, respectively.

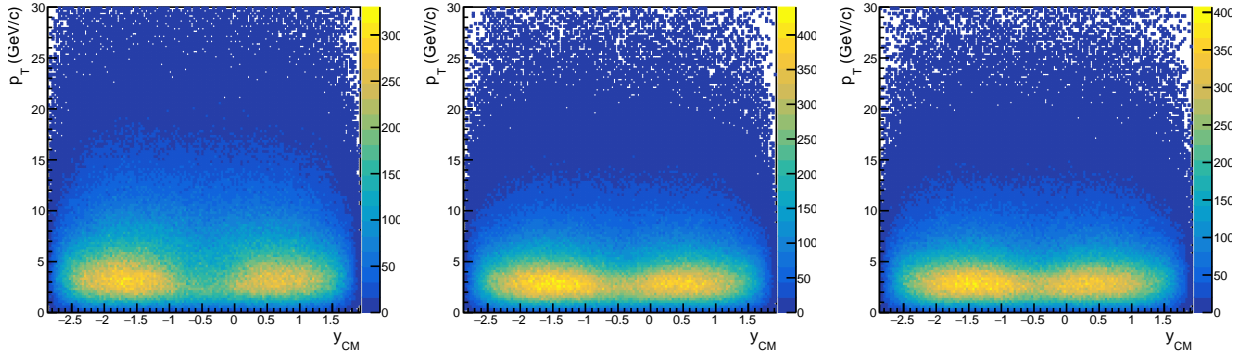


Figure 5.4: Dimuons in acceptance in the fully-reconstructed MC as a function of  $p_T$  and  $y_{CM}$  for pPb collisions. The left, middle and right plots show dimuons in the  $\Upsilon(1S)$ ,  $\Upsilon(2S)$  and  $\Upsilon(3S)$  MC simulations, respectively.

## 5.4 Data Reduction

### 5.4.1 Collision Event Selection

In order to remove beam-related background such as beam-gas interactions in pPb data, inelastic hadronic collisions are selected by requiring the coincidence of the triggering with more than 3 GeV of energy deposited into at least one HF calorimeter tower on each side of the interaction point. The same deposited energy requirement is used as the minimum bias trigger condition as well. This requirement is not applied to pp collisions, which are less susceptible to the photon-induced interactions than pPb collisions.

Both pp and pPb collision events are further selected for retention if they have at least one reconstructed primary vertex composed of two or more associated tracks within 25 cm of the nominal interaction point along the beam axis and within 2 cm in the transverse plane. Furthermore, to reject events due to beams scraping the beampipe, the fraction of good-quality tracks associated with the primary vertex in a collision event is required to be larger than 25 % when there are more than 10 tracks in the event.

For pPb collisions, a study was done [117] to identify and remove multiple interactions per bunch crossing (pileup) events from the data to avoid a potential bias in characterizing

the multiplicity-related variables. As a result of this study, an additional filter (*pileupVertexFilterCutGplus*) is applied to remove pileup events in pPb. With this filter in place, the residual fraction of pileup events is reduced from 3 % to less than 0.2 %. Since pileup only affects the event activity dependence in pPb results, no filter is applied in pp results.

## 5.4.2 Muon Quality Selection

The muon selection criteria for the pPb and pp data are chosen in accordance with the muon POG recommendations for the data acquisition periods corresponding to the respective data. As a result, the criteria are slightly different between the two collision systems. These selections are moreover identical to [29] for pp and [117] for pPb collisions, so that we may use the same *tag-and-probe* correction method as implemented by the respective prior analysis.

In order to reduce the data based on selections on the quality of muon candidates measured, we begin by skimming the prompt-reco data for each collision system by selecting all pairs of muons with an invariant mass larger than  $6 \text{ GeV}/c^2$ . While we use muons primarily identified in the tracker for skimming pPb data, for pp collisions we use muons identified using a global fit to the data from the tracker as well as muon detectors. All charge combinations are considered and every possible combination of muon pairs within an event are retained in the skimmed data. The core package used for skimming, which is structurally identical to the package used by the B physics PInG at CMS for similar analyses, can be found at [https://github.com/CMS-HIN-dilepton/cmssw/tree/Onia\\_AA\\_10\\_3\\_X/HiSkim/HiOnia2MuMu](https://github.com/CMS-HIN-dilepton/cmssw/tree/Onia_AA_10_3_X/HiSkim/HiOnia2MuMu).

Next, using the skimmed data, a ROOT tree is filled with single muon and muon pair observables. The package used for filling the trees for quarkonium studies, colloquially referred to as “onia” trees, is located at [https://github.com/CMS-HIN-dilepton/cmssw/tree/Onia\\_AA\\_10\\_3\\_X/HiAnalysis/HiOnia](https://github.com/CMS-HIN-dilepton/cmssw/tree/Onia_AA_10_3_X/HiAnalysis/HiOnia). To be included in the trees, the skimmed muon pairs must pass the quality selections required to reject background from fake muons while keeping the efficiency of selecting real muons high. The single muons must additionally be

within a defined fiducial acceptance of the CMS detector. For all data used in this analysis, we select muons in the kinematic range  $p_T^\mu > 4 \text{ GeV}/c$ ,  $|\eta_{\text{lab}}^\mu| < 2.4$ , which allows  $\Upsilon$  mesons to be measured down to  $p_T = 0$ . The muon pair kinematic range studied for this analysis is  $p_T^{\mu^+\mu^-} < 30 \text{ GeV}/c$  and  $|y_{\text{lab}}^{\mu^+\mu^-}| < 2.4$ .

## Selections for pPb Collisions

The pPb muon candidates are selected if they pass the *Soft Muon* ID selection, as endorsed by the muon POG for run I analyses, which can be found here: [https://twiki.cern.ch/twiki/bin/view/CMSPublic/SWGuideMuonIdNew\\_Version\\_recommended](https://twiki.cern.ch/twiki/bin/view/CMSPublic/SWGuideMuonIdNew_Version_recommended). Some of the selections are then further tightened for our particular analysis. The complete list of all the selections applied on muons and muon pairs in pPb data is as follows:

- muons are reconstructed as *tracker muons*;
- muon pairs consist of oppositely-charged muons;
- muon pairs originate from a common vertex with a  $\chi^2$  probability  $> 1\%$ ;
- *Soft Muon* ID criteria:
  - tracker muon arbitration is carried out to resolve the ambiguity of segment sharing by picking the best matching based on position and pull requirements;
  - at least one well-matched muon segment in any muon station is required for the track detected in the tracker (*TMOneStationTight*);
  - the number of tracker layers with hits must be  $> 5$  to ensure sufficient transverse momentum resolution of muons;
  - the number of pixel layers with valid hits must be  $> 0$  to suppress muons from decays in flight;
  - the track high purity flag is used to reject bad quality tracks, which consists of a few outliers;
  - the distance between the primary event vertex and the muon track in the transverse plane,  $D_{xy}$  must be  $< 0.3 \text{ cm}$ , and the longitudinal plane,  $D_z$  must be  $< 20.0 \text{ cm}$ .

## Selections for pp Collisions

The pp muon candidates are selected if they pass the *Soft Muon* ID selection, as endorsed by the muon POG for run II analyses, which can be found here: <https://twiki.cern.ch/twiki/bin/view/CMS/SWGuideMuonIdRun2SoftMuon>. Some of the selections are then modified in accordance to [151], resulting in a “hybrid” *Soft Muon* selection. The complete list of all the cuts applied to muons and muon pairs in pp collisions is as follows:

- muons are reconstructed as *global muons*;
- muon pairs consist of oppositely-charged muons;
- muon pairs originate from a common vertex with a  $\chi^2$  probability  $> 1\%$ ;
- “hybrid” *Soft Muon* ID criteria:
  - tracker muon arbitration is carried out to resolve the ambiguity of segment sharing by picking the best matching based on position and pull requirements;
  - at least one well-matched muon segment in any muon station is required for the track detected in the tracker (*TMOneStationTight*);
  - the muon tracks are required to also form a global track (*isGlobal* condition), where the independent information from the silicon tracker and the muon stations are combined in a global fit using all the hits;
  - the number of tracker layers with hits must be  $> 5$  to ensure sufficient transverse momentum resolution of muons;
  - the number of pixel layers with valid hits must be  $> 0$  to suppress muons from decays in flight;
  - no track high purity flag is used;
  - the distance between the primary event vertex and the muon track in the transverse plane,  $D_{xy}$  must be  $< 0.3$  cm, and the longitudinal plane,  $D_z$  must be  $< 20.0$  cm.

# Chapter 6

## Regression Model

With the data set up for analysis, our goal now is to extract the yields of the  $\Upsilon$  states from pp and pPb data using the invariant mass spectra of opposite-sign muon pairs. The yields are counts of events, which are fundamentally Poisson distributed. Since we have relatively high numbers of events per unit of invariant mass that the detector can resolve, by the central limit theorem the measured counts are instantiations of a Gaussian distribution and each measurement has an associated statistical uncertainty given by the standard deviation of the Gaussian.

In order to extract the signal, we need to pick a model that can describe the structures that appear in the spectra which we identify with  $\Upsilon$  peaks. The centers of these peaks naturally correspond to the measured PDG [152] masses of the three states, although they may be shifted relative to these values if the detector systematically measures reconstructed particle momenta to be lower than the true values due to resolution effects and energy loss during detection. Furthermore, the model must be able to classify the muon pairs into  $\Upsilon(1S)$ ,  $\Upsilon(2S)$  and  $\Upsilon(3S)$  states and identify any contributions to the yields from background processes. Indeed, the data and well as physics intuition tell us that the  $\Upsilon$  peaks lie atop a background continuum of opposite-sign muon pairs, whose sources range from decays of other nearby resonances to uncorrelated muon pairs whose reconstructed masses appear in

the  $\Upsilon$  mass window.

We build such a descriptive model using primarily physics motivations, with estimators for the  $\Upsilon(nS)$  yields and background counts as well as a handful of nuisance parameters. We find that linear regression, with some parameter tuning, is sufficient to extract the signals from data. During regression, we employ unbinned maximum likelihood estimation. Our model therefore falls into the class of machine learning models known as generalized linear models (GLMs), and relies on the effective minimization of a linear loss function in order to interpolate between data points (or records) and perform the desired classification. The simplicity of our model for extracting the rare-event  $\Upsilon$  yields from initially noisy collision data is testament to the extensive and clever data manipulation we perform prior to building our analysis framework.

Extracted  $\Upsilon$  yields are used to construct summary statistics, namely the nuclear modification factors  $R_{pA}$  and the forward-backward production ratios  $R_{FB}$ , which may be studied as functions of features in the collision data such as kinematic and event activity variables. In this chapter, we describe the methodology for extracting the  $\Upsilon(nS)$  yields from pp and pPb data. Before we describe our model, let us discuss our choices for cut-off values and bin edges for the independent observables, which we will use to investigate trends of the summary statistics. These choices determine how we split the data prior to performing regression. We will present our results as integrated, corrected ratio values in bins of  $p_T$ ,  $y_{CM}$ ,  $N_{\text{tracks}}$  and  $E_T$ . Therefore, although regression is used to fit the data in one dimension (the invariant dimuon mass) at a time, our GLM must simultaneously describe the data in these additional dimensions as well.

## 6.1 Defining the Analysis Domain

The following range is used for the opposite-sign muon pair invariant mass for all analysis bins:

$$8 \leq m_{\mu\mu} [\text{GeV}/c^2] < 14 .$$

Since the PDG values of the  $\Upsilon(1S)$ ,  $\Upsilon(2S)$  and  $\Upsilon(3S)$  masses are  $9.46 \text{ GeV}/c^2$ ,  $10.02 \text{ GeV}/c^2$  and  $10.36 \text{ GeV}/c^2$ , respectively, and the resolution of the CMS detector for dimuon invariant mass is  $< 10 \text{ MeV}/c^2$ , the chosen mass range provides us with a fairly large window for signal extraction. Since there are no other known or predicted resonances in this invariant mass region, we are able to use this large window to precisely tune the background estimator in our model.

Next, we turn to the choices of dimuon kinematic ranges over which we investigate the  $R_{\text{pA}}$  of the  $\Upsilon$  states. The acceptance of the CMS detector fully determines the studied dimuon  $y_{\text{CM}}$  range, as the approximation  $y_{\text{CM}} \simeq \eta$  holds particularly well for the heavy  $\Upsilon$  mesons. There are two reasons for the choice of the upper bound of  $p_{\text{T}} = 30 \text{ GeV}/c$ . First, it allows the direct and unambiguous comparison of the results presented here with other relevant analyses, including the analysis of  $\Upsilon(\text{nS})$  nuclear modification factors in PbPb collisions [29] as well as the identical analysis comparing excited to ground state charmonia in pPb collisions [116], both at  $\sqrt{s_{\text{NN}}} = 5.02 \text{ TeV}$ . Second, the number of dimuons lost by this selection is relatively small. Thus, although extending the  $p_{\text{T}}$  range for dimuons in the analysis would complicate the procedure, little would be gained from this extension.

To show the small number of events lost due to our upper bound for  $p_{\text{T}}$ , we study the dimuon  $p_{\text{T}}$  distribution of the pPb data in the invariant mass region  $9 < m_{\mu\mu} [\text{GeV}/c^2] < 10.8$ , tightly enclosing the  $\Upsilon$  signal region. A plot of this distribution is shown in figure 6.1. By counting the events in the regions  $p_{\text{T}} < 30 \text{ GeV}/c$  and  $30 \leq p_{\text{T}} < 50 \text{ GeV}/c$ , we see that the fraction of events lost by imposing the  $p_{\text{T}}$  selection at  $30 \text{ GeV}/c$  versus extending it to  $50 \text{ GeV}/c$  is merely 0.044 %.

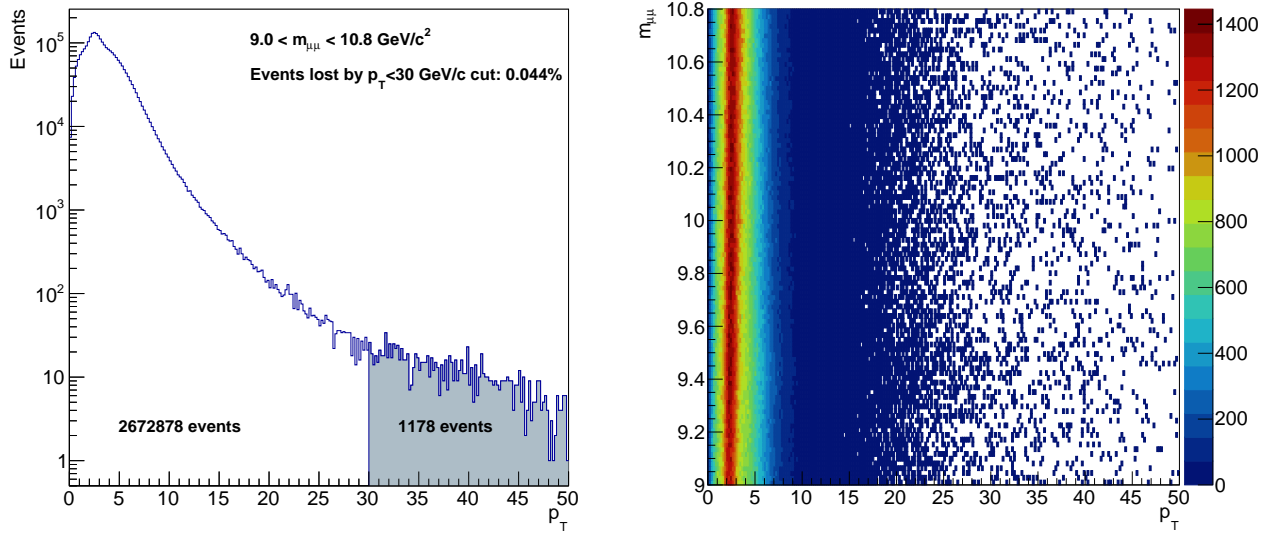


Figure 6.1: Plots of the dimuon  $p_T$  (left) and invariant mass vs  $p_T$  (right) distributions in pPb data.

## 6.2 Data Binning

In order to study the kinematic dependence of the  $R_{pA}$ , we split the data into several bins of the dimuon  $p_T$  and  $y_{CM}$ . The bin edges are inspired primarily by the desire to make direct comparisons to the above-mentioned analyses, while additionally ensuring that there are sufficient muon pairs in each bin for statistically sound signal extraction. The  $p_T$  bin edges used in this analysis are:

- $\Upsilon(1S)$ :  $p_T \in [0, 2, 4, 6, 9, 12, 30] \text{ GeV}/c$ ,
- $\Upsilon(2S)$ :  $p_T \in [0, 4, 9, 30] \text{ GeV}/c$ ,
- $\Upsilon(3S)$ :  $p_T \in [0, 6, 30] \text{ GeV}/c$ .

Since the center of mass of pPb collisions is boosted in the proton-going direction, the rapidity range of reconstructed dimuons in the detector frame  $|y_{\text{lab}}| < 2.4$  corresponds to the center-of-mass (CM) frame rapidity range  $-2.87 < y_{CM} < 1.93$ . Therefore, unlike in the case of symmetric collisions, the  $y_{CM}$  bins in this analysis cannot be cleanly extended to  $|y_{CM}| < 2.4$ . Instead, the symmetric region used is  $|y_{CM}| < 1.93$ , corresponding to the bin edges:

- $\Upsilon(1S)$ :  $y_{\text{CM}} \in [-1.93, -1.2, -0.8, -0.4, 0.0, 0.4, 0.8, 1.2, 1.93]$ ,
- $\Upsilon(2S)$ :  $y_{\text{CM}} \in [-1.93, -0.8, 0.0, 0.8, 1.93]$ ,
- $\Upsilon(3S)$ :  $y_{\text{CM}} \in [-1.93, 0.0, 1.93]$ .

However, since the data are available, we additionally present the cross section of  $\Upsilon$  production in  $-2.87 < y_{\text{CM}} < -1.93$  for all three states. For reproducibility, the correspondence between the  $\Upsilon(1S)$   $y_{\text{CM}}$  and  $y_{\text{lab}}$  bin edges for the first and the second data acquisition periods of pPb data are included below:

- CM frame:  $y_{\text{CM}} \in [1.93, 1.2, 0.8, 0.4, 0.0, -0.4, -0.8, -1.2, -1.93]$ ,
- lab frame, pPb first set:  $y_{\text{lab}}^{\text{1st}} \in [2.4, 1.67, 1.27, 0.87, 0.47, 0.07, -0.33, -0.73, -1.46, -2.4]$ ,
- lab frame, pPb second set:  $y_{\text{lab}}^{\text{2nd}} \in [-2.4, -1.46, -0.73, -0.33, 0.07, 0.47, 0.87, 1.27, 1.67, 2.4]$ .

The forward-to-backward cross section ratio in pPb collisions,  $R_{\text{FB}}$ , is investigated as a function of the measured event activity. We measure event activity near to the measured  $\Upsilon$  using the number of reconstructed tracks,  $N_{\text{tracks}}$ , in  $|\eta_{\text{lab}}| < 2.4$ . To measure event activity further from the  $\Upsilon$ , we use the sum of deposited transverse energy  $E_{\text{T}}$  in  $4 < |\eta_{\text{lab}}| < 5.2$ . As explained in section 2.2.2, the  $N_{\text{tracks}}$  measurement is facilitated by the silicon tracker and the  $E_{\text{T}}$  is determined using the hadronic forward (HF) calorimeters. The pPb data collected using the minimum bias trigger are used to explore the event activity variables before binning choices are made. These data can be found at:

- pPb Minimum Bias: `/eos/cms/store/group/phys_heavyions/yjlee/pPb2013/promptReco/PA2013_HiForest_PromptReco_KrisztianMB_JSonPPb_forestv84.root`

After exploring several possibilities for bin widths and edges, the following were chosen based on uniformity of total  $\Upsilon$  candidates in each bin:

- $E_{\text{T}} \in [0, 12, 19, 27, 120]\text{GeV}$ ,
- $N_{\text{tracks}} \in [0, 40, 62, 88, 400]$ .

Since higher activity collisions are increasingly rare, the yield of  $\Upsilon(3S)$  candidates are particularly diminished in the three highest activity bins in both  $E_{\text{T}}$  and  $N_{\text{tracks}}$ . We therefore replace these bins with one integrated bin covering the same range for  $\Upsilon(3S)$ .

The uncorrected mean values of the event activity variables in minimum bias pPb collisions are  $\langle N_{\text{tracks}} \rangle = 41$  and  $\langle E_{\text{T}} \rangle = 14.7$  GeV. The fraction of pPb minimum bias collisions in each event activity bin is presented in table 6.1.

$N_{\text{tracks}}^{ \eta <2.4}$ Bin	Fraction (%)	$E_{\text{T}}^{ \eta >4}$ Bin	Fraction (%)
0 – 39	58.8	0 – 12	50.2
40 – 61	19.4	12 – 19	20.8
62 – 87	13.3	19 – 27	15.7
88 – 400	8.5	27 – 120	13.3

Table 6.1: Multiplicity-related bins in  $N_{\text{tracks}}^{|\eta|<2.4}$  (left) and  $E_{\text{T}}^{|\eta|>4}$  (right) and the fraction of recorded events belonging to each bin.

## 6.3 Building the Model

### 6.3.1 Signal Model

It is standard to start with a Crystal-Ball (CB) function to model  $\Upsilon$  peaks. A CB consists of a Gaussian that is analytically connected (i.e. such that the function itself and its first derivative are both continuous) to a power-law tail on the left or the low-mass side. The power-law tail is able to capture dimuons that are reconstructed to lower masses than their actual mass due to its daughter muons losing energy in the detector material due to Bremsstrahlung radiation. A CB function was first implemented in [142] and is given by:

$$\text{CB}(x; \bar{x}, n, \alpha, \sigma) = N \cdot \begin{cases} \exp\left(-\frac{(x-\bar{x})^2}{2\sigma^2}\right) & \text{for } (x-\bar{x})\sigma > -\alpha \\ A \cdot (B - \frac{x-\bar{x}}{\sigma})^{-n} & \text{for } (x-\bar{x})\sigma \leq -\alpha \end{cases} \quad (6.1)$$

where

$$A = \left(\frac{n}{|\alpha|}\right)^n \cdot \exp\left(-\frac{|\alpha|^2}{2}\right)$$

$$B = \frac{n}{|\alpha|} - |\alpha|$$

To model each  $\Upsilon$  peak in this analysis, we prefer a probability density function (PDF) consisting of the sum of two CB functions over a single CB or a CB plus a Gaussian, based on goodness-of-fit tests performed on Monte Carlo simulations of  $\Upsilon$  decays [132]. The need for two CB functions is justified on physics grounds because of the varying mass resolution of the detector for different regions of dimuon rapidity. The momentum resolution of single-muon reconstruction in the forward and backward regions of the CMS detector is lower than that of the midrapidity region. As a result, the double CB and the CB-plus-Gaussian prove to be most effective at fitting the peaks across the full rapidity span of the detector by virtue of having two different widths to use for fitting dimuons [33, 132]. We therefore use one of these as the nominal PDF for fitting  $\Upsilon$  peaks while the other is retained for estimating the systematic uncertainty introduced in the results due to such a choice.

We use a goodness-of-fit study to choose the nominal PDF for yield extraction. Since both the double CB and the CB-plus-Gaussian PDFs have the same number of degrees of freedom, we can simply use the  $\chi^2$  per degree of freedom in the fits for the comparison. Tables 6.2 and 6.3 compare the  $\chi^2$  per degree of freedom from fits to pp and pPb data, respectively, obtained using each PDF in turn to extract  $\Upsilon$  yields. The double CB is chosen as the nominal signal PDF since it outperforms the CB-plus-Gaussian in most bins for both pp and pPb data.

Notably, the  $\chi^2$  per degree of freedom between the two PDFs tested are within 0 – 6 % of each other in every bin. Therefore, to study the systematic deviation in the extracted yield, one can use the alternate PDF to fit pseudo-data generated using the fitted nominal PDF. By repeating such fits a large number of times, we are able to tease out the true systematic deviations in the yields arising from fits using different PDFs, without being overly sensitive to the statistical uncertainty inherent in a single regressive fit. We further describe this technique in section 8.1.

Table 6.2: Comparison of  $\chi^2$  per degree of freedom for fits to pp data using a double Crystal Ball (DCB) versus a Crystal Ball plus Gaussian (CBG) as the signal PDF. The DCB is chosen as the nominal signal PDF.

Bin	$\chi^2/\text{ndf}$	
	DCB	CBG
$p_T,  y $ integrated	2.78	2.93
$p_T < 2 \text{ GeV}/c$	1.56	1.56
$2 < p_T < 4 \text{ GeV}/c$	1.68	1.72
$4 < p_T < 6 \text{ GeV}/c$	1.88	1.91
$6 < p_T < 9 \text{ GeV}/c$	1.38	1.42
$9 < p_T < 12 \text{ GeV}/c$	1.13	1.19
$12 < p_T < 30 \text{ GeV}/c$	1.52	1.58
$p_T < 4 \text{ GeV}/c$	2.32	2.33
$4 < p_T < 9 \text{ GeV}/c$	1.79	1.85
$9 < p_T < 30 \text{ GeV}/c$	1.96	2.07
$p_T < 6 \text{ GeV}/c$	2.51	2.55
$6 < p_T < 30 \text{ GeV}/c$	2.48	2.62
$0.00 <  y  < 0.40$	3.10	3.16
$0.40 <  y  < 0.80$	2.17	2.16
$0.80 <  y  < 1.20$	1.40	1.42
$1.20 <  y  < 1.93$	1.19	1.20
$0.00 <  y  < 0.80$	3.98	4.04
$0.80 <  y  < 1.93$	1.48	1.49

Table 6.3: Comparison of  $\chi^2$  per degree of freedom for fits to pPb data using a double Crystal Ball (DCB) versus a Crystal Ball plus Gaussian (CBG) as the signal PDF. The DCB is chosen as the nominal signal PDF.

Bin	$\chi^2/\text{ndf}$	
	DCB	CBG
$p_T, y_{\text{CM}}$ integrated	1.27	1.31
$p_T < 2 \text{ GeV}/c$	1.47	1.46
$2 < p_T < 4 \text{ GeV}/c$	0.88	0.88
$4 < p_T < 6 \text{ GeV}/c$	1.19	1.22
$6 < p_T < 9 \text{ GeV}/c$	0.95	0.96
$9 < p_T < 12 \text{ GeV}/c$	1.09	1.11
$12 < p_T < 30 \text{ GeV}/c$	0.88	0.89
$p_T < 4 \text{ GeV}/c$	1.21	1.20
$4 < p_T < 9 \text{ GeV}/c$	0.98	1.01
$9 < p_T < 30 \text{ GeV}/c$	0.99	1.02
$p_T < 6 \text{ GeV}/c$	1.25	1.26
$6 < p_T < 30 \text{ GeV}/c$	1.03	1.08
$-1.93 < y_{\text{CM}} < -1.20$	0.89	0.88
$-1.20 < y_{\text{CM}} < -0.80$	1.07	1.07
$-0.80 < y_{\text{CM}} < -0.40$	0.91	0.91
$-0.40 < y_{\text{CM}} < 0.00$	1.06	1.08
$0.00 < y_{\text{CM}} < 0.40$	0.71	0.70
$0.40 < y_{\text{CM}} < 0.80$	0.80	0.80
$0.80 < y_{\text{CM}} < 1.20$	0.84	0.84
$1.20 < y_{\text{CM}} < 1.93$	0.81	0.81
$-1.93 < y_{\text{CM}} < -0.80$	1.22	1.23
$-0.80 < y_{\text{CM}} < 0.00$	1.23	1.24
$0.00 < y_{\text{CM}} < 0.80$	0.88	0.87
$0.80 < y_{\text{CM}} < 1.93$	0.91	0.91
$-1.93 < y_{\text{CM}} < 0.00$	1.49	1.51
$0.00 < y_{\text{CM}} < 1.93$	0.88	0.88

A double CB PDF for the  $\Upsilon(1S)$  resonance would appear as follows:

$$\Sigma_{1S}(m_{\mu\mu}; m_0, n, \alpha, \sigma_0, f, x) = f \cdot \text{CB}_1(m_{\mu\mu}; m_0, n, \alpha, \sigma_0) + (1 - f) \cdot \text{CB}_2(m_{\mu\mu}; m_0, n, \alpha, x \cdot \sigma_0) \quad (6.2)$$

However, since both CBs must describe the  $\Upsilon(1S)$  state, they must mutually arrive at the same values for the fitted  $m_0$ ,  $n$ , and  $\alpha$  parameters. The additional parameter,  $x$ , found in the second CB ( $\text{CB}_2$ ), represents the ratio of the two  $\sigma$  parameters, i.e. the widths of the two CBs, and is used to account for the different mass resolution in the mid- and forward-rapidity regions of the detector. Similarly, the  $f$  parameter, which multiplies the first CB ( $\text{CB}_1$ ), represents the ratios of the amplitudes of the  $\Upsilon(1S)$  peaks reconstructed in the two different regions of the detector. In other words, the chosen PDF models the reconstructed  $\Upsilon(1S)$  peak as a simple combination of two identical CBs except for having different mass resolutions. The six independent nuisance parameters for  $\Sigma_{1S}$  are then  $m_0$ ,  $n$ ,  $\alpha$ ,  $f$ ,  $\sigma_0$ ,  $x$ .

Now, an overall signal PDF that combines three PDFs identical to 6.2, one for each  $\Upsilon$  state, without any consideration to the relationship between the parameters across states would result in overfitting. Indeed, the parameters that determine the shape of the CB tails,  $n$  and  $\alpha$ , should be identical for all three states as they are meant to capture energy loss due to muon bremsstrahlung, which is independent of the  $\Upsilon$  state from which the muons originate. Moreover, the scale parameters,  $x$  and  $f$ , between the two CBs should also be identical for different  $\Upsilon$  states. Once again, the relative abundance of barrel- and endcap-region reconstructed dimuons in  $\Upsilon$  peaks is determined, not by the  $\Upsilon$  state, but by the detector. Therefore, prior to combining the double CB PDFs for each  $\Upsilon$  state shown in 6.2 into an overall signal PDF, the parameters  $n$ ,  $\alpha$ ,  $f$  and  $x$  are fixed to be identical for all three states.

Furthermore, any shift in the mass of the reconstructed peaks due to detector resolution should affect all three  $\Upsilon$  states in the same manner. Therefore, we can further assume that

both the width  $\sigma_{nS}$  and the mass  $m_{nS}$  of the excited states scale as:

$$\begin{aligned} m_{nS} &= m_0 \cdot \frac{m_{\text{PDG}}^{nS}}{m_{\text{PDG}}^{1S}} \\ \sigma_{nS} &= \sigma_0 \cdot \frac{m_{\text{PDG}}^{nS}}{m_{\text{PDG}}^{1S}} \end{aligned}$$

With this prescription, the PDFs for the excited states read:

$$\Sigma_{nS}(m_{\mu\mu}; m_0, n, \alpha, \sigma_0, f, x) = \Sigma_{1S}\left(m_{\mu\mu}; m_0 \cdot \frac{m_{\text{PDG}}^{nS}}{m_{\text{PDG}}^{1S}}, n, \alpha, \sigma_0 \cdot \frac{m_{\text{PDG}}^{nS}}{m_{\text{PDG}}^{1S}}, f, x\right)$$

The signal model  $\mathcal{S}$  is then defined as a linear combination of the  $\Upsilon(1S)$ ,  $\Upsilon(2S)$ , and  $\Upsilon(3S)$  PDFs,

$$\begin{aligned} \mathcal{S}(m_{\mu\mu}; N_{\Upsilon(1S)}, N_{\Upsilon(2S)}, N_{\Upsilon(3S)}, m_0, n, \alpha, \sigma_0, f, x) \\ = N_{\Upsilon(1S)} \cdot \Sigma_{1S}(m_{\mu\mu}) + N_{\Upsilon(2S)} \cdot \Sigma_{2S}(m_{\mu\mu}) + N_{\Upsilon(3S)} \cdot \Sigma_{3S}(m_{\mu\mu}) \end{aligned} \quad (6.3)$$

where  $N_{\Upsilon(nS)}$  represent the estimators of the  $\Upsilon(nS)$  yields.

Finally, since fits are performed in all analysis bins separately, parameter correlation across bins can be useful to inform the model as well. The fits in this analysis differ from each other by a single selection on any one variable. Thus, we expect some attributes in the data to either remain uniform or change in a interpretable way when fits are studied as a function of a single variable. Since we have mapped the most interpretable attributes in the data to nuisance parameters in the signal model, the uniformity or trend should be captured by correlations or trends in these parameters across fits in bins of any given variable. The analysis variable with the greatest sensitivity to such interpretable attributes is  $y_{\text{CM}}$ . Since the muon detection technologies and materials are different in the barrel and endcap regions of the detector, we expect the tail parameters,  $n$  and  $\alpha$ , to take different values in these two regions. Within each region, however, they can be expected to stay roughly constant.

Similarly, the scaling parameters,  $x$  and  $f$ , should change according to a distinct trend as we go from mid to forward rapidity, if indeed the two CBs in our signal model each correspond to dimuons reconstructed in one of these two regions of the detector.

The constrained optimization performed on the pp data has already been described in section 4.2.1. We employ a more involved and iterative process for the pPb data, as the data are more sparse and noisy. We perform some initial fits to the data, in order to capture the average behavior of the tail parameters in each of these regions. Using these free-parameter initial fits, we obtain the average value of  $\alpha$  in the midrapidity and the forward rapidity regions, separately for pp and pPb data. We then fix  $\alpha$  to this value and repeat the process to obtain the average value of  $n$  in the next round of fitting. At this stage, we take the precautionary step of releasing the constraint on  $\alpha$  and re-averaging its values over a third round of fitting. Since  $n$  and  $\alpha$  together define the power-law tail of the CBs, they are fundamentally correlated. Therefore, a range of pairs of values  $(n, \alpha)$  will provide similar fits. By allowing  $\alpha$  to readjust its value during the third round of fitting, we can reduce the uncertainty on this value compared to the first round, where there are significant fluctuations due to both  $n$  and  $\alpha$  being free.

Next, we perform fits with both  $n$  and  $\alpha$  fixed to their average values and use these to obtain average values of  $x$  and  $f$ . Finally, we extract the  $\Upsilon$  yields using fits where all four of these parameters are constrained to their average values using a Gaussian penalty to prevent large deviations. In chapter 8 we will discuss the determination of the systematic uncertainty in our results introduced by using this methodology to reduce the allowed phase space of these four signal parameters.

### 6.3.2 Background Model

The three  $\Upsilon$  signal peaks in data lie atop a continuum of background events. The background itself shows characteristic features that can be identified with physics objects or phenomena. The dominant contributor to background is the random combination of uncorrelated single

muons “reconstructed” as dimuons. At high mass, the distribution of background events falls off exponentially, as would be expected from the statistical phase-space factor decrease with increasing energy. For most bins in the analysis, at the low-mass end, the distribution rises somewhat steeply with invariant mass, as if being “turned on”. This feature is artificial; it is introduced by the low- $p_T$  selection on single muons ( $p_T^\mu > 4 \text{ GeV}/c$ ) which limits the dimuons that can be reconstructed in the mass window. The exact location of this artificial turn on varies by bin, in particular depending on the  $p_T$  range of dimuons included in the given bin. For bins that include dimuons down to  $p_T = 0 \text{ GeV}/c$ , the turn on peaks around  $m \approx 8 \text{ GeV}/c^2$ , corresponding to the invariant mass of a pair of two  $p_T^\mu = 4 \text{ GeV}/c$  muons. Similarly, for analysis bins with only higher  $p_T$  dimuons, the turn on peak feature will form at lower masses and may even lie outside the mass window used for fitting. While the low-mass turn on always begins below the  $\Upsilon$  mass range, the combined effect of the turn on and the exponential fall off of the background at higher masses can lead to a more gradual hump throughout the mass window.

To model the background in analysis bins which contain dimuons down to  $p_T = 0 \text{ GeV}/c$ , we use a PDF consisting of a real-valued error function, which is shifted and scaled, multiplied by an exponential. The error function captures the low-mass turn-on feature, while the exponential function models the high-mass fall off. For bins with dimuon  $p_T > 6 \text{ GeV}/c$ , we model the background solely with an exponential function. We note that there are additional physics contributions to the background, the dominant ones being the Drell-Yan muon pairs and muon pairs from the weak decays of open-bottom-hadron pairs, e.g.  $b\bar{b} \rightarrow B^+B^- \rightarrow \mu^+\mu^- + X$ . However, because of the dominance of the combinatorial background, a PDF inspired from the features discussed above is sufficient to describe the observed background distributions in data.

The nominal background PDF,  $\mathcal{B}$ , used in the analysis is constructed as

$$\mathcal{B}(m_{\mu\mu}; \mu, \sigma, \lambda) = \begin{cases} \exp\left(-\frac{m_{\mu\mu}}{\lambda}\right), & \text{if } p_T \geq 6 \text{ GeV}/c \\ \exp\left(-\frac{m_{\mu\mu}}{\lambda}\right) \cdot \frac{1 + \text{Erf}\left(\frac{m_{\mu\mu} - \mu}{\sqrt{2}\sigma}\right)}{2}, & \text{otherwise} \end{cases} \quad (6.4)$$

The background shape depends on three nuisance parameters left free during fitting:

- $\lambda$ , the decay constant of the exponential function.
- $\mu$ , the parameter that controls the location of the kinematic “turn on”. At this location, both the argument and the value of the Erf function equal 0. If one derives the Erf as the integral of a Gaussian, this parameter would mark the location of the mean of the Gaussian.
- $\sigma$ , the width parameter, equal to the  $\sigma$  parameter of the Gaussian distribution from which the error function can be derived. In our case, this parameter is sensitive to the mass resolution as well as the convolution of the single-muon  $p_T$  selection and the underlying dimuon  $p_T$  distribution,

Finally, the function  $\mathcal{F}$  used for fitting the data is the sum of the signal and background PDFs:

$$\begin{aligned} \mathcal{F}(m_{\mu\mu}; N_{\Upsilon(1S)}, N_{\Upsilon(2S)}, N_{\Upsilon(3S)}, N_{\text{Bkgd}}, m_0, \mu, \sigma, \lambda) \\ = \mathcal{S}(m_{\mu\mu}; N_{\Upsilon(1S)}, N_{\Upsilon(2S)}, N_{\Upsilon(3S)}, m_0) + N_{\text{Bkgd}} \cdot \mathcal{B}(m_{\mu\mu}; \mu, \sigma, \lambda) \end{aligned} \quad (6.5)$$

where the normalization  $N_{\text{Bkgd}}$  is the background estimator.

## 6.4 Yield Extraction

Equipped with the above model, we now perform regression on the opposite-sign dimuon invariant mass spectra to extract the  $\Upsilon(nS)$  yields in the various analysis bins. In this section, we provide plots of all nominal fits used to calculate the results presented in chapter 9, including the fitted values of all parameters in each fit. Since each record (number of events) in the invariant mass spectra is normally distributed, for fit validation we will use a simple residual or “pull”: the difference between the record and the prediction from the fitted function, divided by the statistical uncertainty on the record. If the fit is successful and unbiased, the pull will itself be distributed according to a standard Gaussian. We begin with fits on the complete pp and pPb data, without binning in any variable. This is referred to as the integrated bin. We then move to fits where the data are binned in  $p_T$ ,  $y_{CM}$ ,  $N_{\text{tracks}}$  and  $E_T$ .

### 6.4.1 Integrated Bin

Figure 6.2 shows the fit of equation (6.5) to the invariant mass distribution of integrated pp (left) and pPb (right) data. The data are integrated in the dimuon kinematic range  $p_T < 30 \text{ GeV}/c$ ,  $|y_{CM}| < 1.93$ . The data points are the solid black circles in the top panels. The shape fitted to the overall spectra in each plot is represented by a solid blue line, while a dashed blue line represents the background-only component of the fitted counts. The bottom panel in each case shows the pull distribution. The  $\chi^2$  per degree of freedom of fit is indicated in the plots as well. For both the pp and the pPb data, the  $\chi^2$  per degree of freedom is close to unity, indicating a reasonable goodness of fit. However, regression is performed on unbinned data using maximum likelihood estimation, so the  $\chi^2$  is kept simply as a goodness-of-fit measure, but does not play a role in the fit. The pull distributions for both pp and pPb data appear normally distributed, with no systematic deviations in the region of interest.

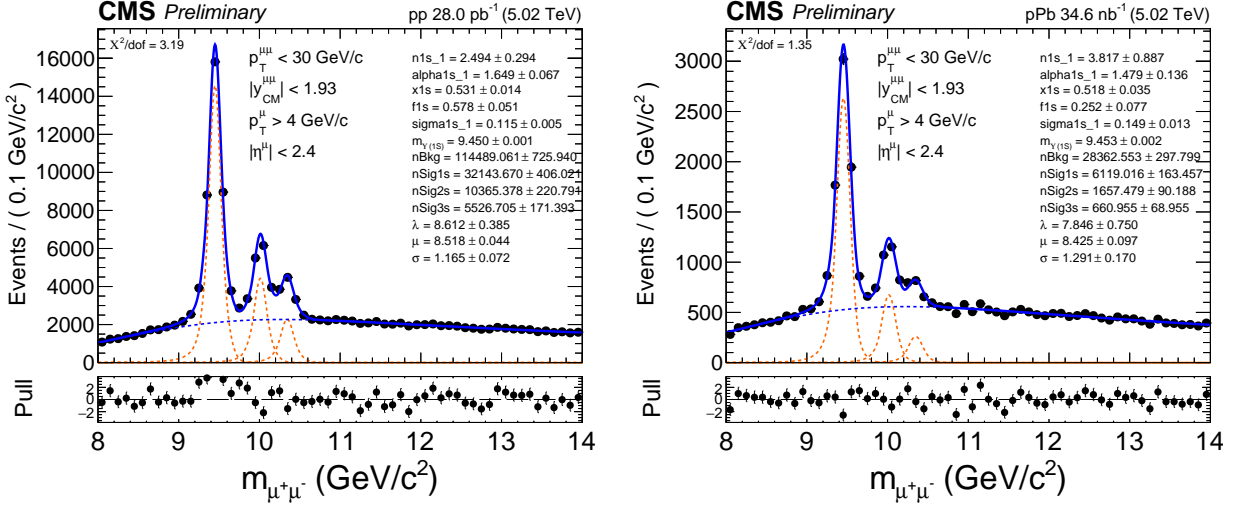


Figure 6.2: Nominal fits to the pp (left) and pPb (right) invariant mass distributions in the integrated bin.

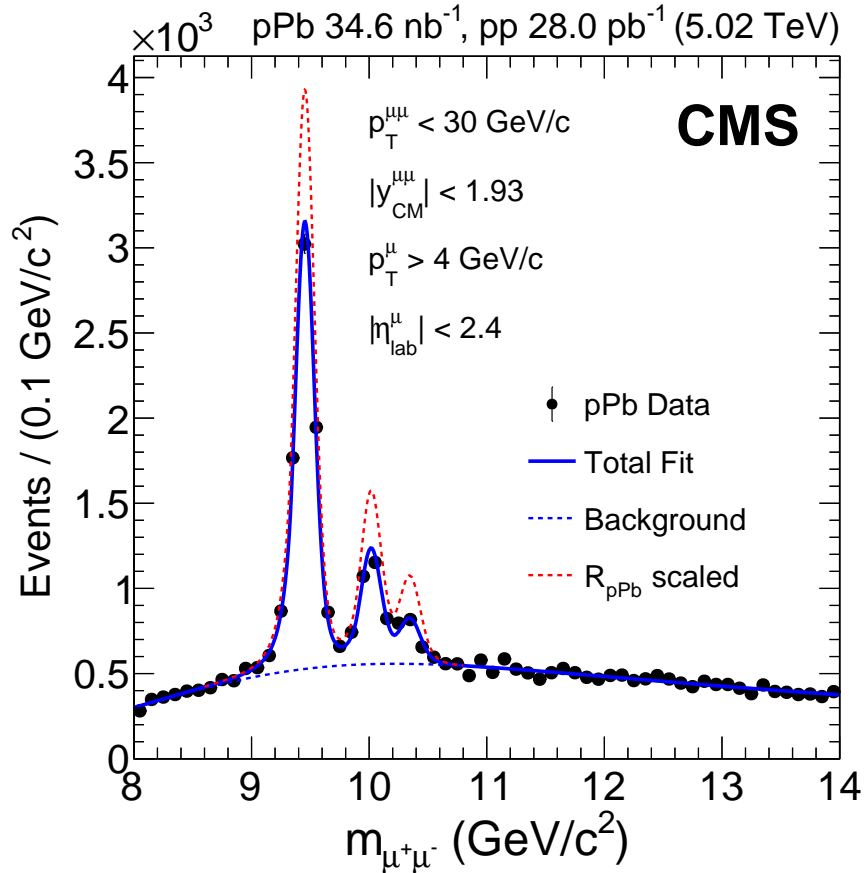


Figure 6.3: A visual representation of the measured  $R_{pA}$  of the three  $\Upsilon$  states. The nominal fit to the pPb data in the integrated  $p_T$ ,  $y_{CM}$  bin is once again shown by the solid blue line. The dashed red line is obtained by scaling the  $\Upsilon(1S)$ ,  $\Upsilon(2S)$ , and  $\Upsilon(3S)$  signal shapes by the inverse of the measured  $R_{pPb}$  for each state.

The yields extracted from the pp and pPb integrated fits are used to determine the integrated  $R_{pA}$  of the three  $\Upsilon$  states. In chapter 9, these are compared directly to the integrated  $R_{AA}$  values we obtained in chapter 4. Figure 6.3 offers a visual representation of the  $R_{pA}$ . The pPb data is shown (black points) with the fit to pPb data (blue solid line). A dashed red line is used to depict the  $\Upsilon(1S)$ ,  $\Upsilon(2S)$ , and  $\Upsilon(3S)$  signal shapes in pPb scaled by the inverse of the measured  $R_{pPb}$  for each state. It is clear from this comparison that the  $\Upsilon$  yields are suppressed in pPb relative to pp under the  $A$ -scaling hypothesis in the integrated kinematic region.

## 6.4.2 Transverse Momentum Binning

Figures 6.4 through 6.14 show the fitted dimuon invariant mass distributions in the  $p_T$  bins used in this analysis. The dimuon rapidity is restricted to be in the symmetric range  $|y_{CM}| < 1.93$ , as discussed in section 6.2. Yields extracted from these fits are used to determine the  $\Upsilon(nS)$  cross sections and  $R_{pA}$  as a function of  $p_T$ . Figure 6.4 shows the lowest  $p_T$  bin in the analysis,  $[0 - 2.0]$  GeV/ $c$ , for pp data on the left panel and for PbPb data on the right panel. The effect of the kinematic peak due to the single muon  $p_T$  cut is most visible in this bin.

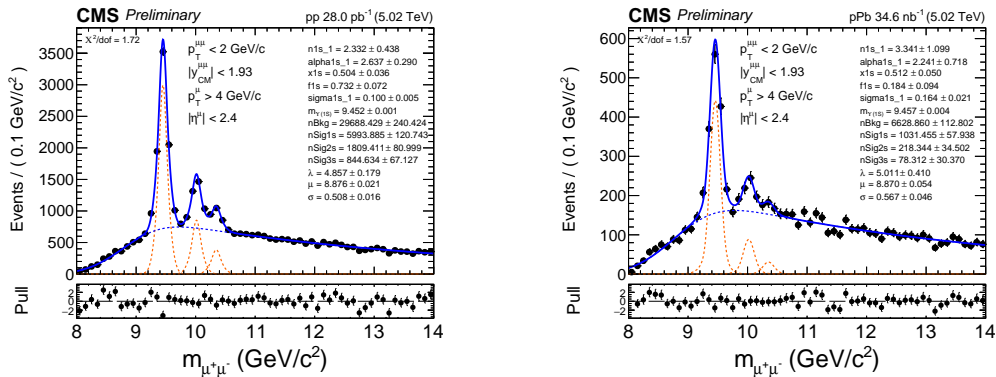


Figure 6.4: Nominal fits to the pp (left) and pPb (right) data for  $p_T \in [0 - 2]$  GeV/ $c$ .

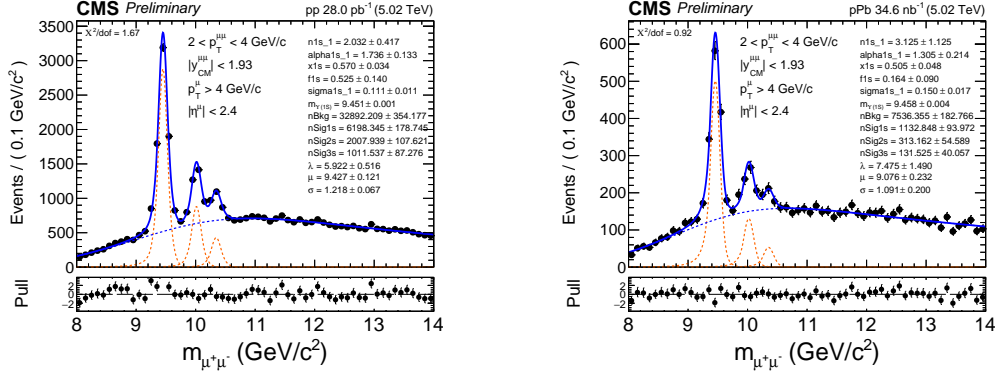


Figure 6.5: Nominal fits to the pp (left) and pPb (right) data for  $p_T \in [2 - 4]$  GeV/c.

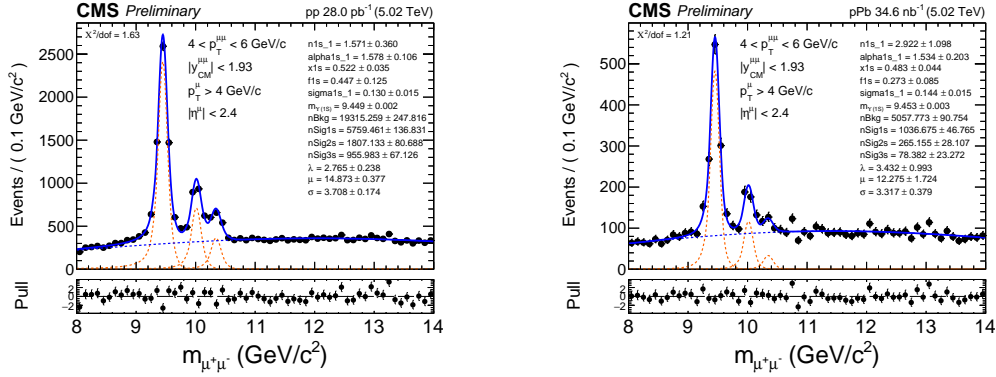


Figure 6.6: Nominal fits to the pp (left) and pPb (right) data for  $p_T \in [4 - 6]$  GeV/c.

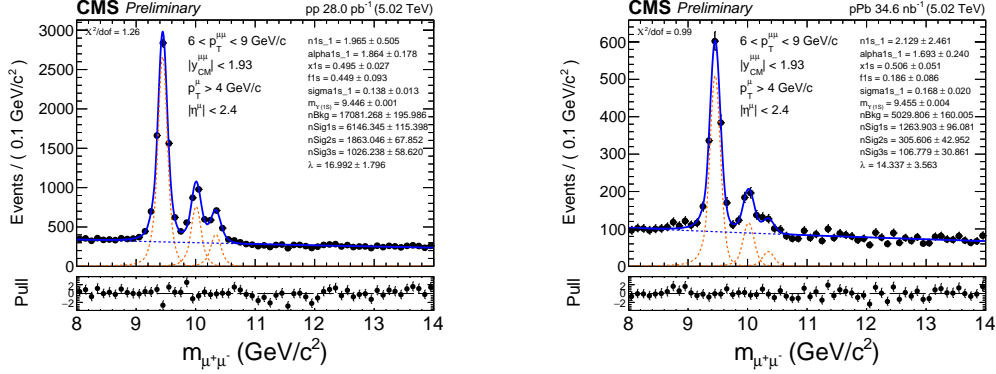


Figure 6.7: Nominal fits to the pp (left) and pPb (right) data for  $p_T \in [6 - 9]$  GeV/c.

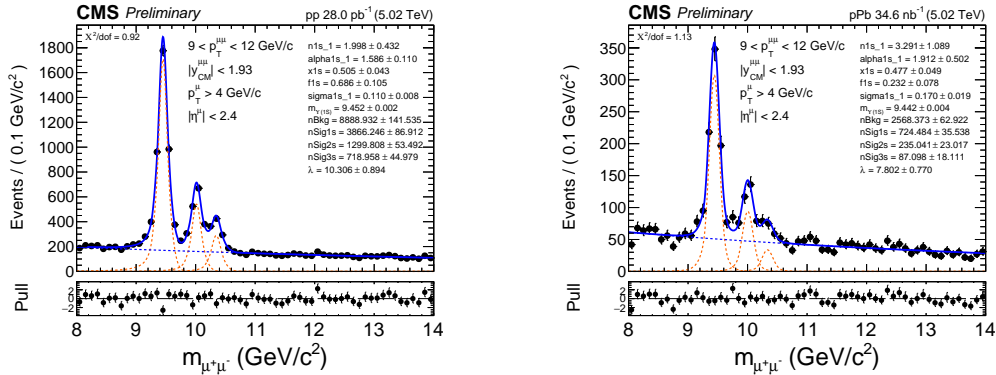


Figure 6.8: Nominal fits to the pp (left) and pPb (right) data for  $p_T \in [9 - 12]$  GeV/c.

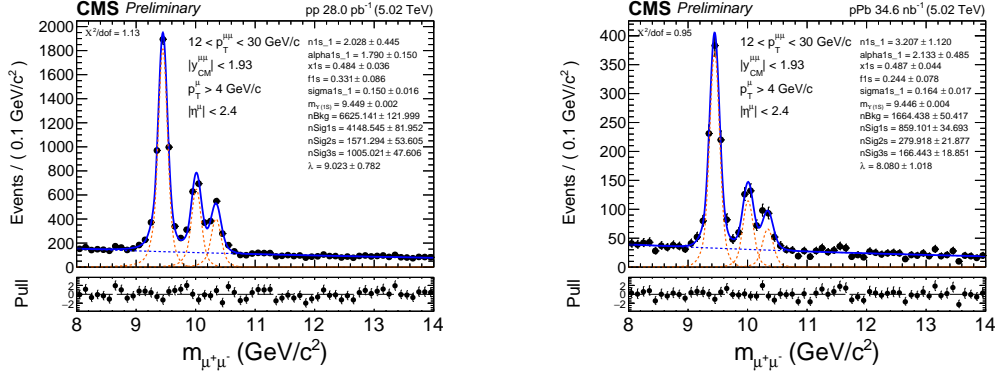


Figure 6.9: Nominal fits to the pp (left) and pPb (right) data for  $p_T \in [12 - 30]$  GeV/c.

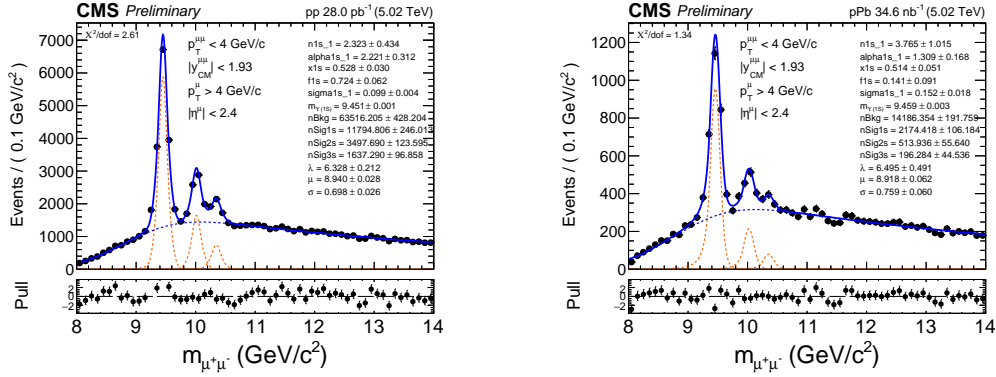


Figure 6.10: Nominal fits to the pp (left) and pPb (right) data for  $p_T \in [0 - 4]$  GeV/c.

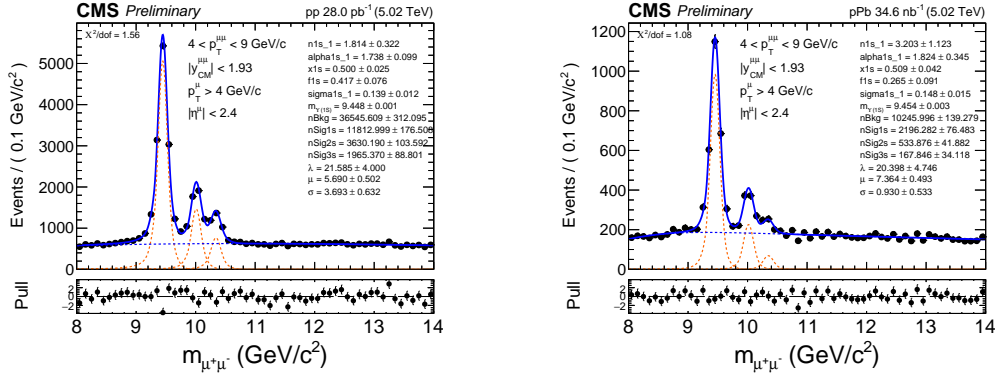


Figure 6.11: Nominal fits to the pp (left) and pPb (right) data for  $p_T \in [4 - 9]$  GeV/c.

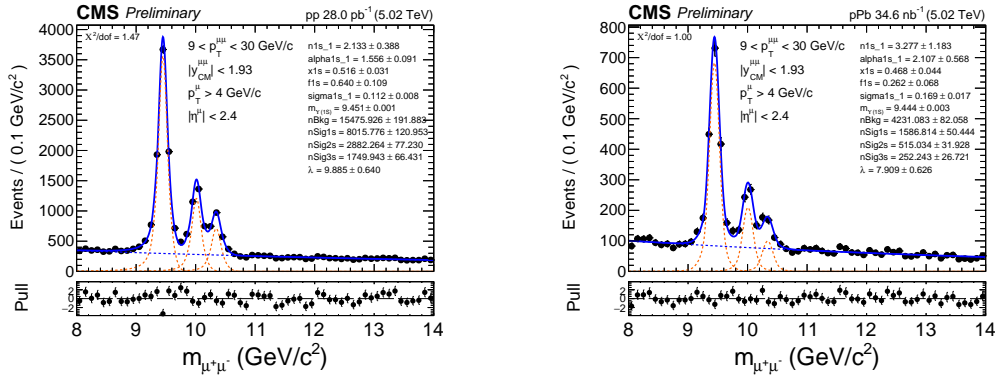


Figure 6.12: Nominal fits to the pp (left) and pPb (right) data for  $p_T \in [9 - 30]$  GeV/c.

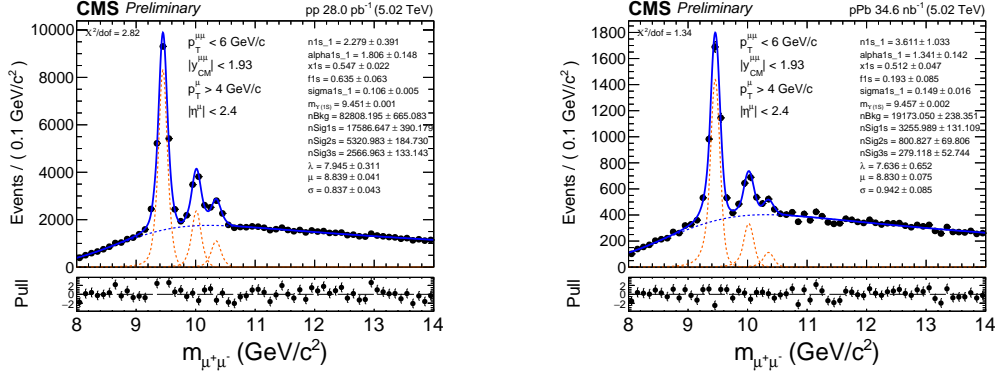


Figure 6.13: Nominal fits to the pp (left) and pPb (right) data for  $p_T \in [0 - 6]$  GeV/c.

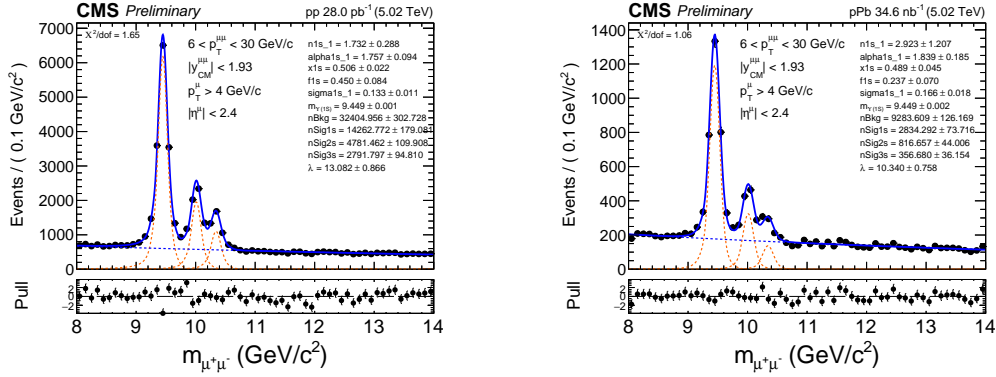


Figure 6.14: Nominal fits to the pp (left) and pPb (right) data for  $p_T \in [6 - 30]$  GeV/c.

### 6.4.3 Rapidity Binning

The figures below show the dimuon invariant mass distributions and the fitted PDFs in  $y_{CM}$  bins, where  $p_T$  is integrated in the range  $[0, 30]$  GeV/c. The yields extracted from these fits are used to determine the  $\Upsilon(nS)$  production cross sections and  $R_{pA}$  as a function of  $y_{CM}$ .

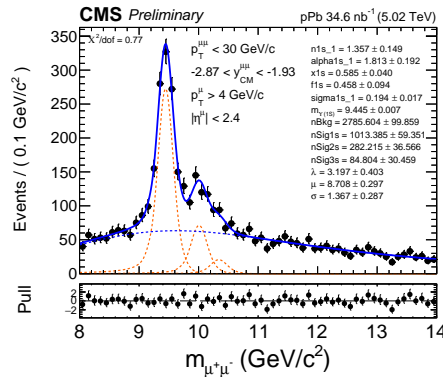


Figure 6.15: Nominal fit to pPb data for  $-2.87 < y_{CM} < -1.93$ .

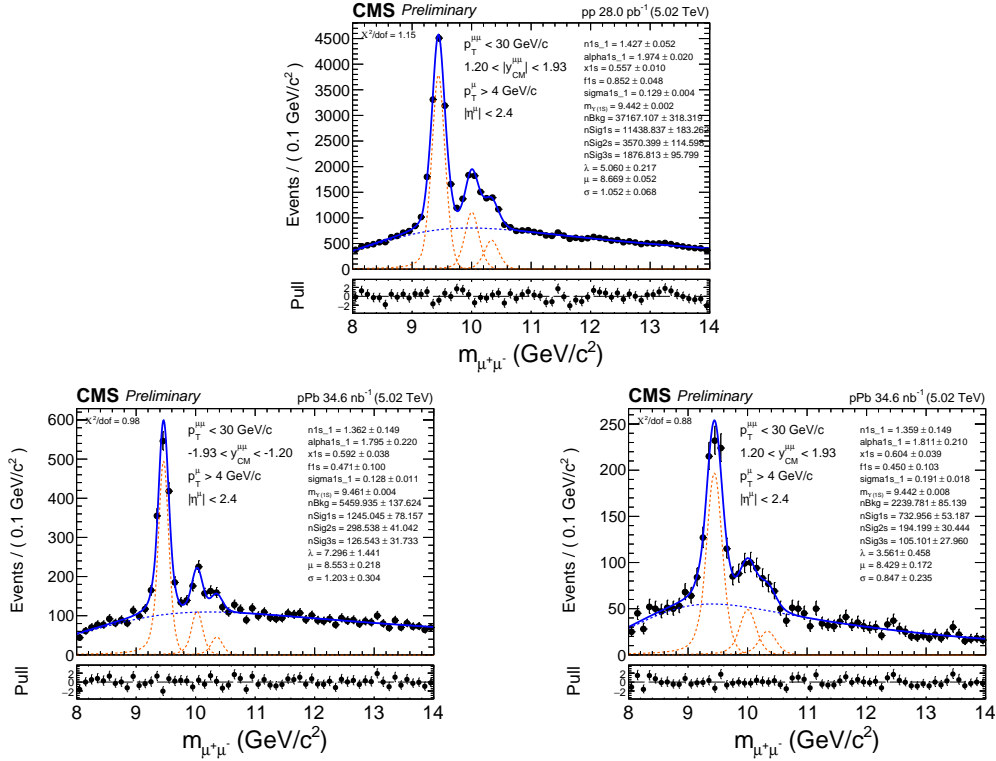


Figure 6.16: Nominal fits to the pp (top) and pPb (bottom) data for  $|y_{\text{CM}}| \in [1.2 - 1.93]$ .

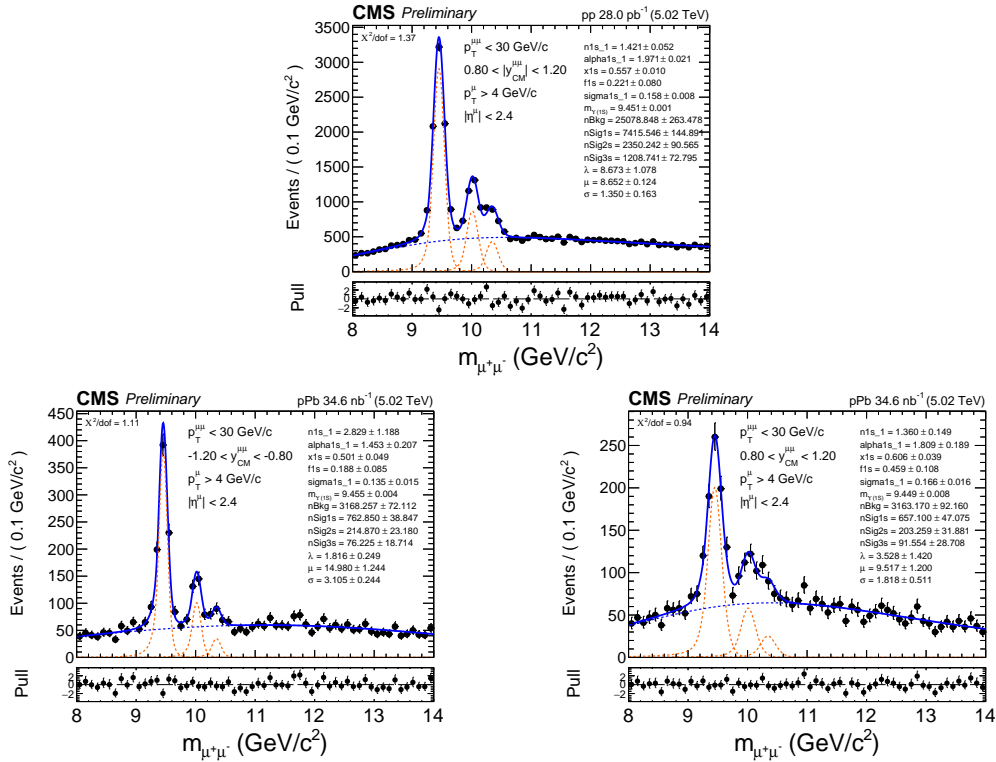


Figure 6.17: Nominal fits to the pp (top) and pPb (bottom) data for  $|y_{\text{CM}}| \in [0.8 - 1.2]$ .

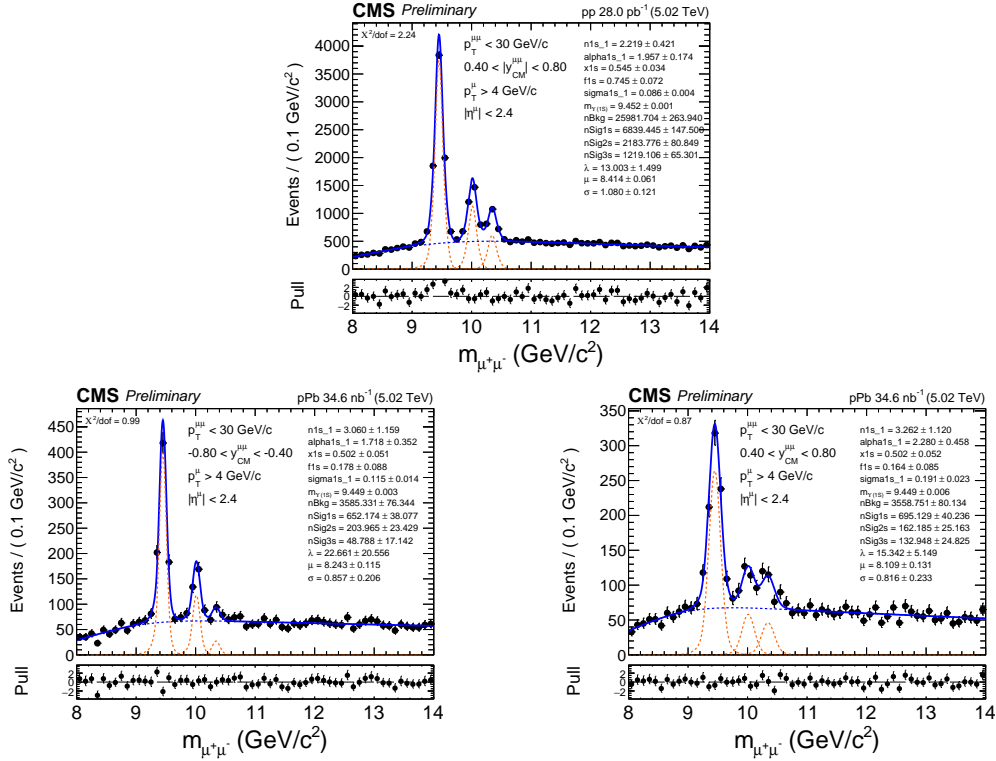


Figure 6.18: Nominal fits to the pp (top) and pPb (bottom) data for  $|y_{\text{CM}}| \in [0.4 - 0.8]$ .

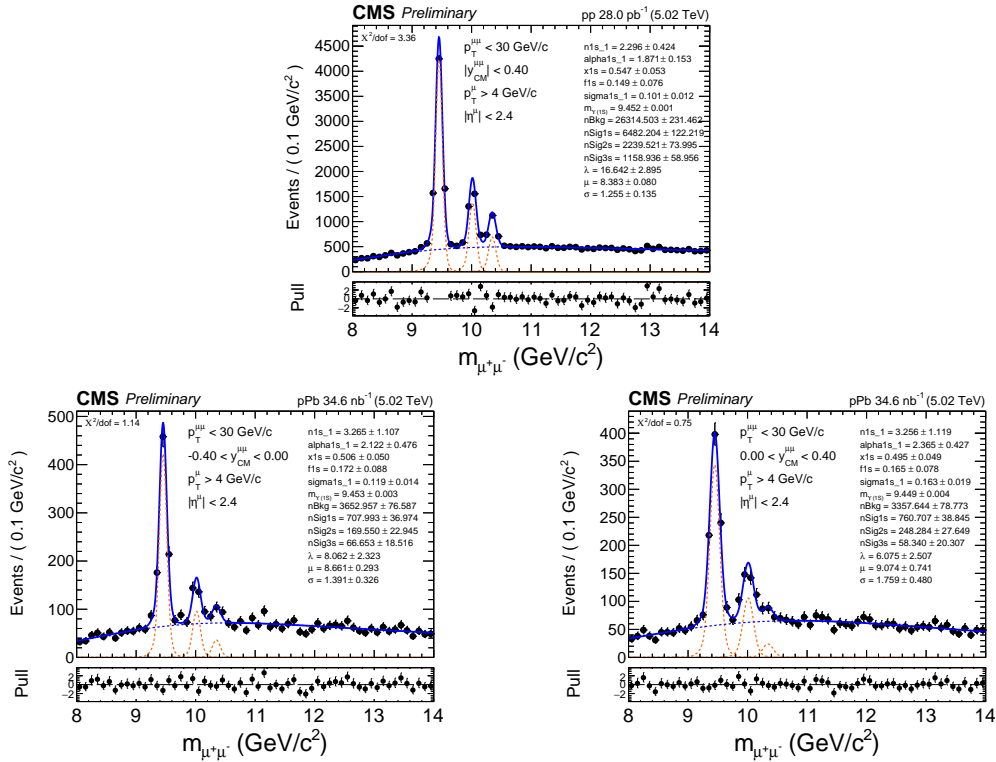


Figure 6.19: Nominal fits to the pp (top) and pPb (bottom) data for  $|y_{\text{CM}}| \in [0 - 0.4]$ .

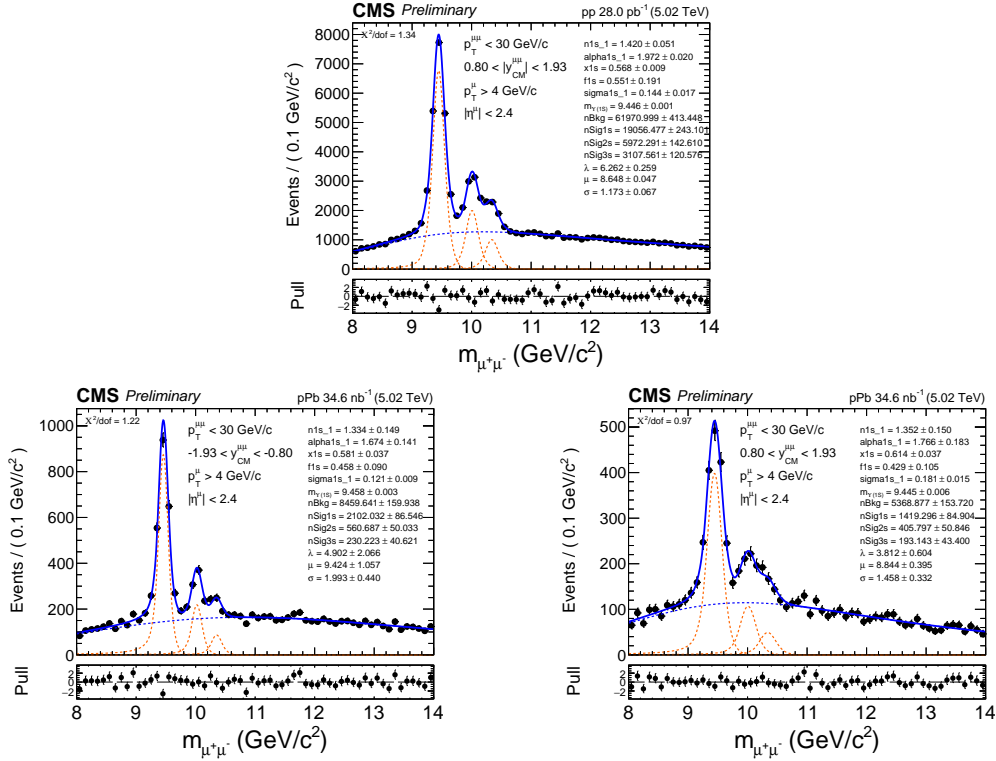


Figure 6.20: Nominal fits to the pp (top) and pPb (bottom) data for  $|y_{CM}| \in [0.8 - 1.93]$ .

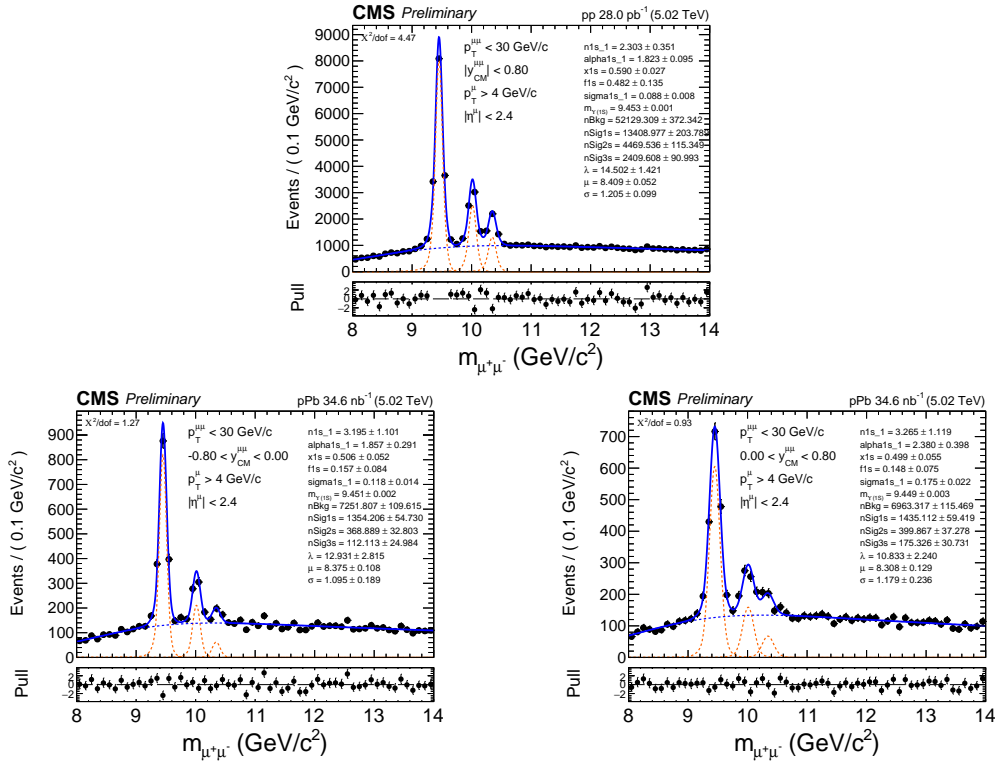


Figure 6.21: Nominal fits to the pp (top) and pPb (bottom) data for  $|y_{CM}| \in [0 - 0.8]$ .

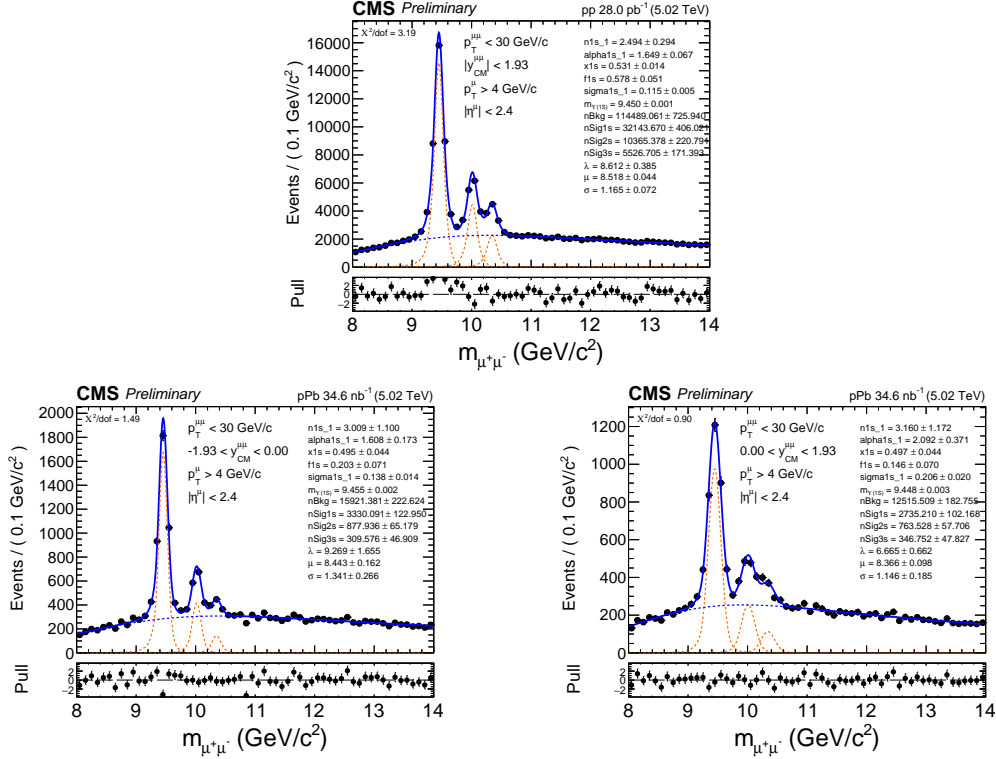


Figure 6.22: Nominal fits to the pp (top) and pPb (bottom) data for  $|y_{\text{CM}}| \in [0 - 1.93]$ .

#### 6.4.4 Additional Kinematic Binning

Beyond simply looking at the  $\Upsilon R_{\text{pA}}$  as functions of  $p_{\text{T}}$  and  $y_{\text{CM}}$ , we can glean additional insight into the effect of nuclear matter on  $\Upsilon$  production by studying the  $R_{\text{pA}}$  of high- vs low- $p_{\text{T}}$   $\Upsilon$  and in the forward vs backward rapidity regions. Since forward rapidity corresponds to the proton-going direction, the  $\Upsilon$  traveling towards backward rapidity are exposed to more nuclear matter from the ion. The  $p_{\text{T}}$  determines the length of time for which the  $\Upsilon$  is exposed to such an excess of nuclear matter in one direction versus the other or, equivalently, the statistical abundance of particles that may be comoving with the  $\Upsilon$ . The bin edges used to obtain the fitted invariant mass distributions below are as follows:

- Low  $p_{\text{T}}$ , backward:  $p_{\text{T}} \in [0, 6]$ ,  $y_{\text{CM}} \in [-1.93, 0.0]$ ,
- Low  $p_{\text{T}}$ , forward:  $p_{\text{T}} \in [0, 6]$ ,  $y_{\text{CM}} \in [0.0, 1.93]$ ,
- High  $p_{\text{T}}$ , backward:  $p_{\text{T}} \in [6, 30]$ ,  $y_{\text{CM}} \in [-1.93, 0.0]$ ,
- High  $p_{\text{T}}$ , forward:  $p_{\text{T}} \in [6, 30]$ ,  $y_{\text{CM}} \in [0.0, 1.93]$ .

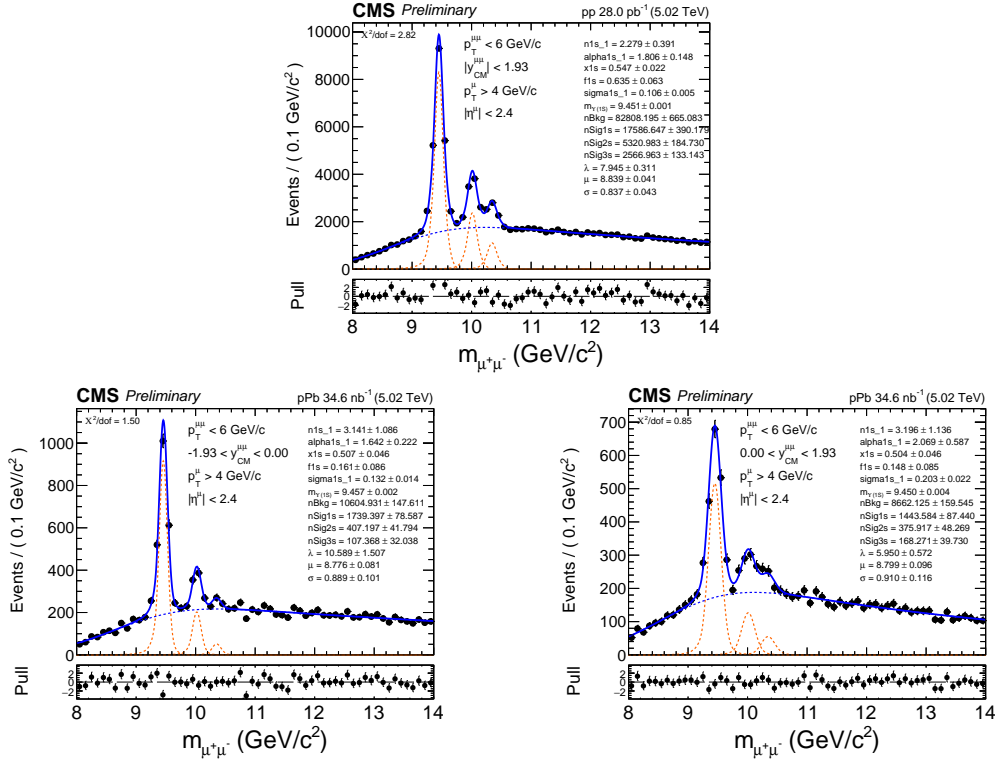


Figure 6.23: Nominal fits to the pp (top) and pPb (bottom) data for  $p_T \in [0, 6]$  GeV/c (low  $p_T$ ) and  $|y_{CM}| \in [0 - 1.93]$ .

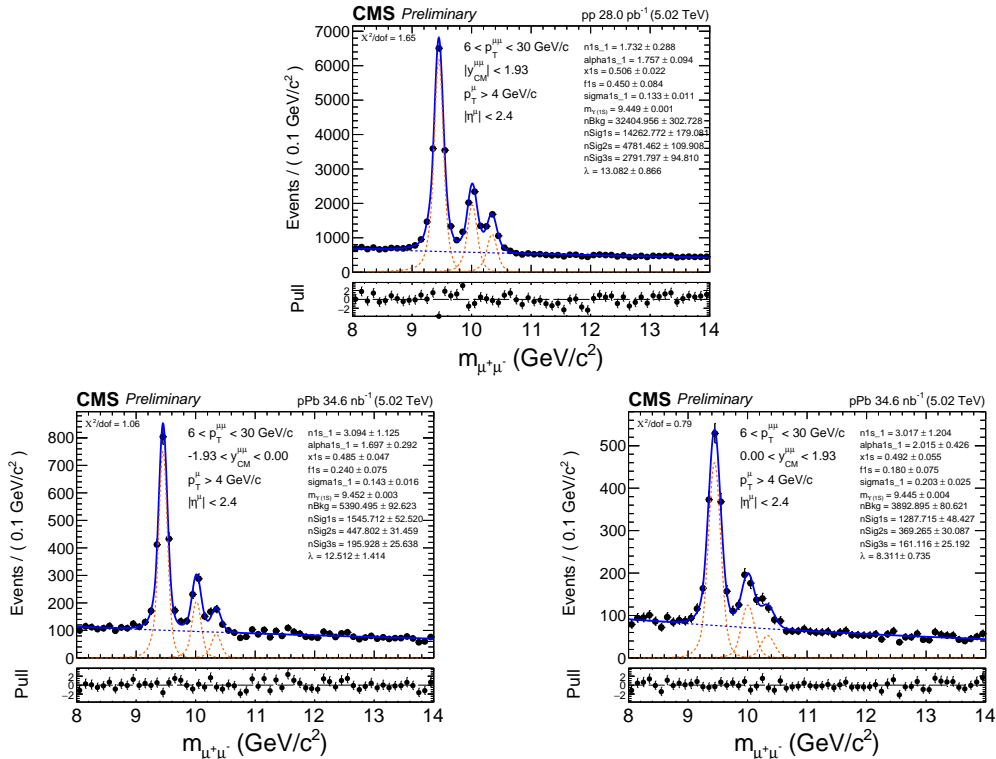


Figure 6.24: Nominal fits to the pp (top) and pPb (bottom) data for  $p_T \in [6, 30]$  GeV/c (high  $p_T$ ) and  $|y_{CM}| \in [0 - 1.93]$ .

## 6.4.5 Activity Binning

Finally, the figures below show the pPb dimuon invariant mass distributions along with the fitted PDFs measured in the backward (left) and forward (right) regions relative to the collision center of mass in bins of event activity variables  $E_T$  and  $N_{\text{tracks}}$ . The results from these fits are used to determine the  $R_{\text{FB}}$  presented in chapter 9.

$E_T$  Bins:

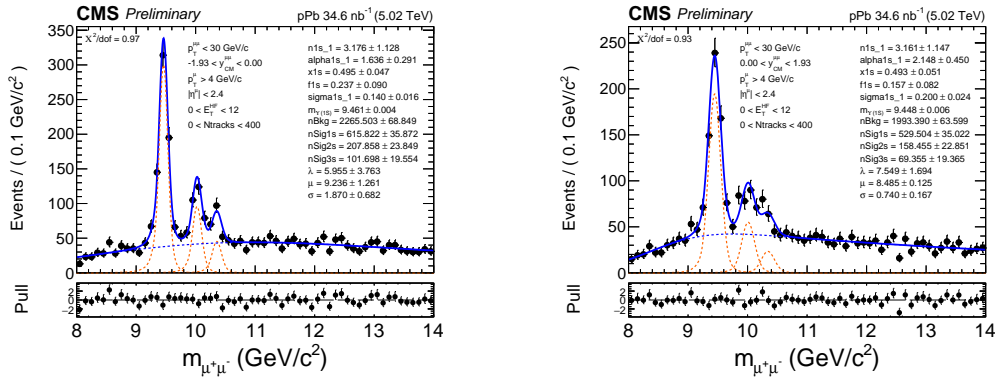


Figure 6.25: Nominal fits to the pPb data in backward (left) and forward (right)  $y_{\text{CM}}$  for  $E_T \in [0 - 12]$  GeV.

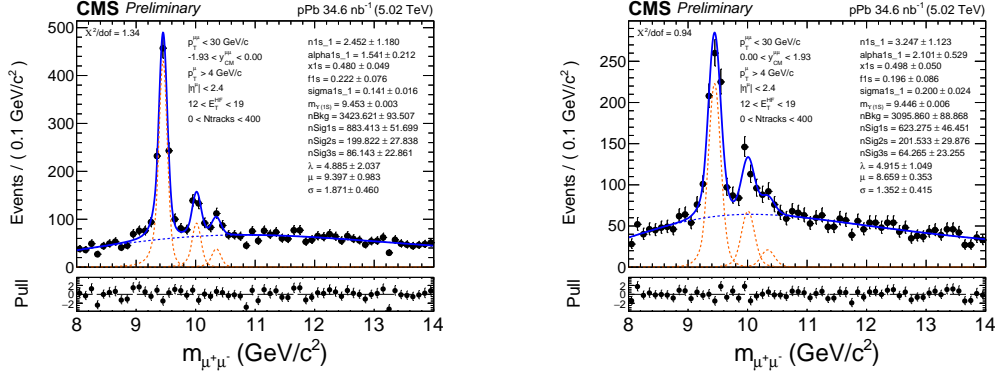


Figure 6.26: Nominal fits to the pPb data in backward (left) and forward (right)  $y_{\text{CM}}$  for  $E_T \in [12 - 19]$  GeV.

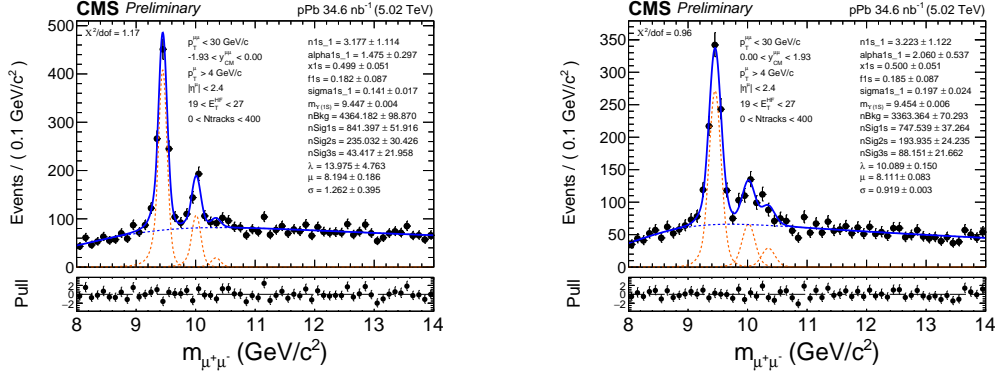


Figure 6.27: Nominal fits to the pPb data in backward (left) and forward (right)  $y_{CM}$  for  $E_T \in [19 - 27]$  GeV.

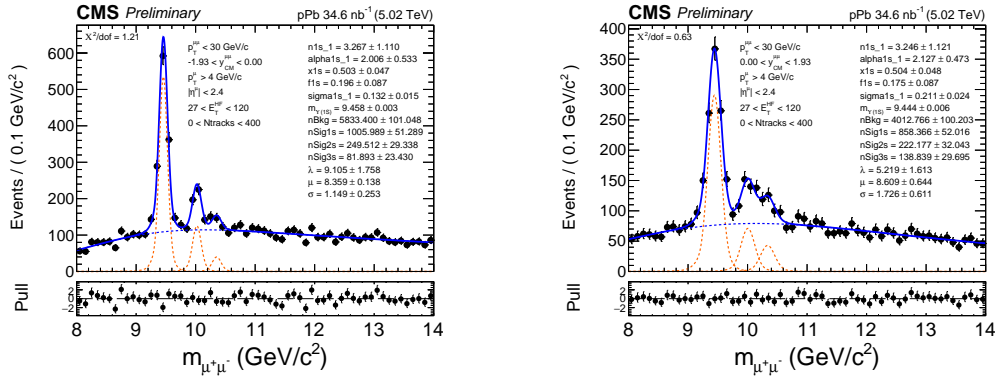


Figure 6.28: Nominal fits to the pPb data in backward (left) and forward (right)  $y_{CM}$  for  $E_T \in [27 - 120]$  GeV.

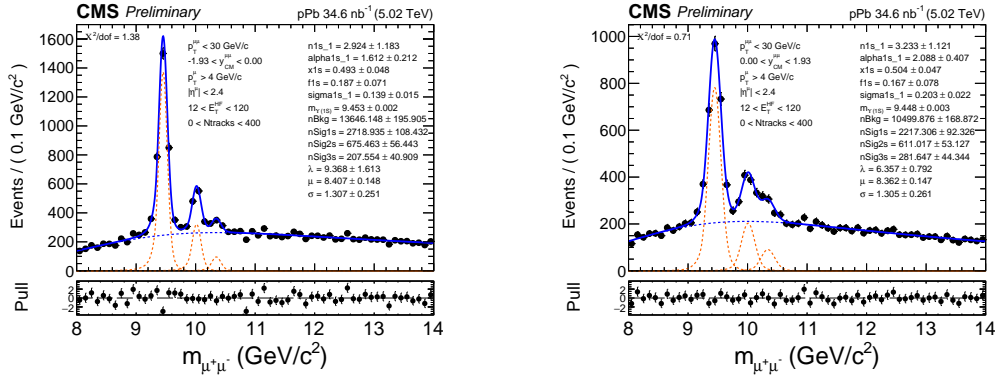


Figure 6.29: Nominal fits to the pPb data in backward (left) and forward (right)  $y_{CM}$  for  $E_T \in [12 - 120]$  GeV.

$N_{\text{tracks}}$  Bins:

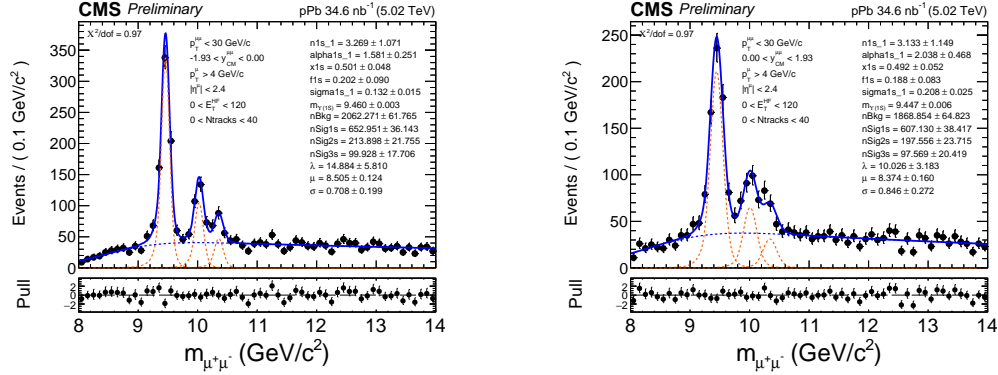


Figure 6.30: Nominal fits to the pPb data in backward (left) and forward (right)  $y_{\text{CM}}$  for  $N_{\text{tracks}} \in [0 - 40]$ .

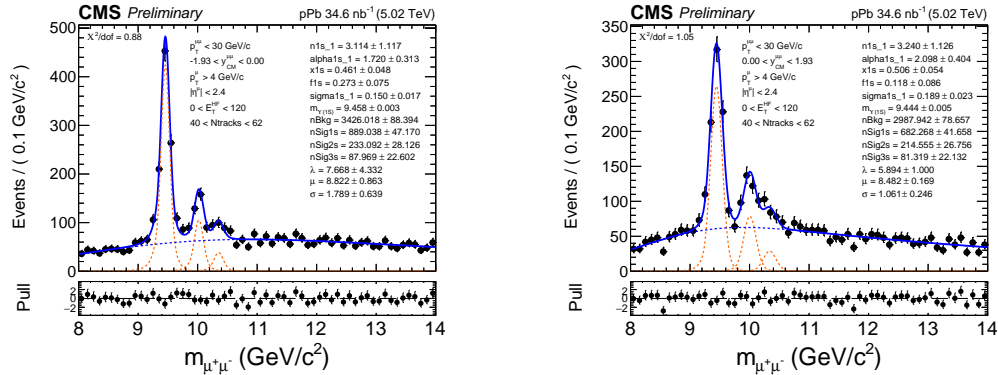


Figure 6.31: Nominal fits to the pPb data in backward (left) and forward (right)  $y_{\text{CM}}$  for  $N_{\text{tracks}} \in [40 - 62]$ .

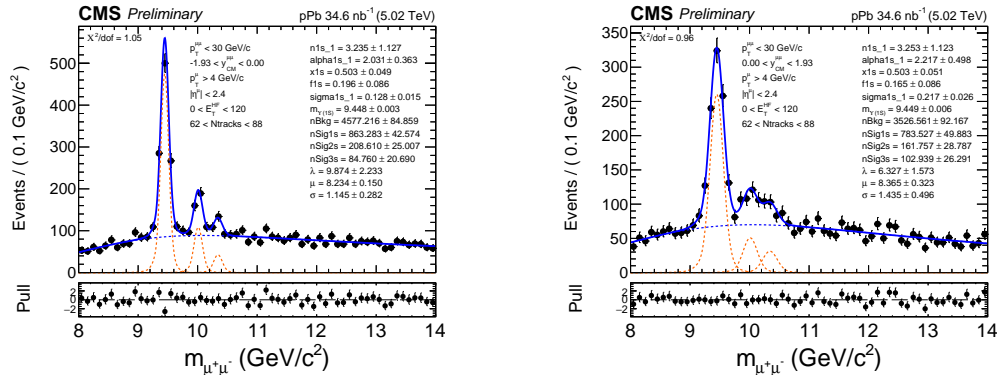


Figure 6.32: Nominal fits to the pPb data in backward (left) and forward (right)  $y_{\text{CM}}$  for  $N_{\text{tracks}} \in [62 - 88]$ .

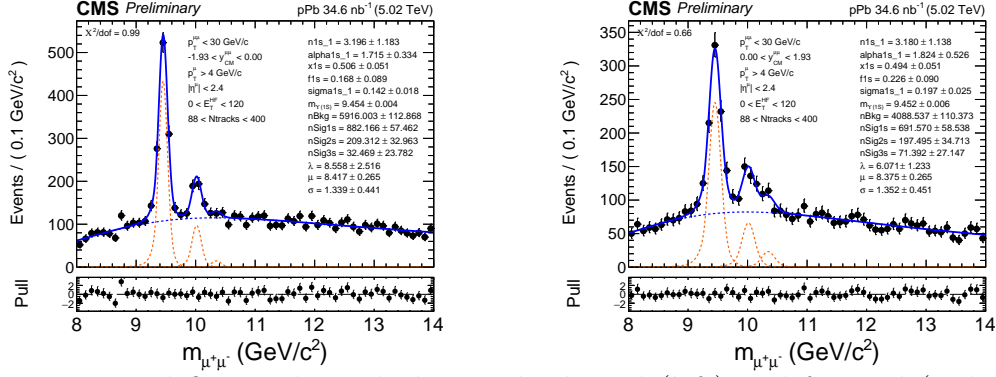


Figure 6.33: Nominal fits to the pPb data in backward (left) and forward (right)  $y_{CM}$  for  $N_{tracks} \in [88 - 400]$ .

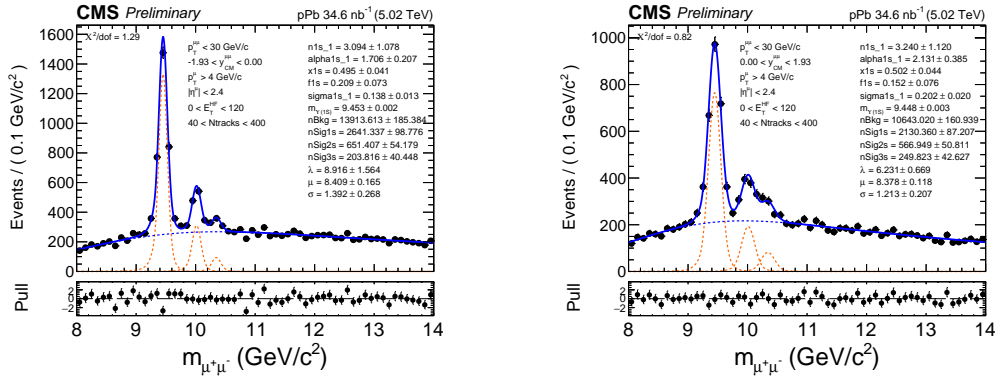


Figure 6.34: Nominal fits to the pPb data in backward (left) and forward (right)  $y_{CM}$  for  $N_{tracks} \in [40 - 400]$ .

# Chapter 7

## Transformation of Extracted Yields

Now that we have extracted the  $\Upsilon(nS)$  yields in the analysis bins of our choice, we need to transform these raw extracted yields into indicators of the phenomena we would like to test or study. In our case, these are the  $R_{pA}$  and  $R_{FB}$  of the  $\Upsilon(1S)$ ,  $\Upsilon(2S)$  and  $\Upsilon(3S)$  resonances, as we have been discussing. Since we boil down our massive data into a fully representative single number in each bin, our indicators are in fact summary statistics. These summary statistics can be directly compared across data pertaining to other particles, other energies, and even other experiments.

In order to transform the extracted yields into  $R_{pA}$  and  $R_{FB}$ , we require a thorough understanding of our detector and its limitations, as well as the data we have collected. The  $\Upsilon$  yields in pp and pPb collisions, as measured by our detector, must be scaled by the inverse of the respective integrated luminosities  $\mathcal{L}_{int}$  collected by the detector under the specified trigger conditions over the full data collection period. This allows us to anticipate the true production cross section of  $\Upsilon$  mesons in the collisions given the number of  $\Upsilon$  events we have been able to reconstruct using our detector and the period of time for which the detector collected data. Additionally, the final values of the summary statistics we present must be fully devoid of dependencies on or biases of the detector and measurement techniques. Two corrections to the extracted yields are identified as necessary, based on the geometri-

cal acceptance of the detector and the imperfect efficiency of data collection and selection techniques. The correction factors used to extrapolate the true production yield, given the measured yield and these quantifiable limitations, are colloquially referred to as acceptance  $a$  and efficiency  $\varepsilon$ , respectively. We devote this chapter to the exploration of these corrections.

No particle detector can provide full solid angle coverage around a collision point since, at the least, the beam pipe needs to traverse the detector. The geometric region for which a detector can provide coverage for the signature of a given physics process (such as a particle decay) is known as the acceptance region of the detector for that process. The most relevant components of the CMS detector for the analysis presented here, the muon detectors, extend to  $|y_{\text{CM}}| < 2.4$  in pseudorapidity. The separation between the first detector component particles produced during collision will encounter (the pixel tracker) and the beam pipe is  $\sim 4$  cm in the barrel region. Thus, muons produced during collisions will only be detected and reconstructed if they have sufficient transverse momentum to reach these detectors, accounting for the curvature of their paths due to the strong magnetic field of the superconducting solenoid.

Even when in acceptance, the desired signature may be missed by the detector, leading to a type II error. Various sources of inefficiency can contribute to the occurrence of such errors, including the dead time of detector components, malfunctioning of electronics, degradation of detector performance over time etc. In this analysis, efficiency is defined as the probability of a muon pair within the acceptance region to be reconstructed by the detector as such. The muon pair and its constituent muons must satisfy all the requirements outlined in section 5.4.2. Additionally, the collision event must fire the dedicated double muon trigger to initiate the reconstruction process.

Since studying such detector limitations using the collected data is fundamentally impossible, Monte Carlo Simulations of  $\Upsilon(1S)$ ,  $\Upsilon(2S)$ , and  $\Upsilon(3S)$  production and reconstruction in pp and pPb collisions are used to estimate the corresponding acceptance and efficiency correction factors. Details of the generation and processing of the MC samples, which each

contain roughly two million simulated collision events, are provided in section 5.3.3. However, since MC simulations are themselves an imperfect approximation to real collision data, data collected from real collisions are compared to simulations and used to improve them whenever possible. One example of such an adjustment is explained in the following section.

## 7.1 Reweighting the Kinematic Distributions in Simulated Data

The kinematic distributions in the PYTHIA8.209 MC simulations are similar to but not completely consistent with those in real pp and pPb data. We find that the discrepancy, while not tremendous, is sufficient to warrant reweighting the dimuon  $p_T$  distribution in MC events to match the distribution observed in data. Figures 7.1 and 7.2 compare the  $p_T$  distributions of reconstructed dimuons in the  $\Upsilon(1S)$  mass range in data and MC in the top panels for pp and pPb, respectively. Each distribution is normalized by its integral. The binning is kept consistent with the  $p_T$  binning used for analysis, except in the low- $p_T$  interval  $0 - 4 \text{ GeV}/c$ , where additional bins are introduced to capture more granular behavior. In the bottom panels, the data/MC ratio of the normalized  $p_T$  distributions are shown, along with fitted instances of the following PDF:

$$y = \frac{A + Bx + Cx^2}{(x - D)^3} \quad (7.1)$$

The form of the PDF is chosen empirically to describe the features seen in the ratio. Three fits are shown, one nominal and two variations that are used to estimate the systematic uncertainty in the results introduced by the choice of the PDF. We will discuss this further in chapter 8. The green curve represents the nominal fit and is used to reweight the  $p_T$  of dimuons in the  $\Upsilon(1S)$  MC when determining the acceptance and efficiency corrections. Similar fits to the  $\Upsilon(2S)$  and  $\Upsilon(3S)$  Data/MC ratios are used to reweight the respective

MC dimuon  $p_T$  spectra. The rapidity distributions in MC are consistent with those in data, requiring no additional weighting versus rapidity.

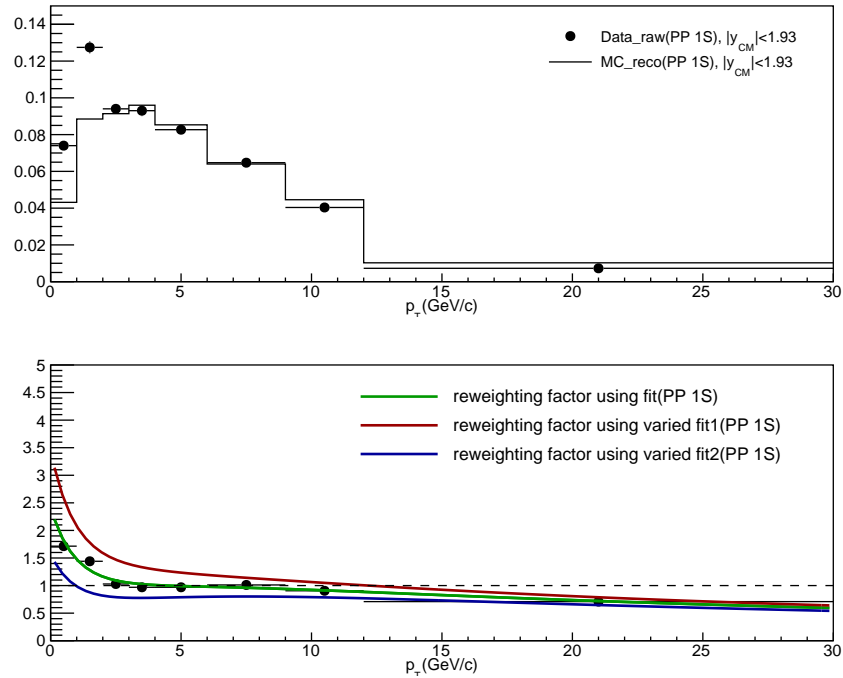


Figure 7.1: The measured  $p_T$  distributions of muon pairs in the  $\Upsilon(1S)$  mass range in data and MC (top) and their ratio (bottom) in pp collisions.

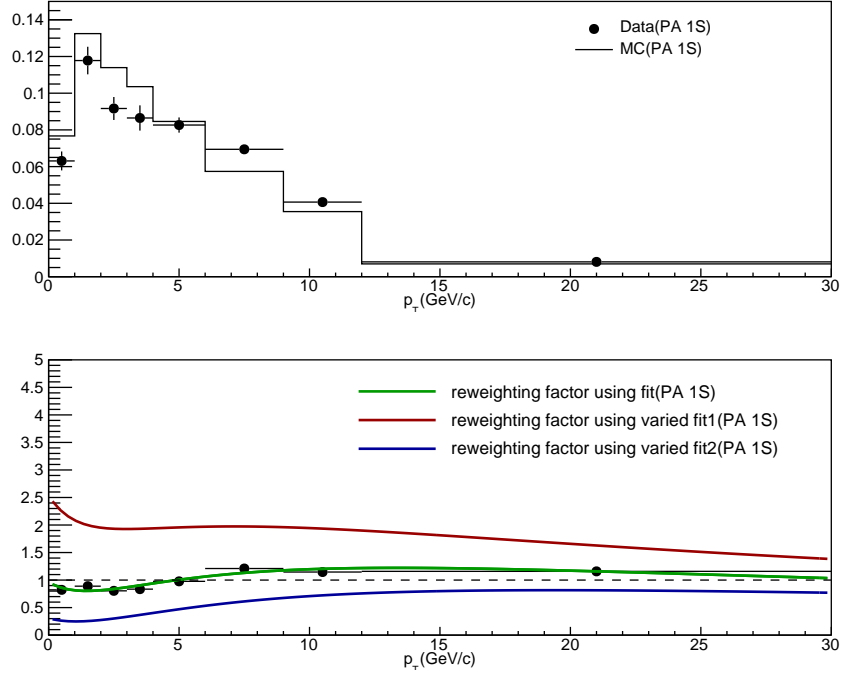


Figure 7.2: The measured  $p_T$  distributions of muon pairs in the  $\Upsilon(1S)$  mass range in data and MC (top) and their ratio (bottom) in pPb collisions.

## 7.2 Acceptance

In this analysis, muon pairs anticipated to be  $\Upsilon$  candidates are considered to be inside the acceptance region if the kinematic variables of both daughter muons are in the ranges:

$$p_{T\text{lab}}^\mu > 4 \text{ GeV}/c$$

$$-2.4 < \eta_{\text{lab}}^\mu < 2.4$$

The bin-wise acceptance corrections for  $\Upsilon(nS)$  in  $|y_{\text{CM}}| < 1.93$  and  $p_T > 0 \text{ GeV}/c$  are computed using  $p_T$ -reweighted generator-level MC, as explained in section 5.3.3. The acceptance correction factor is defined as the fraction of generated dimuons in the kinematic range of the analysis bin in question, whose daughter muons both fall within the acceptance region:

$$a(p_T, y_{\text{CM}}) = \frac{N_{\text{GEN}}(p_T, y_{\text{CM}}; |\eta^\mu| < 2.4, p_T^\mu > 4 \text{ GeV}/c)}{N_{\text{GEN}}(p_T, y_{\text{CM}})} \quad (7.2)$$

The reciprocal of the acceptance value is used as a multiplicative factor to correct the yields when computing the  $R_{pA}$  and  $R_{FB}$ . In this way we compensate for the fraction of  $\Upsilon$  mesons that were produced during collisions but could not be detected by the detector due to its limited spatial extent.

The nominal acceptance correction factors, as well as two variations based on variations of the MC  $p_T$ -reweighting function, are shown as a function of the analysis variables for  $\Upsilon(nS)$  in figures 7.3 to 7.6. In figures 7.7 to 7.12, the acceptance and its variations are shown in the backward and forward rapidity regions for low- and high- $p_T$   $\Upsilon(nS)$ . These corrections can be used to study the  $R_{pA}$  differentially versus  $\Upsilon$  kinematics.

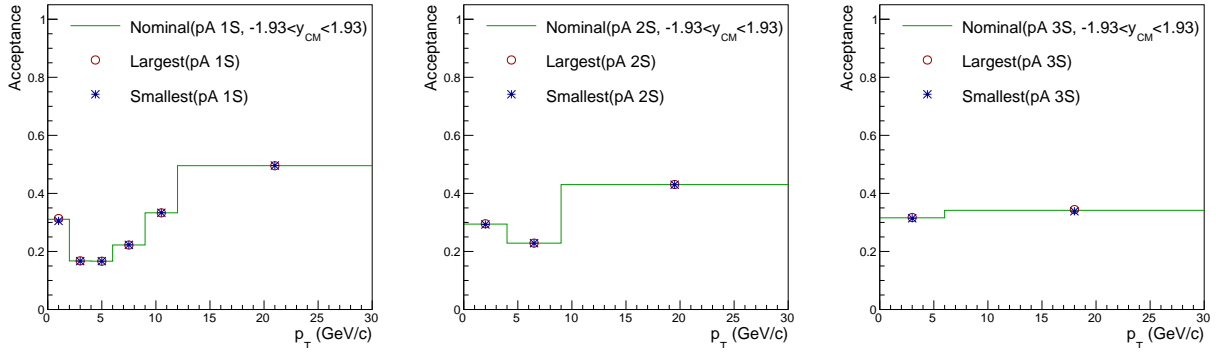


Figure 7.3: Nominal and systematically varied acceptance correction factors as functions of  $p_T$  for  $\Upsilon(1S)$ ,  $\Upsilon(2S)$  and  $\Upsilon(3S)$  in pPb collisions.

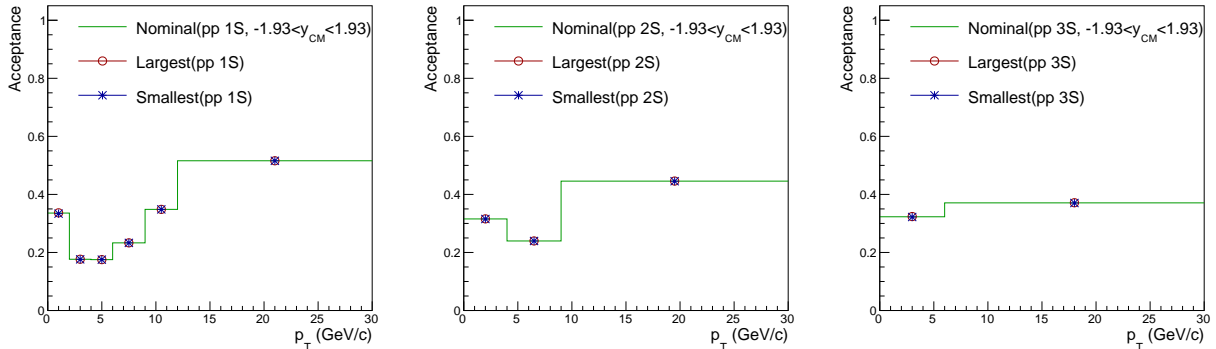


Figure 7.4: Nominal and systematically varied acceptance correction factors as functions of  $p_T$  for  $\Upsilon(1S)$ ,  $\Upsilon(2S)$  and  $\Upsilon(3S)$  in pp collisions.

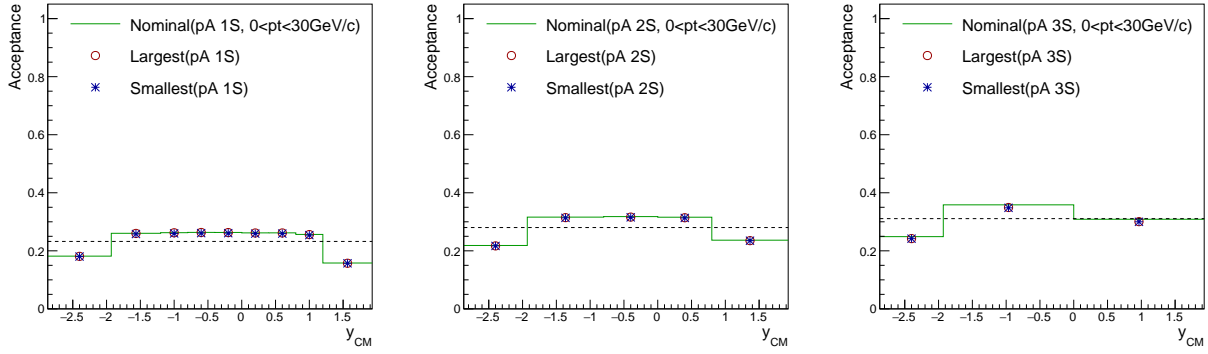


Figure 7.5: Nominal and systematically varied acceptance correction factors as functions of  $y_{CM}$  for  $\Upsilon(1S)$ ,  $\Upsilon(2S)$  and  $\Upsilon(3S)$  in pPb collisions.

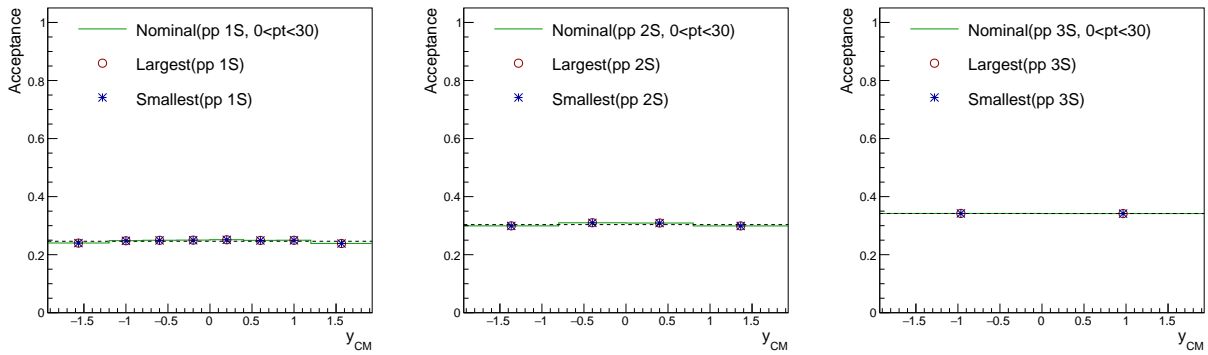


Figure 7.6: Nominal and systematically varied acceptance correction factors as functions of  $|y_{CM}|$  for  $\Upsilon(1S)$ ,  $\Upsilon(2S)$  and  $\Upsilon(3S)$  in pp collisions.

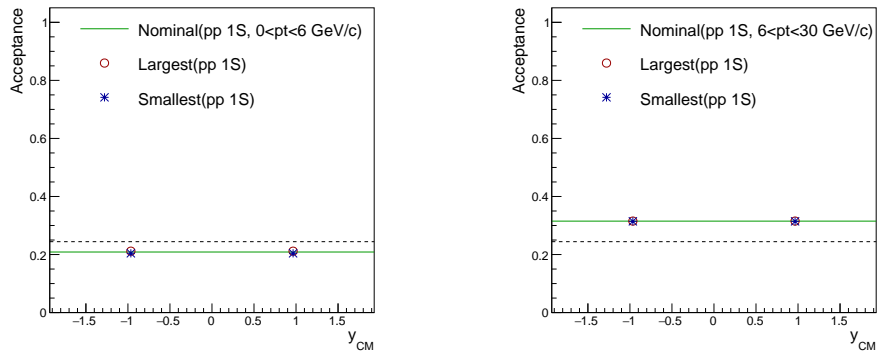


Figure 7.7: Nominal and systematically varied acceptance correction factors in backward and forward regions for low- $p_T$  (left) and high- $p_T$  (right)  $\Upsilon(1S)$  in pp collisions.

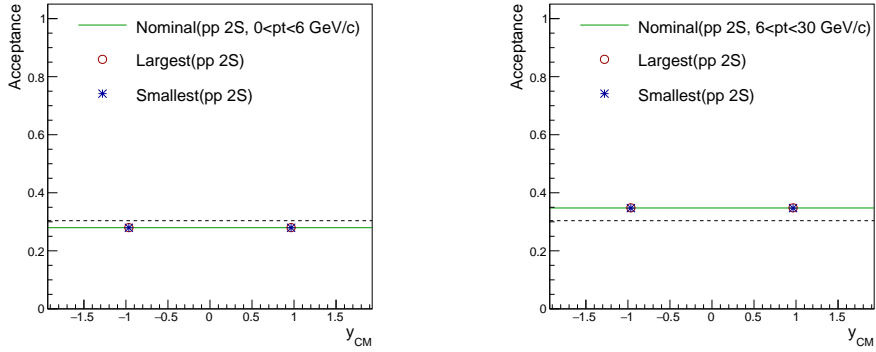


Figure 7.8: Nominal and systematically varied acceptance correction factors in backward and forward regions for low- $p_T$  (left) and high- $p_T$  (right)  $\Upsilon(2S)$  in pp collisions.

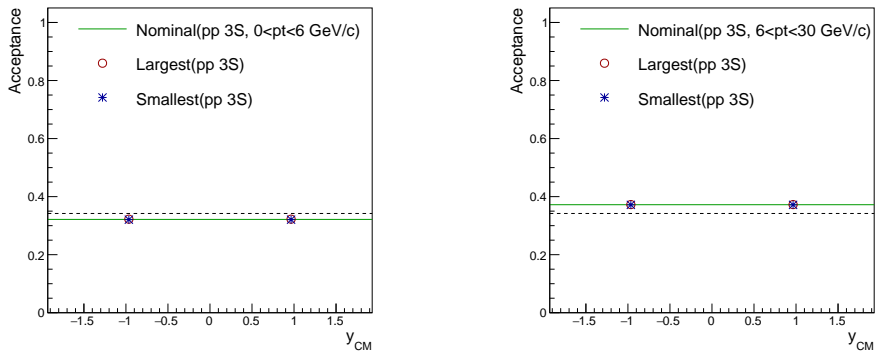


Figure 7.9: Nominal and systematically varied acceptance correction factors in backward and forward regions for low- $p_T$  (left) and high- $p_T$  (right)  $\Upsilon(3S)$  in pp collisions.

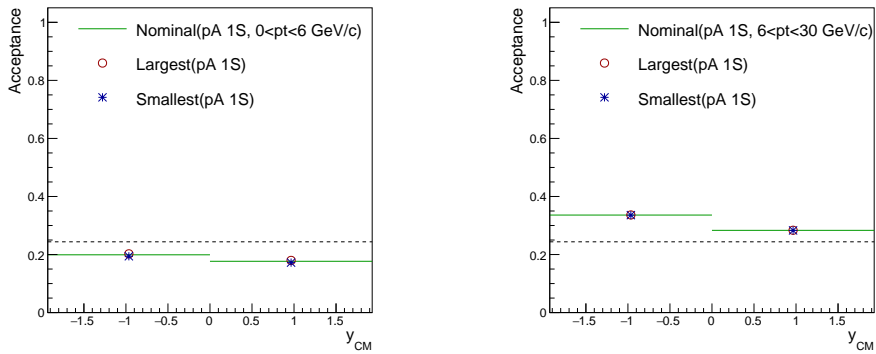


Figure 7.10: Nominal and systematically varied acceptance correction factors in backward and forward regions for low- $p_T$  (left) and high- $p_T$  (right)  $\Upsilon(1S)$  in pPb collisions.

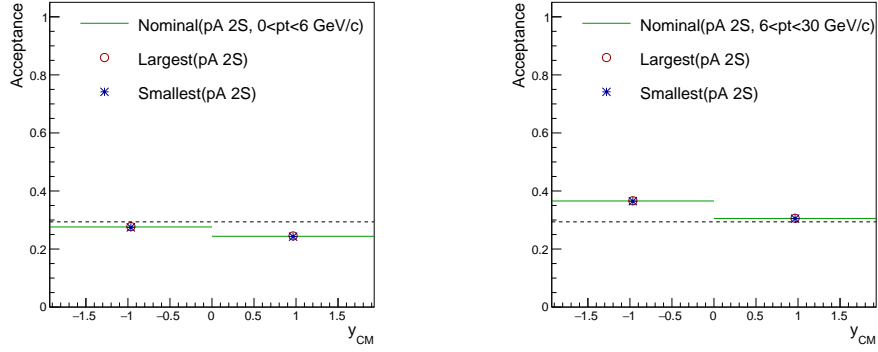


Figure 7.11: Nominal and systematically varied acceptance correction factors in backward and forward regions for low- $p_T$  (left) and high- $p_T$  (right)  $\Upsilon(2S)$  in pPb collisions.

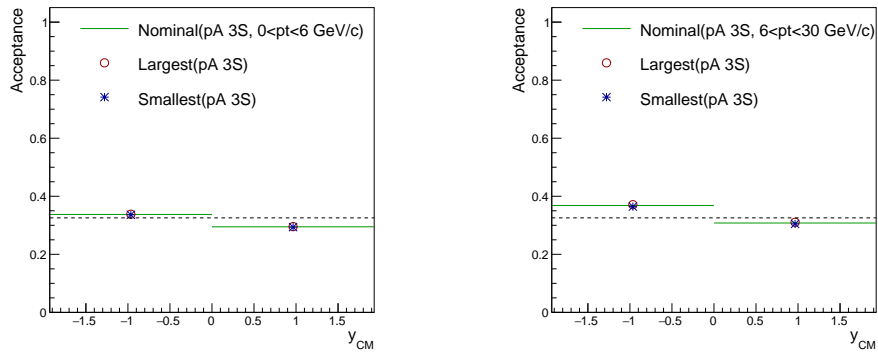


Figure 7.12: Nominal and systematically varied acceptance correction factors in backward and forward regions for low- $p_T$  (left) and high- $p_T$  (right)  $\Upsilon(3S)$  in pPb collisions.

### 7.3 Efficiency

We determine the required correction to the extracted yields due to detector inefficiencies in the following way. Once  $p_T$ -reweighted, the fully-reconstructed MC (see section 5.3.3) is first used to compute the characteristic dimuon reconstruction efficiency as the fraction of generated opposite-sign muon pairs that are successfully identified and reconstructed by the detector and offline algorithms. A secondary correction is then applied to the dimuon efficiency to account for discrepancies between simulated and real single-muon reconstruction. Inefficiencies in single muon reconstruction can be estimated using a method known as *tag-and-probe* (T&P), where a potential dimuon resonance is tagged using one of its daughter muons, while the other is used to probe the efficiency of various steps involved in muon reconstruction. The secondary correction is applied in the form of a data-to-MC ratio of combined single muon reconstruction efficiencies.

The characteristic dimuon reconstruction efficiency,  $\varepsilon_{\text{MC}}[\Upsilon(\text{nS})]$ , has three components: kinematic acceptance, triggering, and muon identification. To begin, the generated muon pairs must be in the relevant  $\Upsilon(\text{nS})$  mass range and the individual muons must be in acceptance, conditions that all reconstructed muon pairs must also satisfy by construction. Additionally, the reconstructed muon pairs must satisfy the relevant trigger condition: `HLT_PAL1DoubleMu0Open_v1` for pPb and `HLT_HIL1DoubleMu0_v1` for pp, as noted in section 5.4.1. This ensures that the muon pair in question would have triggered the targeted dataset even if the event was not otherwise collected. Further, the daughter muons from the reconstructed pair are required to each pass the muon identification cuts, as described in section 5.4.2. Thus, to be considered successfully reconstructed, the ‘accepted’ muon pairs in the fully-reconstructed MC must belong to an event which fired the double muon trigger, be capable of firing the trigger themselves, and decay to single muons that are reconstructed in the tracker and muon detectors as per muon-identification specifications. Succinctly,

$$\varepsilon_{\text{MC}}(p_T, y_{\text{CM}}) = \frac{N_{\text{RECO}}^{\mu^+\mu^-}(p_T, y_{\text{CM}}; \text{acc}, \text{muID}, \text{trigger})}{N_{\text{GEN}}^{\mu^+\mu^-}(p_T, y_{\text{CM}}; \text{acc})} \quad (7.3)$$

The denominator is simply the number of generated muon pairs with single muons in acceptance, i.e. the numerator of the acceptance correction factor in a given  $(p_T, y_{CM})$  bin. The numerator represents the number of reconstructed dimuons within the mass range of a given  $\Upsilon$  state ( $M_{\Upsilon(1S)} = [8.0, 10.0]$  GeV/ $c^2$ ,  $M_{\Upsilon(2S)} = [8.6, 10.6]$  GeV/ $c^2$ , and  $M_{\Upsilon(3S)} = [8.9, 10.9]$  GeV/ $c^2$ ), passing the requirements discussed above. Thus, the criteria required of reconstructed MC  $\Upsilon$  candidate events are identical to those required of events in data during offline reconstruction, with the exception of the mass selection which is not applied to data prior to fitting.

The dimuon reconstruction efficiency based on MC is then corrected using the *tag-and-probe* method. This procedure yields the data-aware efficiency of single muon reconstruction in a given dimuon- $p_T$  range. The initial development and implementation of T&P is documented in reference [153], although the tools discussed there are now outdated. A detailed discussion of muon detection, tracking and identification performance studies at CMS, including the use of T&P, is provided in reference [19].

In both data and MC simulations, muons identified using strict criteria on muon identification, trigger matching and kinematic selections are labeled as tag muons. Tag muons are then used to reconstruct the relatively clean  $J/\psi$  resonance by pairing with probe muons, which are selected using loose requirements, so as not to bias the measured efficiencies. The probe muons are then tested against "passing criteria" corresponding to efficiencies of various parts of the muon reconstruction process. The fraction of muon pairs (i.e.  $J/\psi$  candidates) passing such criteria over all tagged muon pairs embodies the T&P efficiency. Efficiencies obtained in this way are compared between data and simulations. If sufficiently different, a correction given by the ratio of these efficiencies must be applied to any single- or double-muon efficiency determined using MC only.

The T&P efficiency for four selection criteria are investigated in pp data [154]: trigger, muon identification, inner tracking and stand-alone muon reconstruction. Corrections are found to only be needed for the trigger and the inner tracking efficiencies for single muons.

Similarly, two selection criteria are studied in pPb data [155]: inner tracking and the combined trigger and muon ID selections (since these latter two share the same probe criteria). Corrections are only required for the combined criteria. Even when the data-to-simulation discrepancy is not sufficiently large, differences may lead to systematic shifts in estimated MC-based dimuon efficiency. Thus, single-muon efficiencies for which T&P corrections are not required are still propagated to the systematic uncertainty in results. More details of systematic uncertainty estimation can be found in chapter 8.

The data-to-simulation ratios of single-muon efficiencies, called the scaling factors  $SF(p_T^\mu, \eta_{\text{lab}}^\mu)$ , are calculated in several  $p_T^\mu$  and  $\eta_{\text{lab}}^\mu$  bins and fitted using empirical functions. These parametrized SFs are used to correct the dimuon efficiencies  $\varepsilon_{\text{MC}}$  obtained above using a muon-by-muon reweighting of the number of reconstructed muon pairs. Finally, the corrected overall efficiency correction factor reads:

$$\varepsilon_{\text{T\&P corrected}}(p_T, y_{\text{CM}}) = \varepsilon_{\text{MC}}(p_T, y_{\text{CM}}) \times SF(p_T^{\mu^+}, \eta_{\text{lab}}^{\mu^+}) \times SF(p_T^{\mu^-}, \eta_{\text{lab}}^{\mu^-}) \quad (7.4)$$

where

$$SF(p_T^{\mu^\pm}, \eta_{\text{lab}}^{\mu^\pm}) = \frac{\varepsilon(\mu^\pm)_{\text{T\&P}}^{\text{Data}}}{\varepsilon(\mu^\pm)_{\text{T\&P}}^{\text{MC}}} \quad (7.5)$$

In this analysis, we follow the procedure for applying the T&P corrections and determining systematic uncertainty contribution approved by the muon POG for analyses with 2013 pPb data and 2015 pp data. The settings used in the T&P studies for pp and pPb are slightly different, partly because the muon ID requirements are set differently for the two data sets as explained in section 5.4.2. Thus, we use the T&P scale factors obtained in [154] for correcting  $\varepsilon_{\text{MC}}(p_T, y_{\text{CM}})$  in pp and scale factors determined in [155] for correcting  $\varepsilon_{\text{MC}}(p_T, y_{\text{CM}})$  in pPb.

We now present the *tag-and-probe* corrected dimuon reconstruction efficiencies as functions of kinematic variables. The  $p_T$  (left) and  $y_{\text{CM}}$  (right) dependence of  $\Upsilon(1S)$  reconstruction efficiency in pp (top) and pPb (bottom) are shown in figure 7.13. The dashed horizontal lines indicate the integrated efficiency in the given region. The corresponding plots for  $\Upsilon(2S)$

and  $\Upsilon(3S)$  are shown in figures 7.14 and 7.15, respectively.

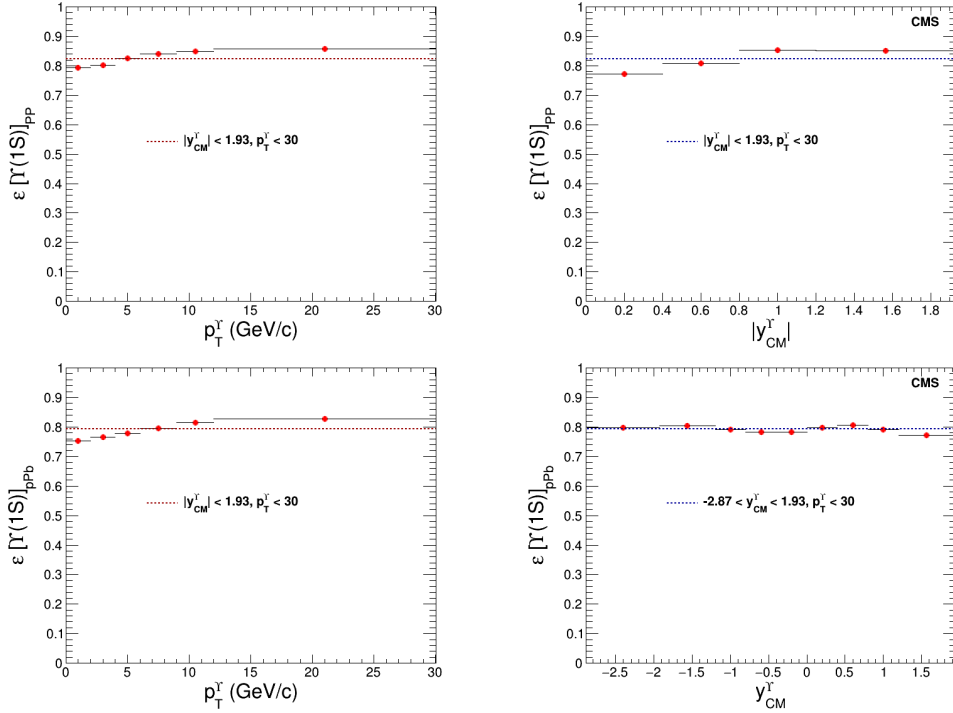


Figure 7.13: T&P corrected reconstruction efficiency for  $\Upsilon(1S)$  as functions of  $p_T$  (left) and  $y_{CM}$  (right) in pp (top) and pPb (bottom) collisions.

Next, we explore the efficiency correction factors for the  $R_{pA}$  in the forward and backward rapidity regions for low and high  $p_T$   $\Upsilon(nS)$ . For each state, efficiency is studied for  $(p_T, y_{CM}) \in [0, 6, 30] \text{ GeV}/c \otimes [-1.93, 0, 1.93]$ . Since the positive and negative rapidity regions are identical for pp collisions, we use  $|y_{CM}| < 1.93$  when determining both the low- and high- $p_T$  efficiencies and use these for correcting the pp yield for both the positive and negative regions. To correct the  $R_{FB}$ , we need the integrated efficiency separately in the forward and backward regions for each state.

Figure 7.16 shows the  $\Upsilon(1S)$  reconstruction efficiency for  $p_T < 6 \text{ GeV}/c$  (left) and  $6 < p_T < 30 \text{ GeV}/c$  (right) in pp collisions, while figure 7.17 shows the efficiency for low- and high- $p_T$   $\Upsilon(1S)$  in the backward- (left) and forward- (right) rapidity regions in pPb collisions. The dashed blue lines in figure 7.17 represent the efficiency integrated over  $p_T$  in the respective rapidity regions. Similar plots for  $\Upsilon(2S)$  are shown in figures 7.18 and 7.19. For  $\Upsilon(3S)$ , since

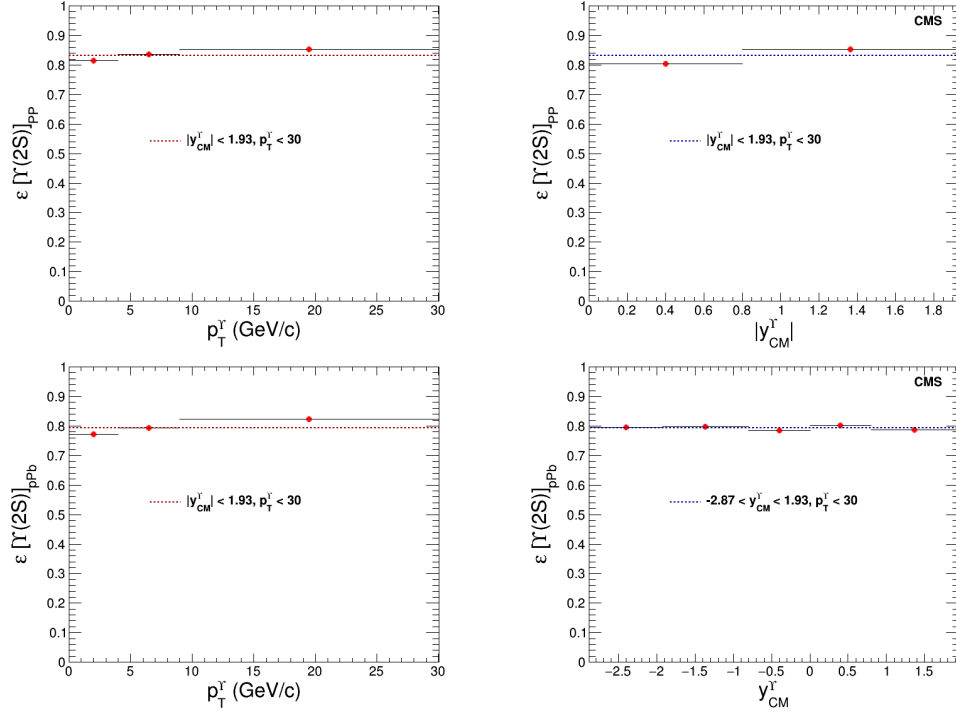


Figure 7.14: T&P corrected reconstruction efficiency for  $\Upsilon(2S)$  as functions of  $p_T$  (left) and  $y_{CM}$  (right) in pp (top) and pPb (bottom) collisions.

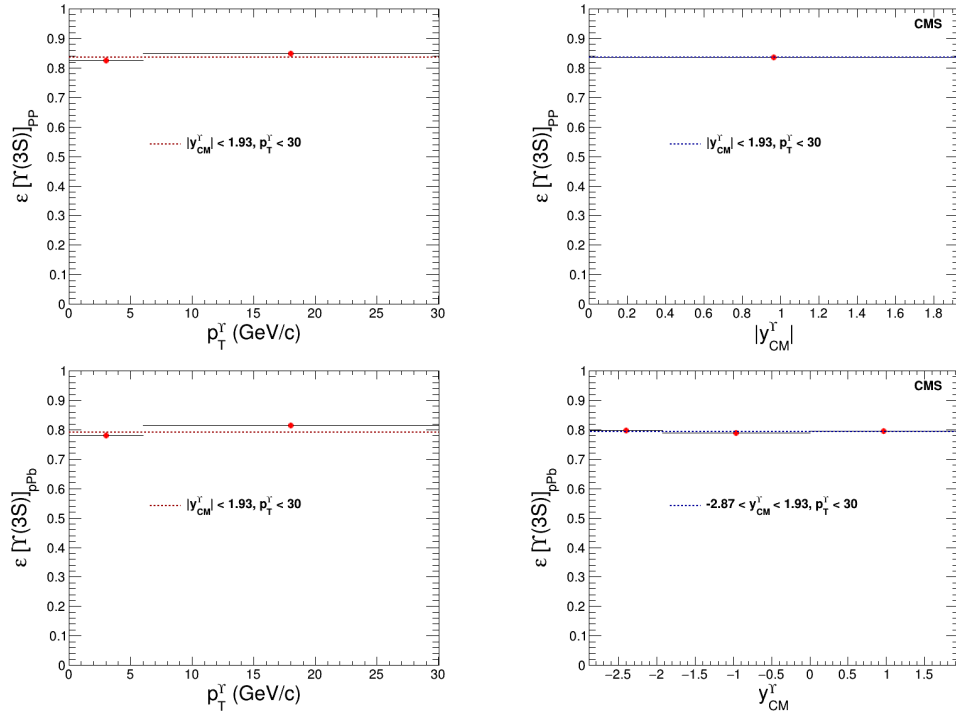


Figure 7.15: T&P corrected reconstruction efficiency for  $\Upsilon(3S)$  as functions of  $p_T$  (left) and  $y_{CM}$  (right) in pp (top) and pPb (bottom) collisions.

the efficiency in the required bins in pp collisions have already been shown in figure 7.15, only the efficiencies in pPb collisions are shown in figure 7.20.

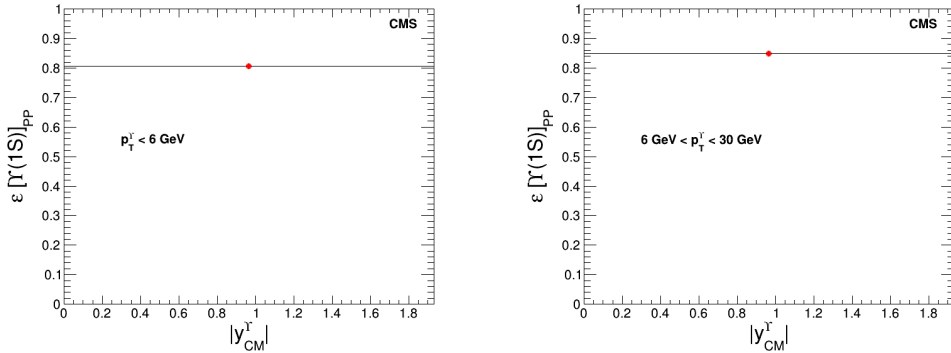


Figure 7.16: T&P corrected reconstruction efficiency for low- (left) and high- (right)  $p_T$   $\Upsilon(1S)$  in pp collisions.

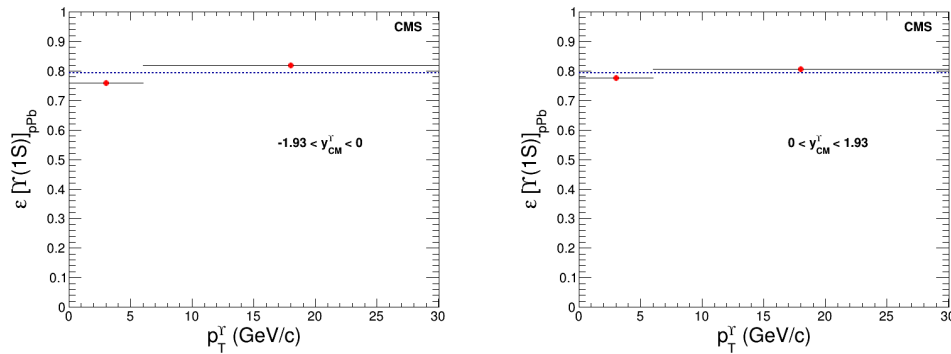


Figure 7.17: T&P corrected reconstruction efficiency of  $\Upsilon(1S)$  mesons for  $(p_T, y_{CM}) \in [0, 6, 30] \text{ GeV}/c \otimes [-1.93, 0, 1.93]$ . The blue line depicts the integrated efficiency in the backward (left) and forward (right) regions, needed for the  $R_{FB}$ .

Finally, we note that T&P corrections alter the MC-based dimuon efficiencies significantly. To validate the methodology, we therefore compare the efficiencies with and without T&P weighting, using the ratio of the two to search for systematic trends. These studies are documented in appendix A.3, along with other consistency checks. The ratios show similar trends as in references [154] and [155] for pp and pPb data, respectively, verifying the need for T&P corrections as well as validating their correct application.

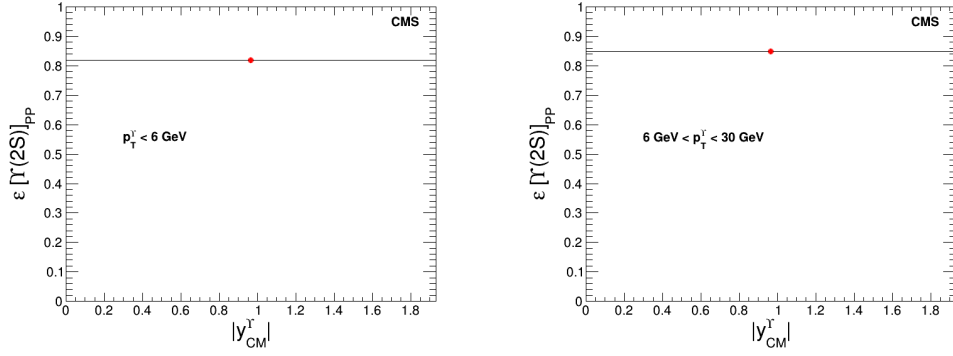


Figure 7.18: T&P corrected reconstruction efficiency for low- (left) and high- (right)  $p_T$   $\Upsilon(2S)$  in pp collisions.

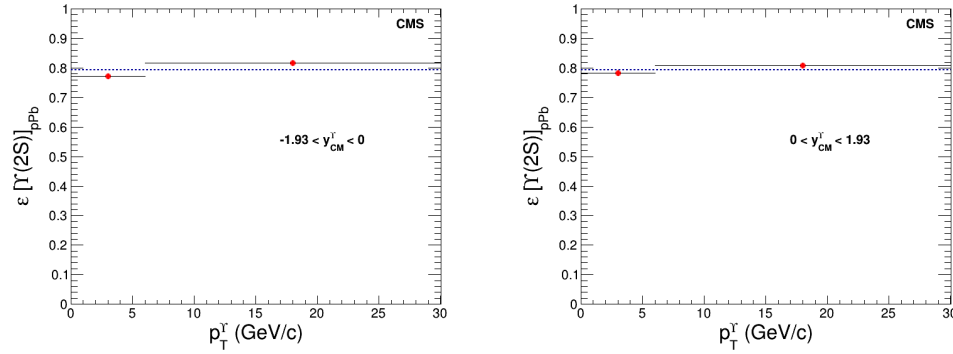


Figure 7.19: T&P corrected reconstruction efficiency of  $\Upsilon(2S)$  mesons for  $(p_T, y_{CM}) \in [0, 6, 30] \text{ GeV}/c \otimes [-1.93, 0, 1.93]$ . The blue line depicts the integrated efficiency in the backward (left) and forward (right) regions, needed for the  $R_{FB}$ .

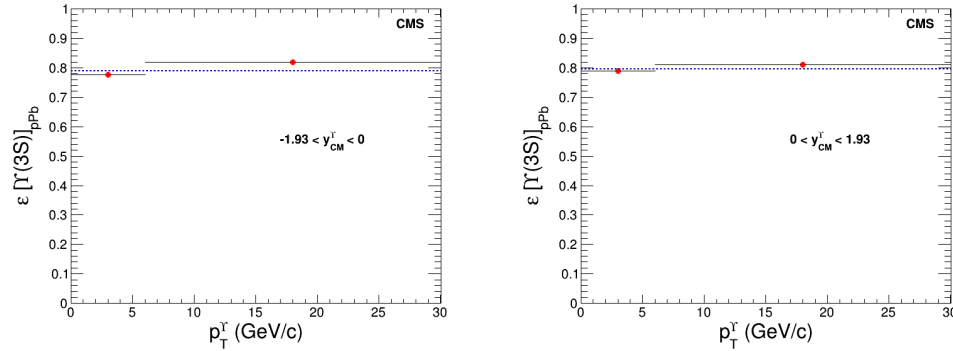


Figure 7.20: T&P corrected reconstruction efficiency of  $\Upsilon(3S)$  mesons for  $(p_T, y_{CM}) \in [0, 6, 30] \text{ GeV}/c \otimes [-1.93, 0, 1.93]$ . The blue line depicts the integrated efficiency in the backward (left) and forward (right) regions, needed for the  $R_{FB}$ .

# Chapter 8

## Estimation of Systematic Uncertainties

We are now ready to transform the  $\Upsilon(\text{nS})$  yields extracted in chapter 6 into the indicators of cold nuclear matter effects (the  $R_{\text{pA}}$  and  $R_{\text{FB}}$ ) using the correction factors from chapter 7. We can calculate these summary statistics and present their values in analysis bins of our choosing to search for trends against independent variables such as  $p_{\text{T}}$ ,  $y_{\text{CM}}$  and event activity. As physicists, and more generally as data scientists, however, we must additionally ascertain the degree of confidence we can reasonably hold in the results we obtain. Since our experimental observables are statistical in nature (e.g. the number of collision events recorded), there is an inherent random or statistical uncertainty in the measurements that we must propagate to any inferred quantity. With a good understanding of the nature of the underlying distributions in data and the degree of correlation in measurements, this is relatively straightforward.

However, based on the complexity of the measurement and calculation, there may be additional uncertainties to consider. If we have made choices when formulating our methodology for extracting results, we must explore the range of possible values for our results based on alternative reasonable choices. This technique of checking the robustness of inferred results

to analysis choices is commonly used to determine the systematic uncertainty in computed results.

In this chapter, we investigate several sources that can introduce systematic uncertainty in the  $R_{\text{pA}}$  and  $R_{\text{FB}}$ . We extracted  $\Upsilon$  yields in chapter 6 using “nominal” models for the signal and background counts in the dimuon invariant mass spectra based on features in data, physics reasoning and goodness-of-fit tests. When determining the acceptance and efficiency correction factors in chapter 7, we justified similar nominal choices for the  $p_{\text{T}}$ -reweighting functions and *tag-and-probe* scale factors. We now explore possible variations of these choices and use them to estimate the systematic uncertainty in the  $R_{\text{pA}}$  and  $R_{\text{FB}}$ . All variations are performed independently in each analysis bin, such that the only possible source of systematic uncertainty that could apply globally to the results in all bins pertains to the uncertainty in the collision luminosity delivered by the LHC to the CMS detector.

The extracted yields are tested by individually varying the signal and background models. In the case of the signal model, in addition to varying the PDF, we can also change the way we reduce the parameter space prior to fitting. Once shown to be uncorrelated, these sources of uncertainty arising from the fitting and yield extraction process can be combined in quadrature to propagate to the results.

Similarly, we can vary whether or not the  $p_{\text{T}}$  spectrum in MC is reweighted, or what PDF is used to bootstrap the weighting factors, to test the degree of variation of the MC-based correction factors. In the case of T&P corrections to the efficiency, we propagate the range of variations in scale factors already investigated in the relevant T&P analyses. These sources of uncertainty in the correction factors are found to be uncorrelated and combined in quadrature as well.

When correlations do exist amongst sources of uncertainty, they will result in smaller variations in the result than when uncertainties are fully uncorrelated. Therefore, by defaulting to this technique of combining largely uncorrelated sources, we may be erring on the side of conservative estimates of the total uncertainty in the results, which is more desirable than

underestimating the uncertainty. However, since we would like to obtain correct estimates, and not just conservative ones, we try to determine and account for correlations amongst sources of uncertainty whenever possible.

## 8.1 Choice of Signal Model

As discussed in section 6.3, both a double crystal ball and a crystal-ball-plus-Gaussian resulted in high goodness-of-fit when tested as possible PDFs to model the signal. Performing slightly better, the double CB was chosen as the nominal signal PDF even though the CB-plus-Gaussian was also a fair choice. We now use the latter as the alternate PDF to extract  $\Upsilon(nS)$  yields. We use these alternate yields to estimate the systematic uncertainty in the  $R_{pA}$  and  $R_{FB}$  introduced by the choice of the specific nominal signal model between the two similarly reasonable options. Parameters of the CB-plus-Gaussian signal PDF are restricted using the same iterative procedure as in the case of the double CB PDF, using preliminary fits based on the alternative PDF in this case.

To capture the systematic deviation of the results based on the choice of the signal model rather than random fluctuations, “pseudoexperiments” are used to test the nominal and alternative PDFs. In each bin, the fitted shape of the nominal signal plus background model  $\mathcal{F}$  (equation (6.5)) is used to generate “pseudodata” using Monte Carlo sampling. The pseudodata is then fit separately with the nominal and alternate signal PDFs, with a loose goodness-of-fit requirement ( $\chi^2/\text{ndf} > 10$ ) to exclude catastrophically failed fits. The yields extracted in each case are recorded and used to determine the relevant ratio, the  $R_{pA}$  or  $R_{FB}$ . The percentage difference between the results obtained using the nominal and alternate signal PDFs on the pseudodata is computed, concluding the pseudoexperiment. Such pseudoexperiments are performed a hundred times for each analysis bin and the percentage deviation in yields between the nominal and alternate fits from the hundred trials are compiled into a histogram. The mean absolute value of these deviations is taken as the

systematic uncertainty in the result due to the choice of the signal PDF.

Histograms of the differences between  $\Upsilon(nS)$  yields extracted using nominal and alternate signal PDFs in the integrated bin for pp and pPb collisions, along with the corresponding differences between the resulting  $R_{pA}$ , are shown in figures 8.1, 8.2 and 8.3. For each state, the percentage uncertainty in the computed  $R_{pA}$  is lower on average than the percentage uncertainties in the individual extracted yields in pp and pPb. Even when the nominal and alternate fits to data from each collision system vary significantly, the nature of the variations are typically similar between the two collision systems. The same experimental facilities, detection techniques and processing software are used for collecting both pp and pPb data, resulting in some inextricable correlations between the two. However, when a ratio of the yields is taken, as in the case of the  $R_{pA}$ , some of these correlations cancel, producing a smaller variation in the ratio than in the individual yields.

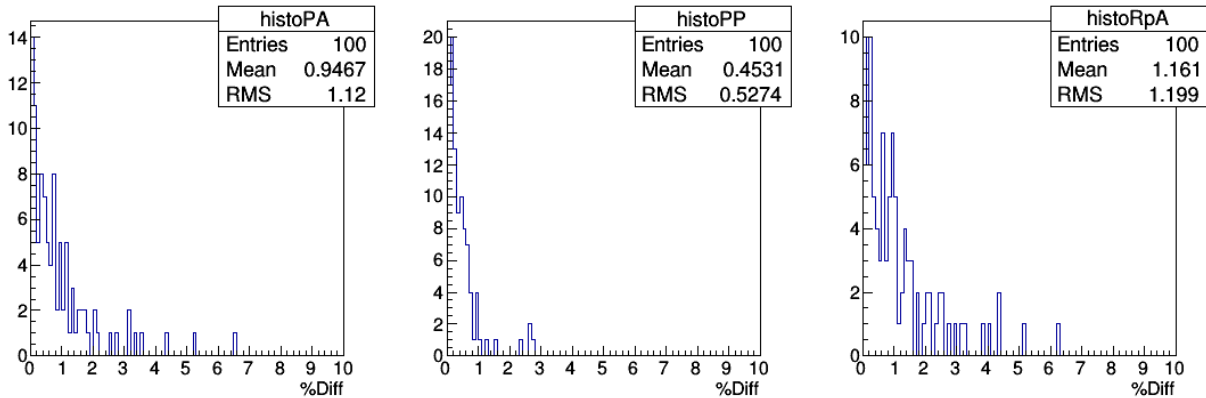


Figure 8.1: Results of a hundred pseudoexperiments in the integrated bin for  $\Upsilon(1S)$  showing the percentage deviations between nominal and alternate signal models in the yields in pp and pPb as well as the  $R_{pA}$ .

In order to estimate the systematic uncertainty in the results due to reducing the allowed phase space of the signal parameters  $n$ ,  $\alpha$ ,  $x$  and  $f$ , we arrive at an alternative reduced space by performing the same sort of iterative fitting as described in section 6.3.1, but by fixing  $n$  (rather than  $\alpha$ ) to its mean from free-parameter fits in the second round of fitting. Thus, in this alternate approach, we propagate the freedom of the two correlated tail parameters into  $\alpha$  rather than  $n$ . In the nominal method,  $\alpha$  was chosen as the parameter to be fixed first

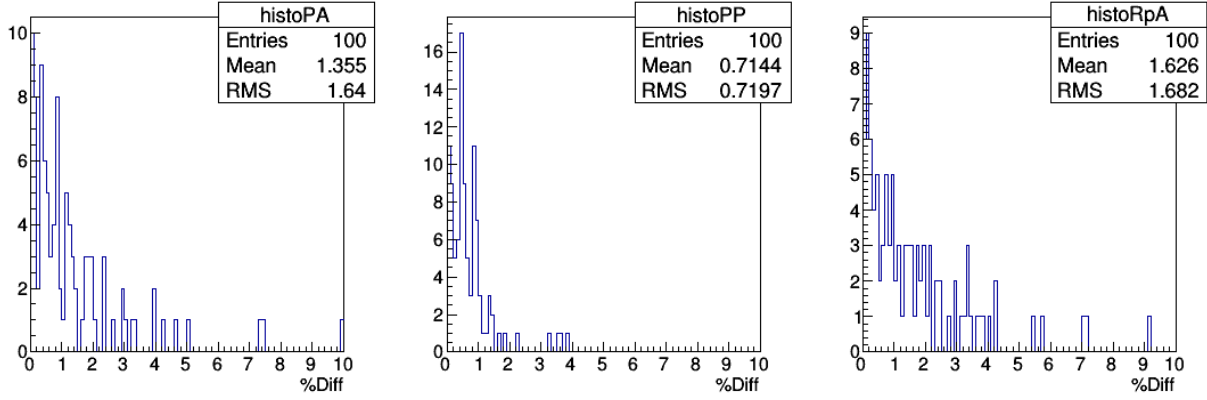


Figure 8.2: Results of a hundred pseudoexperiments in the integrated bin for  $\Upsilon(2S)$  showing the percentage deviations between nominal and alternate signal models in the yields in pp and pPb as well as the  $R_{pA}$ .

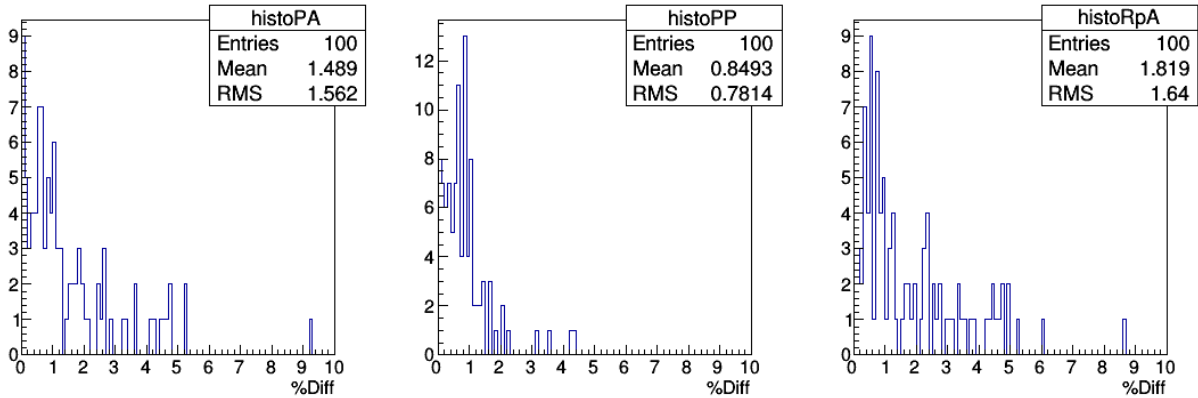


Figure 8.3: Results of a hundred pseudoexperiments in the integrated bin for  $\Upsilon(3S)$  showing the percentage deviations between nominal and alternate signal models in the yields in pp and pPb as well as the  $R_{pA}$ .

because it showed the greatest self-consistency across all bins in the initial fits. However, since  $n$  is also a tail parameter, we could begin by fixing  $n$  instead. Therefore, we use this equally reasonable, albeit slightly less practically ideal, option when determining the systematic uncertainty in the results due to the procedure for parameter phase space reduction. Once again, the percentage difference between the relevant ratio ( $R_{\text{pA}}$  or  $R_{\text{FB}}$ ) using the nominal and alternate reduced phase space is computed and taken as the systematic uncertainty in the result due to this choice. The uncertainties due to choices made in modeling the  $\Upsilon$  signal are determined by combining the uncertainties from the choice of the signal GLM and from choices in parameter restriction in quadrature. They are found to lie within the range 1 – 5 % for the  $R_{\text{pB}}$  and 3 – 9 % for the  $R_{\text{FB}}$  of all  $\Upsilon$  states.

## 8.2 Choice of Background Model

The nominal PDF,  $\mathcal{B}$ , used to model the background when extracting  $\Upsilon(\text{nS})$  yields was defined in equation (6.4). The shape of the background distribution is highly dependent on the  $\Upsilon$  kinematics by virtue of the artificial low-mass turn on, an effect we try to capture using a piecewise function in  $p_{\text{T}}$ . Nonetheless, limitations in  $\mathcal{B}$  begin to surface in analysis bins which are integrated over  $p_{\text{T}}$  but partitioned in  $y_{\text{CM}}$ , a quantity fundamentally related to  $p_{\text{T}}$ . While  $\mathcal{B}$  represents the best choice for the background model, clearly other PDFs could be tried, especially with ad hoc measures to capture the edge cases of kinematic binning. We build such an alternate PDF to test the robustness of our results to differences in the background model. We employ the same technique of repeating pseudoexperiments to estimate the systematic uncertainty in the results due to the choice of background PDF as in the case of the signal PDF.

In analysis bins containing only high- $p_{\text{T}}$  and high- $|y_{\text{CM}}|$   $\Upsilon$ , where the turn-on feature is

absent, we use a power law function as the alternate background PDF:

$$\mathcal{B}' = \frac{m_{\mu\mu}^b}{\left(1 + \frac{m_{\mu\mu}}{m_0}\right)^a} \quad (8.1)$$

where  $a$  and  $b$  are nuisance parameters. Note that unlike the nominal background PDF, this PDF is a function of the fitted mean mass of the  $\Upsilon(1S)$  resonance ( $m_0$ ). The power law functional form is motivated by the shapes of the Drell-Yan and  $b\bar{b}$  decay spectra, both of which fall off as a power law with increasing invariant mass.

Just as in the case of the nominal PDF, the primary motivation driving the choice of the alternate background PDF in bins containing low- $p_T$   $\Upsilon$  is the need to reproduce the turn-on behavior that appears at low invariant mass. In previous bottomonium analyses including [111], the alternative PDF used to model the background in many bins was a fourth-order Chebyshev polynomial. However, by nature polynomials introduce troughs and peaks that have no physical motivation. As an improvement, in this analysis we build a data-driven alternate background PDF that embodies features in the invariant mass spectra of a two-muon decay process in the mass range of  $\Upsilon(nS)$ .

In order to generate the MC simulation of two-muon decays, the parent dimuons are drawn from flat distributions in mass,  $p_T$ ,  $y_{CM}$ , and azimuthal angle  $\phi$ . The parent dimuon then decays to a pair of muons following the conservation laws of a two-body decay. The kinematic distributions of the daughter muons are histogrammed and compared to those of the daughters of reconstructed opposite-sign  $\Upsilon$  candidates in real data in figure 8.4. Since we are interested in the background shape alone, to avoid biasing the distributions with muons from actual  $\Upsilon$  decays, we use only dimuons with  $11 < m_{\mu\mu} < 20 \text{ GeV}/c^2$  in data. The 2-D distribution of single muons in  $p_T$  and  $y_{CM}$  is plotted for opposite-sign dimuon data (top left) and the newly generated MC (top right). Since the distributions in data and MC do not match, the MC single muon distribution is weighted by the data-to-simulation ratio (bottom left) resulting in the weighted single muon distribution in MC (bottom right). Once the

single muons are weighted, the mass distribution of parent dimuons in MC is also weighted using a decaying exponential function, in order to mimic the falling statistical phase factor in real collisions.

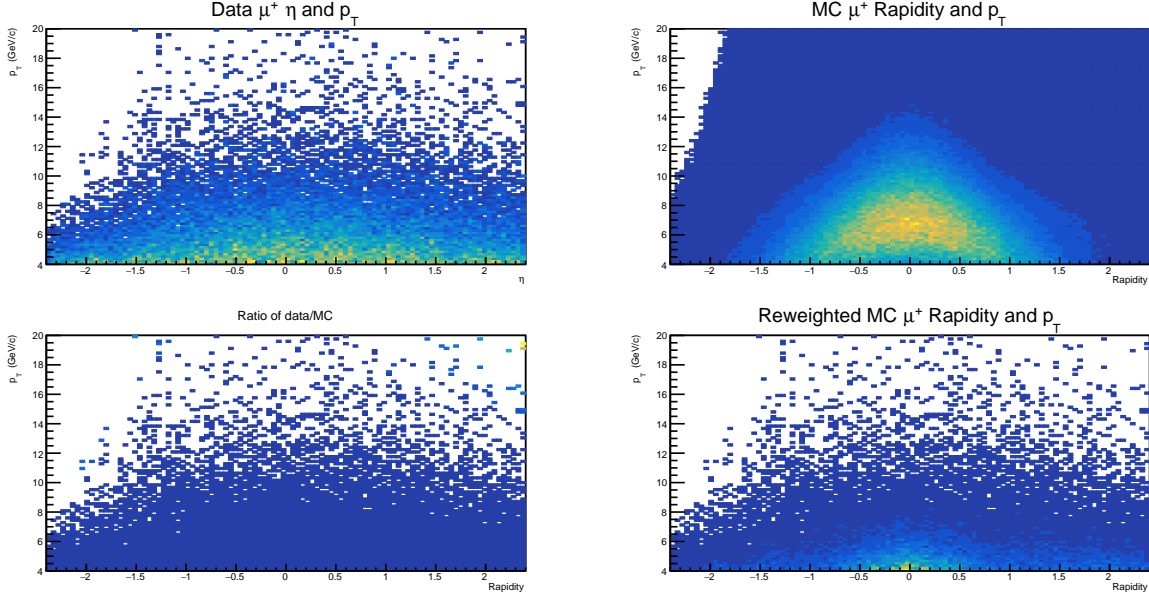


Figure 8.4: Weighting the kinematic distribution of single muons in the MC simulation used to construct the alternate background PDF for pPb collisions in bins containing low- $p_T$   $\Upsilon$ .

Next, the weighted MC is split into four  $p_T$  intervals with the bin edges  $p_T \in [0, 1.5, 3, 4.5, 30]$  GeV/ $c$  and the invariant mass spectrum in each of these bins are fit separately. To fit the first three bins, which contain low- $p_T$  dimuons exclusively, we use the following PDF:

$$\mathcal{B}'' = \begin{cases} \exp\left(-\frac{m_{\mu\mu}}{\lambda}\right) \cdot \left( R \cdot \frac{1 + \text{Erf}\left(\frac{m_{\mu\mu} - \mu_1}{\sqrt{2}\sigma}\right)}{2} + \left(1 - \exp\left(-\frac{m_{\mu\mu} - \mu_2}{\lambda}\right)\right) \right), & \text{if } m_{\mu\mu} \geq \mu_2 \\ \exp\left(-\frac{m_{\mu\mu}}{\lambda}\right) \cdot \left( \frac{1 + \text{Erf}\left(\frac{m_{\mu\mu} - \mu_1}{\sqrt{2}\sigma}\right)}{2} \right), & \text{otherwise} \end{cases} \quad (8.2)$$

which shares many similarities with the nominal background PDF in most bins. The second exponential function introduced here allows us to include another nuisance parameter,  $\mu_2$ , having to do with the turn-on feature. As a result,  $\mathcal{B}''$  is able to reproduce both gradual and sudden turn-on of the background distribution at low mass, as needed. For the last  $p_T$

interval we can once again use a power law PDF, since the high- $p_T$  dimuons in this bin do not show any turn-on behavior at low mass. Plots of the fitted MC invariant mass distributions in the four  $p_T$  bins are shown in figure 8.5.

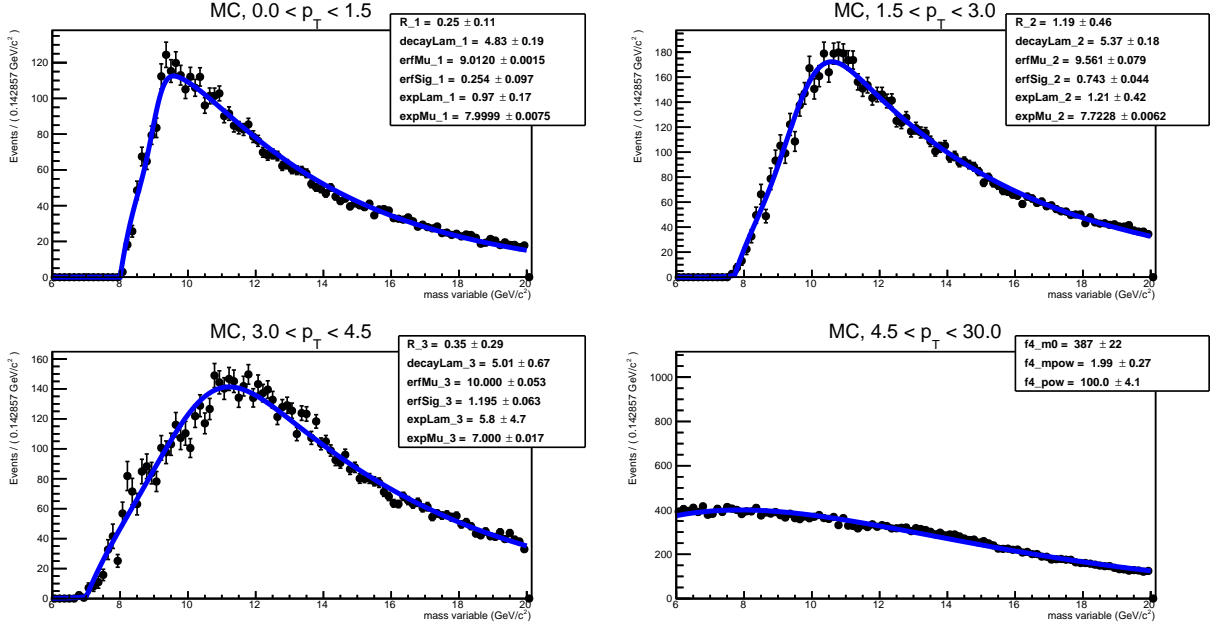


Figure 8.5: Plots of fitted MC invariant mass distributions in the four  $p_T$  intervals:  $p_T \in [0, 1.5, 3, 4.5, 30]$  GeV/ $c$ . The fitted shapes are used as basis functions for building a linear combination which can be used to model the background distribution in most analysis bins.

These four fitted shapes form the basis used to build the alternate background PDF for most bins of the analysis to estimate the systematic uncertainty. A linear combination of the shapes is used, where the coefficients (the amplitude of each shape) are left as free fit parameters and their sum represents the estimator of the number of background events.

After a bin-by-bin study, the power law alternate PDF in equation (8.1) is chosen for all kinematic bins containing exclusively  $\Upsilon$  with  $p_T > 6$  GeV/ $c$  as well as for the  $4 < p_T < 9$  GeV/ $c$  bin, in addition to high- $|y_{\text{CM}}|$  bins. For all other bins in the analysis, the linear combination alternate PDF in equation (8.2) is used.

Equipped with the alternate background PDF everywhere, we now perform pseudoexperiments similar to those described in section 8.1 to estimate the systematic uncertainty in the results arising from the choice of the background GLM. The histogrammed percentage

differences in  $\Upsilon(1S)$  yields in pp and pPb, and the resulting  $R_{pA}$ , from such pseudoexperiments in the integrated bin are shown in figure 8.6. The choice of background model is the dominant source of systematic uncertainty in the results in most analysis bins, producing typical deviations for  $\Upsilon(1S)$ ,  $\Upsilon(2S)$ , and  $\Upsilon(3S)$ , respectively, between 0.5 – 8 %, 1 – 10 %, and 2 – 32 % for the  $R_{pPb}$ , and 2 – 4 %, 5.5 – 10 %, and 9 – 18 % for the  $R_{FB}$ .

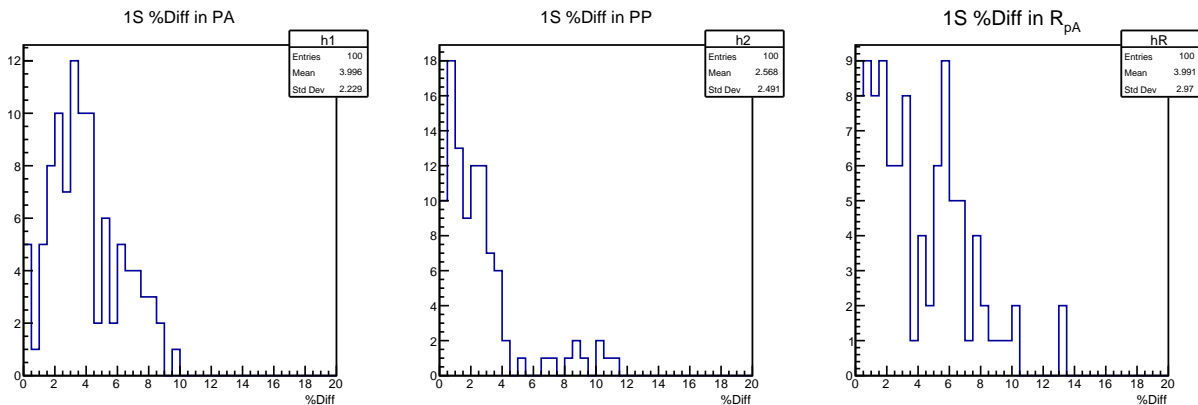


Figure 8.6: Results of a hundred pseudoexperiments in the integrated bin for  $\Upsilon(1S)$  showing the percentage deviations between nominal and alternate background models in the yields in pp and pPb as well as the  $R_{pA}$ .

### 8.3 Choice of Acceptance Correction

The nominal acceptance correction factors are obtained using the  $p_T$ -reweighted generator-level MC samples as explained in 7.2. The major choice made in acceptance determination is the particular procedure for reweighting the  $p_T$  spectra: using an empirical fit to the data-to-simulation ratio of the  $p_T$  spectra to bootstrap the required reweighting everywhere. In order to estimate the systematic uncertainty this choice introduces, we vary each parameter of the fit within its fit uncertainties. The resulting  $p_T$ -reweighting functions are used to compute variations of the acceptance, the largest of which is then propagated to the uncertainty in the results. Reweighting functions with varied fits were shown in section 7.1, and the largest deviations in the acceptance correction factor due to these variations were presented in section 7.2. The relative systematic uncertainty in the results due to acceptance correction

is found to be less than 2 % in all analysis bins.

## 8.4 Choice of Efficiency Correction

The systematic uncertainty in the efficiency correction factors originate from two sources. The first source is the same as for acceptance, i.e. the reweighting of the MC  $p_T$  spectra. Since the margin of error is larger for efficiency corrections than acceptance, we make a more conservative estimate of the effect of  $p_T$  reweighting on the efficiency. As the alternate, we compute the dimuon efficiency without reweighting the MC  $p_T$  spectra. Since the reweighting method is similar for pp and pPb MC, the systematic uncertainty it introduces in the respective efficiency corrections may be correlated. We take correlations into account and allow for possible cancellations by determining the deviation in the ratios ( $R_{pA}$  and  $R_{FB}$ ) directly using efficiency corrections with and without reweighting the MC.

The second source of uncertainty results from the choices made in the *tag-and-probe* method. The systematic uncertainties in the reported T&P scale factors for pp and pPb collisions were estimated in the respective analyses and subsequently approved by the muon POG. These uncertainties are estimated by varying several settings of the invariant mass fits for tag and probe pairs, including changing the mass range, using alternate PDFs to model the signal and background shapes, and changing the probe selection criteria. Two systematic variations are reported for each single-muon efficiency: the maximum and minimum values they can take under these changes. Statistical variations are also incorporated into the uncertainty estimates by performing toy MC studies on the SFs with one hundred iterations. We propagate these reported uncertainties to our results in the following way.

There are eight total sources of uncertainty from T&P corrections for pp and two sources for pPb MC. The contribution of all single-muon efficiencies to the systematic variation in dimuon efficiency are considered, even if correction by the corresponding scaling factor was not required. In cases where SFs are not needed, an overall percentage uncertainty due

to the single-muon efficiency is estimated and combined with uncertainty from variations of SFs. Each of the varied SFs are used to correct each muon in the dimuon efficiency  $\varepsilon_{MC}$  in turn and the resulting corrected efficiencies are compared to the nominal efficiency correction. The percentage deviation of the efficiency due to each source of SF variation is then combined in quadrature to estimate the total systematic uncertainty in the efficiency correction arising from choices made in the T&P technique. In order to determine the uncertainty in the  $R_{pA}$  due to the T&P correction, we further combine the uncertainty in pp and pPb efficiency corrections in quadrature. In this case, we expect few correlations between the T&P corrections for pp and pPb data because of the many differences in the T&P procedures as explained in section 7.3.

The variations in the efficiency correction factors due to variations of T&P techniques (both systematic and statistical) are plotted as functions of  $p_T$  and  $y_{CM}$  for pp and pPb in appendix A.4. The relative contributions of the various sources of systematic variations from the T&P method to the overall uncertainty in the corrected efficiency are plotted as functions of  $p_T$  and  $y_{CM}$  in appendix A.5.

Finally, the systematic uncertainty in the results due to the two sources from efficiency correction—reweighting the MC  $p_T$  spectra and the secondary *tag-and-probe* correction—are combined in quadrature. The systematic uncertainties in the combined efficiency corrections range from 4 – 9 % in the  $R_{pPb}$  and are approximately 2 % in the  $R_{FB}$ .

## 8.5 Study of total systematic uncertainty in results

The total systematic uncertainty in the measurements presented here is obtained by combining in quadrature the uncertainties in the signal and background extractions, as well as in the acceptance and efficiency corrections. The uncertainties in these four sources have roughly the same  $p_T$  and  $y_{CM}$  dependence, if any. The combined systematic uncertainty in the results is found to increase slightly with increasing  $|y_{CM}|$  and with decreasing  $p_T$ . Due

to the asymmetry of pPb collisions, the most forward  $y_{\text{CM}}$  bins, which are at the edge of the detector, have larger systematic uncertainty than the most backward  $y_{\text{CM}}$  bins, as the latter are closer to  $y_{\text{lab}} = 0$ . The total systematic uncertainty also increases with increasing event activity for integrated  $p_{\text{T}}$  and  $y_{\text{CM}}$ .

The contributions of the various sources of systematic uncertainties and the total systematic uncertainties on the results are plotted as a function of the analysis variables below.

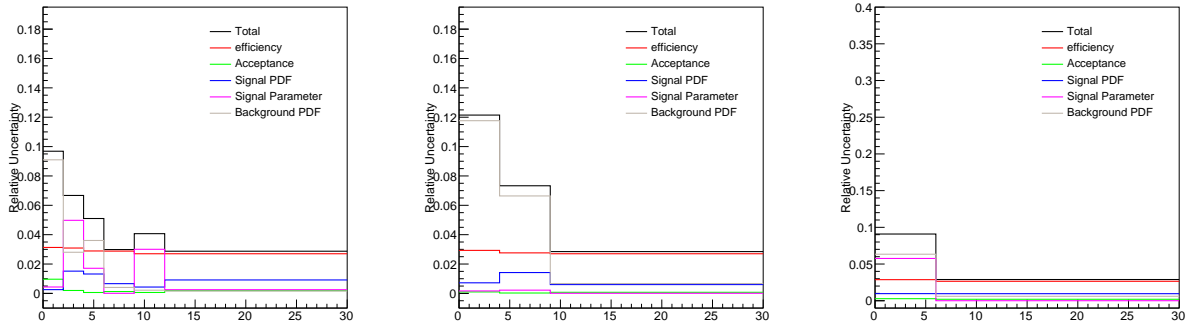


Figure 8.7: Comparison of systematic uncertainties in pp cross section as a function of  $p_{\text{T}}$ .

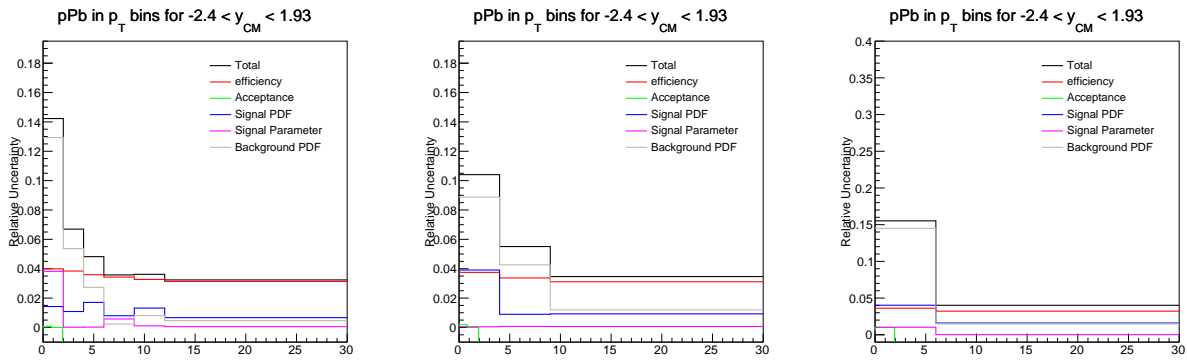


Figure 8.8: Comparison of systematic uncertainties in pPb cross section as a function of  $p_{\text{T}}$ .

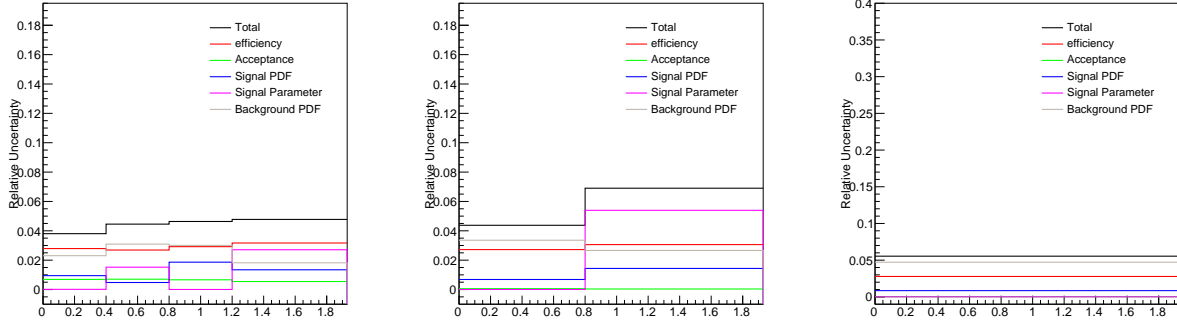


Figure 8.9: Comparison of systematic uncertainties in pp cross section as a function of  $|y_{\text{CM}}|$ .

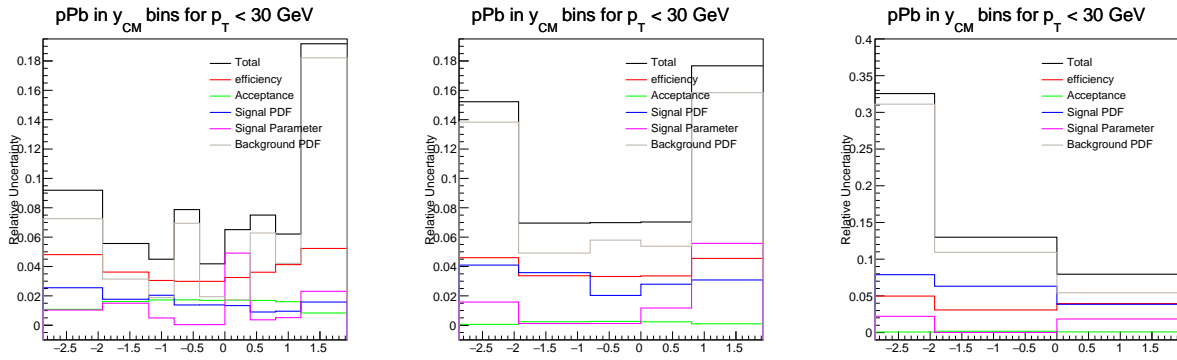


Figure 8.10: Comparison of systematic uncertainties in pPb cross section as a function of  $y_{\text{CM}}$ .

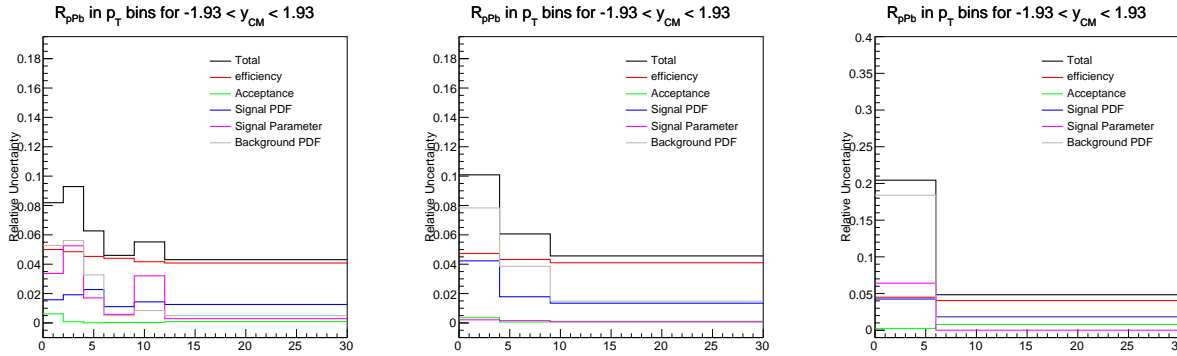


Figure 8.11: Comparison of systematic uncertainties in  $R_{\text{pA}}$  as a function of  $p_{\text{T}}$ .

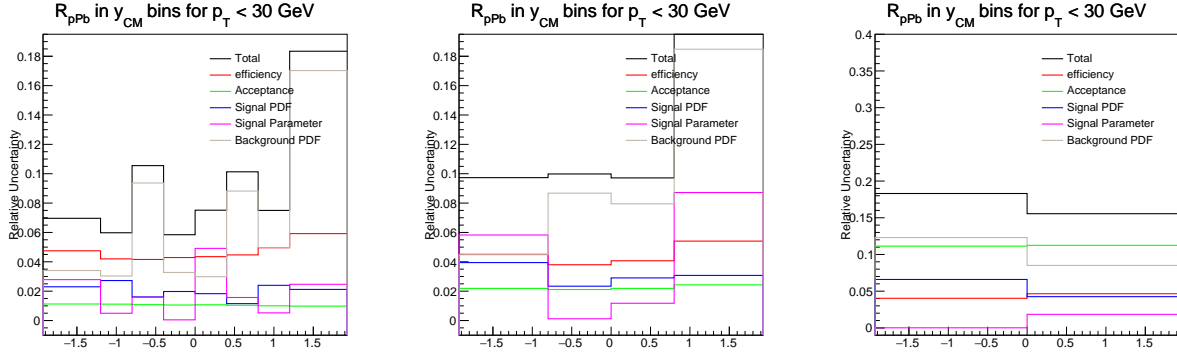


Figure 8.12: Comparison of systematics uncertainties in  $R_{pA}$  as a function of  $y_{CM}$ .

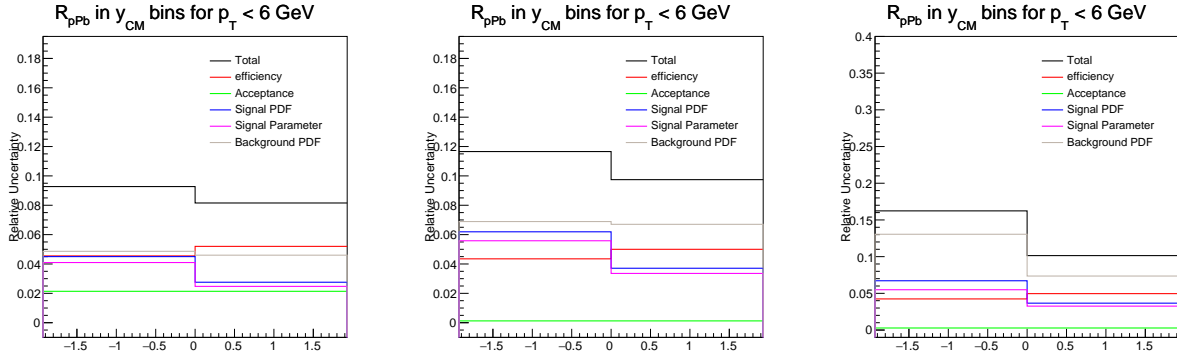


Figure 8.13: Comparison of systematics uncertainties in  $R_{pA}$  in forward and backward  $y_{CM}$  for low  $p_T$ .

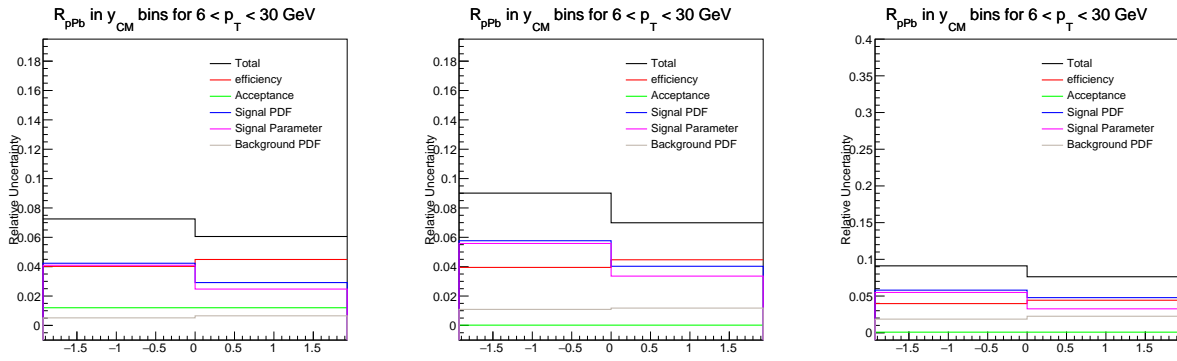


Figure 8.14: Comparison of systematics uncertainties in  $R_{pA}$  in forward and backward  $y_{CM}$  for high  $p_T$ .

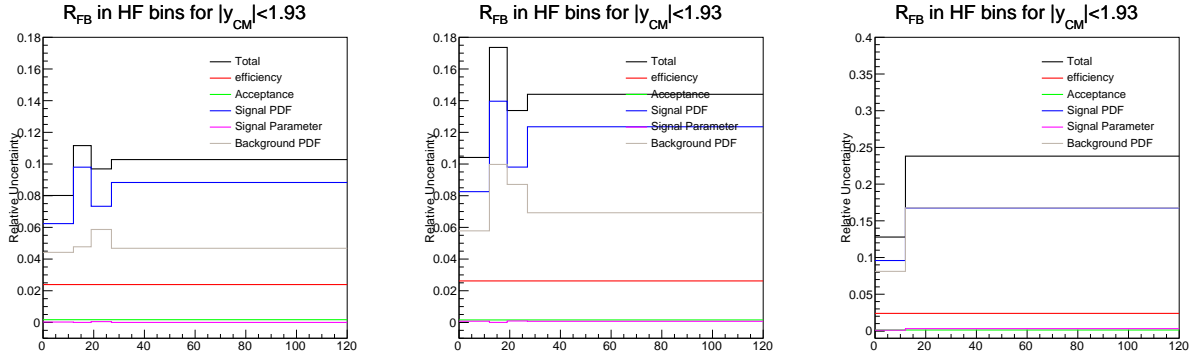


Figure 8.15: Comparison of systematics uncertainties in  $R_{FB}$  as a function of  $E_T$ .

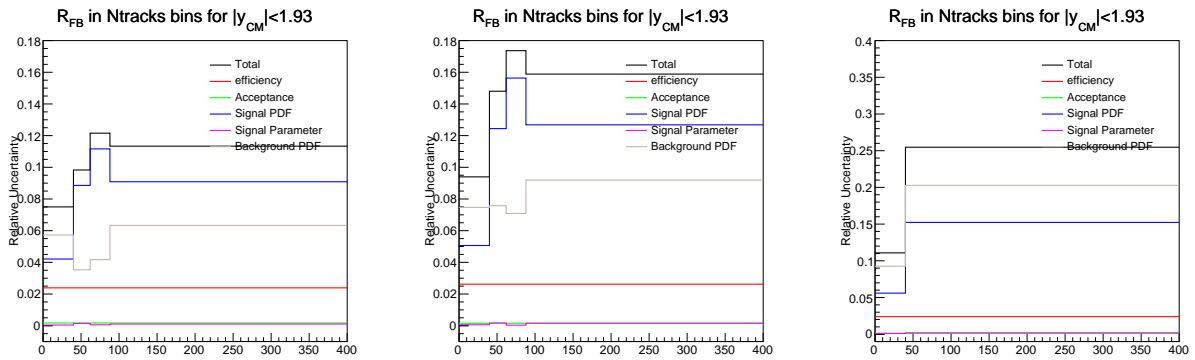


Figure 8.16: Comparison of systematics uncertainties in  $R_{FB}$  as a function of  $N_{tracks}$ .

# Chapter 9

## Results and Discussion

We are finally ready to compute the values of the  $R_{pA}$  and  $R_{FB}$  in our analysis bins, using the measured  $\Upsilon$  yields (chapter 6) and correction factors (chapter 7), and our estimate of systematic uncertainties (chapter 8) in the measurements. There is, however, an intermediate step for us to consider. While we have measured the yield of  $\Upsilon$  mesons in pp and pPb collisions that decayed via the  $\Upsilon(nS) \rightarrow \mu^+\mu^-$  decay channel, in order to make inferences about the effects of cold nuclear matter on  $\Upsilon$  production in general, we would like to bootstrap our results to all  $\Upsilon$  mesons created in the collisions.

We discussed the significance and advantages of studying the bottomonium family through their electromagnetic decay to two leptons in section 1.6 and further motivated our choice of the double-muon channel demonstrating the clean nature of this signature left in particle detectors, particularly in the CMS detector. However, the majority of  $\Upsilon$  mesons created in high-energy collisions actually decay hadronically via  $\Upsilon(nS) \rightarrow ggg$ . For the excited states, feed down to lower excited states is also a prevalent decay mode. Therefore, while we have measured  $\Upsilon$  decays in an important channel, we must be cognizant of the limitations of our measurement. It is only with the help of the larger scope of the entire particle physics community, and in particular the efforts of the particle data group (PDG), that we can contextualize our measurement. We bootstrap our results to  $\Upsilon$  mesons in general by using the

relative frequency of  $\Upsilon(nS) \rightarrow \mu^+\mu^-$  decays compared to all other measured modes of  $\Upsilon(nS)$  decay, a ratio known as the branching fraction  $\mathbb{B}$ . The branching fractions  $\mathbb{B}(\Upsilon(nS) \rightarrow \mu^+\mu^-)$  for  $\Upsilon(1S)$ ,  $\Upsilon(2S)$  and  $\Upsilon(3S)$ , as read from the PDG [152], are  $(2.48 \pm 0.05) \%$ ,  $(1.93 \pm 0.17) \%$  and  $(2.18 \pm 0.21) \%$ , respectively.

## 9.1 Inclusive Cross Section

We now arrive at our projection of the total production cross section of  $\Upsilon(nS)$  mesons in kinematic bins of our analysis:  $\frac{d^2\sigma}{dp_T dy_{CM}}$ , which we can use to compute the ratios  $R_{pA}$  and  $R_{FB}$ . The product of the branching fraction of  $\Upsilon(nS)$  to muon pairs and the double-differential production cross section is obtained experimentally as:

$$\mathbb{B}(\Upsilon(nS) \rightarrow \mu^+\mu^-) \frac{d^2\sigma}{dp_T dy_{CM}} = \frac{N_{\Upsilon(nS)}/(a \cdot \varepsilon)}{\mathcal{L}_{\text{int}} \Delta p_T \Delta y_{CM}} \quad (9.1)$$

where  $N_{\Upsilon(nS)}$  is the extracted raw yield of  $\Upsilon$  mesons in a given  $(p_T, y_{CM})$  bin,  $a$  is the dimuon acceptance correction,  $\varepsilon$  is the dimuon efficiency correction, and  $\mathcal{L}_{\text{int}}$  is the integrated luminosity. Figure 9.1 shows the cross sections of  $\Upsilon(1S)$ ,  $\Upsilon(2S)$ , and  $\Upsilon(3S)$  in pPb collisions in the kinematic regions probed. Since data for both pp collisions and pPb collisions in a symmetric rapidity region are available only for  $|y_{CM}| < 1.93$ , we use this region when investigating the pPb cross section dependence on  $p_T$  and when determining the  $R_{pPb}$  and  $R_{FB}$ . The  $\Upsilon(nS)$  cross sections in pp collisions are also determined for  $|y_{CM}| < 1.93$  as functions of the kinematic variables, as these are needed for  $R_{pPb}$  calculation. These are shown in Fig. 9.2. The  $\Upsilon$  cross sections presented here are inclusive measurements, meaning that corrections based on projected feed down rates of excited states are not applied.

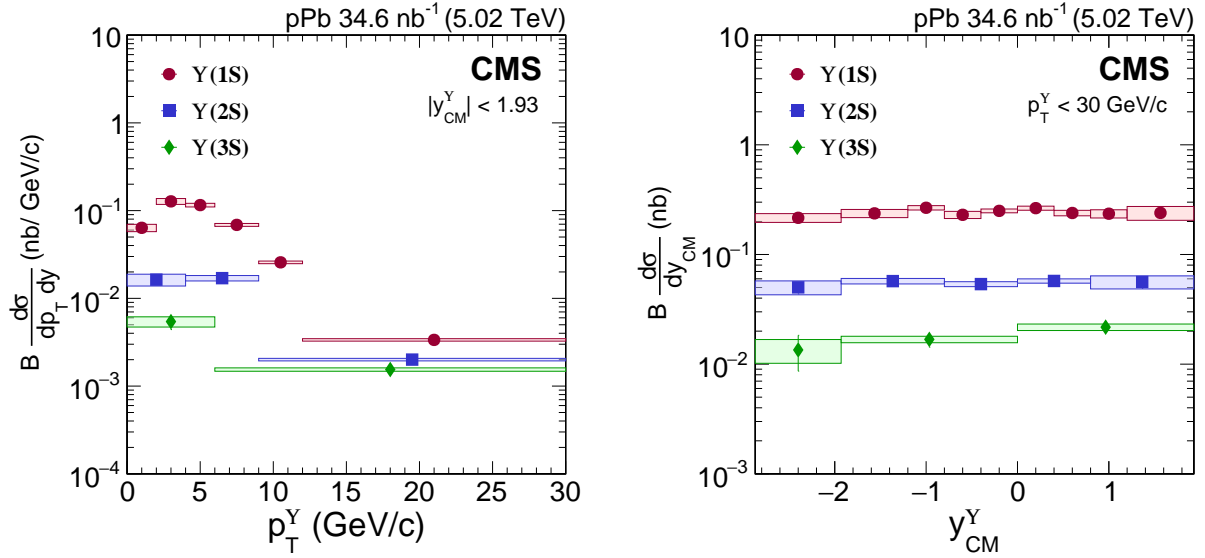


Figure 9.1: Cross section times dimuon branching fraction of  $\Upsilon(1S)$  (red circles),  $\Upsilon(2S)$  (blue squares), and  $\Upsilon(3S)$  (green diamonds) as a function of  $p_T$  (left) and rapidity (right) in pPb collisions. Error bars on the points represent statistical and fit uncertainties and filled boxes represent systematic uncertainties. A 3.5 % global uncertainty in determining the integrated luminosity of pPb collisions, applicable to all points, is not included in the point-by-point uncertainties.

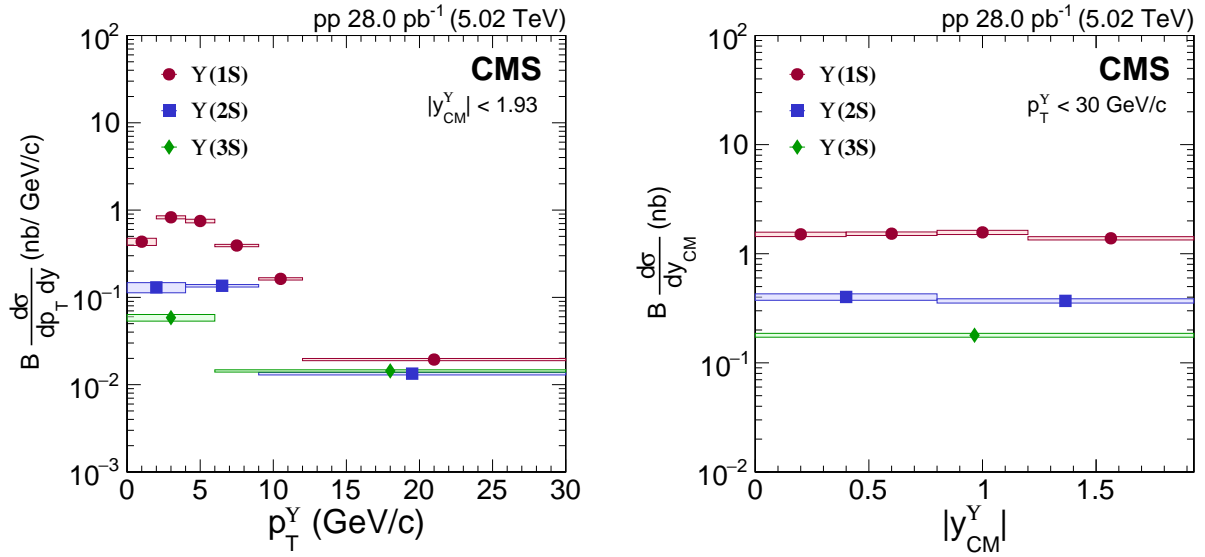


Figure 9.2: Cross section times dimuon branching fraction of  $\Upsilon(1S)$  (red circles),  $\Upsilon(2S)$  (blue squares), and  $\Upsilon(3S)$  (green diamonds) as a function of  $p_T$  (left) and rapidity (right) in pp collisions. Error bars on the points represent statistical and fit uncertainties and filled boxes represent systematic uncertainties. A 2.3 % global uncertainty in determining the integrated luminosity of pp collisions, applicable to all points, is not included in the point-by-point uncertainties.

## 9.2 Cold Nuclear Matter Modification

Figure 9.3 shows the  $\Upsilon(\text{nS})$   $R_{\text{pPb}}$  as a function of  $p_{\text{T}}$  and  $y_{\text{CM}}$ , obtained as

$$R_{\text{pPb}}(p_{\text{T}}, y_{\text{CM}}) = \frac{(\text{d}^2\sigma/\text{d}p_{\text{T}}\text{d}y_{\text{CM}})_{\text{pPb}}}{A(\text{d}^2\sigma/\text{d}p_{\text{T}}\text{d}y_{\text{CM}})_{\text{pp}}} \quad (9.2)$$

where  $A = 208$  is the mass number of the Pb nucleus. As promised, this ratio is representative of the extent to which  $\Upsilon(\text{nS})$  production is suppressed in pPb collisions compared to pp collisions when the yields in pp collisions have been scaled to anticipate the higher production rate due to addition nucleons in the Pb nucleus. We observe that all three  $\Upsilon$  states are suppressed in pPb collisions relative to pp collisions throughout the kinematic region explored, indicating modification by CNM effects in pPb. Similar to the PbPb case [29], the level of suppression for each  $\Upsilon$  state in pPb collisions is consistent with a constant value in the kinematic region studied, although the level of suppression seen in PbPb is much stronger. The ATLAS collaboration reported an increasing  $R_{\text{pPb}}$  with  $p_{\text{T}}$  for  $\Upsilon(1\text{S})$  [30] in a midrapidity region similar to CMS. However, the overall  $p_{\text{T}}$  dependence of  $\Upsilon(1\text{S})$   $R_{\text{pPb}}$  in the two experiments are consistent within uncertainties. A similar  $y_{\text{CM}}$  dependence of the  $\Upsilon(1\text{S})$   $R_{\text{pPb}}$  to the one presented here is measured by the ATLAS collaboration [30] as well.

In the charmonium sector, the CMS collaboration found hints of a sequential suppression pattern, with the  $R_{\text{pPb}}$  of  $\psi(2\text{S})$  being smaller than that of  $J/\psi$  [117] in pPb collisions at  $\sqrt{s_{\text{NN}}} = 5.02$  TeV for backward rapidity and  $p_{\text{T}}^{J/\psi} < 10$  GeV/ $c$  [116]. The results presented here suggest hints of a similar sequential suppression of the  $\Upsilon$  states in the backward rapidity region as well as across the entire  $p_{\text{T}}$  region studied. The measured  $R_{\text{pPb}}$  of  $\Upsilon(1\text{S})$  is systematically greater than that of  $\Upsilon(2\text{S})$ , which in turn is systematically greater than the  $\Upsilon(3\text{S})$   $R_{\text{pPb}}$ , indicating differences in modification to the three states by CNM effects in these regions. In the forward rapidity region, the  $R_{\text{pPb}}$  of the three states appear more mutually consistent.

We further compare the  $y_{\text{CM}}$  dependence of the measured  $R_{\text{pPb}}$  to predictions from three

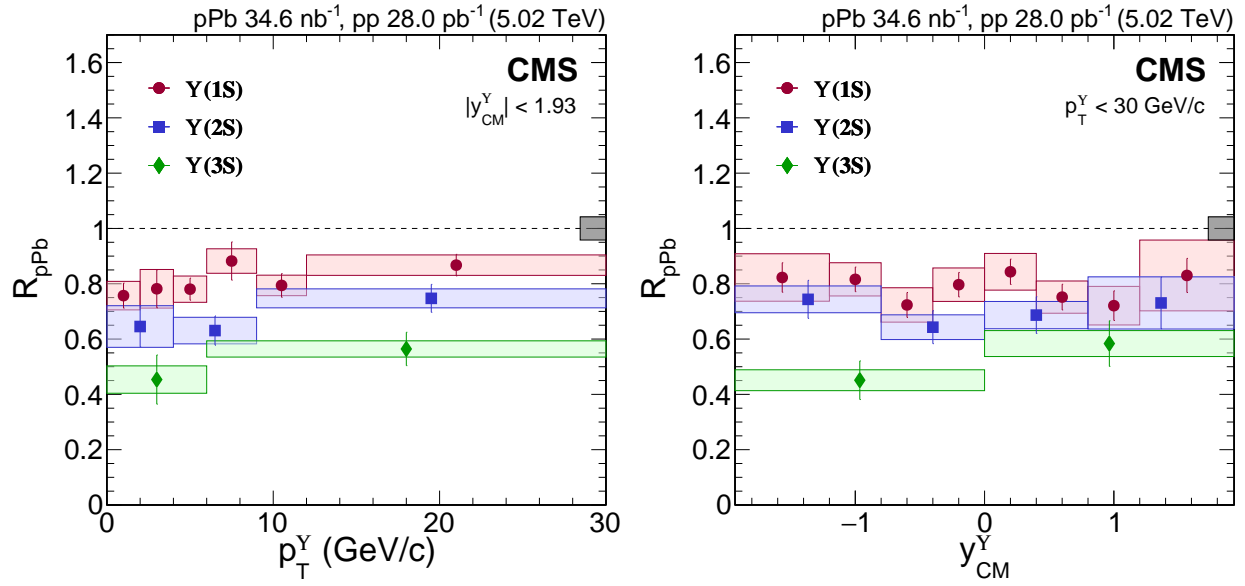


Figure 9.3:  $R_{pPb}$  of  $\Upsilon(1S)$  (red circles),  $\Upsilon(2S)$  (blue squares), and  $\Upsilon(3S)$  (green diamonds) as a function of  $p_T$  for  $|y_{CM}^Y| < 1.93$  (left) and versus  $y_{CM}^Y$  for  $p_T < 30$  GeV/ $c$  (right). Error bars on the points represent statistical and fit uncertainties and filled boxes represent systematic uncertainties. The gray box around the line at unity represents the global uncertainty due to luminosity normalization. All three  $\Upsilon$  states are suppressed in pPb collisions compared to pp collisions throughout the kinematic region explored. For each  $\Upsilon$  state, the measured  $R_{pPb}$  is consistent with a constant value across the kinematic range. The  $\Upsilon$  states show a sequential pattern of suppression, with  $\Upsilon(1S)$  the least suppressed.

CNM models. Shadowing calculations using next-to-leading order nuclear modifications of the PDFs (nPDF) [26] according to EPS09 [88] are provided by R. Vogt. F. Arleo and S. Peigné provide predictions using coherent energy loss (E. Loss) [27] with and without next-to-leading order nPDF calculations using EPS09. Since they affect the pre-hadronized  $Q\bar{Q}$ , both shadowing and energy loss are initial-state effects. Finally, predictions using the comover interaction model (CIM) [28] with two different leading-order nPDF calculations from EPS09 and nCTEQ15 [89] are provided by E. Ferreiro and J.-P. Lansberg. The CIM is a final-state CNM effect.

The initial-state models, which predict equal modification of all bottomonium states, are compared to the measured  $\Upsilon(1S)$   $R_{pPb}$  in Fig. 9.4, with  $R_{pPb}$  predictions from shadowing [26] (left) and the predictions using energy loss only and energy loss with shadowing [27] (right). These models predict  $R_{pPb}$  values that are slightly higher than our measured  $\Upsilon(1S)$   $R_{pPb}$ . Slightly closer agreement with data is observed when the energy loss model is combined with shadowing effects from EPS09.

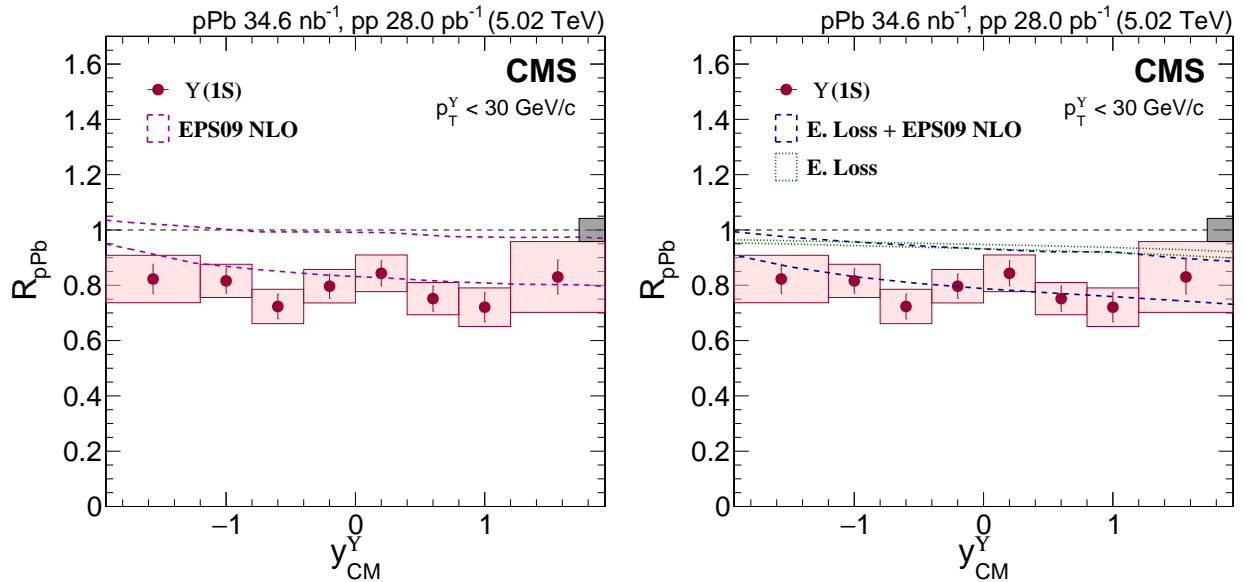


Figure 9.4:  $R_{pPb}$  of  $\Upsilon(1S)$  (red circles) versus  $y_{CM}$  with initial-state model calculations: nPDF modification from R. Vogt [26] (left) and energy loss with and without shadowing corrections from F. Arleo and S. Peigné [27] (right). Error bars on the points represent statistical and fit uncertainties and filled boxes represent systematic uncertainties. The gray box around the line at unity represents the global uncertainty due to luminosity normalization.

In contrast to shadowing and energy loss models, CIM predictions suggest different amounts of modification for the  $\Upsilon(1S)$ ,  $\Upsilon(2S)$ , and  $\Upsilon(3S)$  states in nuclear collisions. The comover framework has two important features that result in differences in modification. First, higher excited states experience stronger comover dissociation rates due to their larger size, which increases their cross section for comover interaction. Second, comover modification of quarkonium states is stronger in regions where the comover densities are larger, such as in the nucleus-going direction in asymmetric proton-nucleus collisions and in regions of higher event activity in nuclear collisions in general. Both features ultimately affect the dissociation rate of a given quarkonium state due to comover interaction [9, 28]. Figure 9.5 shows comparisons of predicted  $R_{pPb}$  in the CIM [28] with the measured  $R_{pPb}$ , for  $\Upsilon(1S)$  (upper left),  $\Upsilon(2S)$  (upper right), and  $\Upsilon(3S)$  (lower). CIM predictions for all three states are illustrated with shadowing corrections using both nCTEQ15 and EPS09. The CIM  $R_{pPb}$  predictions show significant overall suppression for all  $\Upsilon$  states with both shadowing corrections. Moreover, sequential suppression of the  $\Upsilon$  states is predicted, with the least suppression expected for  $\Upsilon(1S)$ . The final-state effect of hadronic comovers yields predictions in better agreement with our data for all three states compared to models incorporating initial-state effects only.

By comparing the  $\Upsilon$   $R_{pPb}$  in the forward (proton-going) and backward (lead-going) directions, we can investigate the dependence of bottomonium suppression on the amount of nuclear matter present. Figure 9.6 shows the  $R_{pPb}$  of  $\Upsilon$  states for  $-1.93 < y_{CM} < 0$  and  $0 < y_{CM} < 1.93$  in the low  $p_T$  (left) and high  $p_T$  (right) regions. We find indication of slightly greater separation of the suppression levels of low- $p_T$   $\Upsilon(nS)$  in the lead-going versus the proton-going  $y_{CM}$  directions. A similar observation was made by CMS in the charmonium sector [116], where the modification levels of  $\psi(2S)$  and  $J/\psi$  with  $p_T < 10$  GeV/ $c$  was found to be more separated in the backward region, while both states experienced similar modification in the forward region.

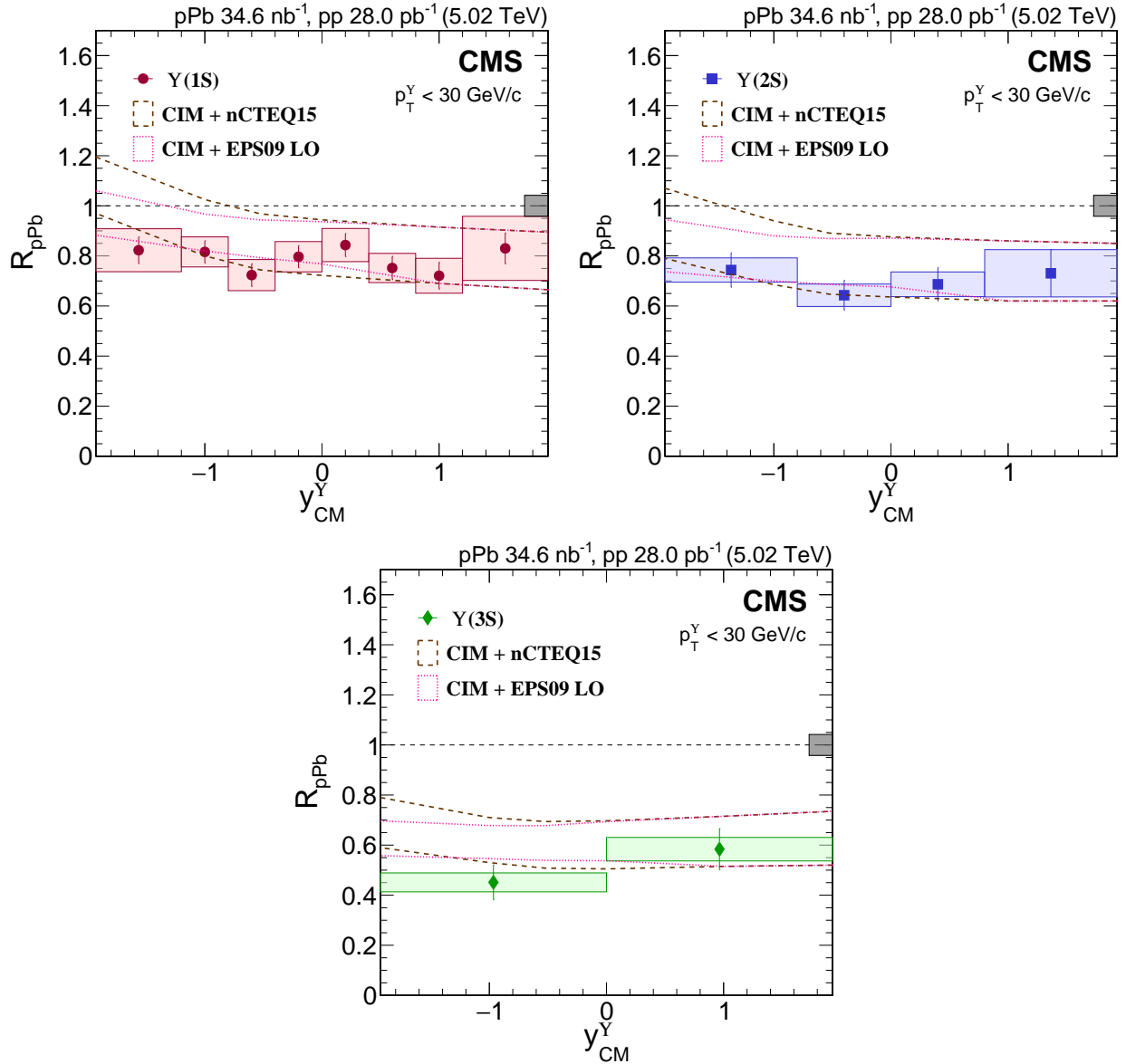


Figure 9.5:  $R_{pPb}$  versus  $y_{CM}$  with comover effect predictions from E. Ferreiro and J.-P. Lansberg [28] with shadowing corrections using nCTEQ15 and EPS09 for  $\Upsilon(1S)$  (upper left; red circles),  $\Upsilon(2S)$  (upper right; blue squares) and  $\Upsilon(3S)$  (lower; green diamonds). Error bars on the points represent statistical and fit uncertainties and filled boxes represent systematic uncertainties. The gray box around the line at unity represents the global uncertainty due to luminosity normalization.

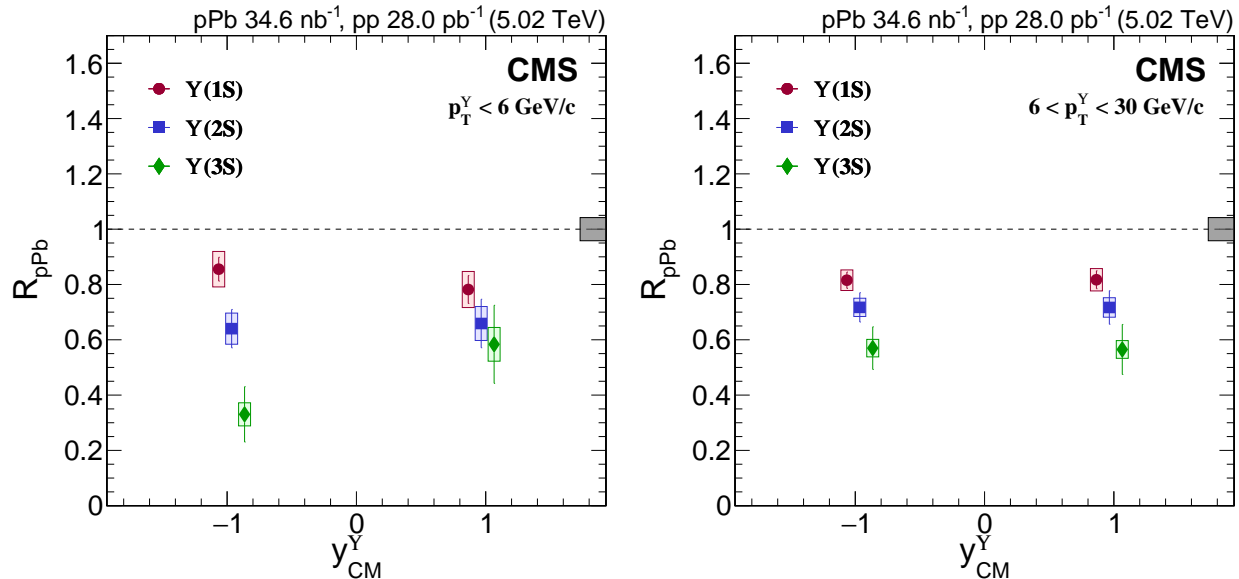


Figure 9.6:  $R_{\text{pPb}}$  of  $\Upsilon(1\text{S})$  (red circles),  $\Upsilon(2\text{S})$  (blue squares), and  $\Upsilon(3\text{S})$  (green diamonds) at forward and backward rapidity for  $0 < p_{\text{T}} < 6 \text{ GeV}/c$  (left) and  $6 < p_{\text{T}} < 30 \text{ GeV}/c$  (right). The points are shifted horizontally for better visibility. Error bars on the points represent statistical and fit uncertainties and filled boxes represent systematic uncertainties. The gray box around the line at unity represents the global uncertainty due to luminosity normalization.

### 9.3 Forward-Backward Production Ratio

We study the forward-backward production ratio of  $\Upsilon$  mesons in pPb defined as follows,

$$R_{\text{FB}}(p_{\text{T}}, y_{\text{CM}} > 0) = \frac{(d^2\sigma(p_{\text{T}}, y_{\text{CM}})/dp_{\text{T}}dy_{\text{CM}})}{(d^2\sigma(p_{\text{T}}, -y_{\text{CM}})/dp_{\text{T}}dy_{\text{CM}})} \quad (9.3)$$

where  $y_{\text{CM}}$  is positive. We measure event activity near to the measured  $\Upsilon$  using the number of reconstructed tracks,  $N_{\text{tracks}}$ , in  $|\eta_{\text{lab}}| < 2.4$ . To measure event activity further from the  $\Upsilon$ , we use the sum of deposited transverse energy  $E_{\text{T}}$  in  $4 < |\eta_{\text{lab}}| < 5.2$ . Figure 9.7 shows the  $R_{\text{FB}}$  as a function  $N_{\text{tracks}}$  (left), and  $E_{\text{T}}$  (right). The uncorrected mean values of the event activity variables in minimum bias pPb collisions are  $\langle N_{\text{tracks}} \rangle = 41$  and  $\langle E_{\text{T}} \rangle = 14.7 \text{ GeV}$ . The measured  $R_{\text{FB}}$  remains consistent with unity at all levels of event activity for all three  $\Upsilon$  states. This observation is independent of the pseudorapidity region used to measure activity. The ALICE collaboration determined an  $R_{\text{FB}}$  consistent with unity for  $\Upsilon(1\text{S})$  for

integrated event activity for very forward  $y_{\text{CM}}$   $\Upsilon$  mesons [31]. The LHCb collaboration, also measuring  $\Upsilon(1\text{S})$   $R_{\text{FB}}$  in the very forward region, reported an integrated  $R_{\text{FB}}$  slightly less than unity [32]. By contrast to  $\Upsilon$  results, the  $R_{\text{FB}}$  for prompt and nonprompt  $J/\psi$  were found by CMS to diminish with increasing  $E_{\text{T}}$  [117].

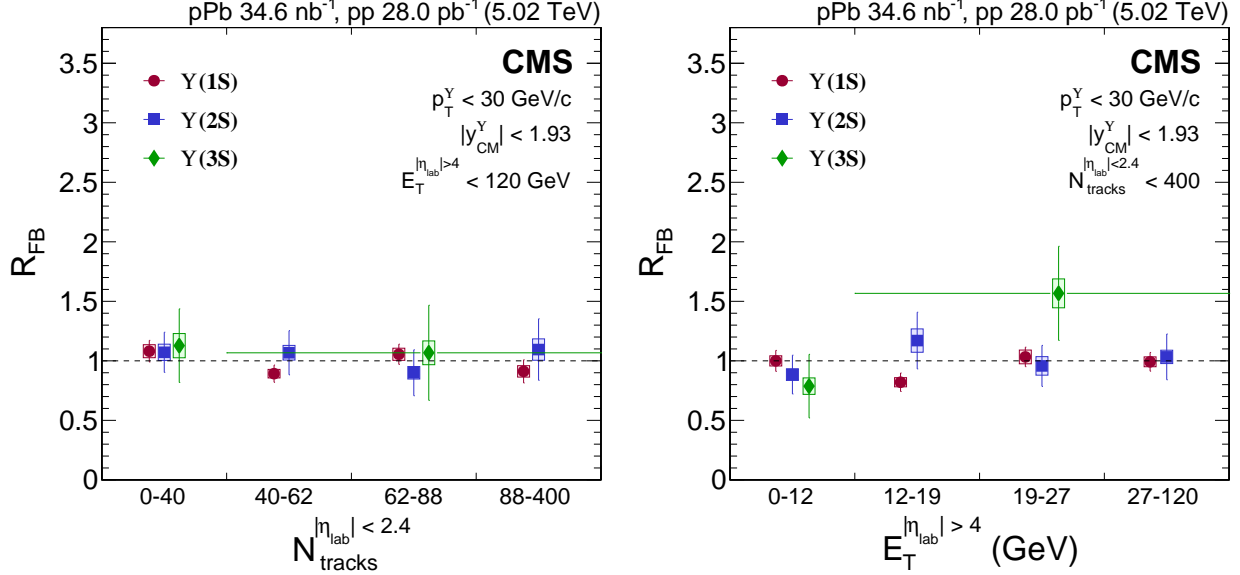


Figure 9.7:  $R_{\text{FB}}$  vs.  $N_{\text{tracks}}$  at mid pseudorapidity (left) and vs.  $E_{\text{T}}$  at forward/backward pseudorapidity (right) of  $\Upsilon(1\text{S})$  (red circles),  $\Upsilon(2\text{S})$  (blue squares), and  $\Upsilon(3\text{S})$  (green diamonds) for  $p_{\text{T}} < 30$  GeV/ $c$  and  $|y_{\text{CM}}| < 1.93$ . Error bars on the points represent statistical and fit uncertainties and filled boxes represent systematic uncertainties.

## 9.4 Suppression in Hot and Cold Nuclear Matter

Figure 9.8 shows the integrated  $R_{\text{pPb}}$  of  $\Upsilon$  states as well as, for comparison, the  $R_{\text{AA}}$  observed in PbPb collisions [29] at  $\sqrt{s_{\text{NN}}} = 5.02$  TeV. The 95 % confidence level on the  $\Upsilon(3\text{S})$   $R_{\text{AA}}$  is depicted using an arrow. The data indicate a sequential ordering of nuclear modification for the  $\Upsilon$  family with  $R_{\text{pPb}}(1\text{S}) > R_{\text{pPb}}(2\text{S}) > R_{\text{pPb}}(3\text{S})$ :

$$\Upsilon(1\text{S}) R_{\text{pPb}} = 0.773 \pm 0.023(\text{stat}) \pm 0.074(\text{syst})$$

$$\Upsilon(2\text{S}) R_{\text{pPb}} = 0.673 \pm 0.039(\text{stat}) \pm 0.083(\text{syst})$$

$$\Upsilon(3\text{S}) R_{\text{pPb}} = 0.514 \pm 0.056(\text{stat}) \pm 0.094(\text{syst})$$

We determine the  $p$ -values of the observed suppression in pPb collisions relative to pp collisions, under the hypothesis of  $A$ -scaling, to be  $1.70 \times 10^{-3}$ ,  $1.81 \times 10^{-4}$ , and  $4.45 \times 10^{-6}$  for  $\Upsilon(1S)$ ,  $\Upsilon(2S)$ , and  $\Upsilon(3S)$ , respectively. The corresponding significances ( $z$ -scores) are 2.9, 3.6, and 4.4 standard deviations, respectively. Furthermore, the  $p$ -values of additional suppression of excited states compared to the ground state are found to be  $1.45 \times 10^{-1}$  for  $\Upsilon(2S)$  and  $1.03 \times 10^{-2}$  for  $\Upsilon(3S)$ , corresponding to significances of 1.1 and 2.3 standard deviations, respectively. The differences in suppression level of the three states can be explained by the presence of final-state effects in pPb, such as the comover effect previously discussed. The observed differences in pPb are much more modest than the sequential suppression seen in PbPb [29]. A comparison of the  $R_{AA}$  to the  $R_{pPb}$ , scaled to reflect the presence of two lead nuclei instead of one in PbPb collisions, is needed to determine whether hot nuclear matter effects in the QGP result in additional suppression of bottomonia in PbPb. Additional modification in PbPb collisions compared to pPb collisions can be caused by the presence of color deconfinement as predicted by references [44, 54, 55, 59, 110], and possibly even enhanced comover interaction effects also present in the dense medium [28].

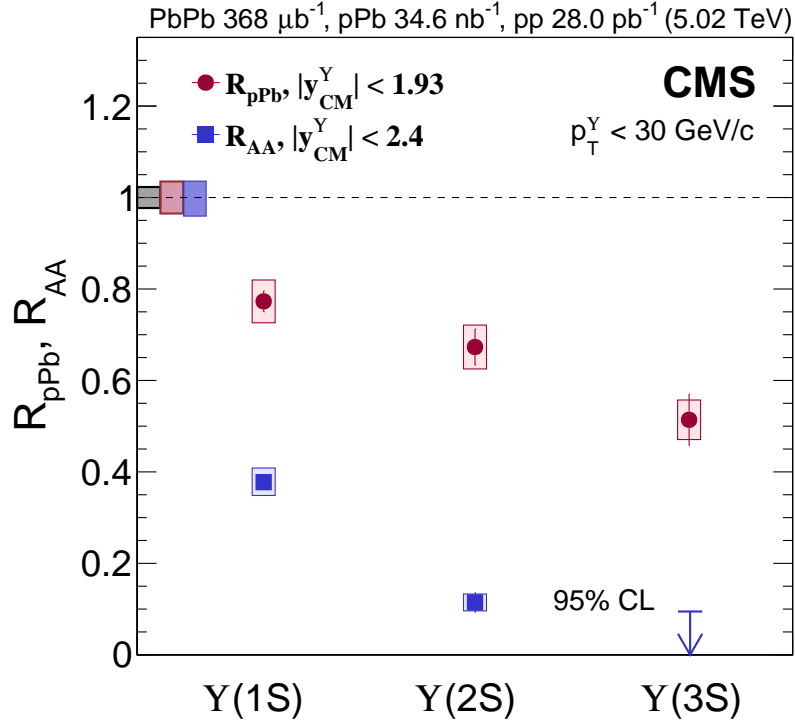


Figure 9.8:  $R_{\text{pPb}}$  of  $\Upsilon(1\text{S})$ ,  $\Upsilon(2\text{S})$  and  $\Upsilon(3\text{S})$  (red circles) for the integrated kinematic range  $0 < p_T < 30 \text{ GeV}$  and  $|y_{\text{CM}}| < 1.93$ . The  $R_{\text{pPb}}$  results are compared to the CMS results on  $\Upsilon$   $R_{\text{AA}}$  (blue squares for  $\Upsilon(1\text{S})$  and  $\Upsilon(2\text{S})$  and blue arrow for  $\Upsilon(3\text{S})$  at 95 % confidence level) for  $0 < p_T < 30 \text{ GeV}$  and  $|y_{\text{CM}}| < 2.4$  at the same energy [29]. Error bars represent statistical and fit uncertainties and filled boxes around points represent systematic uncertainties. The gray and red boxes around the line at unity depict the uncertainty in the pp and pPb luminosity normalizations, respectively. The blue box around unity depicts the global uncertainty pertaining to PbPb data.

## 9.5 Comparisons to Other Experiments

The four experiments at the LHC together provide coverage for collision data over a fairly large pseudorapidity range. The CMS and ATLAS experiments provide coverage at mid pseudorapidity, while ALICE and LHCb cover the complementary backward and forward regions. Although there are minor holes, the rapidity coverage for the  $R_{\text{pA}}$  of  $\Upsilon$  mesons extends to  $-4.46 < y_{\text{CM}} < 4.0$  when the results are combined. With the publication of the results presented in this report, all four experiments will have published the  $\Upsilon(1\text{S})$   $R_{\text{pA}}$  at 5.02 TeV [30, 31, 32]. Figure 9.9 shows the  $\Upsilon(1\text{S})$   $R_{\text{pA}}$  versus  $y_{\text{CM}}$  measured by the four LHC experiments. The data are compared to predictions from nPDF [26] (left) and E. Loss [27] (right) model calculations. While there is general agreement of the predictions with the data within uncertainties in the forward region starting at midrapidity, both predictions show worse agreement in the backward region, particularly overestimating the enhancement of the  $R_{\text{pA}}$  compared to the ALICE measurement at most backward rapidity. The two models predict very different behaviors of the  $R_{\text{pA}}$  at very forward rapidity. The current data do not have strong discerning power over these initial-state models. Data to be collected during run III of the LHC, with expected smaller uncertainties, will further help us study CNM modifications of  $\Upsilon$  yields in pPb collisions.

The ALICE and LHCb experiments have additionally reported the integrated  $\Upsilon(1\text{S})$   $R_{\text{FB}}$  in their respective rapidity regions [31, 32]. To compare our results to these values directly, we extract the  $\Upsilon(1\text{S})$  yields from the same fits that were used to extract  $\Upsilon(3\text{S})$  yields for the  $R_{\text{pA}}$  measurement, i.e. for  $0 < p_{\text{T}} < 30$  GeV/ $c$  in the  $-1.93 < y_{\text{CM}} < 0$  and  $0 < y_{\text{CM}} < 1.93$  bins. We then determine the integrated  $\Upsilon(1\text{S})$   $R_{\text{FB}}$  using the techniques described in chapters 7 and 8. Figure 9.10 shows the integrated  $\Upsilon(1\text{S})$   $R_{\text{FB}}$  values measured by the three experiments as a function of  $y_{\text{CM}}$ . While both CMS and ALICE have measured an  $R_{\text{FB}}$  consistent with unity, the ALICE measurement sits comfortably below the line at unity, indicating a relative suppression of the  $\Upsilon(1\text{S})$  yield at forward compared to backward rapidity. While the ALICE and LHCb data are mutually in agreement within uncertainties, whether or not the data

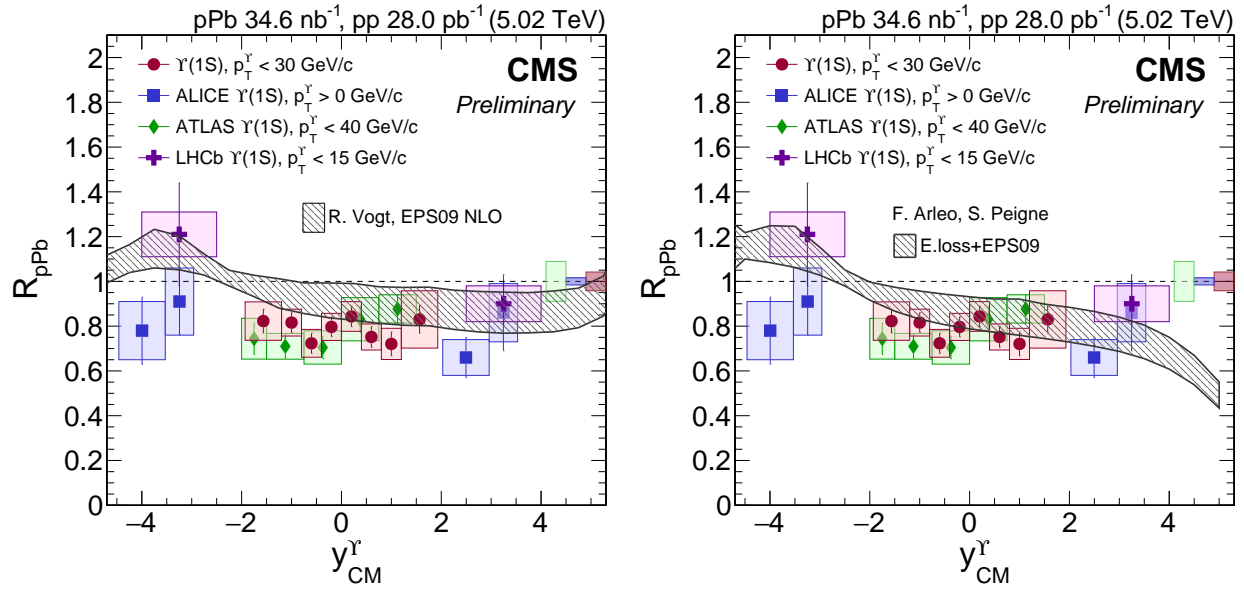


Figure 9.9:  $R_{pPb}$  of  $\Upsilon(1S)$  versus  $y_{CM}$  according to CMS (red circles), ATLAS [30] (green diamonds), ALICE [31] (blue squares) and LHCb [32] (purple vertical crosses) compared to predictions (shaded gray region) using nPDF [26] (left) and E. loss [27] (right) effects. Error bars on the points represent statistical and fit uncertainties and filled boxes represent systematic uncertainties. The green, blue and red boxes around the line at unity depict the global uncertainties for the ATLAS, ALICE and CMS data, respectively. All the uncertainty in the LHCb data are already incorporated into the uncertainties on the values shown.

indicate an  $R_{\text{FB}} < 1$  away from midrapidity is, nonetheless, in tension.

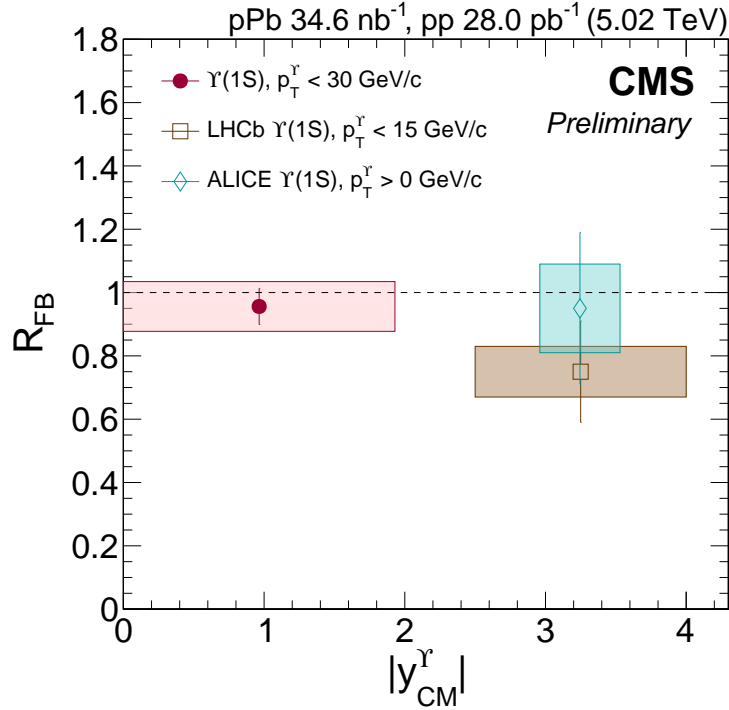


Figure 9.10: Integrated  $R_{\text{FB}}$  of  $\Upsilon(1\text{S})$  mesons according to CMS (red circle), ALICE [31] (teal open diamond) and LHCb [32] (brown open square) as a function of  $y_{\text{CM}}$ . Error bars represent statistical and fit uncertainties and filled boxes around points represent systematic uncertainties.

## 9.6 Conclusions

In summary, we studied the  $\Upsilon$  family in proton-lead (pPb) collisions at  $\sqrt{s_{\text{NN}}} = 5.02$  TeV in this report, measuring their production cross sections in a large kinematic interval around midrapidity. Using proton-proton collision data obtained at the same center-of-mass energy, we measured the pPb nuclear modification factors for the three  $\Upsilon$  states decaying in the dimuon channel. The  $\Upsilon$  yields are suppressed in pPb collisions relative to pp collisions under the hypothesis of  $A$ -scaling for all three states. Moreover, sequential ordering of the  $R_{\text{pPb}}$ , consistent with predictions from hadronic comover effects, is observed, indicating the presence of final-state effects in pPb collisions.

We observe the suppression of all three  $\Upsilon$  states in pPb collisions in the full kinematic range studied. No significant trend is seen for the suppression as functions of  $p_T$  or  $y_{CM}$ , although there is some indication of higher separation in the level of suppression of low- $p_T$  excited state  $\Upsilon$  in the lead-going direction.

Additionally, we studied the forward-backward production ratios of  $\Upsilon$  states as functions of event activity recorded both near to and far away from the rapidity region where  $\Upsilon$  mesons were measured. The  $R_{FB}$  values are consistent with unity for all states, independent of the region used to measure activity.

Finally, we compared integrated nuclear modification factors for  $\Upsilon$  to those obtained in lead-lead collisions at the same center-of-mass energy. The  $R_{AA}$  values are much smaller than the corresponding  $R_{pPb}$  value for each state, as expected in the presence of two lead ions as well as deconfinement effects in lead-lead collisions. Together, all of these results will help to elucidate the contributions of cold and hot nuclear matter effects to the modification of bottomonia in heavy-ion collisions.

We have seen in this report the pivotal role that nuclear modification factors of heavy flavor mesons, in particular quarkonia, play in constraining the hydrodynamic properties of the early-stage QGP such as its temperature and bulk viscosity. By measuring moments of their flow, we can also use these hard probes to study the expansion of the late-stage QGP, which provides a look into the nature of the initial spatial anisotropy of the medium.

Far from equilibrium, the QGP expands anisotropically, with the pressure gradient determined by the temperature and energy density distributions resulting from the initial ion-ion collision [107]. Throughout the extended period of hydrodynamic evolution of the plasma, its pressure anisotropy evolves as well, reaching eventual isotropy and complete thermalization at a much later time [156]. This directed expansion of the QGP and its constituents is known as flow. The second moment of the late-stage flow, known as elliptic flow  $v_2$ , which quantifies the discrepancy between the transverse and longitudinal pressures, therefore embodies a measure of the initial anisotropy and well as its evolution.

The  $v_2$  of the bulk of the plasma can be measured using the constituent light partons. Heavy quarks, on the other hand, exhibit different collective properties than the bulk, since they are created in initial hard scatterings and do not equilibrate with the early-stage QGP. In order for the bulk flow to be transmitted to heavy quarks, there need to be frequent and relatively-hard collisions between the heavy quarks and the light partons in the QGP after the spatial anisotropy of the plasma has been converted to momentum space anisotropy (which takes time). Much like ordinary diffusion, this transfer is gradual and extends throughout the hydrodynamic evolution, with the heavy flavor mesons with low transverse momentum ( $\lesssim T$ ) being the most affected.

The  $v_2$  of heavy flavor mesons with higher transverse momentum, however, is determined predominantly by the path lengths of the heavy quarks in the QGP [24, 141, 157, 158, 159, 160], since heavy quarks and heavy flavor mesons are affected in a myriad of ways inside the QGP (see sections 1.2 to 1.4). Therefore, measurements of the elliptic flow of open and hidden heavy flavor, and in particular its transverse-momentum dependence, can help investigate momentum transfer mechanisms and the in-medium modification of the Debye mass in the plasma, as well as properties of the early-stage QGP such as its temperature and energy profiles, spacial anisotropies, and shear and bulk viscosities [156, 157, 158, 159, 160]. Future studies of bottomonia in pPb and PbPb collisions should be geared towards such measurements to complement the measurement of nuclear modification factors presented here.

# Appendix A

## Consistency Checks

We present studies consisting of comparisons and cross checks that justify some of the choices we made in this analysis. First, we justify the merging of the two sets of pPb data to be analyzed as one. This study is presented in A.1.

Next, since we use pp data that has previously been analyzed by other teams at CMS, we can test our analysis software against theirs. We compare the computed  $\Upsilon$  cross sections with those from reference [33] to ensure that they agree in shared bins between the two analysis. This cross check is included in A.2.

Finally, we perform some checks on the efficiency corrections which combines the MC dimuon efficiency and the T&P single-muon efficiency corrections. In A.3 we study the dimuon efficiency with and without the T&P corrections. We include plots of variations of the efficiency correction factors due to variations in the T&P corrections in A.4. These variations are used to determine the systematic uncertainty in the results due to efficiency correction. In A.5 we present the relative contributions of T&P uncertainties to the total uncertainty in efficiency. We use the  $\Upsilon(1S)$  bins as representatives for all three checks.

## A.1 Comparison of $\Upsilon$ cross sections in pPb data in two directions

Before merging the two pPb data sets corresponding to the two beam directions, we fit them individually using fitting techniques described in 6.3 and extract the  $\Upsilon$  yields. We use these yields to determine the cross section of each state in the two runs. The cross sections are shown in figures A.1, A.2 and A.3. Since the  $\Upsilon$  cross sections in pPb data with and without the beams reversed are in agreement within statistical uncertainties, we conclude that the detector is sufficiently uniform that the two sets of data can be reliably merged.

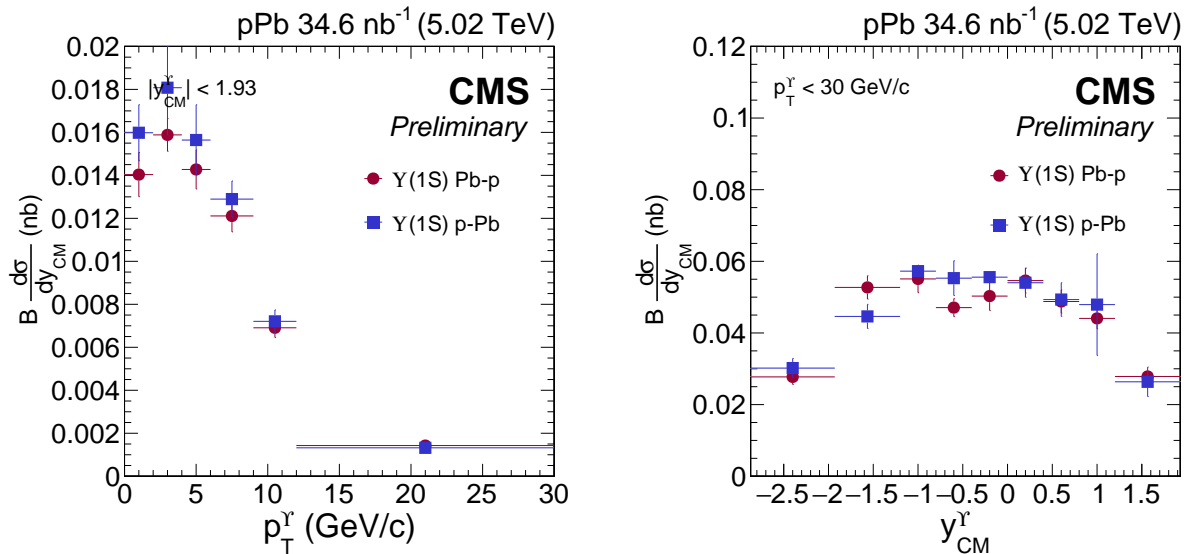


Figure A.1: Comparison of cross sections of  $\Upsilon(1S)$  using yields extracted from Pb-p and p-Pb data.

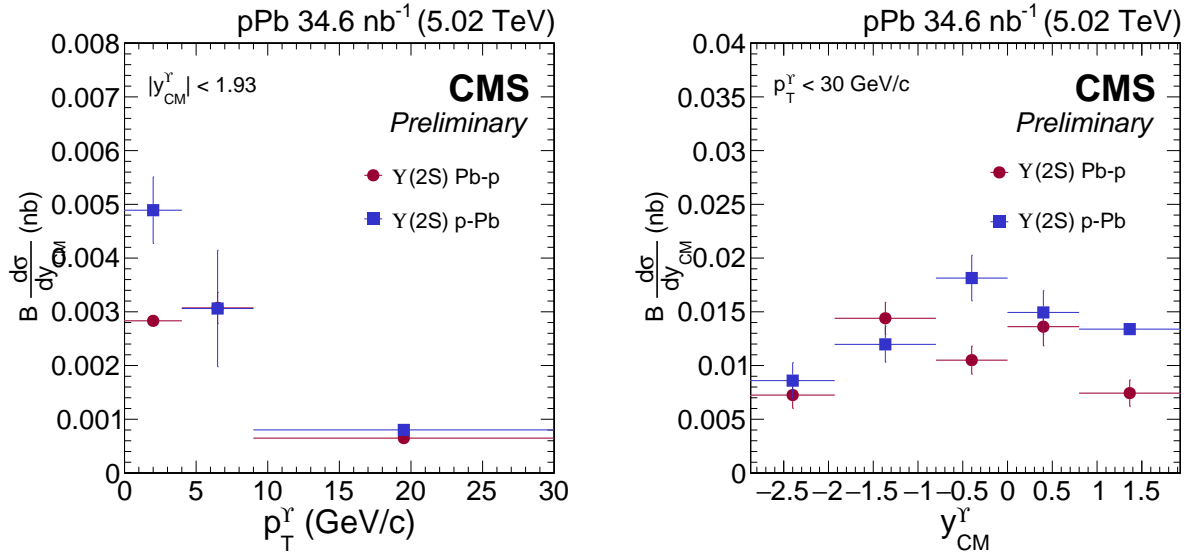


Figure A.2: Comparison of cross sections of  $\Upsilon(2S)$  using yields extracted from Pb-p and p-Pb data.

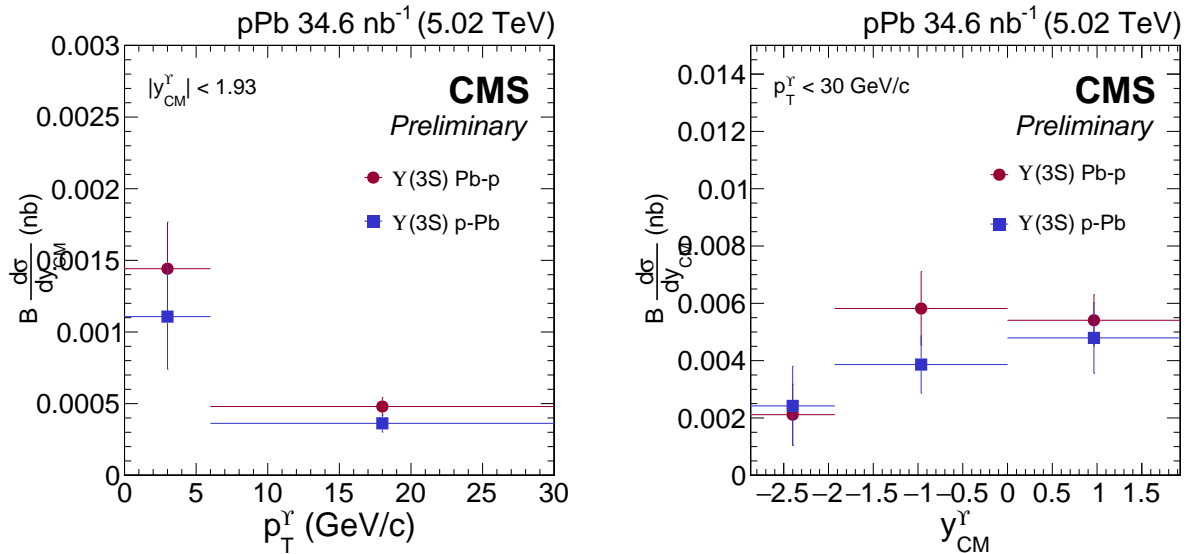


Figure A.3: Comparison of cross sections of  $\Upsilon(3S)$  using yields extracted from Pb-p and p-Pb data.

## A.2 Comparison of $\Upsilon$ cross sections in pp data measured in two analyses

The cross sections of  $\Upsilon(1S)$ ,  $\Upsilon(2S)$  and  $\Upsilon(3S)$  as functions of  $p_T$  and  $|y|$  in pp collisions obtained in this report are compared with those from reference [33] in figure A.4. The results are found to be consistent within statistical and systematic uncertainties, validating the analysis methodology reported here.

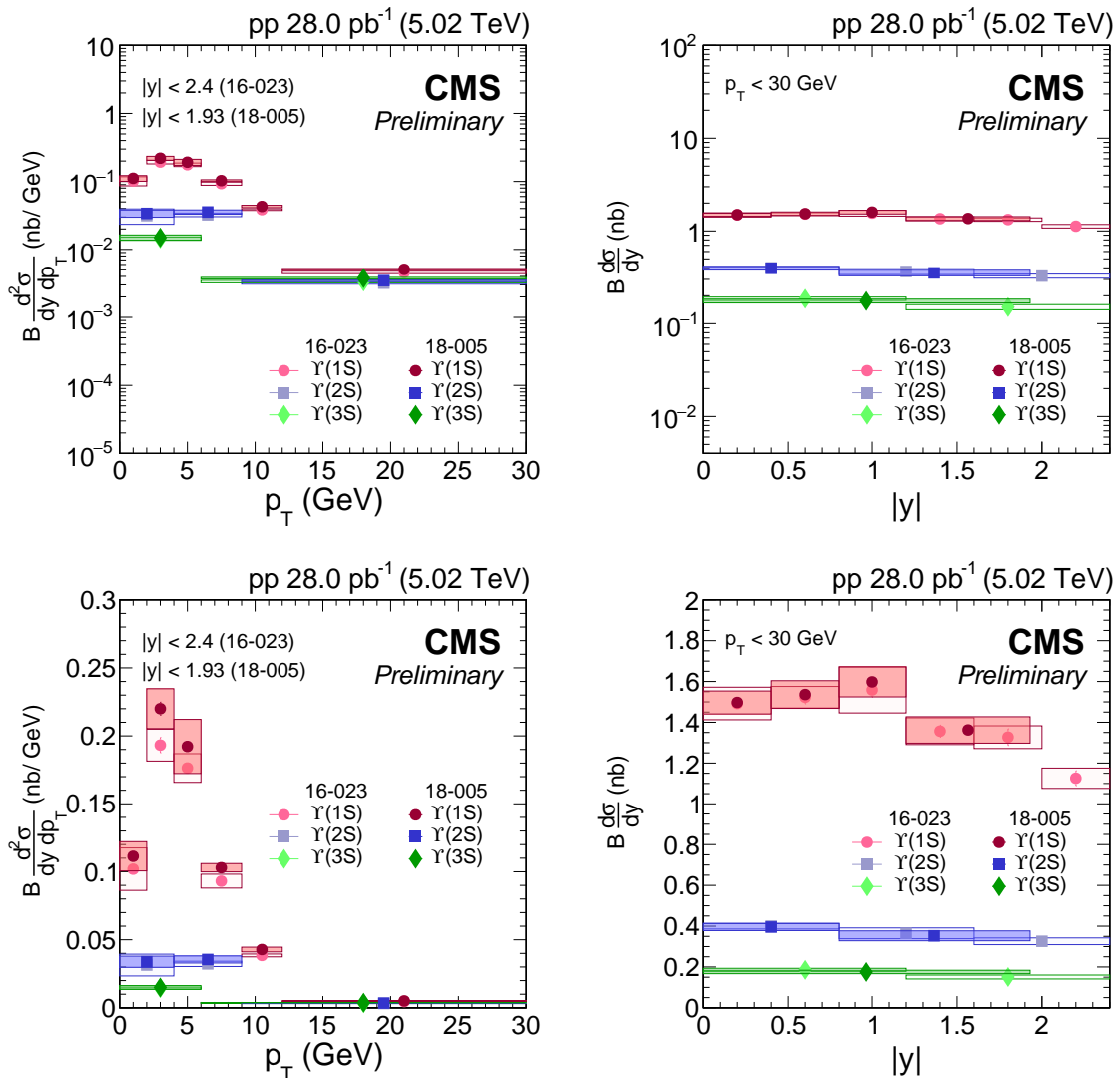


Figure A.4: Cross Section of  $\Upsilon(1S)$ ,  $\Upsilon(2S)$  and  $\Upsilon(3S)$  as a function of  $p_T$  and  $|y|$  in pp collisions obtained in the analysis presented here compared with those obtained in reference [33] on a log scale (top) and a linear scale (bottom).

### A.3 Study of efficiency with and without T&P weighting

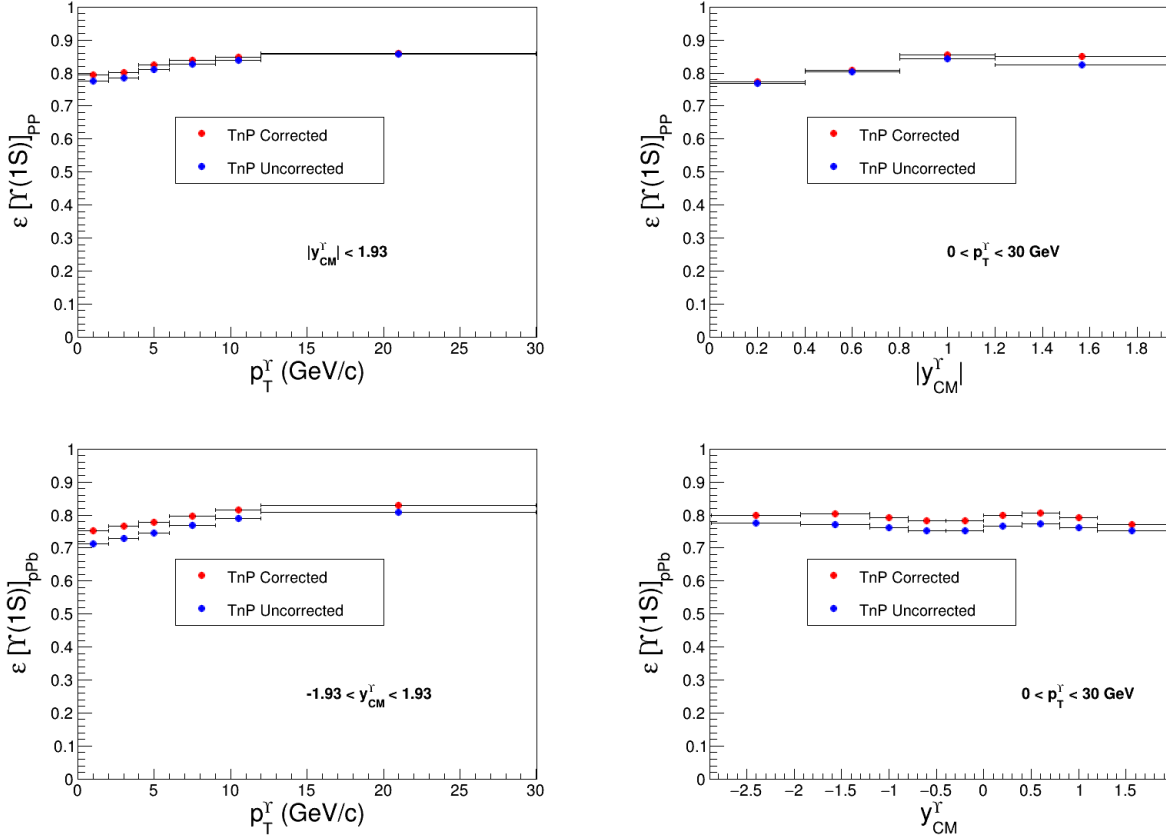


Figure A.5: Efficiencies of  $\Upsilon(1S)$  versus  $p_T$  and rapidity in pp (top) and pPb (bottom) MC with and without T&P weighting.

## A.4 Variations in efficiency due to sources of T&P uncertainty

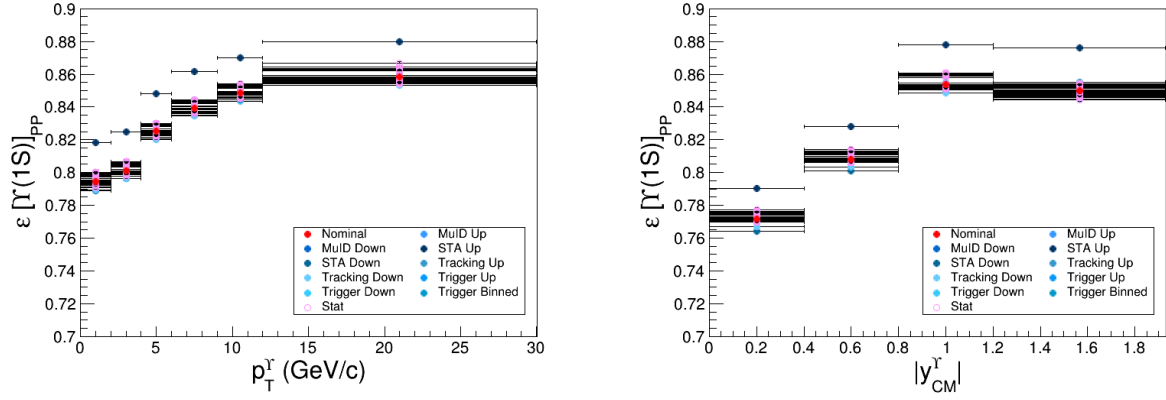


Figure A.6: Variations in the  $\Upsilon(1S)$  efficiency in pp collisions due to T&P corrections shown as a function of  $p_T$  and  $|y|$ .

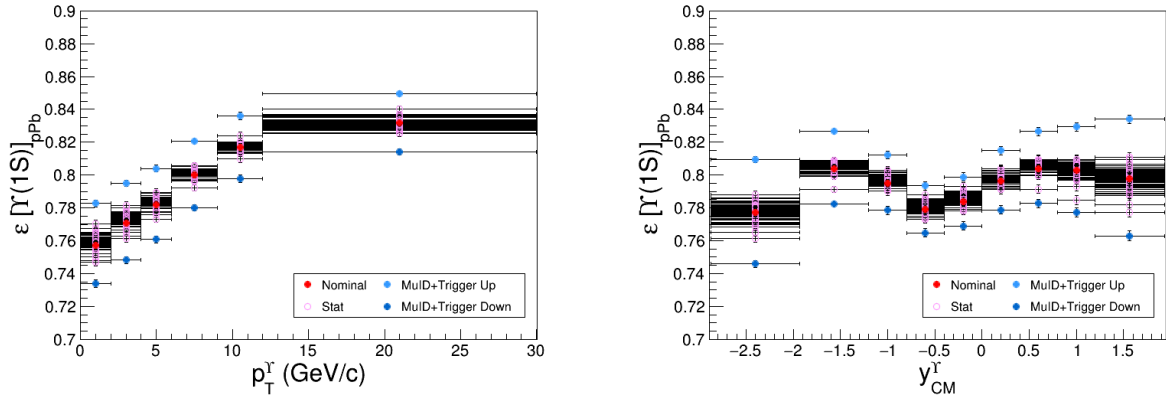


Figure A.7: Variations in the  $\Upsilon(1S)$  efficiency in pPb collisions due to T&P corrections shown as a function of  $p_T$  and  $y_{CM}$ .

## A.5 Relative contributions of T&P uncertainties

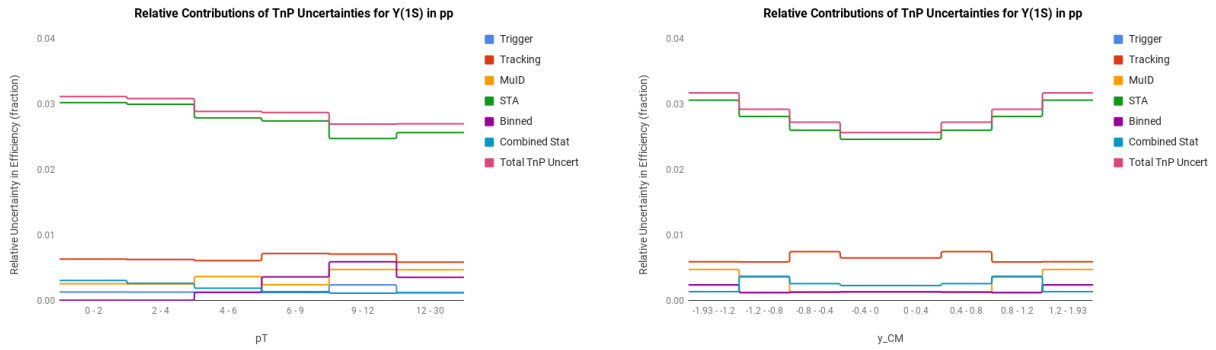


Figure A.8: Relative contributions to the uncertainty in  $\Upsilon(1S)$  efficiency of various sources of T&P systematic variations in pp collisions.

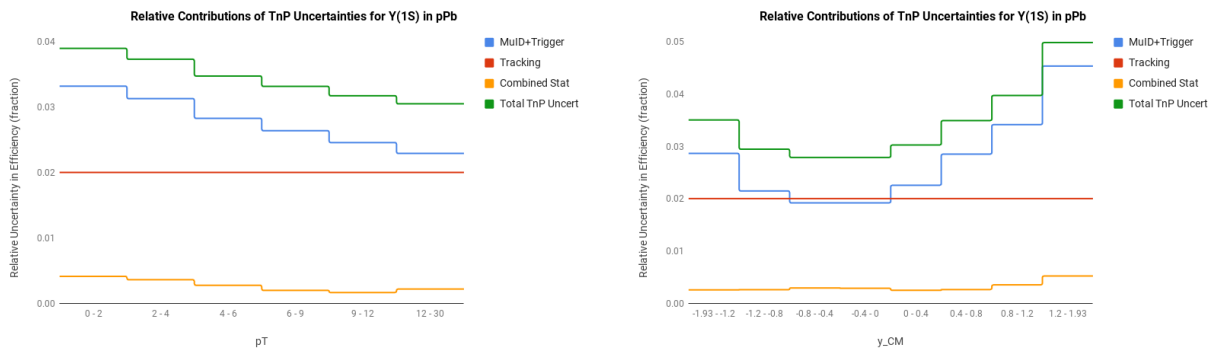


Figure A.9: Relative contributions to the uncertainty in  $\Upsilon(1S)$  efficiency of various sources of T&P systematic variations in pPb collisions.

# Bibliography

- [1] S. M. Ryan. The symmetries of qcd (and consequences). [https://www.rug.nl/research/vsi/events/qu8/talks/qu8sym\\_ryan.pdf](https://www.rug.nl/research/vsi/events/qu8/talks/qu8sym_ryan.pdf), Mar 2018.
- [2] A. Deur, S. J. Brodsky, and G. F. de Teramond. The QCD Running Coupling. *Prog. Part. Nucl. Phys.*, 90:1–74, 2016. doi: 10.1016/j.pnpnp.2016.04.003.
- [3] A. Maire. Phase diagram of QCD matter : Quark-Gluon Plasma, Jun 2015. URL <https://cds.cern.ch/record/2025215>. General Photo.
- [4] A. Rothkopf. Quarkonium. [https://indico.cern.ch/event/656452/contributions/2953749/attachments/1648288/2635177/QM2018\\_QUARKONIUM\\_FINAL.pdf](https://indico.cern.ch/event/656452/contributions/2953749/attachments/1648288/2635177/QM2018_QUARKONIUM_FINAL.pdf), May 2018.
- [5] Y. Burnier, O. Kaczmarek, and A. Rothkopf. Quarkonium at finite temperature: Towards realistic phenomenology from first principles. *JHEP*, 12:101, 2015. doi: 10.1007/JHEP12(2015)101.
- [6] K. J. Eskola, P. Paakkinen, H. Paukkunen, and C. A. Salgado. EPPS16: Nuclear parton distributions with LHC data. *Eur. Phys. J. C*, 77(3):163, 2017. doi: 10.1140/epjc/s10052-017-4725-9.
- [7] F. Gelis, T. Lappi, and R. Venugopalan. High energy scattering in Quantum Chromodynamics. *Int. J. Mod. Phys.*, E16:2595–2637, 2007. doi: 10.1142/S0218301307008331.

- [8] F. Arleo and S. Peigné. Heavy-quarkonium suppression in p-A collisions from parton energy loss in cold QCD matter. *JHEP*, 03:122, 2013. doi: 10.1007/JHEP03(2013)122.
- [9] E. G. Ferreira. Excited charmonium suppression in proton–nucleus collisions as a consequence of comovers. *Phys. Lett.*, B749:98–103, 2015. doi: 10.1016/j.physletb.2015.07.066.
- [10] R. Vogt. *Ultrarelativistic Heavy-Ion Collisions*. Elsevier, Oxford, UK, 2007.
- [11] E. G. Ferreira and C. Pajares. High multiplicity  $pp$  events and  $J/\psi$  production at LHC. *Phys. Rev. C*, 86:034903, 2012. doi: 10.1103/PhysRevC.86.034903.
- [12] P. Mouche. Overall view of the LHC. Vue d’ensemble du LHC, Jun 2014. URL <https://cds.cern.ch/record/1708847>. General Photo.
- [13] T. Sakuma and T. McCauley. Detector and event visualization with SketchUp at the CMS experiment. *J. Phys. Conf. Ser.*, 513(2):022032, jun 2014. doi: 10.1088/1742-6596/513/2/022032.
- [14] CMS Collaboration. The CMS experiment at the CERN LHC. *JINST*, 3:S08004, 2008. doi: 10.1088/1748-0221/3/08/S08004.
- [15] A. Rao and E. Butz. Extraction of CMS Barrel Pixel (BPIX) detector prior to upgrade. CMS Collection., Jan 2017. URL <https://cds.cern.ch/record/2243068>.
- [16] View of the inside of the TIB Layer 3. Vue de l’intérieur de la couche 3 du TIB. CMS Collection., May 2003. URL <https://cds.cern.ch/record/937277>.
- [17] D. Barney. HB+ prepares for insertion into the CMS solenoid. CMS Collection., Mar 2006. URL <https://cds.cern.ch/record/938513>.
- [18] L. Guiraud. The CMS forward calorimeter with quartz fibres. Aug 1999. URL <https://cds.cern.ch/record/40755>.

- [19] CMS Collaboration. Performance of CMS muon reconstruction in  $pp$  collision events at  $\sqrt{s} = 7$  TeV. *JINST*, 7:P10002, 2012. doi: 10.1088/1748-0221/7/10/P10002.
- [20] D. Acosta. Muon detectors in cms. <http://www.phys.ufl.edu/~acosta/cms/cmshi.pdf>, Feb 2002.
- [21] M. F. Shopova and P. Iaydjiev. Performance of the CMS RPC system – from LS1 upgrade to RUN2 at LHC, Mar 2018. URL <http://cds.cern.ch/record/2626243>. Presented 12 Jun 2018.
- [22] G. S. Chahal. Data Monte Carlo preparation in CMS. [https://conference.ippp.dur.ac.uk/event/704/attachments/3462/3813/CMS\\_data\\_mc\\_IPPP.pdf](https://conference.ippp.dur.ac.uk/event/704/attachments/3462/3813/CMS_data_mc_IPPP.pdf), May 2018.
- [23] B. Krouppa and M. Strickland. Predictions for bottomonia suppression in 5.023 TeV Pb-Pb collisions. *Universe*, 2(3):16, 2016. doi: 10.3390/universe2030016.
- [24] X. Du, R. Rapp, and M. He. Color Screening and Regeneration of Bottomonia in High-Energy Heavy-Ion Collisions. *Phys. Rev. C*, 96(5):054901, 2017. doi: 10.1103/PhysRevC.96.054901.
- [25] CMS Collaboration. Suppression of  $\Upsilon(1S)$ ,  $\Upsilon(2S)$  and  $\Upsilon(3S)$  production in PbPb collisions at  $\sqrt{s_{NN}} = 2.76$  TeV. *Phys. Lett. B*, 770:357, 2017. doi: 10.1016/j.physletb.2017.04.031.
- [26] R. Vogt. Shadowing effects on  $J/\psi$  and  $\Upsilon$  production at energies available at the CERN Large Hadron Collider. *Phys. Rev. C*, 92(3):034909, 2015. doi: 10.1103/PhysRevC.92.034909.
- [27] F. Arleo and S. Peigné. Quarkonium suppression in heavy-ion collisions from coherent energy loss in cold nuclear matter. *JHEP*, 10:073, 2014. doi: 10.1007/JHEP10(2014)073.

- [28] E. G. Ferreira and J.-P. Lansberg. Is bottomonium suppression in proton-nucleus and nucleus-nucleus collisions at LHC energies due to the same effects? *JHEP*, 10:094, 2018. doi: 10.1007/JHEP03(2019)063,10.1007/JHEP10(2018)094. [Erratum: *JHEP*03,063(2019)].
- [29] CMS Collaboration. Measurement of nuclear modification factors of  $\Upsilon(1S)$ ,  $\Upsilon(2S)$ , and  $\Upsilon(3S)$  mesons in PbPb collisions at  $\sqrt{s_{NN}} = 5.02$  TeV. *Phys. Lett. B*, 790:270 – 293, 2019. ISSN 0370-2693. doi: 10.1016/j.physletb.2019.01.006.
- [30] ATLAS Collaboration. Measurement of quarkonium production in proton–lead and proton–proton collisions at 5.02 TeV with the ATLAS detector. *Eur. Phys. J. C*, 78(3):171, 2018. doi: 10.1140/epjc/s10052-018-5624-4.
- [31] ALICE Collaboration. Production of inclusive  $\Upsilon(1S)$  and  $\Upsilon(2S)$  in p-Pb collisions at  $\sqrt{s_{NN}} = 5.02$  TeV. *Phys. Lett.*, B740:105–117, 2015. doi: 10.1016/j.physletb.2014.11.041.
- [32] LHCb Collaboration. Study of  $\Upsilon$  production and cold nuclear matter effects in  $p$ Pb collisions at  $\sqrt{s_{NN}}=5$  TeV. *JHEP*, 07:094, 2014. doi: 10.1007/JHEP07(2014)094.
- [33] CMS Collaboration. Measurement of Nuclear Modification Factors of  $\Upsilon(nS)$  Mesons in PbPb Collisions at  $\sqrt{s_{NN}} = 5.02$  TeV. Technical report, CERN, Geneva, 2017. URL <http://cds.cern.ch/record/2244680>.
- [34] H. Sazdjian. Introduction to chiral symmetry in QCD. *EPJ Web. Conf.*, 137:02001, 2017. doi: 10.1051/epjconf/201713702001.
- [35] G. M. Prosperi, M. Raciti, and C. Simolo. On the running coupling constant in QCD. *Prog. Part. Nucl. Phys.*, 58:387–438, 2007. doi: 10.1016/j.pnpnp.2006.09.001.
- [36] C. Nassif, J. A. Helayel-Neto, and P. Silva. Asymptotic freedom and quarks confinement treated through thompson’s approach. *Can. J. Phys.*, 94, 06 2007. doi: 10.1139/cjp-2016-0242.

- [37] M. Botje. Quantum chromo dynamics. <https://www.nikhef.nl/~h24/qcdcourse/section-6.pdf>, Dec 2013.
- [38] F. Gelis, E. Iancu, J. Jalilian-Marian, and R. Venugopalan. The Color Glass Condensate. *Ann. Rev. Nucl. Part. Sci.*, 60:463–489, 2010. doi: 10.1146/annurev.nucl.010909.083629.
- [39] Y. V. Kovchegov and E. Levin. *Quantum Chromodynamics at High Energy*. Cambridge Monographs on Particle Physics, Nuclear Physics and Cosmology. Cambridge University Press, 2012. doi: 10.1017/CBO9781139022187.
- [40] S. Borsanyi. Frontiers of finite temperature lattice QCD. *EPJ Web Conf.*, 137:01006, 2017. doi: 10.1051/epjconf/201713701006.
- [41] P. Di Vecchia. Large N gauge theories and AdS/CFT correspondence. In *Superstrings and related matters*, pages 1–70, 1999.
- [42] E. Witten. Anti-de Sitter space, thermal phase transition, and confinement in gauge theories. *Adv. Theor. Math. Phys.*, 2:505–532, 1998. doi: 10.4310/ATMP.1998.v2.n3.a3. [,89(1998)].
- [43] M. Caselle. Lattice gauge theories and the AdS/CFT correspondence. *Int. J. Mod. Phys.*, A15:3901–3966, 2000. doi: 10.1142/S0217751X00002042,10.1016/S0217-751X(00)00204-2,10.1142/S0217751X00002044.
- [44] N. Brambilla et al. Heavy quarkonium: progress, puzzles, and opportunities. *Eur. Phys. J. C*, 71:1534, 2011. doi: 10.1140/epjc/s10052-010-1534-9.
- [45] R. Averbeck. Heavy-flavor production in heavy-ion collisions and implications for the properties of hot QCD matter. *Prog. Part. Nucl. Phys.*, 70(159), 2013. doi: 10.1016/j.pnpnp.2013.01.001.
- [46] A. Bazavov et al. Chiral crossover in QCD at zero and non-zero chemical potentials. *Phys. Lett. B*, 795:15 – 21, 2019. ISSN 0370-2693. doi: 10.1016/j.physletb.2019.05.013.

- [47] HotQCD Collaboration. The QCD crossover at zero and non-zero baryon densities from Lattice QCD. *Nucl. Phys. A*, 982:847 – 850, 2019. ISSN 0375-9474. doi: 10.1016/j.nuclphysa.2018.08.025.
- [48] E. Megias, E. R. Arriola, and L. L. Salcedo. The Quark-antiquark potential at finite temperature and the dimension two gluon condensate. *Phys. Rev. D*, 75:105019, 2007. doi: 10.1103/PhysRevD.75.105019.
- [49] S. J. Brodsky and R. Shrock. Condensates in quantum chromodynamics and the cosmological constant. 108(1):45–50, 2011. doi: 10.1073/pnas.1010113107.
- [50] STAR Collaboration. Bulk Properties of the Medium Produced in Relativistic Heavy-Ion Collisions from the Beam Energy Scan Program. *Phys. Rev. C*, 96(4):044904, 2017. doi: 10.1103/PhysRevC.96.044904.
- [51] M. A. Stephanov. Non-Gaussian fluctuations near the QCD critical point. *Phys. Rev. Lett.*, 102:032301, 2009. doi: 10.1103/PhysRevLett.102.032301.
- [52] M. Asakawa and M. Kitazawa. Fluctuations of conserved charges in relativistic heavy ion collisions: An introduction. *Prog. Part. Nucl. Phys.*, 90:299 – 342, 2016. ISSN 0146-6410. doi: 10.1016/j.ppnp.2016.04.002.
- [53] M. A. Stephanov. On the sign of kurtosis near the QCD critical point. *Phys. Rev. Lett.*, 107:052301, 2011. doi: 10.1103/PhysRevLett.107.052301.
- [54] J. W. Harris and B. Müller. The search for the quark gluon plasma. *Ann. Rev. Nucl. Part. Sci.*, 46(1):71–107, 1996. doi: 10.1146/annurev.nucl.46.1.71.
- [55] J. F. Gunion and R. Vogt. Determining the existence and nature of the quark-gluon plasma by Upsilon suppression at the LHC. *Nucl. Phys. B*, 492:301–337, 1997. doi: 10.1016/S0550-3213(97)80037-5.
- [56] M. Strickland. Thermal Bottomonium Suppression. *AIP Conf. Proc.*, (1520):179–184, 2013. doi: 10.1063/1.4795953.

- [57] F. Arleo, C.-J. Naim, and S Platchkov. Initial-state energy loss in cold QCD matter and the Drell-Yan process. *JHEP*, 01:129, 2019. doi: 10.1007/JHEP01(2019)129.
- [58] N. Armesto and E. Scomparin. Heavy-ion collisions at the Large Hadron Collider: a review of the results from Run 1. *Eur. Phys. J. Plus*, 131(3):52, 2016. doi: 10.1140/epjp/i2016-16052-4.
- [59] A. Andronic et al. Heavy-flavour and quarkonium production in the LHC era: from proton-proton to heavy-ion collisions. *Phys. J. C*, 76(107), 2016. doi: 10.1140/epjc/s10052-015-3819-5.
- [60] R. Sharma and I. Vitev. High transverse momentum quarkonium production and dissociation in heavy ion collisions. *Phys. Rev. C*, 87(4):044905, 2013. doi: 10.1103/PhysRevC.87.044905.
- [61] T. Matsui and H. Satz.  $J/\psi$  Suppression by Quark-Gluon Plasma Formation. *Phys. Lett.*, B178:416–422, 1986. doi: 10.1016/0370-2693(86)91404-8.
- [62] S. Digal, P. Petreczky, and H. Satz. Quarkonium Feed-Down and Sequential Suppression. *Phys.Rev. D*, 64(094015), 2001. doi: 10.1103/PhysRevD.64.094015.
- [63] S. Kim, P. Petreczky, and A. Rothkopf. In-medium quarkonium properties from a lattice QCD based effective field theory. *Nucl. Phys.*, A956:713–716, 2016. doi: 10.1016/j.nuclphysa.2015.12.011.
- [64] A. Rothkopf. What lattice QCD spectral functions can tell us about heavy quarkonium in the QGP. *PoS, ICHEP2016*:362, 2016.
- [65] Y. Burnier, M. Laine, and M. Vepsalainen. Dimensionally regularized Polyakov loop correlators in hot QCD. *JHEP*, 01:054, 2010. doi: 10.1007/JHEP01(2010)054,10.1007/JHEP01(2013)180. [Erratum: JHEP01,180(2013)].

- [66] N. Brambilla, J. Ghiglieri, P. Petreczky, and A. Vairo. The Polyakov loop and correlator of Polyakov loops at next-to-next-to-leading order. *Phys. Rev. D*, 82:074019, 2010. doi: 10.1103/PhysRevD.82.074019.
- [67] A. Jakovac, P. Petreczky, K. Petrov, and A. Velytsky. Quarkonium correlators and spectral functions at zero and finite temperature. *Phys. Rev. D*, 75:014506, 2007. doi: 10.1103/PhysRevD.75.014506.
- [68] M. Laine, O. Philipsen, P. Romatschke, and M. Tassler. Real-time static potential in hot QCD. *JHEP*, 03:054, 2007. doi: 10.1088/1126-6708/2007/03/054.
- [69] S. Chen and M. He. Gluo-dissociation of heavy quarkonium in the quark-gluon plasma reexamined. *Phys. Rev. C*, 96(3):034901, 2017. doi: 10.1103/PhysRevC.96.034901.
- [70] J.-P. Blaizot, D. De Boni, P. Faccioli, and G. Garberoglio. Heavy quark bound states in a quark–gluon plasma: Dissociation and recombination. *Nucl. Phys.*, A946:49–88, 2016. doi: 10.1016/j.nuclphysa.2015.10.011.
- [71] R. Arnaldi. Experimental overview on quarkonium production. *Nucl. Phys. A*, 956: 128–135, 2016. doi: 10.1016/j.nuclphysa.2016.03.033.
- [72] R. Vogt. Cold nuclear matter effects on  $J/\psi$  and  $\Upsilon$  production at energies available at the CERN Large Hadron Collider (LHC). *Phys. Rev. C*, 81:044903, Apr 2010. doi: 10.1103/PhysRevC.81.044903.
- [73] A. Accardi et al. Parton Propagation and Fragmentation in QCD Matter. *Riv. Nuovo Cim.*, 32:439–553, 2010. doi: 10.1393/ncr/i2009-10048-0.
- [74] M. C. Chu and T. Matsui. Dynamic Debye screening for a heavy-quark-anti-quark pair traversing a quark - gluon plasma. *Phys. Rev. D*, 39:1892, 1989. doi: 10.1103/PhysRevD.39.1892.

- [75] J. L. Albacete and C. Marquet. Gluon saturation and initial conditions for relativistic heavy ion collisions. *Prog. Part. Nucl. Phys.*, 76:1–42, 2014. doi: 10.1016/j.pnpnp.2014.01.004.
- [76] PHENIX Collaboration. Creation of quark–gluon plasma droplets with three distinct geometries. *Nat. Phys.*, 15:214–220, 2019. doi: 10.1038/s41567-018-0360-0.
- [77] J. L. Nagle and W. A. Zajc. Small system collectivity in relativistic hadronic and nuclear collisions. *Annual Review of Nuclear and Particle Science*, 68(1):211–235, 2018. doi: 10.1146/annurev-nucl-101916-123209.
- [78] K. Dusling, W. Li, and B. Schenke. Novel collective phenomena in high-energy proton–proton and proton–nucleus collisions. *Int. J. Mod. Phys.*, E25(01):1630002, 2016. doi: 10.1142/S0218301316300022.
- [79] ALICE Collaboration. Search for collectivity with azimuthal  $J/\psi$ -hadron correlations in high multiplicity p-Pb collisions at  $\sqrt{s_{NN}}= 5.02$  and 8.16 TeV. *Phys. Lett.*, B780:7–20, 2018. doi: 10.1016/j.physletb.2018.02.039.
- [80] K. J. Eskola. Scale dependence of nuclear gluon structure. *Nucl. Phys. B*, 400(1):240–266, 1993. ISSN 0550-3213. doi: 10.1016/0550-3213(93)90406-F.
- [81] M. Arneodo. Nuclear effects in structure functions. *Phys. Rept.*, 240:301–393, 1994. doi: 10.1016/0370-1573(94)90048-5.
- [82] W. Z. Ben. Shadowing, dipions and the EMC effect. *Z. Phys. C Particles and Fields*, 46(2):293–297, Jun 1990. ISSN 1431-5858. doi: 10.1007/BF01556007.
- [83] L. L. Frankfurt, M. I. Strikman, and S. Liuti. Evidence for enhancement of gluon and valence-quark distributions in nuclei from hard lepton-nucleus processes. *Phys. Rev. Lett.*, 65:1725–1728, Oct 1990. doi: 10.1103/PhysRevLett.65.1725.

- [84] J.J. Aubert et al. The ratio of the nucleon structure functions  $F_2^N$  for iron and deuterium. *Phys. Lett. B*, 123(3):275 – 278, 1983. ISSN 0370-2693. doi: 10.1016/0370-2693(83)90437-9.
- [85] Y. L. Dokshitzer. Calculation of the Structure Functions for Deep Inelastic Scattering and  $e^+e^-$  Annihilation by Perturbation Theory in Quantum Chromodynamics. *Sov. Phys. JETP*, 46:641–653, 1977. [*Zh. Eksp. Teor. Fiz.*73,1216(1977)].
- [86] A. D. Martin. Proton structure, Partons, QCD, DGLAP and beyond. *Acta. Phys. Polon.*, B39:2025–2062, 2008.
- [87] PHENIX Collaboration. Centrality dependence of  $\pi_0$  and  $\eta$  production at large transverse momentum in  $\sqrt{s_{NN}}=200$  GeV d+Au collisions. *Phys. Rev. Lett.*, 98:172302, 2007. doi: 10.1103/PhysRevLett.98.172302.
- [88] K. J. Eskola, H. Paukkunen, and C. A. Salgado. EPS09: A New Generation of NLO and LO Nuclear Parton Distribution Functions. *JHEP*, 04:065, 2009. doi: 10.1088/1126-6708/2009/04/065.
- [89] K. Kovariik et al. nCTEQ15: Global analysis of nuclear parton distributions with uncertainties in the CTEQ framework. *Phys. Rev. D*, 93:085037, Apr 2016. doi: 10.1103/PhysRevD.93.085037.
- [90] I. Balitsky. Operator expansion for high-energy scattering. *Nucl. Phys.*, B463:99–160, 1996. doi: 10.1016/0550-3213(95)00638-9.
- [91] Y. V. Kovchegov. Unitarization of the BFKL pomeron on a nucleus. *Phys. Rev. D*, 61:074018, 2000. doi: 10.1103/PhysRevD.61.074018.
- [92] L.V. Gribov, E.M. Levin, and M.G. Ryskin. Semihard processes in QCD. *Phys. Rep.*, 100(1):1 – 150, 1983. ISSN 0370-1573. doi: 10.1016/0370-1573(83)90022-4.
- [93] F. Arleo, S. Peigné, and T. Sami. Revisiting scaling properties of medium-induced gluon radiation. *Phys. Rev. D*, 83:114036, 2011. doi: 10.1103/PhysRevD.83.114036.

- [94] E. G. Ferreiro, F. Fleuret, J.-P. Lansberg, and A. Rakotozafindrabe. Impact of the Nuclear Modification of the Gluon Densities on  $J/\psi$  production in  $p\text{Pb}$  collisions at  $\sqrt{s_{\text{NN}}} = 5$  TeV. *Phys. Rev. C*, 88(4):047901, 2013. doi: 10.1103/PhysRevC.88.047901.
- [95] C. Lourenco, R. Vogt, and H. K. Woehri. Energy dependence of  $J/\psi$  absorption in proton-nucleus collisions. *JHEP*, 02:014, 2009. doi: 10.1088/1126-6708/2009/02/014.
- [96] N. Armesto and A. Capella. A Quantitative reanalysis of  $J/\psi$  suppression in nuclear collisions. *Phys. Lett.*, B430:23–31, 1998. doi: 10.1016/S0370-2693(98)00487-0.
- [97] R. Vogt.  $J/\psi$  production and suppression. *Phys. Rep.*, 310(4):197 – 260, 1999. ISSN 0370-1573. doi: 10.1016/S0370-1573(98)00074-X.
- [98] NA3 Collaboration. Experimental  $J/\psi$  hadronic production from 150 to 280 GeV/c. *Z. Phys. C*, 20(CERN-EP-83-86):101–116. 43 p, Jun 1983. doi: 10.1007/BF01573213.
- [99] NA50 Collaboration.  $J/\psi$  and  $\psi'$  production and their normal nuclear absorption in proton-nucleus collisions at 400 GeV. *Eur. Phys. J. C*, 48(CERN-PH-EP-2006-018. CERN-PH-EP-2006-018. 2):329–341. 21 p, Jul 2006. doi: 10.1140/epjc/s10052-006-0079-4.
- [100] NA50 Collaboration. Charmonium production and nuclear absorption in p-A interactions at 450 GeV. *Eur. Phys. J. C*, 33(CERN-EP-2003-037):31–40. 16 p, Jun 2003. doi: 10.1140/epjc/s2003-01539-y.
- [101] E866 Collaboration. Measurement of  $J/\psi$  and  $\psi'$  Suppression in pA Collisions at 800 GeV/c. *Phys. Rev. Lett.*, 84(nucl-ex/9909007. LA-UR-99-5007):3256–3260. 5 p, Sep 1999. doi: 10.1103/PhysRevLett.84.3256.
- [102] HERA-B Collaboration. Kinematic distributions and nuclear effects of  $J/\psi$  production in 920 GeV fixed-target proton-nucleus collisions. *Eur. Phys. J. C*, 60:525–542, 2009. doi: 10.1140/epjc/s10052-009-0965-7.

- [103] PHENIX Collaboration. Cold Nuclear Matter Effects on  $J/\psi$  as Constrained by Deuteron-Gold Measurements at  $\sqrt{s_{\text{NN}}} = 200\text{-GeV}$ . *Phys. Rev. C*, 77:024912, 2008. doi: 10.1103/PhysRevC.77.024912,10.1103/PhysRevC.79.059901. [Erratum: *Phys. Rev. C*79,059901(2009)].
- [104] B. Chen and J. Zhao. Bottomonium continuous production from unequilibrium bottom quarks in ultrarelativistic heavy ion collisions. *Phys. Lett. B*, 772, 04 2017. doi: 10.1016/j.physletb.2017.07.054.
- [105] ALICE Collaboration.  $J/\psi$  production and nuclear effects in p-Pb collisions at  $\sqrt{s_{\text{NN}}} = 5.02\text{ TeV}$ . *JHEP*, 02:073, 2014. doi: 10.1007/JHEP02(2014)073.
- [106] ALICE Collaboration. Suppression of  $\psi(2S)$  production in p-Pb collisions at  $\sqrt{s_{\text{NN}}} = 5.02\text{ TeV}$ . *JHEP*, 12:073, 2014. doi: 10.1007/JHEP12(2014)073.
- [107] B. S. Kasmaei and M. Strickland. Dilepton production and elliptic flow from an anisotropic quark-gluon plasma. *Phys. Rev. D*, 99:034015, Feb 2019. doi: 10.1103/PhysRevD.99.034015.
- [108] L. D. McLerran and T. Toimela. Photon and dilepton emission from the quark-gluon plasma: Some general considerations. *Phys. Rev. D*, 31:545–563, Feb 1985. doi: 10.1103/PhysRevD.31.545.
- [109] B. Krouppa, A. Rothkopf, and M. Strickland. Bottomonium suppression using a lattice QCD vetted potential. *Phys. Rev. D*, 97(1):016017, 2018. doi: 10.1103/PhysRevD.97.016017.
- [110] A. Emerick, X. Zhao, and R. Rapp. Bottomonia in the Quark-Gluon Plasma and their Production at RHIC and LHC. *Eur. Phys. J. A*, 48(72), 2012. doi: 10.1140/epja/i2012-12072-y.
- [111] CMS Collaboration. Suppression of Excited  $\Upsilon$  States Relative to the Ground State

- in Pb-Pb Collisions at  $\sqrt{s_{\text{NN}}}=5.02\text{TeV}$ . *Phys. Rev. Lett.*, 120(14):142301, 2018. doi: 10.1103/PhysRevLett.120.142301.
- [112] R. Gavai et al. Quarkonium production in hadronic collisions. *Int. J. Mod. Phys.*, A10: 3043–3070, 1995. doi: 10.1142/S0217751X95001443.
- [113] H. S. Chung. Review of quarkonium production: status and prospects. In *13th Conference on Quark Confinement and the Hadron Spectrum (Confinement XIII) Maynooth, Ireland, July 31-August 6, 2018*, 2018.
- [114] ALICE Collaboration.  $J/\psi$  Production as a Function of Charged Particle Multiplicity in  $pp$  Collisions at  $\sqrt{s} = 7$  TeV. *Phys. Lett.*, B712:165–175, 2012. doi: 10.1016/j.physletb.2012.04.052.
- [115] CMS Collaboration. Event activity dependence of  $\Upsilon(\text{nS})$  production in  $\sqrt{s_{\text{NN}}}=5.02$  TeV pPb and  $\sqrt{s}=2.76$  TeV pp collisions. *JHEP*, 04:103, 2014. doi: 10.1007/JHEP04(2014)103.
- [116] CMS Collaboration. Measurement of prompt  $\psi(2\text{S})$  production cross sections in proton-lead and proton-proton collisions at  $\sqrt{s_{\text{NN}}} = 5.02$  TeV. 2018. doi: 10.3204/PUBDB-2018-02204.
- [117] CMS Collaboration. Measurement of prompt and nonprompt  $J/\psi$  production in pp and pPb collisions at  $\sqrt{s_{\text{NN}}} = 5.02$  TeV. *Eur. Phys. J. C*, 77(4):269, 2017. doi: 10.1140/epjc/s10052-017-4828-3.
- [118] ALICE Collaboration. Suppression of  $\Upsilon(1\text{S})$  at forward rapidity in Pb–Pb collisions at  $\sqrt{s_{\text{NN}}} = 2.76$  TeV. *Phys. Lett. B*, 738:361, 2014. doi: 10.1016/j.physletb.2014.10.001.
- [119] PHENIX Collaboration.  $J/\psi$  Production vs Centrality, Transverse Momentum, and Rapidity in Au+Au Collisions at  $\sqrt{s_{\text{NN}}}= 200$  GeV. *Phys. Rev. Lett.*, 98:232301, 2007. doi: 10.1103/PhysRevLett.98.232301.

- [120] STAR Collaboration. Energy dependence of  $J/\psi$  production in Au+Au collisions at  $\sqrt{s_{\text{NN}}} = 39, 62.4$  and 200 GeV. *Phys. Lett. B*, 771:13, 2017. doi: 10.1016/j.physletb.2017.04.078.
- [121] STAR Collaboration. Suppression of  $\Upsilon$  production in d+Au and Au+Au collisions at  $\sqrt{s_{\text{NN}}}=200$  GeV. *Phys. Lett. B*, 735:127, 2014. doi: 10.1016/j.physletb.2014.06.028. [Erratum: 10.1016/j.physletb.2015.01.046].
- [122] CMS Collaboration. Strong suppression of  $\Upsilon$  excited states in PbPb collisions at  $\sqrt{s_{\text{NN}}} = 5.02$  TeV. *Phys. Rev. Lett.*, 120:142301, 2018. doi: 10.1103/PhysRevLett.120.142301.
- [123] ALICE Collaboration.  $\Upsilon$  suppression at forward rapidity in Pb-Pb collisions at  $\sqrt{s_{\text{NN}}}=5.02$  TeV. 2018.
- [124] CMS Collaboration. Relative modification of prompt  $\psi(2S)$  and  $J/\psi$  yields from pp to PbPb collision at  $\sqrt{s_{\text{NN}}}=5.02$  TeV. *Phys. Rev. Lett.*, 188:162301, 2017. doi: 10.1103/PhysRevLett.118.162301.
- [125] CMS Collaboration. Measurement of prompt and nonprompt charmonium suppression in PbPb collisions at 5.02 TeV. *Eur. Phys. J. C*, 78(6):509, 2018. doi: 10.1140/epjc/s10052-018-5950-6.
- [126] S. MYERS. The large hadron collider 2008–2013. *Int. J. Mod. Phys. A*, 28(25):1330035, 2013. doi: 10.1142/S0217751X13300354.
- [127] CMS Collaboration. Technical proposal for the upgrade of the CMS detector through 2020. Technical Report CERN-LHCC-2011-006. LHCC-P-004, Jun 2011. URL <https://cds.cern.ch/record/1355706>.
- [128] A. Heister. Phase I and Phase II CMS upgrade. In *Proceedings, 14th ICATPP Conference on Astroparticle, Particle, Space Physics and Detectors for Physics Applications*

- (*ICATPP 2013*): Como, Italy, September 23-27, 2013, pages 354–359, 2014. doi: 10.1142/9789814603164\_0054.
- [129] A. Saha. Phase 1 upgrade of the CMS pixel detector. *JINST*, 12(02):C02033–C02033, feb 2017. doi: 10.1088/1748-0221/12/02/c02033.
- [130] S. I. Cooper. Phase I Upgrade of the CMS Hadron Calorimeter. *Nuclear and Particle Physics Proceedings*, 273-275:1002 – 1007, 2016. ISSN 2405-6014. doi: 10.1016/j.nuclphysbps.2015.09.157. 37th International Conference on High Energy Physics (ICHEP).
- [131] C. Loizides, J. Nagle, and P. Steinberg. Improved version of the PHOBOS Glauber Monte Carlo. *SoftwareX*, 1(2):13–18, 2015. doi: 10.1016/j.softx.2015.05.001.
- [132] CMS Collaboration. Strong suppression of  $\Upsilon$  excited states in PbPb collisions at  $\sqrt{s_{\text{NN}}}$  = 5.02 TeV. Technical report, CERN, Geneva, 2016. URL <http://cds.cern.ch/record/2217909>.
- [133] D. E. Groom, N. V. Mokhov, and S. I. Striganov. Muon stopping power and range tables 10 mev–100 tev. *At. Data Nucl. Data Tables*, 78(2):183 – 356, 2001. ISSN 0092-640X. doi: 10.1006/adnd.2001.0861.
- [134] T. Sjöstrand et al. An Introduction to PYTHIA 8.2. *Comput. Phys. Commun.*, 191: 159–177, 2015. doi: 10.1016/j.cpc.2015.01.024.
- [135] S. Agostinelli et al. GEANT4: A Simulation toolkit. *Nucl. Instrum. Meth.*, A506: 250–303, 2003. doi: 10.1016/S0168-9002(03)01368-8.
- [136] I. P. Lokhtin and A. M. Snigirev. A model of jet quenching in ultrarelativistic heavy ion collisions and high- $p_{\text{T}}$  hadron spectra at RHIC. *Eur. Phys. J. C*, 45:211, 2006. doi: 10.1140/epjc/s2005-02426-3.

- [137] CMS Collaboration. Description and performance of track and primary-vertex reconstruction with the CMS tracker. *JINST*, 9:P10009, 2014. doi: 10.1088/1748-0221/9/10/P10009.
- [138] CMS Collaboration. Transverse momentum and pseudorapidity distributions of charged hadrons in pp collisions at  $\sqrt{s} = 0.9$  and 2.36 TeV. *JHEP*, 02:041, 2010. doi: 10.1007/JHEP02(2010)041.
- [139] CMS Collaboration. Observation and studies of jet quenching in PbPb collisions at nucleon-nucleon center-of-mass energy = 2.76 TeV. *Phys. Rev. C*, 84:024906, 2011. doi: 10.1103/PhysRevC.84.024906.
- [140] CMS Collaboration. Charged-particle nuclear modification factors in PbPb and pPb collisions at  $\sqrt{s_{NN}} = 5.02$  TeV. *JHEP*, 04:039, 2017. doi: 10.1007/JHEP04(2017)039.
- [141] G. Aarts et al. Heavy-flavor production and medium properties in high-energy nuclear collisions – What next? *Eur. Phys. J. A*, 53:93, 2017. doi: 10.1140/epja/i2017-12282-9.
- [142] M. J. Oreglia. *A study of the reactions  $\psi' \rightarrow \gamma\gamma\psi$* . PhD thesis, Stanford University, 1980. URL <http://www.slac.stanford.edu/cgi-wrap/getdoc/slac-r-236.pdf>. SLAC Report R-236 p.184.
- [143] Particle Data Group. Review of particle physics. *Chin. Phys. C*, 40:100001, 2016. doi: 10.1088/1674-1137/40/10/100001.
- [144] M. L. Miller, K. Reygers, S. J. Sanders, and P. Steinberg. Glauber modeling in high energy nuclear collisions. *Ann. Rev. Nucl. Part. Sci.*, 57:205, 2007. doi: 10.1146/annurev.nucl.57.090506.123020.
- [145] CMS Collaboration. CMS luminosity calibration for the pp reference run at  $\sqrt{s} = 5.02$  TeV. CMS Physics Analysis Summary CMS-PAS-LUM-16-001, 2016. URL <https://cds.cern.ch/record/2235781>.

- [146] G. J. Feldman and R. D. Cousins. A unified approach to the classical statistical analysis of small signals. *Phys. Rev. D*, 57:3873, 1998. doi: 10.1103/PhysRevD.57.3873.
- [147] B. Krouppa, R. Ryblewski, and M. Strickland. Bottomonia suppression in 2.76 TeV Pb–Pb collisions. *Phys. Rev. C*, 92:061901, 2015. doi: 10.1103/PhysRevC.92.061901.
- [148] ALICE Collaboration. Differential studies of inclusive  $J/\psi$  and  $\psi(2S)$  production at forward rapidity in Pb–Pb collisions at  $\sqrt{s_{\text{NN}}} = 2.76$  TeV. *JHEP*, 05:179, 2016. doi: 10.1007/JHEP05(2016)179.
- [149] CMS Collaboration. Measurement of prompt  $\psi(2S) \rightarrow J/\psi$  yield ratios in Pb-Pb and  $p$ - $p$  collisions at  $\sqrt{s_{\text{NN}}} = 2.76$  TeV. *Phys. Rev. Lett.*, 113:262301, 2014. doi: 10.1103/PhysRevLett.113.262301.
- [150] E. Barberio and Z. Was. PHOTOS - a universal Monte Carlo for QED radiative corrections: version 2.0. *Comput. Phys. Commun.*, 79(2):291 – 308, 1994. ISSN 0010-4655. doi: 10.1016/0010-4655(94)90074-4.
- [151] CMS Collaboration. Dimuon performance studies in 2015 5.02 TeV pp and PbPb Data. Technical report, CERN, Geneva, 2016. URL <http://cms.cern.ch/iCMS/user/noteinfo?cmsnoteid=CMS%20AN-2016/048>.
- [152] M. Tanabashi et al. Particle Data Group. *Phys. Rev. D*, 98:030001, 2018.
- [153] Adam N et al. Generic Tag and Probe Tool for Measuring Efficiency at CMS with Early Data. CMS Note 2009/111, 2009. URL [http://cms.cern.ch/iCMS/jsp/openfile.jsp?tp=draft&files=AN2009\\_111\\_v1.pdf](http://cms.cern.ch/iCMS/jsp/openfile.jsp?tp=draft&files=AN2009_111_v1.pdf).
- [154] A. G. S. Leiton et al. Muon performance studies in 2015 5.02 TeV pp and PbPb Data. CMS Note 2016/048, 2016. URL <http://cds.cern.ch/record/2217888>.
- [155] M. Jo et al. Measurement of prompt and nonprompt  $J/\psi$  production in pp and pPb collisions at  $\sqrt{s_{\text{NN}}} = 5.02$  TeV. CMS Note 2013/346, 2013. URL <http://cms.cern.ch/iCMS/user/noteinfo?cmsnoteid=CMS%20AN-2013/346>.

- [156] W. Busza, K. Rajagopal, and W. van der Schee. Heavy Ion Collisions: The Big Picture, and the Big Questions. *Ann. Rev. Nucl. Part. Sci.*, 68:339–376, 2018. doi: 10.1146/annurev-nucl-101917-020852.
- [157] M. Nahrgang et al. Elliptic and triangular flow of heavy flavor in heavy-ion collisions. *Phys. Rev. C*, 91(1):014904, 2015. doi: 10.1103/PhysRevC.91.014904.
- [158] G. D. Moore and D. Teaney. How much do heavy quarks thermalize in a heavy ion collision? *Phys. Rev. C*, 71:064904, 2005. doi: 10.1103/PhysRevC.71.064904.
- [159] H. van Hees and R. Rapp. Thermalization of heavy quarks in the quark-gluon plasma. *Phys. Rev. C*, 71:034907, 2005. doi: 10.1103/PhysRevC.71.034907.
- [160] J. Uphoff, O. Fochler, Z. Xu, and C. Greiner. Elliptic Flow and Energy Loss of Heavy Quarks in Ultra-Relativistic heavy Ion Collisions. *Phys. Rev. C*, 84:024908, 2011. doi: 10.1103/PhysRevC.84.024908.